# Topics in Core-Collapse Supernova Theory: The Formation of Black Holes and the Transport of Neutrinos

Thesis by

Evan Patrick O'Connor

In Partial Fulfillment of the Requirements

for the Degree of

Doctor of Philosophy

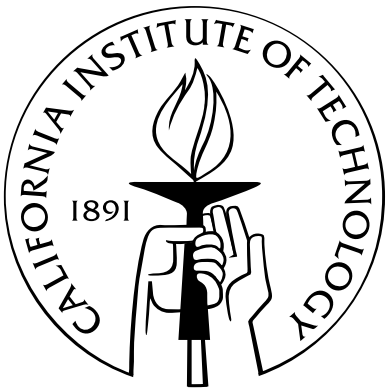


California Institute of Technology

Pasadena, California

2012

(Defended May 21, 2012)

# Acknowledgements

First and foremost, I have the pleasure of acknowledging and thanking my advisor, Christian Ott, for his commitment and contribution to my research over the last four years. Christian, your attention to detail, desire for perfection, exceptional physical insight, and unwavering stance against the phrase *direct black hole formation* are qualities I admire and strive to reproduce in my own research. From our very first meeting, Christian has been an staunch advocate for open science, a philosophy that he has instilled in me throughout my time at Caltech and one that I plan on maintaining in my future career.

I also thank the love of my life. Erin, there are so many reasons to be thankful to you. You are the best part of each and every day. On the science front, thank you for all our neutrino discussions, enlightening me on so many different aspects of neutrinos, and keeping my theoretical meanderings grounded in experimental reality. I am indebted to you for all your support, encouragement, persistence, and love throughout the writing of this thesis and I look forward to repaying that debt soon.

Thank you to my family, as always, your constant encouragement and support in everything I do is greatly appreciated. I am so glad that most of you had a chance to come visit me in Pasadena at some point throughout my time here. I am very much looking forward to moving closer to home, even if it does mean the return of a real winter.

I would like to thank all of my collaborators and scientific mentors. Notably, Christian Ott and Luc Dessart who have help contribute to the work presented in this thesis; but also those whom I have worked/collaborated with throughout my graduate career, in particular, Ernazar Abdikamalov, Basudeb Dasgupta, Gang Shen, and Chuck Horowitz, but of course many others. During my first year at UPEI, Derek Lawther converted me from Engineering to Physics with his timely letter encouraging me to pursue physics. Later on, Michelle Cottreau, Heather Hughes, and Sean Dougherty slowly converted me to astrophysics, and finally Achim Schwenk brought me away from the dark side and into the realm of theoretical astrophysics. Many of my research techniques, principles, and talents stem from my undergraduate honours advisor Sheldon Opps, for which I will be forever grateful. A special thanks to James Polson, and a later nudge by Achim Schwenk, for suggesting that I reach for the top when searching for graduate schools.

To my fellow Tapir graduate students, particularly my awesome officemate Jeff Kaplan; the Tapir postdocs; and the Tapir faculty and staff: thanks for all the interesting discussions, Thursday enlightenment sessions, helpful advice, and support. I would also like to thank all of the friends I have made at Caltech over the last five years. TNDs are on my list as one of the best memories of Caltech—I will miss them and you.

# Abstract

Core-Collapse Supernovae are one of the most complex astrophysical systems in the universe. They deeply entwine aspects of physics and astrophysics that are rarely side by side in nature. To accurately model core-collapse supernovae one must self-consistently combine general relativity, nuclear physics, neutrino physics, and magneto-hydrodynamics in a symmetry-free computational environment. This is a challenging task, as each one of these aspects on its own is an area of great study. We take an open approach in an effort to encourage collaboration in the core-collapse supernovae community.

In this thesis, we develop a new open-source general-relativistic spherically-symmetric Eulerian hydrodynamics code for studying stellar collapse, protoneutron star formation, and evolution until black hole formation. `GR1D` includes support for finite temperature equations of state and an efficient and qualitatively accurate treatment of neutrino leakage. `GR1D` implements spherically-symmetric rotation, allowing for the study of slowly rotating stellar collapse. `GR1D` is available at http://www.stellarcollapse.org

We use `GR1D` to perform an extensive study of black hole formation in failing core-collapse supernovae. Over 100 presupernova models from various sources are used in over 700 total simulations. We systematically explore the dependence of black hole formation on the input physics: initial zero-age main sequence (ZAMS) mass and metallicity, nuclear equation of state, rotation, and stellar mass loss rates. Assuming the core-collapse supernova mechanism fails and a black hole forms, we find that the outcome, for a given equation of state, can be estimated, to first order, by a single parameter, the compactness of the stellar core at bounce. By comparing the protoneutron star structure at the onset of gravitational instability with solutions of the Tolman-Oppenheimer-Volkof equations, we find that thermal pressure support in the outer protoneutron star core is responsible for raising the maximum protoneutron star mass by up to 25% above the cold neutron star value. By artificially increasing neutrino heating, we find the critical neutrino heating efficiency required for exploding a given progenitor structure and connect these findings with ZAMS conditions. This establishes, albeit approximately, for the first time based on actual collapse simulations, the mapping between ZAMS parameters and the outcome of core collapse.

We also use `GR1D` to study proposed progenitors of long-duration $\gamma$-ray bursts. We find that many

of the proposed progenitors have core structures similar to garden-variety core-collapse supernovae. These are not expected to form black holes, a key ingredient of the collapsar model of long-duration $\gamma$-ray bursts. The small fraction of proposed progenitors that are compact enough to form black holes have fast rotating iron cores, making them prone to a magneto-rotational explosion and the formation of a protomagnetar rather than a black hole.

Finally, we present preliminary work on a fully general-relativistic neutrino transport code and neutrino-interaction library. Following along with the trends explored in our black hole formation study, we look at the dependence of the neutrino observables on the bounce compactness. We find clear relationships that will allow us to extract details of the core structure from the next galactic supernova. Following the open approach of `GR1D`, the neutrino transport code will be made open-source upon completion. The open-source neutrino-interaction library, `NuLib`, is already available at http://www.nulib.org.

# Contents

# List of Figures

# List of Tables

# Chapter 1

# Overview

## 1.1 Main Results of this Thesis

This thesis focuses on the formation of black holes in failing core-collapse supernovae. While black holes have been studied in the context of core collapse for over 40 years, there has been no systematic examination of black hole formation in stellar core collapse. Perhaps the foremost reason why such a study has not been performed is we do not have a compelling theory for the core-collapse supernova central engine. However, regardless of how core-collapse supernovae explode, we know that they do and that they robustly explode for garden-variety massive stars. Also, it is most likely that some core-collapse supernovae fail to explode; we see stellar mass black holes in binary star systems throughout the galaxy. While supernova theory may not yet be at a point where we can say conclusively whether a given massive star will end its life in an explosion or in the formation of black hole, it is worth exploring whether we can make statements on what conditions make black hole formation more likely. This is what we attempt in this thesis.

### 1.1.1 `GR1D` and Other Open-Source Codes

To explore black hole formation in stellar collapse one needs several pieces of technology. One of the major byproducts of this thesis is `GR1D`, an open-source, general-relativistic, Eulerian hydrodynamics code for studying the formation of neutron stars and black holes in the context of stellar collapse. This open-source code was the first of its kind in the core-collapse community and an attempt to encourage openness in an otherwise very secretive community. Having `GR1D` open-source also removes a significant hurdle for new researchers who want to study core collapse. In addition to `GR1D`, several other open-source initiatives are either a part of the thesis (such as `NuLib`) or have been contributed to during the development of `GR1D` (`EOSdriver`, `EOSmaker` and several equation of state tables). All of these are available on http://www.stellarcollapse.org.

As of the writing of this thesis many studies have independently made use of the open-source

codes we have made available. In particular, Dessart et al. (2010) have made direct use of `GR1D` to collapse iron cores of massive stars, which they then proceed to blow up and follow through an explosion. Fernández (2012), Shen et al. (2011b) have used our equation of state tables and routines. There are also several more studies that are in the process of using our technology and expect interesting results forthcoming.

One of the other motivations for developing a spherically-symmetric code is to have a test bed for multidimensional implementations of supernova microphysics. We have already ported the neutrino leakage scheme in `GR1D` to the 3+1 general relativistic code `Zelmani`. The first use of this implementation has been to study the gravitational wave signature of rotating-core collapse and how it is affected by the neutrino deleptonization and energy leakage in the early postbounce phase (Ott et al. 2012).

### 1.1.2 Black Holes in Stellar Collapse

Work in this thesis has revealed for the first time that if the core-collapse supernova shock fails to be reenergized and a black hole forms, its properties can be easily predicted from one parameter, $\xi_{2.5}$, extracted from the structure of the progenitor star at core bounce and the chosen equation of state. This is something that could only have been realized by performing a systematic study of hundreds of progenitor stars—one or two detailed simulations of select models is not enough to uncover the systematic trends in progenitor structure and equation of state presented in this thesis. We find that the black hole formation time is essentially set by the free fall time of a critical mass element whose mass is similar to assumed equation of state's maximum mass. This time is unlikely to be affected by multidimensional effects because the accretion onto the central protoneutron star is supersonic and will remain roughly spherical for nonrotating or slowly rotating progenitors even in multiple dimensions.

The mass at which the protoneutron star will become unstable and collapse to a black hole depends on the equation of state and also on $\xi_{2.5}$. Progenitors with higher values of $\xi_{2.5}$ have larger thermal support. This can increase the maximum mass by up to 25% above the cold neutron star value. The extent of the thermal support also depends on the equation of state.

We further exploited the idea of discovering systematic trends by launching artificial neutrino-driven explosions and measuring how fundamental properties of the neutrino mechanism depend on the progenitor model. We find that for progenitors with high compactness, i.e., those that form black holes the fastest, the heating efficiency needed for a successful neutrino-driven explosion increases. This is because a explosion must be launched earlier to avoid black hole formation. If black hole formation occurs at late times, the neutrino mechanism is allowed to work after the accretion rate drops and therefore can be less efficient. We make a prediction, the first based on a systematic study of black hole formation, about which progenitor structures have the predisposition to black

hole formation via a failed core-collapse supernova. By linking a given progenitor core structure back to the zero-age main sequence properties of the star we can then make predictions on the number of failed core-collapse supernovae. For solar metallicity stars we predict that 0%–7% of all stellar collapses will fail. For very low or zero metallicity progenitors, the percentage can reach $\sim 15\%$. The large range of the predicted percentage of failed supernovae in solar metallicity stars is due to the uncertainty in massive star evolution, in particular the mass loss rates of very massive stars. Interestingly, but not surprisingly based on our results, we do not predict a single mass cut for successful/failed core-collapse supernovae. This is due to the complicated mapping of the initial conditions on the zero-age main sequence to the presupernova structure.

A rapidly spinning black hole is the central building block in the collapsar mechanism for long duration $\gamma$-ray bursts. We explore the effect of rotation in several models by applying a parameterized rotation law and seeing how the black hole formation properties are affected. For high rotation, we find that the initial dimensionless spin of the black hole may be limited by nonaxisymmetric instabilities. We then apply our black hole prediction techniques to the available set of proposed progenitors of long-duration $\gamma$-ray bursts. Surprisingly, we find that most proposed progenitors are no more likely to form black holes than the standard progenitors of garden-variety supernovae. Of the few models that have high enough compactness to potentially form a black hole, all of them have a huge amount of rotation. This makes them prone to a magneto-rotational induced explosion, which could very likely prevent black hole formation. It is imperative that one considers not just the angular momentum distribution but also the bounce compactness when judging the merits of a particular model as a progenitor of a long-duration $\gamma$-ray burst.

## 1.2 Related Work Not Contained in this Thesis

While the focus of my research has been on black hole formation and the development of techniques for neutrino transport in core-collapse supernovae, I have made contributions to many related works during my time at Caltech. I briefly describe these below.

With the supernova group at Caltech, led by Christian Ott and using the fully general-relativistic three-dimensional stellar collapse code `Zelmani`, I have contributed to the study of black hole formation and the associated gravitational wave signature in the core collapse of a rotating massive star (Ott et al. 2011). This paper was the first study to self-consistently evolve a presupernova model from the onset of core collapse, and track the evolution through both the protoneutron star and black hole formation phases. We find that for rotating progenitors, a unique gravitational waveform is predicted from failed supernovae.

We have also investigated both the neutrino and gravitational wave signature, and the correlations between them, in the early postbounce phase of rotating iron core collapse (Ott et al. 2012).

This study makes use of the equations of state and the leakage scheme developed as part of this thesis. The leakage scheme is implemented in `Zelmani` via a ray-by-ray approach. We find that a strong quadrupolar mode of oscillation is induced due to the rotation-induced oblate structure of the collapsing iron core. This quadrupolar mode gives rise to gravitational waves and variations in the neutrino luminosity that correlate with the fundamental mode. We make estimates on the detectability of such signals.

Along with Basudeb Dasgupta (OSU) and Christian Ott, I have investigated the role of collective neutrino oscillations on the core-collapse supernova mechanism (Dasgupta et al. 2012) by performing two-dimensional Newtonian simulations with spectral neutrino transport in `VULCAN/2D`. We explore the possibility that such oscillations may increase the amount of neutrino heating by inducing a swap of the softer electron-type neutrino spectra with the hard heavy-lepton neutrino spectra below the gain region in the early postbounce phase. We find that for typical early postbounce conditions such oscillations do not occur until large radii, and therefore are unlikely to influence neutrino heating and therefore the neutrino-driven explosion mechanism.

Finally, with Gang Shen (LANL,IU) and Chuck Horowitz (IU), I have helped develop and implement finite temperature equations of state for use in astrophysical simulations (Shen et al. 2011a). In this paper we take a relativistic mean-field interaction that reproduces many nuclear parameters and better matches the astrophysical constraints placed on the nuclear equation of state.

## 1.3 Thesis Structure

This thesis in divided into four main chapters in addition to this overview.

1. Chapter 2 serves as a general introduction to supernovae with a focus on the theory and observational signatures of core-collapse supernovae. We leave specific introductions, such as literature reviews on black hole formation and neutrino transport, to the individual chapters.

2. In Chapter 3, we present `GR1D`, the code developed as part of this thesis for studying black hole formation in stellar collapse. This includes details on `GR1D`'s neutrino leakage scheme, how we treat rotation in `GR1D`, and our equation of state implementation. It contains several code tests, starting with basic hydrodynamics and moving up through relativistic hydrodynamics to general-relativistic hydrodynamics and black hole formation. Appendix A and Appendix B are associated with this chapter, they provide a detailed derivation of `GR1D`'s evolution equations.

3. Chapter 4 presents the various studies we have done with `GR1D` on black hole formation. We divide the chapter into two main sections, one focusing on nonrotating models and the other focusing on rotating models. In the nonrotating section we perform over 700 stellar collapse simulations utilizing four equations of state and over 100 presupernova models. We

systematically explore black hole formation and its dependence on progenitor structure and the nuclear equation of state. We explore how black hole formation may effect the neutrino mechanism, and make predictions on black hole populations. For the rotation section of this chapter we explore the affect of rotation on black hole formation and on the potential development of nonaxisymmetric instabilities. We then use actual rotating progenitors from stellar evolution calculations and assess their potential for black hole formation and their prospects as progenitors of long-duration $\gamma$-ray bursts.

4. In Chapter 5, we present a new neutrino transport code for studying core-collapse supernovae. The scheme evolves the first two moments of the neutrino distribution function, making the approximation that the anisotropy in the distribution function is small. The scheme is designed with multidimensional simulations in mind. This chapter includes several code tests, a comparison to full Boltzmann neutrino transport simulations, and a preliminary look at the progenitor dependence of observable neutrino properties. This chapter also sets the stage for future work. Appendix C is associated with this chapter; it provides full details of all the neutrino interactions currently included in our neutrino transport scheme. This Appendix forms the basis for `NuLib`, our open-source neutrino interaction library.

# Chapter 2

# Introduction

The field of core-collapse supernova theory arguably began with the groundbreaking prediction of Baade and Zwicky (1934b) that supernovae represent the transition of ordinary stars to neutron stars. This remarkable insight came a mere two years after the discovery of the neutron by Chadwick (1932) and the prediction of neutron stars by Landau (Bethe 1990, Landau 1932). Around this time at Caltech, Zwicky started to systematically observe galaxies to discover supernovae, finding $\sim$20 in the decade following his and Baade's seminal paper. In the present day, we have automated supernova observing factories, like the Caltech-led Palomar Transient Factory (PTF) (Law et al. 2009), that now observe *at least* one supernova a day. The theory behind supernovae has come a long way since Baade & Zwicky (Baade and Zwicky 1934a,b). A lot of the questions one can ask have answers, however, some fundamental questions still remain unsolved. In this Chapter, I aim to describe what we know, and what is still unknown about supernovae, I will focus on supernovae that are associated with the collapse of the iron core in evolved massive stars.

## 2.1 Observations of Core-Collapse Supernovae

It soon became clear in the early days of supernova observations that (at least) two types of supernovae existed: Type-I, which have no observable hydrogen lines, and Type-II, which do have strong hydrogen lines. Observers have maintained this convention of classifying supernovae, although there are now many subcategories to both Type-I and Type-II supernovae.

*Type-Ia supernovae*, which in the volume-limited Lick Observatory Supernova Search (LOSS, Li et al. 2011) comprise $\sim$24% of all supernovae, are supernovae that contain no hydrogen absorption lines in their spectra, but do display strong silicon II absorption lines. These supernovae are thermonuclear explosions of carbon-oxygen white dwarfs. One of the two big unanswered questions in Type-Ia supernova theory is, what is the origin of Type-Ia supernova progenitors? Two competing theories include the double-degenerate model and the single-degenerate model. In the double-degenerate model, gravitational radiation causes a binary white-dwarf system to inspiral over

time and eventually merge; this potentially leaves a hypermassive white dwarf that is initially thermally supported above the Chandrasekhar mass. The settling of the high-entropy merger remnants onto the inner core slowly raises the temperature, eventually triggering the runaway thermonuclear explosion. The single-degenerate model consists of a white dwarf accreting from a companion star, e.g., a subgiant or red giant. As more material is accreted, the central temperature increases and, like in the double-degenerate scenario, a runaway explosion is triggered. The other large uncertainty in Type-Ia supernova theory is the process by which the carbon is ignited (Hillebrandt and Niemeyer 2000). Simulations have shown that in a pure deflagration, i.e., a subsonic burning front, the outer layers of the white dwarf expand before ignited. This leads to too many intermediate mass elements compared to what is observed. However, a pure detonation, a supersonic burning front, has the opposite problem. It produces too little intermediate mass elements and instead forming too many iron-group nuclei. The delayed detonation model, where a deflagration transitions into a detonation can be made to reproduce observed abundances, but the physical mechanism of the transition is unclear. Type-Ia supernovae are not the topic of this thesis; we refer the reader to reviews Hillebrandt and Niemeyer (2000), Wang and Han (2012) on Type-Ia supernovae for more detailed information.

All of the remaining types and subtypes of supernovae stem from essentially the same process, the collapse of the iron core in an evolved massive star, it is the central engine of these supernovae that is of interest in this thesis. Before delving further into the inner workings of a core-collapse supernova in the following section, I will briefly describe the various electromagnetic observational signatures of core-collapse supernovae. The two other subcategories of Type-I supernovae classify the hydrogen-poor core-collapse events. These two subcategories encompass $\sim 19\%$ of all supernovae. The remaining supernovae are of Type-II and comprise $\sim 54\%$ of observed supernovae in the LOSS survey. Type-II are divided into four main categories, but as previously mentioned, all contain strong hydrogen lines in their spectra.

*Type-Ib* and *Type-Ic supernovae*, like the Type-Ia supernovae do not shown hydrogen lines in their spectra. They are distinguished from Type-Ia supernovae by the lack of silicon II lines. Type-Ic supernovae differ from Type-Ib supernovae by the lack of helium lines in their spectra. This suggests that Type-Ib supernovae have lost their hydrogen envelope during an earlier evolutionary stage, while Type-Ic supernovae have lost both the hydrogen and helium envelopes. In the LOSS survey, Type-Ib and Type-Ic supernovae comprise $\sim 19\%$ of all supernovae. Of these 19%, roughly 21% are of Type-Ib, 54% are of Type-Ic and the remaining 25% are classified as Type-Ibc-pec. Type-Ibc-pec is a catchall category for peculiar supernovae that lack hydrogen such as the broad line Type-Ic supernovae associated with long-duration $\gamma$-ray bursts.

*Type-II Plateau (P) supernovae* are by far the most common supernovae, making up $\sim 70\%$ of Type-II supernovae and almost 40% of all supernovae (Li et al. 2011). They are distinguished from other subtypes by the presence of an optical-luminosity plateau phase lasting $\sim 100$ days. The

progenitors of Type-IIP supernovae are red supergiants with large hydrogen envelopes. They are thought to come from stars with zero-age main sequence (ZAMS) masses between $\sim$ 8.5–16.5 $M_{\odot}$ (Smartt et al. 2009). The evolution of the light curve after the shock traverses the envelope and breaks out of the star is first determined by the photosphere slowly receding in mass through the expanding hydrogen envelope as the hydrogen recombines and cools, this is the plateau phase. Later, like most supernovae, the light curve is set by the radioactive decay of $^{56}$Co, and much later by $^{44}$Ti.

*Type-IIb supernovae* are a transitional type of supernovae. Early on in the evolution there are strong hydrogen lines, however after a period of time these hydrogen lines disappear, and the supernova transitions to a Type-Ib. From single star evolution one may expect that a very small population of massive stars exists that has a thin hydrogen layer, these would naturally give rise to a Type-IIb supernovae. However the high percentage of Type-IIb in the LOSS survey, $\sim$12% of all Type-II supernovae, suggests there may be another, dominant, evolutionary channel for Type-IIb supernovae, namely mass-stripping binary stars (Claeys et al. 2011, Woosley et al. 1994).

*Type-IIn supernovae* are Type-II supernovae that show narrow emission lines. The narrow nature of the lines means that the material must be moving slowly, this is interpreted as circumstellar material being excited by the interaction with the supernova shock wave. The amount of circumstellar material suggests that large mass loss, most likely episodic, occurs very close to the time of core collapse (Kiewe et al. 2012). Type-IIn supernovae make up $\sim$9% of Type-II supernovae in the LOSS volume-limited survey.

*Type-II Linear (L) supernovae* comprise $\sim$10% of Type-II supernovae in the LOSS survey. They are characterized by the linear decline of the light curve, and the lack of a prominent plateau phase. Little is known about Type-II-L supernovae, they can be extremely luminous (Miller et al. 2009), and may have yellow supergiants as progenitors (Elias-Rosa et al. 2010).

The vast observational landscape of core-collapse supernovae arises because of the large diversity in the presupernova structure of massive stars. Type-Ib (Type-Ic) supernovae come from stars that have, through some process, lost their hydrogen (and helium) envelope; Type-IIP supernovae originate from stars have a large hydrogen envelope at the point of core collapse; and Type-IIn supernovae have, through some process, expelled large amounts of mass in the years preceding core collapse. However, regardless of which evolutionary path massive stars take, it will ultimately undergo core collapse.

## 2.2 Core-Collapse Theory

For all stars with a ZAMS mass larger than 8–10 $M_{\odot}$, the end of hydrostatic stellar evolution is marked by one of the most energetic events in the modern universe, a core-collapse supernova. The core of such massive stars become unstable to gravitational collapse when the gravitational force can

no longer be balanced by the electron degeneracy pressure of the inert iron core. Thus, the core-collapse phase of a core-collapse supernova begins. The mass of the iron core at this time is referred to as the effective Chandrasekhar mass; it is set by the electron fraction and, to a lesser extent, the thermal content. For massive stars with a ZAMS mass between $\sim$ 8–100 $M_\odot$ this can vary between 1.2–2.0 $M_\odot$. The final iron core mass, and the entire presupernova structure, is a strong function of the evolutionary history of massive stars. While a very interesting topic on its own, we must refer the reader to Woosley et al. (2002) for an in depth review of massive star evolution, also Limongi and Chieffi (2006), Paxton et al. (2011).

The iron core collapses on roughly a free fall time. This is $\mathcal{O}$(100 ms) for a typical massive star but can last up to 500 ms for the most massive iron cores. The collapsing core separates into a homologously collapsing inner core (i.e., $v \propto r$) and a supersonically in-falling outer core. The delineating point is the sonic point, where the fluid velocity equals the local sound speed. The mass coordinate of the sonic point plays an important role in core-collapse supernovae. When nuclear densities are reached the equation of state stiffens and the collapse halts. The inner core, which is in sonic contact, elastically rebounds. The kinetic energy of the in-falling inner core is converted to outgoing kinetic energy via an outward propagating pressure wave. When the pressure wave reaches the sonic point it steepens into a shock wave. This shock wave carries with it the kinetic energy of the collapsing inner core; a larger collapsing inner core delivers a larger amount of energy to the shock wave. The mass of the homologously collapsing inner core is set by matter electron fraction and temperature. The thermodynamic configuration of the matter is set by the progenitor model and the detailed deleptonization history of the core-collapse phase.

The outgoing shock wave, for a standard core-collapse supernova, is what will eventually explode the star. It is the primary goal of core-collapse theory to quantitatively describe how this shock wave leads to an explosion. Other fundamental issues in core-collapse theory include what is the final compact remnant, what heavy nuclei are synthesized, and what are the observational signatures (including electromagnetic, gravitational, and neutrino). In the event that the shock wave is not successful in exploding the star, the likely outcome is a black hole. We know that this must happen as many stellar mass black hole candidates exist, however, what stars make black holes is an open question. This is the main topic of this thesis.

## 2.3 The Quest for the Explosion Mechanism

For over 40 years, the evolution of the supernova shock wave after its formation has been studied in great detail. However, how a star explodes remains the biggest unsolved problem in core-collapse theory. What is known is that in all but the lowest mass progenitors (i.e., O-Ne-Mg cores, for example, Kitaura et al. 2006) soon after the shock is formed, within 100 ms, it stalls and becomes an

accretion shock (i.e., $v_{\rm shock} \sim 0$). This occurs because the pressure of the matter behind the shock is not large enough to overcome the ram pressure of the in-falling outer core. Two physical phenomena are responsible for reducing the pressure of the material behind the shock and lead to its stagnation. As the in-falling material slows through the shock, the kinetic energy is converted to internal energy. This increase in internal energy ($\sim$8–9 MeV baryon$^{-1}$) dissociates the heavy iron-group nuclei into neutrons, protons, and $\alpha$-particles at the cost of softening the equation of state. The other cause of the shock stalling is the copious emission of neutrinos, and therefore thermal energy, from the hot postshock region.

The stalled shock must be reenergized before sufficient matter is accreted onto the protoneutron star to cause a further gravitational instability, this time the collapse of the protoneutron star to a black hole. Several theories for the supernova explosion mechanism have been proposed. They all rely on the conversion of a fraction of the energy released during the gravitational collapse of the iron core to a neutron star ($\sim 3 \times 10^{53} = 300\,B$) to the kinetic energy of the explosion (i.e., for a typical supernova, $\mathcal{O}$ ($10^{51}$ ergs $= 1\,B$)). The remaining energy is radiated in neutrinos or converted to rotational energy, if the iron core had some initial angular momentum. We describe the various proposed supernova explosion mechanisms below.

### 2.3.1 The Neutrino-Driven Explosion Mechanism

The most ubiquitous mechanism is the neutrino mechanism, originally proposed by Wilson (1985). In all core-collapse supernova simulations that include basic neutrino physics, a heating region develops behind the shock. Neutrinos from the protoneutron star begin to decouple from the matter when the interaction length scale (i.e., the neutrino mean free path) becomes too large to maintain equilibrium with the surrounding matter, this decoupling is predominantly due to the decrease in the density with increasing radius. This occurs at a reference radius called the neutrinosphere, usually defined to be the radius where the mean neutrino optical depth is 2/3, this roughly corresponds to a matter density of $\rho \sim 10^{11-12}$ g cm$^{-3}$. Outside of the neutrinosphere, lingering neutrino interactions with the matter preferentially transfer energy from the neutrino field to the matter. The *gain region*, where neutrino heating dominates over neutrino cooling, develops between $\sim$ 100 km and the shock. For a successful neutrino driven explosion, the heating in the gain region is large enough to increase the pressure behind the shock above the ram pressure of the infalling material. In 1D and 2D, the neutrino mechanism is not a robust core-collapse supernova explosion mechanism. In 1D, even with the most sophisticated neutrino physics (Lentz et al. 2011, Liebendörfer et al. 2001, 2004, Rampp and Janka 2000, Thompson et al. 2003), it often fails to reenergize the shock at all. In 2D, while some successful neutrino-driven explosions are observed to occur with the most sophisticated neutrino physics, (Buras et al. 2006a, Müller et al. 2011, 2012, Yakunin et al. 2010), they are typically under-energetic compared to canonical observed core-collapse supernova explosions. The

neutrino mechanism in 3D is still under investigation. Exploratory simulations with ad-hoc neutrino heating and cooling are currently giving contradictory results. Nordhaus et al. (2010b) claim that the critical luminosity needed to explode in 3D is lower (by $\sim 20\%$) than in 2D, however Hanke et al. (2011) see no reduction in the critical luminosity when going from 2D to 3D. It is crucial to accurately model the neutrinos and their interactions with the matter in order to fully capture the neutrino mechanism. This makes simulations computationally demanding and complex; more sophisticated neutrino treatment in 3D is needed before conclusions can be reached. An excellent analytic break-down of the neutrino mechanism is presented in Pejcha and Thompson (2012), where they investigate previous analytic approaches to describing the neutrino mechanism, discuss the thermodynamic conditions in the postshock region when the neutrino mechanism is successful, and study how increased dimensionality can improve the efficacy of the neutrino mechanism.

### 2.3.2 The Magneto-Rotational Explosion Mechanism

For magnetized protoneutron stars that are sufficiently rapidly rotating, LeBlanc and Wilson (1970) proposed, with more recent work by Burrows et al. (2007b), Dessart et al. (2008), Obergaulinger et al. (2009), Shibata et al. (2006), Takiwaki et al. (2004), the magneto-rotational mechanism. Unlike the neutrino mechanism, provided the conditions present themselves, this explosion mechanism is robust in producing a successful and energetic supernova via a jet-driven explosion. However, this explosion mechanism requires large magnetic fields and rotation. The leading theory to generate the large magnetic field needed to power such an explosion is the magneto-rotational instability (MRI) (Balbus and Hawley 1991). In the context of protoneutron stars, the MRI occurs whenever there is strong differential rotation and a seed magnetic field. In theory, it grows the magnetic field on a dynamical time scale, which for fast rotating protoneutron stars is $\mathcal{O}$(ms) (Obergaulinger et al. 2009). This allows the magnetic field to reach the required values for a magneto-rotational explosion within the first $\mathcal{O}(100\,\mathrm{ms})$. Numerically modeling the magneto-rotational explosion mechanism self-consistently is difficult, as it requires one to resolve the fastest growing mode of the MRI. For typically magnetic fields in protoneutron stars this scale is $\mathcal{O}$(m). Larger initial magnetic fields increase this scale and allow numerical simulations to resolve the MRI on a global scale (Obergaulinger et al. 2006a,b), but are currently not predicted from stellar evolution models. Unfortunately, the rotation rates needed for magneto-rotational driven explosions are not predicted to occur in garden-variety massive stars. So while the magneto-rotational mechanism may be robust in reviving the shock, it cannot be the explanation for every core-collapse event we observe, rather perhaps only $\mathcal{O}(1\%)$ (Woosley and Heger 2006).

### 2.3.3 Other Explosion Mechanisms

The unsuccessful attempts to simulate the explosion of core-collapse supernova have led to several other proposals for the core-collapse supernova mechanism. Burrows et al. (2006a) propose the *acoustic mechanism*. They find in their 2D axisymmetric simulations that the standing accretion shock instability (SASI) generates downstreams onto the protoneutron star core that lead to the excitation of g-modes. These g-modes create sound waves that propagate out into the postshock region where they steepen into shocks, depositing their energy and eventually reenergizing the shock. This proposed explosion mechanism is not without its caveats. Weinberg and Quataert (2008) have found that unresolved daughter modes would saturate the g-mode that drives the explosion at amplitudes much less than that needed for the observed explosion. The numerically observed explosions also are *1)* unconfirmed by other core-collapse supernova codes, and *2)* sufficiently under-energetic to explained observed explosion energies. It is also unclear if such oscillations would be present in full 3D simulations. However, the acoustic mechanism provides a clear observational signature in gravitational waves for a galactic core-collapse supernova (Ott et al. 2006a).

Another recently proposed mechanism for reenergizing the supernova shock is the QCD phase transition mechanism of Sagert et al. (2009). As the protoneutron star accretes material the central density slowly increases. If a QCD phase transition occurs at central densities reached in the early postbounce phase that this would trigger a second collapse of the core, this time to a quark star. Much like the standard iron core collapse case, the protoneutron star collapse will be halted at higher densities. This will create a second shock wave that will propagate out and, in the simulations of Sagert et al. (2009), reenergize the shock causing a successful explosion. However, with the recent observation of $1.97 \pm 0.04\, M_{\odot}$ neutron star (Demorest et al. 2010), the critical density of such a QCD phase transition is forced to higher densities. It is unclear if such a transition would occur early enough in the postbounce phase to affect the explosion mechanism. Much like the acoustic mechanism, there is a clear observational signature of the QCD phase transition induced explosion, Dasgupta et al. (2010) predict a strong $\bar{\nu}_e$ signal from the second collapse, which would be observable within the galaxy.

### 2.3.4 Missing Physics

It may well be that case that the crucial piece of physics that leads to a successful core-collapse supernova explosion is something that has been neglected or not considered at all. Small changes to specific elements of core-collapse theory are unlikely to make a qualitative difference on the outcome because of the strong feedback. This is colloquially known as Mazurek's Law name after physicist Ted Mazurek. However, dramatic changes in the underlying physics may have a large effect. We have already alluded to one potential missing piece of physics: three dimensions. Transitioning

from one dimension to two dimensions changed the picture a lot (Murphy and Burrows 2008). The extra degree of freedom allows hydrodynamic instabilities to develop such as convection and the standing accretion shock instability (SASI). These increase the dwell time of the fluid in the gain region, allowing for a more efficient neutrino mechanism. Indeed, there is a consensus that neutrino driven explosions are easier to obtain in two dimensions than in one dimension (Hanke et al. 2011, Murphy and Burrows 2008, Nordhaus et al. 2010b). The transition from two to three dimensions is less clear. Without the axial symmetry constraint imposed by two-dimensional simulations and due to the nature of turbulence in three dimensions compared to two, it is unclear if the large scale shock excursions seen in two dimensions will carry over to three dimensions. Preliminary work has been done on the supernova mechanism in three dimensions (Burrows et al. 2012, Hanke et al. 2011, Kuroda et al. 2012, Nordhaus et al. 2010b), but as of yet there is no consensus on its effect. This will required detailed simulations with more sophisticated neutrino transport.

One of the most puzzling questions is, if the neutrino mechanism is successful in three dimensions, how can canonical supernova explosion energies be reached when the most accurate one- and two-dimensional simulations of garden-variety massive stars predict roughly a tenth of what is observed (Müller et al. 2012). A recent example of a potential game-changing piece of physics is collective neutrino oscillations in the early postbounce phase (Chakraborty et al. 2011a,b, Dasgupta et al. 2012, Suwa et al. 2011). Under certain conditions similar to those found in the early postbounce phase of core-collapse supernovae, it is possible for the neutrino spectra to collectively oscillate. One consequence is that the electron neutrino and antineutrino spectra swap with the heavy-lepton neutrino spectra. If this exchange occurs before the gain radius, there is a potentially large, $\mathcal{O}(100\%)$, increase in the neutrino heating. However it has been shown (Chakraborty et al. 2011a,b, Dasgupta et al. 2012) that such exchange does not seem to occur at small enough radii to have an effect on the explosion mechanism.

### 2.3.5 Failed Supernovae

In a significant fraction of core-collapse events the explosion mechanism must be successful to reproduce observed core-collapse supernovae rates. However, it is most likely that some fraction of core collapses do not give rise to a successful explosion, rather they are failed supernovae. If the shock fails to be reenergized, matter will continue to accrete onto the protoneutron star. Eventually the protoneutron star will surpass the maximum mass that can be supported by the nuclear equation of state. It will then collapse to a black hole. This is likely the only pathway to produce the observed stellar mass black hole binary star systems, the prototype black hole binary star system being Cygnus X-1. After the black hole forms there are several possible outcomes. If the progenitor star is nonrotating or rotating slowly, it is likely that matter will continue to accrete into the black hole until the entire star is consumed, producing an *unova* (Kochanek et al. 2008). If enough rotation is

present a disk may form around the black hole feeding it on an accretion time scale. Furthermore, if the disk forms at sufficiently small radii, Woosley (1993) proposes that a long-duration $\gamma$-ray burst may develop. Failed supernovae are the main focus of this thesis. We delay a detailed introduction until Chapter 4.

## 2.4 Signatures of the Supernova Central Engine

Unfortunately, the electromagnetic observations of core-collapse supernovae carry no direct information on the central engine of the supernova itself. For this we must rely on either neutrinos or gravitational waves. Such detections are rare, the LOSS survey predicts that the expected supernova rate in the Milky Way is 2.84±0.60 supernovae per century (within a systematic uncertainty factor of ∼2) (Li et al. 2011). Most of the current and future neutrino detectors (Borexino, HALO, IceCube, KamLAND, SNO+, Super-Kamiokande) will be able to detect neutrinos from a galactic supernova; in 1987 Kamiokande-II (Hirata et al. 1987) and IMB (Bionta et al. 1987) both detected a handful of neutrinos from SN1987A in the Large Magellanic Cloud. The prospects for gravitational waves are less certain, largely owing to the fact that gravitational wave have not yet been observed. However, it is predicted that galactic events should be detectable in current and future gravitational wave detectors (Ott 2009). A detection of either or both would provide supernova theorists with a plethora of information much like the case following SN1987A. We report on some aspects of the core-collapse supernova central engine that can be unveiled with a future detection of neutrinos and/or gravitational waves. We also briefly discuss indirect probes of the core-collapse supernova central engine.

### 2.4.1 Neutrino Signatures

For a core-collapse supernova at a fiducial galactic distance of 10 kpc, the total number of expected neutrinos in the SuperKamiokande water-Cherenkov detector is ∼8000. These ∼8000 neutrinos (although most detections will actually be electron antineutrinos) are emitted starting at core bounce and continuing until a black hole forms or the protoneutron star has cooled sufficiently that the neutrino emission rate drops below the detection threshold (∼20 s). These neutrinos can tell us a great deal about the inner workings on the core-collapse supernova engine (Vogel 2002). How the luminosity, spectral shape, and flavor content change with time can be matched with theory to reveal details of the underlying progenitor models, nuclear equation of state, and neutrino oscillation parameters (both collective and MSW). Decoupling these from each other may prove to be the most difficult task.

More specific questions may also be answered. The absolute mass scale of neutrinos can be limited by time of flight measurements of the neutrinos (Beacom and Vogel 1998a,b). Temporal

variations in the total neutrino signal, (Brandt et al. 2011, Lund et al. 2010), especially if coincident with a gravitational wave signature, (Ott et al. 2012), can reveal properties of the fluid motions in the protoneutron star and postshock region. One proposed supernova mechanism, the QCD phase transition model of Sagert et al. (2009), predicts a unique electron antineutrino signal that would be observable from a galactic supernova. Kinks in the observed energy spectrum signal collective neutrino oscillations and can help distinguish the neutrino mass hierarchy and determine neutrino mixing parameters (Duan et al. 2010). Even standard neutrino oscillations (via the MSW effect) can relay information of the density structure in the early postexplosion phase (Duan and Kneller 2009). The incredible sensitivity of the IceCube detector to the overall neutrino luminosity may allow the precise determination of the time of bounce to within 3.5 ms (Halzen and Raffelt 2009). This timing information may be crucial for gravitational wave analysts to extract a gravitational wave signal from their data. If a black hole forms within the detection window for neutrinos, one expects a sharp drop in the neutrino signal. This may happen in a failed supernova before the shock is reenergized, or after the shock is launched via fallback or due to a late-time phase transition in the protoneutron star (Baumgarte et al. 1996a,b). Such an event would allow for an even more precise measurement of the neutrino absolute mass scale (Beacom et al. 2001) and perhaps reveal telling information on the nuclear equation of state.

Relic supernova neutrinos are supernova neutrinos from distant sources. On average we would expect to detect much less than one neutrino from each of these distance sources. However, integrated over all core-collapse supernovae, of which there is $\mathcal{O}(1\text{–}10)$ per second in the observable universe, we expect a relic supernova neutrino background. This background has not yet been detected, but the most recent upper limits from almost 3000 days of live time at SuperKaminokande are $N_{\rm relic}^{E>17.6\,\rm MeV} < 2.95 \pm 0.15\ \bar{\nu}_e\ \rm cm^{-2}\ s^{-1}$ (Bays et al. 2012). This limit puts constraints on a combination of the total energy released in electron antineutrinos and the associated energy spectrum. The limits are very close to current theoretical predictions. This suggests relic neutrinos may soon be discovered with more exposure time and/or a megaton-class neutrino detector.

### 2.4.2 Gravitational Wave Signatures

While no gravitational waves have been observed from any source, such detections are routinely expected in the next generation of gravitational wave detectors, cf. Advanced LIGO and Advanced VIRGO (LIGO, Virgo). Gravitational waves from core-collapse supernovae are very weak and a detection of garden-variety core-collapse supernovae in gravitational waves is predicted only for galactic supernovae (Ott 2009). Such a signal would be invaluable, gravitational waves carry direct information on the dynamics of the supernova central engine. It is likely the case that if such a signal were to be observed within a few kpc, we would be able to distinguish the explosion mechanism (Logue et al. 2012). Each mechanism has a characteristic signature: the magneto-rotational mechanism,

due to the rapidly rotating core, has a strong gravitational wave signature at bounce. The neutrino mechanism has a lower signal driven by convection and, at least in two-dimensional simulations, the SASI. The acoustic mechanism has a strong gravitational wave signature as the protoneutron star core pulsates. A failed supernova with sufficient rotation also has a characteristic gravitational wave signal with a distinctive pulse both at core bounce and at the moment of black hole formation (Ott et al. 2011).

### 2.4.3 Indirect Probes of the Central Engine

There are many ways to indirectly probe the supernova central engine. For example, using the observed mass distribution of neutron stars and black holes in observed neutron star–white dwarf, neutron star–neutron star, and low- and high-mass x-ray binaries (Farr et al. 2011, Özel et al. 2010, 2012, Pejcha et al. 2012). Typical pulsar kick speeds are $\sim 200\,\mathrm{km\ s^{-1}}$ and may also give an indirect probe of the central engine of core-collapse supernovae (Nordhaus et al. 2010a). Similarly, asymmetries in the explosion eject or net polarizations in the observed photons possibly hint at asymmetries in the underlying mechanism. Measurements of nucleosynthetic yields, either through chemical analysis of stellar atmospheres, presolar grains, or observations of supernova remnants also give clues regarding the central engine. However all these methods usually contain unknown systematics, suffer from low statistics, and/or require assumptions of the underlying populations of stars and stellar evolutions processes.

# Chapter 3

# General Relativistic Hydrodynamics and Core-Collapse Supernova Microphysics[1]

## 3.1 Introduction

General relativistic computational models of stellar collapse have a long pedigree, starting with the spherically symmetric (1D) Lagrangian work of May and White in the mid-1960s (May and White 1966), based on the comoving GR hydrodynamics formulation in orthogonal coordinates by Misner and Sharp (Misner and Sharp 1964) and using a finite-difference scheme with an artificial viscosity (Von Neumann and Richtmyer 1950) approach to handle shocks. Much subsequent 1D GR work (Baumgarte et al. 1995, Liebendörfer et al. 2002, Miralles et al. 1991, Schinder et al. 1988, Swesty 1995, van Riper 1979) was based on this or similar approaches, including full radiation-hydrodynamics stellar collapse and core-collapse supernova simulations with finite-temperature microphysical equations of state (EOS) (Baron et al. 1985, 1989, Bruenn 1985, Liebendörfer et al. 2004, Wilson 1971). Eulerian formulations, more suited for extension to multidimensional simulations, were introduced later and used maximal slicing (Mezzacappa and Matzner 1989, Shapiro and Teukolsky 1979, 1980, Wilson 1979), or radial-gauge, polar-slicing (RGPS) (Gourgoulhon 1991). These schemes, with the exception of Gourgoulhon (1991), who employed pseudospectral methods, still used artificial viscosity approaches to shock treatment. More accurate, high-resolution shock-capturing (HRSC) approaches to GR stellar collapse based on higher-order Gudonov schemes and Riemann solvers were introduced by Marti et al. (1990) and Yamada (1997) in the Lagrangian context, by Martí et al. (1991) in the fixed-background Eulerian case, and by Romero et al. (1996) and

[1] A large part of this chapter is taken from the article *A New Open-Source Code for Spherically-Symmetric Stellar Collapse to Neutron Stars and Black Holes.* O'Connor, E. & Ott, C.D., Classical and Quantum Gravity **27** 114103 (2010): Special Issue of invited papers from MICRA2009 held at the Niels Bohr International Academy, Copenhagen, August 24–28, 2009. Reproduced with permission from IOP Publishing. This chapter also contains work from the proceedings of the 'Hamburg Neutrinos from Supernova Explosions, Haνse 2011' Ott, C.D., O'Connor, E. & Dasgupta, B.

Noble (2003) in the RGPS Eulerian frame. Yamada's approach was later extended to include microphysical EOS and radiation transport (Sumiyoshi et al. 2005, Yamada et al. 1999). Gourgoulhon and Haensel (1993) included an approximate neutrino transport treatment in their code. Preliminary results of Romero's code with a microphysical EOS and a neutrino leakage scheme were published in Romero et al. (1997) and Pons et al. (1997).

State-of-the-art simulations of stellar collapse and of the postbounce supernova evolution strongly suggest that multidimensional dynamics is crucial for the core-collapse supernova mechanism to succeed in massive stars (e.g., Hanke et al. 2011, Kuroda et al. 2012, Murphy and Burrows 2008, Nordhaus et al. 2010b, Takiwaki and Kotake 2011). Present multidimensional core-collapse supernova codes are either Newtonian (Burrows et al. 2007c, Hanke et al. 2011, Nordhaus et al. 2010b, Obergaulinger and Janka 2011, Ott et al. 2008, Suwa et al. 2010, Swesty and Myra 2009, Takiwaki and Kotake 2011) or employ Newtonian dynamics with relativistic corrections to the gravitational potential (Bruenn et al. 2009, Buras et al. 2006a, Marek and Janka 2009, Müller et al. 2010, Müller et al. 2012). Multidimensional simulations in conformally flat (Isenberg 2008) or full GR traditionally relied on simple analytic EOS and polytropic initial models and neglected crucial neutrino effects (see, e.g., Dimmelmeier et al. 2002a, 2005, Shibata and Sekiguchi 2004, 2005). Only recently have the first axisymmetric (2D) (Dimmelmeier et al. 2007, 2008, Sekiguchi and Shibata 2011) and 3D (Kuroda et al. 2012, Ott et al. 2007a,b, 2012) GR core-collapse simulations become available that employ microphysical EOS, approximate treatment of deleptonization in the collapse phase and in the very recent case of Ott et al. (2012) and Kuroda et al. (2012), approximate neutrino leakage or transport in the postbounce phase.

In this chapter, we describe the foundations of a new and open approach to the stellar collapse and core-collapse supernova problem in GR. We discuss the formulation and implementation of the code `GR1D`, a new, spherically-symmetric Eulerian GR code for stellar collapse to neutron stars and black holes with approximate pre- and postbounce neutrino treatment. We release `GR1D` and all its microphysics and input physics as open source to be downloaded from `http://www.stellarcollapse.org`. It is meant to complement open-source 3D GR codes that do not come with microphysics and neutrino approximations. At the same time, we intend `GR1D` to serve as an efficient 1D GR test bed for new modeling technology to be eventually incorporated in multidimensional codes. In addition, `GR1D` and its microphysics components can readily be adapted for use in the computational modeling of problems involving some or much of the same physics as in the stellar collapse problem, e.g., the postmerger phase of double neutron-star or black-hole–neutron-star coalescence.

We base `GR1D` on the conceptually simple and computationally efficient RGPS formalism of Gourgoulhon (1991). `GR1D`, like the code of Romero et al. (1996), employs a Eulerian formulation of GR hydrodynamics with HRSC and works on nonequidistant grids. For the first time in the 1D

GR context, we derive and implement in GR1D an extension of the 1D GR hydrodynamics equations to include rotation in an effective fashion. For completeness and comparison of Newtonian and GR dynamics, GR1D also implements 1D Newtonian hydrodynamics. GR1D operates with analytic EOS as well as with tabulated microphysical EOS through a general EOS interface. We discuss and provide EOS tables for the EOS of Lattimer-Swesty EOS (Lattimer and Swesty 1991) and the one of Shen et al. (1998a,b, 2011c). Furthermore, we discuss and include in GR1D the deleptonization treatment of Liebendörfer (2005) for the collapse phase and a postbounce 3-flavor neutrino treatment based on the leakage schemes of Ruffert et al. (1996) and Rosswog and Liebendörfer (2003) as well as an approximate way of including neutrino heating.

Due to these approximations in the neutrino treatment, GR1D in its present form cannot be used for accurate simulations addressing the core-collapse supernova mechanism or neutrino-induced nucleosynthesis. However, we find that with the present treatment, GR1D reproduces very well qualitatively the salient features of the postbounce evolution of core-collapse supernovae as predicted by full 1D radiation-hydrodynamics simulations. Moreover, we find that GR1D may be used to make quantitatively reliable predictions on the time of black hole formation in failing core-collapse supernovae and on the maximum mass of the protoneutron star. The next major update to GR1D is the inclusion of spectral neutrino transport (see Chapter 5).

This chapter is structured as follows. In Section 3.2 and Section 3.3, we discuss our 1D GR hydrodynamics and curvature equations and their implementation in GR1D. Section 3.5 introduces the EOS provided with GR1D and in Section 3.6 we detail our prebounce deleptonization and postbounce leakage and neutrino heating schemes. A number of code tests are presented in Section 3.7.

We assume spacelike signature $(-,+,+,+)$ and, unless mentioned otherwise, use units of $G = c = M_\odot = 1$, but use cgs units for the microphysics and neutrino leakage/heating quantities.

## 3.2 Spacetime Equations

We follow Gourgoulhon (1991), Romero et al. (1996) who formulate the $3+1$ GR curvature and hydrodynamics equations in radial-gauge, polar slicing (RGPS) coordinates. In these coordinates and in spherical symmetry, the shift vector vanishes and the metric is diagonal and closely resembles the Schwarzschild metric. The invariant line element is

$$\begin{aligned} ds^2 &= g_{\mu\nu} dx^\mu dx^\nu \ , \\ &= -\alpha(r,t)^2 dt^2 + X(r,t)^2 dr^2 + r^2 d\Omega^2 \ , \end{aligned} \tag{3.1}$$

where $\alpha$ and $X$ can be written more conveniently as functions of a metric potential, $\Phi(r,t)$, and the enclosed gravitational mass $M_{\rm grav}(r,t) = m(r,t)$,

$$\alpha(r,t) = \exp\left[\Phi(r,t)\right], \qquad X(r,t) = \left(1 - \frac{2m(r,t)}{r}\right)^{-1/2} . \tag{3.2}$$

We assume ideal hydrodynamics for which the fluid stress-energy tensor is

$$T^{\mu\nu} = \rho h u^\mu u^\nu + P g^{\mu\nu} , \tag{3.3}$$

where $\rho$ is the baryonic density, $P$ is the fluid pressure, $h$ is the specific enthalpy equal to $1 + \epsilon + P/\rho$ with $\epsilon$ being the specific internal energy. $u^\mu$ is the four-velocity and, in 1D, is equal to $[W/\alpha, Wv^r, 0, 0]$. $W = \left(1 - v^2\right)^{-1/2}$ is the Lorentz factor and $v = Xv^r$. The equation for the gravitational mass needed for determining the metric coefficient $X(r,t)$ of Equation 3.2 is derived from the Hamiltonian constraint equation and reads

$$m(r,t) = 4\pi \int_0^r (\rho h W^2 - P) r'^2 dr' . \tag{3.4}$$

The expression for the metric potential $\Phi(r,t)$ is determined via the momentum constraints, taking into account the polar slicing condition that imposes $\mathrm{Tr}K = K_r{}^r$, where $K_{ij}$ is the extrinsic curvature tensor (see Gourgoulhon 1991, Noble 2003 for details). It reads,

$$\Phi(r,t) = \int_0^r X^2 \left[\frac{m(r',t)}{r'^2} + 4\pi r' (\rho h W^2 v^2 + P)\right] dr' + \Phi_0 , \tag{3.5}$$

$\Phi_0$ is determined by matching the solution at the star's surface ($r = R_\star$) to the Schwarzschild metric,

$$\Phi(R_\star, t) = \ln\left[\alpha(R_\star, t)\right] = \frac{1}{2} \ln\left[1 - \frac{2m(R_\star, t)}{R_\star}\right] . \tag{3.6}$$

We use standard 2$^{\rm nd}$ order methods to perform the integral in Equation 3.5 and obtain values at cell centers as well as at cell interfaces. As we shall se in the next section, The integrand for Equation 3.4 can be written purely as a function of conserved, cell-averaged variables and therefore the volume integral is trivial and exact.

## 3.3 GR Hydrodynamics in 1D Radial-Gauge, Polar Slicing

The evolution equations for the matter fields are derived from the local conservation laws for the stress-energy tensor, $\nabla_\mu T^{\mu\nu} = 0$, and for the matter current density $\nabla_\mu J^\mu = 0$. This conservation laws are evaluated in the Eulerian frame assuming the spacetime structure given in the previous section. We write the GR hydrodynamics equations along the lines of the flux-conservative Valencia

formulation (e.g., Banyuls et al. 1997, Font 2008, Font et al. 2000) with modifications for spherically-symmetric flows proposed by Romero et al. (1996) and neutrino sources. Evaluation of the neutrino sources in the Eulerian frame is presented in Section A.1. The derivation of the evolution equations is presented in Appendix A.2.

We write the set of evolution equations as,

$$\partial_t \vec{U} + \frac{1}{r^2}\partial_r \left[\frac{\alpha r^2}{X}\vec{F}\right] = \vec{\mathcal{S}} \tag{3.7}$$

where $\vec{U}$ is the set of conserved variables, $\vec{F}$ is their flux vector, and $\vec{\mathcal{S}}$ is the vector containing gravitational, geometric, and neutrino-matter interaction sources and sinks. In 1D and without rotation, $\vec{U} = [D, DY_e, S^r, \tau]$. The conserved variables are functions of the primitive variables $\rho, Y_e, \epsilon, v$, and $P$ and are given by

$$\begin{aligned} D &= \alpha X J^t = X\rho W \ , \\ DY_e &= \alpha X Y_e J^t = X\rho W Y_e \\ S^r &= \alpha X T^{tr} = \rho h W^2 v \ , \\ \tau &= \alpha^2 T^{tt} - D = \rho h W^2 - P - D \ , \end{aligned} \tag{3.8}$$

where $Y_e$ is the electron fraction, the number of electrons per baryon, and the only compositional variable needed to describe matter in nuclear statistical equilibrium (NSE). Note that there is a misprint in the central part of Equation 9 of Romero et al. (1996) which is missing a factor of $X$ which we have corrected here. The flux $\vec{F}$ is given by $\vec{F} = [Dv, DY_e v, S^r v + P, S^r - Dv]$ and the sources and sinks are given by

$$\begin{aligned} \vec{\mathcal{S}} = \Big[ & 0, R^{\nu}_{Y_e}, (S^r v - \tau - D)\alpha X \left(8\pi r P + \tfrac{m}{r^2}\right) + \alpha P X \tfrac{m}{r^2} \\ & + \tfrac{2\alpha P}{Xr} + Q^{\nu,\mathrm{E}}_{S^r} + Q^{\nu,\mathrm{M}}_{S^r}, Q^{\nu,\mathrm{E}}_{\tau} + Q^{\nu,\mathrm{M}}_{\tau} \Big] \ . \end{aligned} \tag{3.9}$$

The source and sink terms $R^{\nu}_{Y_e}, Q^{\nu,\mathrm{E}}_{S^r}, Q^{\nu,\mathrm{M}}_{S^r}, Q^{\nu,\mathrm{E}}_{\tau}$, and $Q^{\nu,\mathrm{M}}_{\tau}$ are associated with neutrinos and are discussed in Appendix A.1 and Appendix A.2.

We use a semidiscrete approach and first discretize Equation 3.7 in space, then apply the method of lines (MoL, Hyman 1976) and perform the time integration of the conserved variables via standard $2^{\mathrm{nd}}$- or $3^{\mathrm{rd}}$-order Runge-Kutta integrators with a Courant factor of 0.5.

The spatial discretization follows the finite-volume approach (e.g., Font 2008, Romero et al. 1996) and all variables are defined at cell centers $i$ and must be reconstructed (i.e., interpolated) at cell interfaces, where intercell fluxes are computed. This interpolation must be monotonic to ensure stability. We use the nominally $3^{\mathrm{rd}}$ order (in smooth parts of the flow) piecewise-parabolic

method (PPM, Colella and Woodward 1984) to interpolate the primitive variables and then set up the conserved variables at the cell interfaces. We also implement piecewise-constant reconstruction as well as piecewise-linear (total-variation-diminishing [TVD]) reconstruction with Van Leer's limiter (van Leer 1977). The latter we use exclusively in the innermost 3 to 5 zones to avoid oscillations near the origin.

Once the variables have been reconstructed at the cell interfaces, we evaluate the physical interface fluxes $\vec{F}_{i+1/2}$ with the HLLE Riemann solver (Einfeldt 1988). The right-hand-side (RHS) flux update term for $\vec{U}_i$ then reads,

$$\mathrm{RHS}_i = -\frac{1}{r_i^2 \Delta r_i}\left[\frac{\alpha_{i+1/2} r_{i+1/2}^2}{X_{i+1/2}}\vec{F}_{i+1/2} - \frac{\alpha_{i-1/2} r_{i-1/2}^2}{X_{i-1/2}}\vec{F}_{i-1/2}\right] . \tag{3.10}$$

Gravitational, geometrical, and neutrino-matter interaction sources/sinks are not taken into account in the flux computation and are coupled into the MoL integration.

After the update of the conserved variables $D$, $DY_e$, $S^r$ and $\tau$, primitive variables $\rho$, $Y_e$, $v$, $\epsilon$, and $P(\rho, \epsilon, Y_e)$ must be extracted since they are needed for the next time step. In the general case, the primitive variables (with the exception of $Y_e$) cannot be expressed algebraically in terms of the conserved variables (see, e.g., Font et al. 2000). Hence, we employ an iterative approach and make an initial guess using $P_{\mathrm{old}}$ from the previous time step,

$$v = \frac{S^r}{\tau + D + P_{old}} , \quad \rho = \frac{D}{XW} , \quad \epsilon = \frac{\tau + D + P_{old}(1 - W^2)}{\rho W^2} - 1, \tag{3.11}$$

where we note that $X$ can be calculated from the conserved variables as $\rho h W^2 - P = \tau + D$. $W$ is calculated from the estimate of $v$. We then call the EOS to obtain a new pressure and iterate this process using a Newton-Raphson method until convergence (we typically stop the iteration at a fractional pressure difference of $10^{-10}$ between iteration steps).

## 3.4 Extension to 1.5D: Including Rotation

Lagrangian spherically-symmetric stellar evolution codes have long included rotation and rotational effects in an approximate fashion (e.g., Endal and Sofia 1978, Heger et al. 2000, Hirschi et al. 2004). The way this is typically done is to make the assumption that the star has constant angular velocity on spherical shells. In order to compute the effective specific centrifugal force acting on a fluid parcel, we compute the angular average of $(\vec{\omega} \times \vec{r})^2$ on a spherical shell of radius $r$, which leads to $f_{\mathrm{cent}} = 2/3\,\omega^2 r$. In Newtonian Lagrangian calculations, specific angular momentum $j = \omega r^2$ is conserved by construction and the effective centrifugal force appears in the momentum equation. Relatively recently, such an approach has also been taken in the Newtonian 1D core collapse calculations of

Ott et al. (2006b), Thompson et al. (2005) in order to take into account the effect of rotation approximately. In the Eulerian frame and in GR the situation is more complicated. We must solve an equation for angular momentum conservation on top of taking into account a centrifugal force term in the momentum equation. We begin by defining an azimuthal Eulerian velocity $v^{\phi}(=\omega)$ and, in order to obtain a quantity of dimension velocity, we also define $v_{\varphi} = rv^{\phi}$ (note that $u^{\phi} = Wv_{\varphi}/r$). With finite $v^{\phi}$, $T^{r\phi}$ is finite and $W$ becomes $W = (1 - v^2 - 2/3v_{\varphi}^2)^{-1/2}$ in our effective approach. We provide derivation details in Section A.2 and present here only the results. The modified stress-energy tensor leads to an additional equation for angular momentum conservation analogous to Equation 3.7,

$$\partial_t(S_{\phi}) + \frac{1}{r^2}\partial_r\left(\frac{\alpha r^2}{X}F_{\phi}\right) = \mathcal{S}_{\phi} \tag{3.12}$$

where

$$\begin{aligned} S_{\phi} &= \rho h W^2 v_{\varphi} r \ , \\ F_{\phi} &= \rho h W^2 v_{\varphi} r v = S_{\phi} v \ , \\ \mathcal{S}_{\phi} &= \rho h W^2 \alpha v v_{\varphi} X \left[4\pi r^2 P + \frac{m}{r}\right] \ . \end{aligned} \tag{3.13}$$

Also, an additional term, accounting for the centrifugal force,

$$+\alpha\frac{2}{3}\left(\frac{\rho h W^2 {v_{\varphi}}^2}{Xr}\right) \ , \tag{3.14}$$

appears on the RHS of the equation for $S^r$. Finally, the change of the stress-energy tensor also has an effect on the metric potential $\Phi$, whose equation is now given by

$$\partial_r\Phi = X^2\left[\frac{m}{r^2} + 4\pi r\left(\rho h W^2(v^2 + \frac{2}{3}v_{\varphi}^2) + P\right)\right] \ . \tag{3.15}$$

We implement this 1.5D treatment of rotation in `GR1D`, but keep the metric diagonal. The 1.5D treatment should be rather accurate for slow rotation, and, as shown by Ott et al. (2006b), will still capture qualitatively the effect of centrifugal support due to rapid rotation. For completeness, we note that the total angular momentum of the system (see, e.g., Cook et al. 1992) is given by,

$$J = \int_0^{\infty} T^t_{\phi}\sqrt{-g}\, d^3x = \frac{8\pi}{3}\int_0^{\infty} \rho h X W^2 r v_{\varphi} r^2 dr \ , \tag{3.16}$$

where we include a factor of 2/3 to account for the angular average. The rotation parameter $\beta$, defined as the ratio $T/|W_{\rm grav}|$ of rotational kinetic to gravitational energy is

$$T/|W_{\rm grav}| = \frac{T}{|M_{\rm grav} - M_{\rm proper} - T|} \ , \tag{3.17}$$

where

$$T = \frac{1}{2}\int_0^\infty \omega T^t_\phi \sqrt{-g} d^3x = \frac{4\pi}{3}\int_0^\infty \rho h X W^2 v^2_\varphi r^2 dr \ , \tag{3.18}$$

where again a factor of 2/3 in the last step is from performing an angular average. $M_{\rm proper}$ is given by,

$$M_{\rm proper} = 4\pi \int_0^\infty (\rho + \rho\epsilon)\, X W r^2 dr \ , \tag{3.19}$$

and $M_{\rm grav}$ is specified by Equation 3.4.

## 3.5 Equations of State (EOS)

An EOS is needed to close the system of GR hydrodynamics equations and provide the pressure as well as other thermodynamic quantities as a function of density, temperature (or specific internal energy), and composition. In `GR1D`, we include for test simulations the standard analytic polytropic (isentropic "cold", $P = K\rho^\Gamma$) and the $\Gamma$-law EOS ("hot", $P = (\Gamma - 1)\rho\epsilon$). These are inappropriate for stellar collapse since they do not capture the stiffening of the EOS at nuclear density. An analytic EOS, able to capture this effect qualitatively and include nonisentropic effects, is the *hybrid* EOS (Janka et al. 1993) which we include in `GR1D` and discuss in Section 3.5.1. For a more realistic description of the thermodynamics of nuclear matter, an EOS built from a microphysical finite-temperature model for nuclear matter is needed. This is also a prerequisite for any kind of neutrino treatment, since crucial compositional information as well as chemical potentials must be derived from a microphysical model. Such microphysical EOS are too complicated to be computed on the fly in a simulation and are used in tabulated form with interpolation. `GR1D` is able to handle such EOS and we provide tables at `http://www.stellarcollapse.org/microphysics` for the EOS of Lattimer and Swesty (1991) (LS EOS) and for the one of Shen et al. (1998a,b, 2011c) (HShen EOS). The details of these tables and the routines facilitating their use are discussed in Section 3.5.2 and Section 3.5.3. In Section 3.5.4 we review the current state of observational and nuclear theory constraints on the neutron star mass versus radius relation.

### 3.5.1 Hybrid EOS

The hybrid EOS found widespread use in early multidimensional simulations of rotating core collapse (e.g., Dimmelmeier et al. 2002a, Zwerger and Müller 1997), but was shown by Dimmelmeier et al. (2007, 2008) to lead in some cases to qualitatively incorrect results for the collapse dynamics and the resulting gravitational wave signal. We include it in `GR1D`, because its analytic nature provides for very fast calculations, allowing us to readily test the GR hydrodynamics of `GR1D`.

The hybrid EOS splits the pressure into a polytropic (cold) and a thermal component,

$$P = P_{\rm cold} + P_{\rm thermal} \ . \tag{3.20}$$

The cold part is piecewise polytropic. It is composed of a polytropic EOS with $\Gamma = \Gamma_1$ for densities below nuclear ($\rho_{\rm nuc}$) and another polytropic EOS with $\Gamma = \Gamma_2$ for densities above $\rho_{\rm nuc}$. The two are smoothly matched at $\rho_{\rm nuc}$ which makes the polytropic constant $K_2$ of the high-density part a function of the two $\Gamma$s, of $K_1$, and of the transition density $\rho_{\rm nuc}$ (see, e.g., Janka et al. 1993, Read et al. 2009, Zwerger and Müller 1997 for a description of the procedure and detailed expressions). The thermal part is modeled via a $\Gamma$-law with $\Gamma_{\rm th}$. It becomes relevant only after core bounce when shocks are present, making the flow nonadiabatic. Its contribution is determined via the thermal specific internal energy which is the difference between the primitive variable $\epsilon$ and the cold specific internal energy, $\epsilon_{\rm th} = \epsilon - \epsilon_{\rm cold}$.

For collapse simulations, we set $K_1 = 1.2435 \times 10^{15} (Y_e)^{4/3}$ [cgs] (the value appropriate for a relativistic degenerate gas of electrons, Shapiro and Teukolsky 1983, Zwerger and Müller 1997) with $Y_e = 0.5$. We choose a value below, but close to 4/3 for $\Gamma_1$ and typically set $\Gamma_2 = 2.5$ to mimic the stiff nuclear EOS above $\rho_{\rm nuc}$ which we set to $2 \times 10^{14}\,{\rm g\,cm^{-3}}$. $\Gamma_{\rm th}$ we normally keep at 1.5 to model a mixture of relativistic ($\Gamma = 4/3$) and nonrelativistic ($\Gamma = 5/3$) thermal contributions. This leads to rapid shock propagation and explosion. When simulating black hole formation with the hybrid EOS, we set $\Gamma_{\rm th}$ to smaller values. This reduces the postshock thermal pressure and leads to shock stagnation.

### 3.5.2 Lattimer-Swesty EOS

The LS EOS (Lattimer and Swesty 1991) is derived from a finite-temperature compressible liquid-droplet model (Lattimer et al. 1985) with a Skyrme nuclear force, uses the single heavy nucleus approximation, and assumes nuclear statistical equilibrium (NSE). NSE holds at $T \gtrsim 0.5\,{\rm MeV}$ which in core collapse and supernova matter is typically the case at $\rho \gtrsim$ few $\times 10^7\,{\rm g\,cm^{-3}}$.

The LS EOS routines are open source and available from the Stony Brook group[2]. We employ their baryonic parts to generate tables with nuclear incompressibilities $K_0$ of 180 MeV, 220 MeV, and 375 MeV (the larger $K_0$, the stiffer the nuclear EOS). Hereafter, we refer to these $K_0$-variants of the LS EOS as LS180, LS220, and LS375. The symmetry energy $S_v$ is set in all variants to 29.3 MeV for all $K_0$. Electrons and photons are added using the routines provided by Timmes's EOS[3] (Timmes and Arnett 1999).

We compute the maximum cold neutron star masses for the three LS EOS variants by setting $T =$ 0.1 MeV, assuming neutrino-less $\beta$-equilibrium and solving the Tolman-Oppenheimer-Volkoff (TOV)

[2] `http://www.astro.sunysb.edu/dswesty/lseos.html`
[3] `http://cococubed.asu.edu/code_pages/eos.shtml`

equations (Oppenheimer and Volkoff 1939). The results are $1.83\,M_\odot$ ($2.13\,M_\odot$), $2.04\,M_\odot$ ($2.41\,M_\odot$), $2.72\,M_\odot$ ($3.35\,M_\odot$) for gravitational (baryonic) mass and for $K_0 = 180\,\mathrm{MeV}$, $K_0 = 220\,\mathrm{MeV}$, and $K_0 = 375\,\mathrm{MeV}$, respectively. The coordinate radii of neutron stars with a gravitational mass of $1.4\,M_\odot$ are 12.1 km, 12.7 km, and 13.5 km.

Our LS EOS tables have 18 evenly spaced points per decade in $\log_{10}\rho$ ranging from $10^3$–$10^{16}\,\mathrm{g\,cm^{-3}}$, 30 points per decade in $\log_{10} T$ ranging from $10^{-2}$–$10^{2.4}\,\mathrm{MeV}$, and 50 points equally spaced in electron fraction from 0.035 to 0.53. This table resolution is sufficiently good to allow the use of simple and fast tri-linear interpolation (in $\log_{10}(\rho)$, $\log_{10}(T)$, $Y_e$), in collapse simulations while maintaining good thermodynamic consistency. In tests of adiabatic collapse, the inner-core entropy is conserved to $\sim 1\%$ from the onset of collapse to core bounce.

To generate the LS EOS tables, we employ the LS EOS at densities above $10^8\,\mathrm{g\,cm^{-3}}$, but, due to unreliable convergence, use linear extrapolation of the Helmholtz free energy $F$ in $Y_e$ for $Y_e > 0.5$ and in $T$ at $T < 0.06\,\mathrm{MeV}$. Note that the latter is far away from NSE, but is never reached by core-collapse trajectories at $\rho > 10^8\,\mathrm{g\,cm^{-3}}$. At densities below $10^8\,\mathrm{g\,cm^{-3}}$, we use the Timmes EOS (Timmes and Arnett 1999) and assume that the matter is an ideal gas composed of electrons, photons, neutrons, protons, alpha particles, and heavy nuclei with the average $A$ and $Z$ given by the LS EOS at the transition. Since the specific internal energies returned by the baryonic part of the Timmes EOS do not contain the nuclear binding energy, we shift the zero point of the Timmes EOS so that the returned specific internal energies are consistent with the LS EOS values at the transition point. For simplicity, we keep baryonic compositional variables fixed at the values obtained from the LS EOS at the transition density. These particular choices for the baryonic component have little effect at low densities where the thermodynamics are dominated by electrons at low to intermediate temperatures and by photons at high temperatures. However, for full core-collapse supernova simulations that intend to address also nuclear burning and nucleosynthesis aspects, a more involved consistent NSE/non-NSE EOS treatment involving the advection of many chemical species and a treatment of their interactions with a nuclear reaction network is necessary. We will leave such a treatment to future work (but see, e.g., Buras et al. 2006b, Rampp and Janka 2002 for discussions of such implementations).

When using finite-temperature microphysical NSE EOS such as the LS EOS in GR hydrodynamics codes, two additional caveats need to be taken into account: *(1)* The thermodynamic potential from which all dependent variables are derived is the Helmholtz free energy $F$. This makes the EOS a function of $\{\rho, T, Y_e\}$ while GR hydrodynamics codes such as `GR1D` operate on the primitive thermodynamic and compositional variables $\{\rho, \epsilon, Y_e\}$. Hence, in a typical EOS call it is first necessary to determine $T(\rho, \epsilon, Y_e)$ through a root-finding procedure, before the dependent variables can be obtained through tri-linear interpolation in $\{\rho, T, Y_e\}$. *(2)* In contrast to Newtonian hydrodynamics that involves only differences of the specific internal energy $\epsilon$, GR codes depend directly on $\epsilon$

through its contribution to the matter stress-energy tensor. Hence, it is important to find and use a physically correct energy zero point and ensure that there are no rest-mass contributions included in $\epsilon$.

### 3.5.3 Table-Based EOS

The standard HShen EOS (Shen et al. 1998a,b, 2011c) is based on a relativistic mean-field model for nuclear interactions (TM1), assumes NSE, and is extended with the Thomas-Fermi approximation to describe the homogeneous phase of matter as well as the inhomogeneous matter composition. $K_0$ of the HShen EOS is 281 MeV and the symmetry energy $S_v$ has a value of 36.9 MeV. The authors of the HShen EOS provide the baryonic component[4] in tabulated form only. Several other table-based finite temperature EOS have recently become available for use in simulations of core-collapse supernovae. These include several tables from Gang Shen and collaborators[5] Shen et al. (2011a,b) and several from Matthias Hempel and collaborators[6] Hempel and Schaffner-Bielich (2010), Hempel et al. (2011). Both of these EOS are based on the relativistic mean field model. The underlying interactions are NL3 and FSU for the Gang Shen EOS and TMA and DD2 for the Hempel EOS.

From the provided table of the nuclear EOS, we generate a larger table with additional variables needed in hydrodynamical simulations. Our tables are uniformly spaced with $\sim 20$ points per decade in $\log_{10}\rho$ from $10^3$–$10^{16}\,\mathrm{g\,cm^{-3}}$, $\sim 40$ points per decade in $\log_{10} T$ from $10^{-2}$–$10^{2.4}$ MeV, and $\sim 50$ points in $Y_e$ covering the interval 0.01–0.56. The exact parameters depend on the bound of the original EOS table. We interpolate all dependent variables from the original tables using the cubic Hermite interpolation function given in Timmes and Swesty (2000) modified to have monotonic interpolation behavior according to the prescription of Steffen (1990). The interpolation is performed first bicubic in $\rho, T$, then cubic in $Y_e$. Alternatively to the just described, one could interpolate the Helmholtz free energy $F$ and rederive dependent variables by taking derivatives of $F$ on the interpolated table (see, e.g., Timmes and Swesty 2000). We decided against this approach, since it would require quintic interpolation and the knowledge of the second derivatives of $F$ at each point in the original table, some of which would have to be computed by taking second derivatives in the coarse original table. Also, compositional information cannot be obtained directly from $F$ and would have to be interpolated from the original table. We perform the described interpolation at densities above $\sim 10^7\,\mathrm{g\,cm^{-3}}$. For points with $T < 0.1$ MeV we extrapolate most variables linearly, keeping only the compositions fixed. We add photons and electrons after interpolation using the routines of the Timmes EOS. At densities below $\sim 10^7\,\mathrm{g\,cm^{-3}}$, we employ the Timmes EOS in the same fashion as described in the above for the LS EOS. We use `EOSmaker` to convert the nuclear EOS tables to our standard format and `EOSdriver` to incorporate the tables into our hydrodynamic

[4] `http://user.numazu-ct.ac.jp/~sumi/eos`
[5] `http://cecelia.physics.indiana.edu/gang_shen_eos/`
[6] `http://phys-merger.physik.unibas.ch/~hempel/eos.html`

simulations. Both of these routines, as well as several pregenerated EOS tables in our format, are available on www.stellarcollapse.org

We compute the maximum cold neutron star masses for the table-based EOS in the same way as for the LS EOS and find $2.23\,M_\odot$, $1.77\,M_\odot$, $2.77\,M_\odot$, $1.75\,M_\odot$, $2.42\,M_\odot$, $2.01\,M_\odot$, for the gravitational maximum mass of the H. Shen TM1 (Shen et al. 2011c), H. Shen TM1+$\Lambda$ (Shen et al. 2011c), G. Shen NL3 (Shen et al. 2011b), G. Shen FSU (Shen et al. 2011a), M. Hempel TMA (Hempel et al. 2011) and M. Hempel DD2 (Hempel, (unpublished)), respectively. The baryonic maximum masses for the same set of EOS are $2.60\,M_\odot$, $1.99\,M_\odot$, $3.35\,M_\odot$, $1.99\,M_\odot$, $2.90\,M_\odot$, $2.31\,M_\odot$. The coordinate radii of neutron stars with a gravitational mass of $1.4\,M_\odot$ are 14.6 km, 14.6 km, 15.0 km, 12.8 km, 13.2 km, 13.8 km.

### 3.5.4 Neutron Star Mass vs. Radius Relation Constraints

A stringent constraint on the nuclear EOS is set by precision mass measurements of neutron stars in binary systems. The 2-$M_\odot$ ($[1.97 \pm 0.04]\,M_\odot$) neutron star of Demorest et al. (2010) rules out a large range of soft hadronic, mixed hadronic-exotic, and strange-quark matter EOS (Lattimer and Prakash 2011, Özel et al. 2010). Recently, Hebeler et al. (2010) have carried out chiral effective field theory calculations of neutron-rich matter below nuclear saturation density, strongly constraining the $P(\rho)$ relationship in this regime. They derived a radius constraint for a 1.4-$M_\odot$ neutron star of $10.5\,\mathrm{km} \lesssim R \lesssim 13.3\,\mathrm{km}$ (these numbers would be shifted up by $\sim$400 m if a detailed crust treatment was included) by requiring that all EOS support neutron stars with mass $\gtrsim 2\,M_\odot$ and pass through the $P(\rho)$ range allowed by their calculations. Steiner et al. (2010) and Özel et al. (2010) analyzed observations from accreting and bursting neutron stars to obtain neutron star mass-radius constraints. Such observations and their interpretations should be taken with a grain of salt, since large systematic uncertainties are attached to the models that are required to infer mass and radius and to the assumptions made in their statistical analysis. For example, Steiner et al. (2010) and Özel et al. (2010), starting with different assumptions, derive rather different 2-$\sigma$ mass-radius constraints from the same set of sources.

In Figure 3.1, we contrast the various observational constraints on the neutron star mass and radius with the gravitational mass versus radius curve generated via the TOV equations for each EOS mentioned in Section 3.5.2 and Section 3.5.3. Figure 3.1 shows that none of the current set of available EOS allow for a 2-$M_\odot$ neutron star while at the same time being consistent with the current mass-radius constraints from observations. The crux is that the EOS needs to be sufficiently stiff to support 2-$M_\odot$ neutron stars *and* at the same time sufficiently soft to make neutron stars with moderate radii in the canonical mass range. This balance appears to be difficult to realize. The stiff set of RMF EOS produce systematically too large neutron stars. The soft compressible liquid-droplet LS180 EOS (Lattimer and Swesty 1991) agrees well with the mass-radius constraints, but is ruled

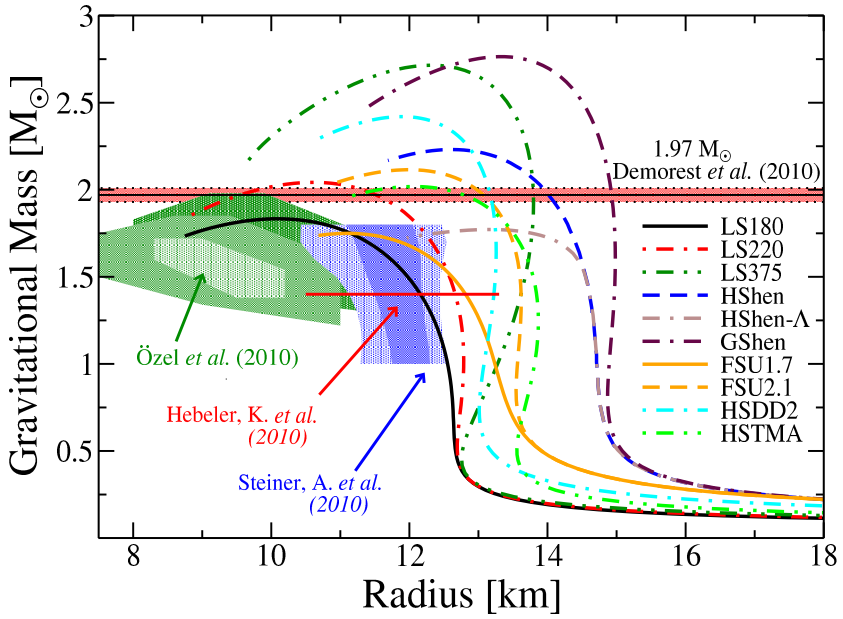


Figure 3.1: Mass-radius relations for 10 publicly available finite-temperature EOS along with several constraints. The EOS are taken from Hempel et al. (2011), Lattimer and Swesty (1991), Shen et al. (2011a,b,c) and Hempel, (unpublished) and the Tolman-Oppenheimer-Volkoff equation is solved with $T = 0.1\,\mathrm{MeV}$ and neutrino-less $\beta$-equilibrium imposed. The family of LS EOS is based on the compressible liquid-droplet model (Lattimer and Swesty 1991) while all other EOS are based on relativistic mean field theory. The nuclear theory constraints of Hebeler et al. (2010) assume a maximum mass greater than $2\,M_\odot$ and do not take into account a crust (which would increase the radius by $\sim$400 m). EOS that do not support a mass of at least $1.97 \pm 0.04\,M_\odot$ are ruled out (Demorest et al. 2010, Lattimer and Prakash 2011). Özel et al. (2010) analyzed three accreting and bursting neutron star systems and derived mass-radius regions shown in green. Steiner et al. (2010) performed a combined analysis of six accreting neutron star systems, shown are 1-$\sigma$ and 2-$\sigma$ results in blue.

out by its failure to support a 2-$M_\odot$ neutron star. Closest to satisfying all constraints are the LS220 EOS of Lattimer and Swesty (1991) and the yet unpublished HSDD2 EOS of Hempel, (unpublished) based on the RMF model of Typel et al. (2010). For the majority of work in this thesis, we make use of the LS220 or the HShen EOS. Some results were obtained before the measurement of the $1.97 \pm 0.04\,M_\odot$ neutron star, and therefore make use of the now ruled out LS180 EOS.

## 3.6 Neutrino Leakage and Heating

### 3.6.1 Deleptonization and Electron Capture in the Collapse Phase

Electron capture on free and bound protons during the collapse phase leads to the emission of neutrinos that stream away from the core and carry away net lepton number at densities below $\sim 10^{12}\,\mathrm{g\,cm^{-3}}$. The change of the electron fraction $Y_e$ in the collapse phase due to deleptonization

has important dynamical consequences. A reduction of $Y_e$ leads to a decrease of the mass of the homologously collapsing inner core whose kinetic energy is initially imparted on the supernova shock and which turns into the protoneutron star core after bounce (Bethe 1990). We take electron capture in collapse into account in `GR1D` with the approximate scheme of Liebendörfer (2005) who observed that $Y_e$ of infalling mass elements depends primarily on the local matter density $\rho$ and can be parameterized with rather high precision on the basis of radiation-hydrodynamic calculations.

Operator-split, after a hydrodynamics update, we compute the change in $Y_e$,

$$\Delta Y_e = \min\left[0, \overline{Y}_e(\rho) - Y_e\right] \ , \tag{3.21}$$

which ensures for consistency that a change in $Y_e$ is either negative or 0. We use for $\overline{Y}_e(\rho)$ the fitting formula given in Liebendörfer (2005) with parameters $\rho_1 = 3 \times 10^7\,\mathrm{g\ cm^{-3}}$, $\rho_2 = 2 \times 10^{13}\,\mathrm{g\ cm^{-3}}$, $Y_1 = 0.5$, $Y_2 = 0.278$, and $Y_c = 0.035$ corresponding to the 15-$M_\odot$ model of Woosley and Weaver (1995), evolved as model G15 by Liebendörfer et al. (2005). `GR1D` also contains an interpolation routine to use numerical $\overline{Y}_e(\rho)$ data.

Electron capture leads to a change in the entropy ($s$, the specific entropy in units of $k_\mathrm{B}$/baryon) that is injected into the matter by the thermalization of high energy neutrinos in the core at densities below an assumed trapping density $\rho_\mathrm{trap} = 2 \times 10^{12}\,\mathrm{g\,cm^{-3}}$. The entropy change is given by

$$\Delta s = -\Delta Y_e \frac{\mu_p - \mu_n + \mu_e - E_\nu}{k_\mathrm{B} T} \ . \tag{3.22}$$

$E_\nu$ is the energy of the escaping neutrinos (set to 10 MeV). $\mu_p$, $\mu_n$, and $\mu_e$ are the proton, neutron, and electron chemical potentials including rest mass, respectively. Following Liebendörfer (2005), we set $\Delta s = 0$ if $\mu_p - \mu_n + \mu_e < E_\nu$ and above $\rho_\mathrm{trap}$. After updating the entropy, we use the EOS to update the specific internal energy $\epsilon$ for consistency with the new $Y_e$ and $s$.

We employ the outlined deleptonization scheme until core bounce (defined as the time when the peak entropy of the inner core surpasses 3 $k_B$/baryon) and until 5 ms after bounce for yet unshocked regions of the outer core that will settle in the high-density outer protoneutron star and only in this way assume realistic postbounce $Y_e$.

### 3.6.2 Postbounce Deleptonization and Neutrino Heating/Cooling

At core bounce a strong hydrodynamic shock wave is generated that travels outward into the outer core, heating and dissociating infalling heavy nuclei into nucleons. Electron capture occurs rapidly on free protons and a sea of electron neutrinos ($\nu_e$) builds up and is released in the $\nu_e$ burst when the shock breaks through the neutrinosphere[7], deleptonizing the postshock region and leaving behind a

[7]The neutrinosphere is the effective "decoupling" surface of neutrinos where the optical depth $\tau_\nu$ of the supernova matter is 2/3. Its position depends strongly on neutrino energy.

"trough" in the $Y_e$ profile (e.g., Thompson et al. 2003). The softening of the EOS due to dissociation of nuclei and postshock energy loss to escaping neutrinos lead the shock to stall and turn into an accretion shock soon after bounce. In the hot postshock region, electrons are less degenerate and positrons appear and are captured on neutrons, leading to a rise of the $\bar{\nu}_e$ luminosity. In addition, in the protoneutron star and in the postshock region, neutrinos and antineutrinos of all flavors are emitted by thermal processes.

The simple $\overline{Y}_e(\rho)$ parameterization discussed in the previous section (Section 3.6.1) is not adequate to capture these effects and, in principle, a full neutrino energy-dependent radiation-hydrodynamics treatment would be needed for accurately capturing postbounce neutrino effects. Such a treatment is being added in a future version of `GR1D` (see Section 5). In the present version of `GR1D`, we approximate postbounce neutrino transport by a gray (energy-averaged) neutrino leakage scheme augmented with a simple prescription for neutrino heating in the postshock region. This approach captures the most important qualitative aspects of the postbounce evolution well and, as we demonstrate in Section 4.1.3.2, is sufficiently quantitatively accurate to make reliable predictions of the time of black hole formation and the maximum protoneutron star mass in failing core-collapse supernovae.

Our implementation in `GR1D` combines elements of the neutrino leakage schemes of Ruffert et al. (1996) and of Rosswog and Liebendörfer (2003). We consider three neutrino species, $\nu_e$, $\bar{\nu}_e$, and $\nu_x$. In the latter, we lump together $\mu$ and $\tau$ neutrinos and antineutrinos since they interact only by neutral-current processes in the core-collapse context and have very similar cross sections. The mean (energy-averaged) optical depth is

$$\tau_{\nu_i}(r) = \int_r^\infty \kappa_t(\nu_i)\, X dr \ , \tag{3.23}$$

where $\kappa_t(\nu_i)$ is the mean transport opacity equal to the sum of absorptive and scattering opacities[8] for neutrino species $\nu_i$. We follow Ruffert et al. (1996) in the calculation of $\kappa_t(\nu_i)$ and of the approximate neutrino degeneracy parameters ($\eta_{\nu_i} = \mu_{\nu_i}/T$). We consider opacity contributions from neutrino scattering on neutrons, protons, and heavy nuclei and absorption of neutrinos (antineutrinos) on neutrons (protons). For heavy-lepton neutrinos that are never degenerate, we set $\eta_{\nu_x} = 0$. $\eta_{\nu_e}$ is known (*1*) in $\beta$-equilibrium where $\eta^{\rm eq}_{\nu_e} = \eta_e + \eta_p - \eta_n$ (where we include the rest mass in the chemical potentials) and (*2*) in the free streaming limit, where $\eta^{\rm stream}_{\nu_e} = 0$. Furthermore, $\eta^{\rm eq}_{\bar{\nu}_e} = -\eta^{\rm eq}_{\nu_e}$. In between the two regimes, the neutrino distribution function cannot be derived from first principles and neutrino transport is necessary for a correct estimate of $\eta_{\nu_e}$ and $\eta_{\bar{\nu}_e}$. As an approximation, we

[8] Note that the opacities for neutrino number and neutrino energy transport differ. Hence, the optical depths for number and energy transport must be computed separately Ruffert et al. (1996). We neglect this subtlety and use the optical depths for energy transport throughout `GR1D`.

interpolate between (*1*) and (*2*) using the optical depth,

$$\eta_{\nu_i} = \eta^{\rm eq}_{\nu_i}(1 - e^{-\tau_{\nu_i}(\eta_{\nu_i})}) \ . \tag{3.24}$$

Note that $\tau_{\nu_i}$ depends on $\eta_{\nu_i}$ and vice versa. Hence, we iterate their calculation until convergence is reached[9].

Knowing $\tau_{\nu_i}$ and $\eta_{\nu_i}$, we use the leakage scheme of Rosswog and Liebendörfer (2003) to calculate the neutrino emission rates for the capture processes $p + e^- \rightarrow \nu_e + n$ and $e^+ + n \rightarrow \bar{\nu}_e + p$ and thermal emission via electron-positron annihilation and plasmon decay to $\nu\bar{\nu}$ pairs. We modify the scheme of Rosswog and Liebendörfer (2003) in the following ways: (*i*) we use the interpolated $\eta_{\nu_i}$ from above instead of the equilibrium values suggested in Rosswog and Liebendörfer (2003), (*ii*) we increase their diffusion time scale $t^{\rm diff}_{\nu_i}$ by a factor of 2 to obtain more reasonable neutrino luminosity predictions, and (*iii*) for simplicity, we use the analytic thermal emissivities from Ruffert et al. (1996). Following Rosswog and Liebendörfer (2003), we then interpolate the effective volumetric energy loss $Q^{\rm leak}_{\rm eff}$ (erg/cm$^3$/s) and effective number loss $R^{\rm leak}_{\rm eff}$ (#/cm$^3$/s) between the limits of diffusive emission (subscript "diff") and free emission (subscript "loc") using

$$\chi^{\rm leak}_{{\rm eff},\nu_i} = \chi^{\rm leak}_{{\rm loc},\nu_i}/(1 + \chi^{\rm leak}_{{\rm loc},\nu_i}/\chi^{\rm leak}_{{\rm diff},\nu_i}) \ , \tag{3.25}$$

where $\chi = Q$ for energy loss and $\chi = R$ for number loss (see Rosswog and Liebendörfer 2003 for definitions and details). We define the neutrino luminosity seen by an observer at rest at radius $r$ in the coordinate frame by summing up the effective energy emission rates from each zone interior to $r$, transforming from the fluid rest frame (FRF) to the coordinate frame (CF), and applying the redshift (see Appendix B for details),

$$L^{\rm CF}_{\nu_i}(r) = 4\pi \int_0^r \left[\frac{\alpha(r')}{\alpha(r)}\right] Q_{{\rm eff},\nu_i}(r')[\alpha(r')W(r')(1 + v(r'))]X(r')r'^2 dr' \ . \tag{3.26}$$

For an observer at rest at $r = \infty$ ($\alpha(\infty) = 1$),

$$L_{\nu_i}(\infty) = 4\pi \int_0^\infty \alpha(r')\, Q_{{\rm eff},\nu_i}(r')[\alpha(r')W(r')(1 + v(r'))]X(r')r'^2 dr' \ . \tag{3.27}$$

It is useful to note the neutrino luminosity as seen by an observer at rest in the fluid rest frame at radius $r$,

$$L^{\rm FRF}_{\nu_i}(r) = \frac{L^{\rm CF}_{\nu_i}(r)}{\alpha(r)W(r)(1 + v(r))} \ , \tag{3.28}$$

where the denominator transforms the luminosity from the frame of an observer at rest in the

[9]Initially we choose $\kappa_{\nu_i}(r) = 10^{-5}{\rm cm}^{-1}$ determine $\tau_{\nu_i}$ through Eq. 3.23 and iterate Eq. 3.24. For all subsequent times we use the previously determined value of $\tau_{\nu_i}$ as a starting point, convergence (fractional difference in $\kappa_{\nu_i} < 10^{-10}$) is typically reached after three iterations.

coordinate frame Equation 3.26 to the fluid rest frame.

#### 3.6.2.1 Neutrino Heating.

In addition to the above leakage scheme, we include a parameterized heating scheme to mimic neutrino absorption in the postshock region. Heating occurs at intermediate to low optical depths where neutrinos begin to decouple from matter and a net energy transfer from neutrinos to the fluid is possible (see, e.g., Janka 2001). The dominant heating processes are the charged-current capture reactions of $\nu_e$ on neutrons and $\bar{\nu}_e$ on protons. We take the absorption cross sections from Rosswog and Liebendörfer (2003),

$$\sigma_{\mathrm{heat},\nu_e} = \frac{(1+3g_A^2)}{4}\sigma_0 \frac{\langle\epsilon^2\rangle^{\mathrm{ns}}_{\nu_e}}{(m_e c^2)^2}\langle 1-f_{e^-}\rangle \ , \tag{3.29}$$

$$\sigma_{\mathrm{heat},\bar{\nu}_e} = \frac{(1+3g_A^2)}{4}\sigma_0 \frac{\langle\epsilon^2\rangle^{\mathrm{ns}}_{\bar{\nu}_e}}{(m_e c^2)^2}\langle 1-f_{e^+}\rangle \tag{3.30}$$

where $\sigma_0$ is a reference weak-interaction cross section equal to $1.76\times10^{-44}\,\mathrm{cm}^2$, $g_A \sim -1.25$, and the Fermi blocking factors $\langle 1-f_i\rangle$ are defined analogously to Rosswog and Liebendörfer (2003), Ruffert et al. (1996). In the postshock region the positron blocking term is negligible but the electron blocking term can be significant around the time of bounce. Following Janka (2001), we set the mean squared neutrino energy to $\langle\epsilon^2\rangle^{\mathrm{ns}}_{\nu_i} = T(\tau_{\nu_i}=\frac{2}{3})^2\mathcal{F}_5(\eta^{\mathrm{ns}}_{\nu_i})/\mathcal{F}_3(\eta^{\mathrm{ns}}_{\nu_i})$, where $T(\tau_{\nu_i}=\frac{2}{3})$ is the temperature at the neutrinosphere of species $i$, superscript ns denotes neutrinospheric values, and $\mathcal{F}_n(\eta)=\int_0^\infty \frac{x^n dx}{\exp(x-\eta)+1}$ is the $n^{\mathrm{th}}$ Fermi integral (we approximate Fermi integrals via the formulae given in Takahashi et al. (1978)).

Given the neutrino luminosity $L^{\mathrm{FRF}}_{\nu_i}(r)$ obtained from the leakage scheme Equation 3.28, we write the local neutrino heating rate in units of $\mathrm{erg\,cm^{-3}\,s^{-1}}$ as

$$Q^{\mathrm{heat}}_{\nu_i}(r) = f_{\mathrm{heat}}\frac{L^{\mathrm{FRF}}_{\nu_i}(r)}{4\pi r^2}\sigma_{\mathrm{heat},\nu_i}\frac{\rho}{m_u}X_i\left\langle\frac{1}{F_{\nu_i}}\right\rangle e^{-2\tau_{\nu_i}} \ , \tag{3.31}$$

where $m_u$ is atomic mass unit and the mass fraction $X_i = X_n$ in the case of $\nu_e$ absorption and $X_i = X_p$ for $\bar{\nu}_e$s. $\langle 1/F_{\nu_i}\rangle$ is the mean inverse flux factor describing the degree of forward-peaking of the radiation field (e.g., Janka 2001, Ott et al. 2008; $\langle 1/F_{\nu_i}\rangle$ is 1 for free streaming and diverges at high optical depth). We estimate $\langle 1/F_{\nu_i}\rangle$ by the interpolation $\langle 1/F_{\nu_i}(\tau)\rangle = 4.275\tau + 1.15$, which reproduces the predicted values of 4 at the neutrinosphere (Janka 2001) and levels off at a value of 1.15 at low optical depth in the outer postshock region. We choose the latter value instead of 1, because ($a$) the radiation field becomes fully forward peaked only outside the shock (e.g., Ott et al. 2008), and ($b$) the linear interpolation in $\tau$ drops off too quickly compared to full simulations Ott et al. (2008), hence the higher floor value to compensate. Finally, we introduce the attenuation factor $e^{-2\tau_{\nu_i}}$ to cut off heating near and below the neutrinosphere and the scaling factor $f_{\mathrm{heat}}$ to

allow for an ad-hoc increase of the heating rate. Once the heating rate for a computational cell is computed, we reduce the outgoing luminosity by the deposited power for overall energy conservation. In the coordinate frame Equation 3.26 now becomes,

$$L^{\rm CF}_{\nu_i}(r) = 4\pi \int_0^r \left[\frac{\alpha(r')}{\alpha(r)}\right] \left[Q_{{\rm eff},\nu_i}(r') - Q^{\rm heat}_{\nu_i}(r')\right] \left[\alpha(r')W(r')(1+v(r'))\right] X(r') r'^2 dr' \ . \tag{3.32}$$

Along with the energy deposition goes a change in $Y_e$ which can be written as

$$R^{\rm heat}_{Y_e} = \frac{Q^{\rm heat}_{\nu_e}}{\langle \epsilon^{\rm ns}_{\nu_e} \rangle} - \frac{Q^{\rm heat}_{\bar{\nu}_e}}{\langle \epsilon^{\rm ns}_{\bar{\nu}_e} \rangle} \ , \tag{3.33}$$

where we approximate the mean neutrino energies based on their neutrinospheric values as $\langle \epsilon^{\rm ns}_{\nu_i} \rangle = T(\tau_{\nu_e} = \frac{2}{3}) \mathcal{F}_5(\eta^{\rm ns}_{\nu_i}) / \mathcal{F}_4(\eta^{\rm ns}_{\nu_i})$ (Rosswog and Liebendörfer 2003).

To caution the reader, we point out that the simple gray heating scheme presented in the above is not self-consistent and cannot replace a radiation transport treatment that allows emission and absorption to balance. While we find that the combination of gray leakage/heating reproduces the overall qualitative dynamical features observed in postbounce radiation-hydrodynamic simulations, quantitative aspects are not captured as well. This is true in particular in highly dynamical situations shortly after bounce when we observe an unphysical rise of the electron fraction due to heating in the lower postshock region.

We couple the neutrino leakage/heating scheme with the GR hydrodynamics in `GR1D` through source/sink terms on the RHS of the GR hydrodynamics equations in MoL. Neutrino–matter interactions occur in the fluid rest frame where the total energy and number changes are given by

$$Q^0_{\rm E} = Q^{\rm heat}_{\rm total} - Q^{\rm leak}_{\rm eff,total} \ , \quad R^0_{Y_e} = R^{\rm heat}_{\rm total} + R^{\rm leak}_{\rm eff,total} \ , \tag{3.34}$$

where $Q^{\rm heat}_{\rm total}$ and $Q^{\rm leak}_{\rm eff,total}$ are always positive or zero and $R^{\rm heat}_{\rm total}$ and $R^{\rm leak}_{\rm eff,total}$ may be positive or negative. Following Müller (2009), Pons et al. (1997), transforming these terms to the coordinate frame via the methods laid out in Appendix A, we obtain the neutrino heating/cooling and deleptonization source/sink terms for the RHS in the MoL integration,

$$R^{\nu}_{Y_e} = \alpha X R^0_{Y_e} \ , \quad Q^{\nu,E}_{S^r} = \alpha v W Q^0_{\rm E} \ , \quad Q^{\nu,E}_{\tau} = \alpha W Q^0_{\rm E} \ . \tag{3.35}$$

### 3.6.3 Neutrino Pressure

Electron neutrinos above trapping density in the inner core during the final phases of collapse and in the postbounce protoneutron star contribute to the pressure (with relative importance of up to $\sim 10\%$ around core bounce Ott 2006). We neglect neutrino contributions to pressure below $\rho_{\rm trap}$ where they are small, but otherwise follow Liebendörfer (2005) and assume electron neutrinos and

antineutrinos to be a perfect Fermi gas. The pressure is then given by

$$P_\nu = \frac{4\pi}{3(hc)^3} T^4 \left[F_3(\eta_\nu) + F_3(-\eta_\nu)\right] \ , \tag{3.36}$$

where $\eta_\nu = \mu_\nu / T$ and $\mu_\nu = \mu_e - \mu_n + \mu_p$, where the chemical potentials include rest mass contributions. $F_3$ is the $3^{\rm rd}$ Fermi integral which we approximate following Bludman and van Riper (1977).

We treat neutrinos and fluid separately from each other and treat momentum transfer between the neutrino radiation field and the fluid approximately using the radial gradient of the neutrino pressure as suggested by Liebendörfer (2005). We couple this radiation stress into `GR1D`'s MoL integration of the GR momentum ($S^r$) and energy ($\tau$) equations via source terms (see Appendix A for a derivation; we neglect rotational effects in these source terms),

$$Q^{\nu,\rm M}_{S^r} = -\alpha W \frac{\partial P_\nu}{\partial r} \ , \qquad\qquad Q^{\nu,\rm M}_{\tau} = -\alpha W v \frac{\partial P_\nu}{\partial r} \ . \tag{3.37}$$

In addition to the force on the fluid due to the neutrino pressure gradient, we take into account pressure of the neutrino radiation field by adding $P_\nu$ to Equation 3.4 and Equations 3.5 and 3.15. These contributions are derived by modifying the stress-energy tensor,

$$T^{\alpha\beta} = \rho \left[1 + \epsilon + \left(\frac{P + P_\nu}{\rho}\right)\right] u^\alpha u^\beta + g^{\alpha\beta}(P + P_\nu) \ , \tag{3.38}$$

$\tau^\nu_m$ and $\tau^\nu_\Phi$ are then given by Noble (2003)

$$\tau^\nu_m = \rho W^2 (P_\nu/\rho) - P_\nu = (W^2 - 1) P_\nu \ , \tag{3.39}$$

$$\tau^\nu_\Phi = \rho W^2 v^2 (P_\nu/\rho) + P_\nu = (W^2 v^2 + 1) P_\nu \ . \tag{3.40}$$

Including these terms, Eq. 3.4 and Eqs. 3.5 become,

$$m(r,t) = 4\pi \int_0^r (\rho h W^2 - P + \tau^\nu_m) r'^2 dr' \ . \tag{3.41}$$

$$\Phi(r,t) = \int_0^r X^2 \left[\frac{m(r',t)}{r'^2} + 4\pi r' (\rho h W^2 v^2 + P + \tau^\nu_\Phi)\right] dr' + \Phi_0 \ , \tag{3.42}$$

We note that if rotation is included, we modify our terms as discussed in Section 3.4, i.e. $v^2$ in Equations 3.40 and 3.42 and the Lorentz factor is replaced with $v^2 + \frac{2}{3} v^2_\varphi$.

## 3.7 Code Tests

In the following, we provide results from a set of standard and stringent relativistic hydrodynamics code tests for which analytic results exist. These involve two planar shocktube problems in Section 3.7.1, the spherical Sedov blast wave problem in Section 3.7.2, and Oppenheimer-Snyder collapse in Section 3.7.3. Finally, in Section 3.7.4, we present results from a collapse simulation of a $n = 3$ polytrope and demonstrate convergence of the hydrodynamics scheme in `GR1D`. With this selection, we test a broad range of aspects of potential problems to be addressed with `GR1D`: special relativistic effects, geometrical effects, and fully general-relativistic collapse dynamics. We delay comparing our neutrino leakage scheme to full Boltzmann radiation transport until Chapter 4.

### 3.7.1 Relativistic Shocktube

We assume flat space and planar geometry and perform the two relativistic shocktube tests proposed by Martí and Müller (2003). We use a $\Gamma-$law EOS with $\Gamma = 5/3$ and a grid of length 1 with a cell spacing of $dx = 0.001$. The starting values of the density, pressure and velocity are summarized in Table 3.1. The left panel of Figure 3.2 shows the exact results for velocity, density, and pressure of the mildly relativistic problem #1 at $t = 0.4$. Superposed are the numerical results obtained with `GR1D` that reproduce the exact results nearly perfectly. Problem #2 is a more stringent test and involves Lorentz factors of up to 6 in the forward propagating shock and a very thin shell of trailing matter. As shown in the right panel of Section 3.2, `GR1D` reproduces the exact solution at $t = 0.4$ very well almost everywhere, but fails to completely resolve the thin shell of relativistic matter. This is most likely due to the rather diffusive nature of the HLLE Riemann solver employed in `GR1D` (see, e.g., Dimmelmeier et al. 2002b, Ott 2006 for comparable results obtained with a nominally more accurate scheme). In an attempt to obtain results closer to the analytic solution we use $3^{rd}$-order Runge-Kutta time integration for this test case. These deviations are not worrying since the shocks that obtain in stellar collapse are much less relativistic than that of problem #2. If `GR1D` were to be applied to ultra relativistic outflows (e.g., in a GRB), a more precise treatment of the Riemann problem would likely be necessary.

| P1 | | P2 | |
|---|---|---|---|
| $r < 0.5$ | $r > 0.5$ | $r < 0.5$ | $r > 0.5$ |
| $\rho = 10$ | $\rho = 1$ | $\rho = 1$ | $\rho = 1$ |
| $P = 13.33$ | $P = 0$ | $P = 10^3$ | $P = 0.01$ |
| $v = 0$ | $v = 0$ | $v = 0$ | $v = 0$ |

Table 3.1: Initial conditions for two relativistic shocktube problems as presented in Martí and Müller (2003)

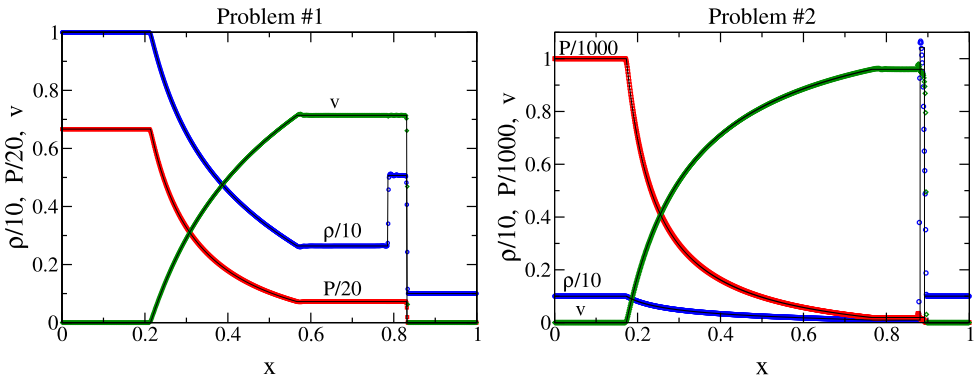


Figure 3.2: Relativistic shocktube simulations: Initial conditions taken from Martí and Müller (2003) and provided in Table 3.1. The pressure, density, and velocity are shown at $t = 0.4$ for problem #1 (left panel) and problem #2 (right panel). For reference, in both figures the pressure is denoted by boxes (red), density by circles (blue) and velocity by diamonds (green). The analytic solution is denoted by the solid line. Both problems were run with a Courant factor of 0.5 and $3^{\rm rd}$-order Runge-Kutta integration.

### 3.7.2 Sedov Blast Wave

The above shocktube tests demonstrated the ability of `GR1D` to capture shocks and solve the special-relativistic hydrodynamic equations in planar geometry. Here we go back to Newtonian hydrodynamics and test instead spherical hydrodynamics with Sedov's blast wave problem (Sedov 1959). For a comparison with a large number of hydrodynamics codes, we use the initial conditions of Tasker et al. (2008). The grid setup is in spherical geometry with (dimensionless) $r_{max} = 10$ and $N = 400$ cells which corresponds to the maximum mesh refinement level used in Tasker et al. (2008). We deposit a constant specific internal energy into a sphere of radius $r = 0.0875$, corresponding to a total (dimensionless) energy of $E_o = 10^5$, into a background medium of (dimensionless) $\rho_0 = 1$. We set the background energy density to an insignificant amount and use a $\Gamma$-law EOS with $\Gamma = 5/3$. Figure 3.3 depicts the comparison of our numerical solution with the exact result for density, velocity and pressure at $t = 0.1$ normalized in such a way that the value of all variables at the shock is 1. `GR1D` performs very well in the region behind the shock and provides an adequate, though not perfect, solution near the shock.

In addition to the Newtonian Sedov blast wave problem, we have also considered its relativistic variant discussed in Anninos et al. (2005). These authors used 17 levels of adaptive mesh refinement (AMR) and we find that the lack of AMR in `GR1D` makes it computationally impossible to adequately resolve the relativistic Sedov problem. This, however, is not a problem for the application of `GR1D`

to the stellar collapse problem, since the shocks appearing there are only mildly relativistic.

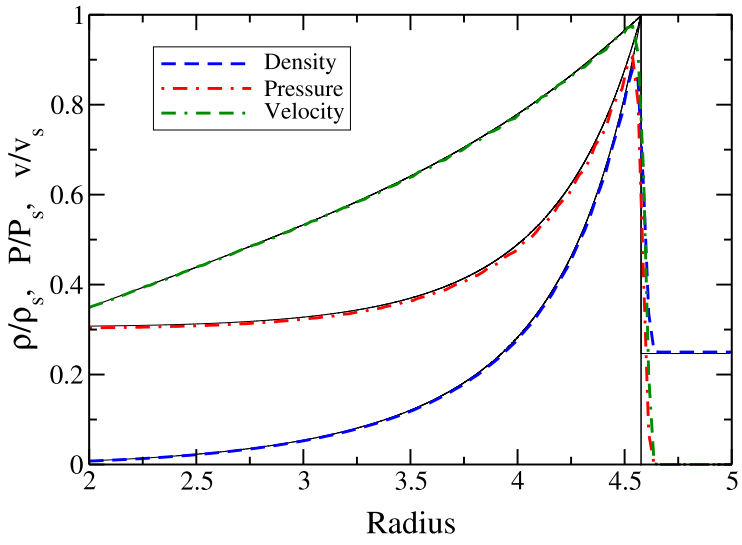


Figure 3.3: The Sedov blast wave problem and exact solution at $t = 0.1$. Shown are the numerical results with the exact solution underlying the various curves of density, pressure and velocity. Both the exact solution and the numerical result are normalized to the analytic value at the shock. $\rho_s = 4$, $P_s = 252.255$ and $v_s = 13.757$.

### 3.7.3 Oppenheimer-Snyder Collapse

For the final test problem for which an exact solution exists, we perform a simulation of the Oppenheimer-Snyder collapse (OSC) (Oppenheimer and Volkoff 1939) of a constant-density sphere of pressureless ($P = 0$) dust. The exact solution of OSC in RGPS spacetime has been laid out by Gourgoulhon (1993), Petrich et al. (1986). We choose $M = M_\odot$, $R_\star = 10M_\odot$. We perform the OSC test with the standard version of `GR1D` described in Sections 3.2 and 3.3 of this paper and do not make special adjustments for the code to operate with $P = 0$. Hence, we set the pressure to a small, but nonzero value, using a polytropic EOS with $K = 10^{-20}$ and $\Gamma = 5/3$. In the artificial atmosphere outside the dust ball, we set the density to $1\,\mathrm{g\,cm^{-3}}$. We use 9000 equidistant zones to model OSC with `GR1D`. This is needed to capture the growing coordinate singularity at $R = 2M$

In Figure 3.4, we compare numerical and exact density and lapse profiles of OSC at $t = 30$, 35, 40, 43, and 60 $M_\odot$. Following Romero et al. (1996), we normalize the central density to the value at $t = 0$. The overall agreement is excellent. However, we notice two slight deviations: (*1*), near the origin, we observe a small build up of material. This is present also in the OSC test of Romero et al. (1996) and probably due to diverging terms near the origin. We do not notice this effect in our stellar collapse calculations, most likely because of the stabilizing effect of the large pressure

in the protoneutron star. (*2*), at late times ($t > 50M_\odot$), the numerical $\alpha$ decreases more slowly than its exact counterpart and begins to deviate significantly at $\alpha(r = 0) \lesssim 0.001$. We attribute this to numerical inaccuracies developing due (*a*) to the metric coefficient $X$ becoming singular as $R_\star \to 2M_\odot$, (*b*) to the extreme density gradient developing at the surface at late times, and (*c*) to the fact that we use the standard version of `GR1D` without special adjustments for the OSC problem (as, e.g., made by Romero et al. 1996).

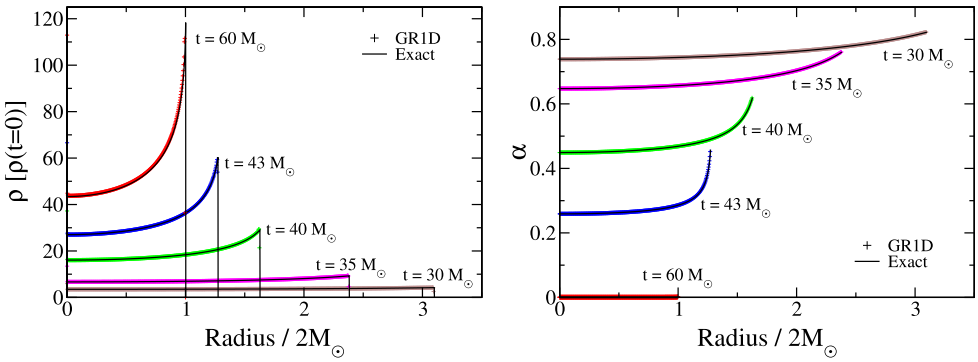


Figure 3.4: Oppenheimer-Snyder collapse of a pressureless dust ball. Shown are the numerical (plus symbols) and exact (solid lines) density (left panel) and lapse (right panel) profiles for various times. The density is normalized to the density at $t = 0$. The simulation uses 9000 equally spaced grid points across the domain of $20\,M_\odot$. Initially one solar mass is distributed with constant density in a sphere of radius $10\,M_\odot$. For clarity, we show only every third data point.

### 3.7.4 Hybrid Core Collapse: Convergence

In this section, we present simulations of nonrotating core collapse and present proof of convergence for `GR1D`. We utilize the hybrid EOS described in Section 3.5.1, taking $\Gamma_1 = 1.28$, $\Gamma_2 = 2.5$, $\Gamma_{\rm th} = 1.5$ and $K = 4.935 \times 10^{14}$[cgs]. Following Ott (2006), we use as initial data an $n = 3$ polytrope with a central density of $\rho_c = 5 \times 10^{10}\mathrm{g/cm}^3$ and a $K$ value as above and initially zero radial velocity. We simulate the evolution with `GR1D` for equally spaced grids of three different resolutions ($N_{\rm zones} = 500,\ 1500$ and $4500$) to test the self-convergence of the code. The self-convergence factor at convergence order $n$ of a quantity $q$ is given by,

$$Q = \frac{q_1 - q_2}{q_2 - q_3} = \frac{(dx_1)^n - (dx_2)^n}{(dx_2)^n - (dx_3)^n}\ , \tag{3.43}$$

where $q_i$ is the numerical result from the simulation with the corresponding resolution and $dx$ is the zone width. For this convergence test, $dx_1 = 3dx_2 = 9dx_3$. In the lower panel of Figure 3.5, we show the self-convergence of $M_{\rm grav}$ at $t = -3.3\,$ms (before bounce) as well as at $t = 16.6$ ms and $t = 26.6$ ms after bounce.

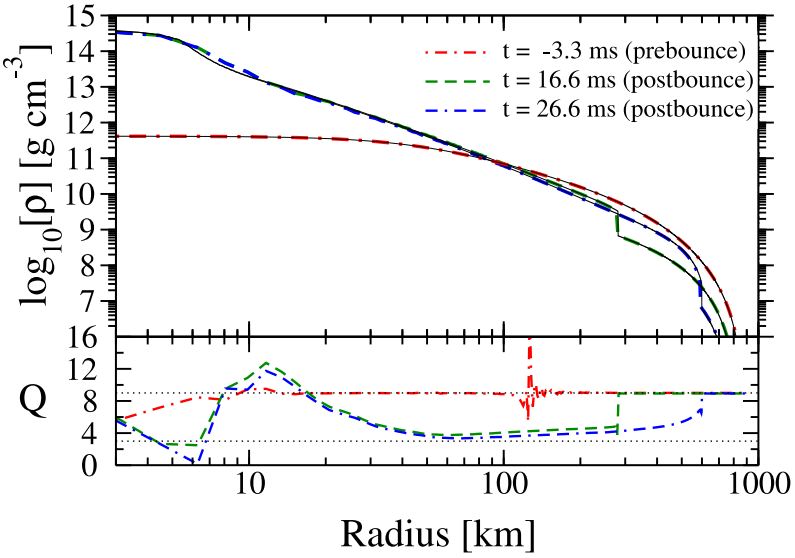


Figure 3.5: Radial density profiles and self-convergence for core collapse using the hybrid EOS. **Top:** Density profiles of the core collapse for various times including in the prebounce phase, and after the shock has propagated through $\sim$ 300 and 600 km. We show the low resolution profile (segmented lines) as well as the high resolution profile (solid lines) for comparison. **Bottom:** Self-convergence of the enclosed gravitational mass, $m(r)$. Dotted lines at Q=3 and 9 denote expected values for 1$^{\rm st}$- and 2$^{\rm nd}$-order convergence.

We generally see the expected 2$^{\rm nd}$-order convergence (Q=9) in smooth parts of the flow, but note several interesting features: (*1*) before bounce (red, dot-dashed curve) and near 120 km where the convergence spikes, the velocity is peaking, causing a reduction in convergence. (*2*), during the postbounce phase, convergence in the shocked region drops to 1$^{\rm st}$ order, this is characteristic of HRSC schemes in the presence of shocks. (*3*), finally, during the postbounce phase for $r < 20$ km, the steepness of the density gradient at the protoneutron star surface and the coarseness of the grid lead to *local* nonconvergence. We note that the lowest resolution used here is $dx \sim 2$ km and that deviations in the density profile compared to higher-resolution simulations can be seen in the top panel of Figure 3.5.

## 3.8 Summary

In this paper, we have presented the details of our new open-source Eulerian 1.5D GR hydrodynamics code `GR1D`. `GR1D` is intended primarily for the simulation of stellar collapse to neutron stars and black holes and, for the first time in the 1D GR context, includes an approximate way of accounting for stellar rotation consistent with that used in state-of-the-art calculations of stellar evolution (e.g.,

Heger et al. 2005). GR1D also includes an approximate neutrino leakage/heating scheme for estimating the effect of neutrinos during stellar collapse.

Many 1D GR (radiation)-hydrodynamics formulations have been presented in the past ∼50 years. Yet, there is presently no open-source 1D GR stellar collapse code available to the broader community. The primary motivation driving the development of GR1D is the need for such an open-source code that may be used as a codebase, benchmark, and test bed for improved modeling technology to be included in multidimensional GR codes addressing core-collapse supernova explosions, but also failing core-collapse supernovae, black hole formation, and the postmerger evolution of binary neutron-star and neutron-star–black-hole coalescence. Equipped with an approximate neutrino-leakage scheme to capture the key effects associated with neutrino heating and cooling, the version of GR1D discussed in this paper is a solid starting point for the next generation of astrophysically-relevant multidimensional GR simulations.

# Chapter 4

# Black Hole Formation in Failing Core-Collapse Supernovae[1]

It is currently unclear what fraction of massive stars form black holes and through which channel. Pre-explosion observations of progenitors of successful core-collapse supernovae suggest progenitor masses $\lesssim$ 17–20 $M_\odot$ (Smartt et al. 2009) for standard Type II-P supernovae. Assuming, as one suggestion by authors, that most other core-collapse supernovae fail or make black holes after a successful but undetectable explosion, this would correspond to a black hole fraction upper limit of $\lesssim$ 30–35 % of massive stars above 8 $M_\odot$ (assuming a Salpeter initial mass function). However, alternative interpretations exist and have been summarized by Smith et al. (2011). Theoretical work by Timmes et al. (1996), Fryer (1999), Heger et al. (2003), and Eldridge and Tout (2004) provided rough estimates on the outcomes of stellar collapse as a function of progenitor ZAMS mass and metallicity. Leaving effects due to binary evolution aside, Zhang et al. (2008) performed an extensive study of fallback in artificially driven, spherically-symmetric core-collapse supernova explosions and estimated that zero-metallicity stars form black holes in 20–50 % of all core-collapse events with an average black hole mass of 6–10 $M_\odot$. For solar metallicity stars, due to increased mass loss during evolution, they found black holes to form at a significantly lower rate and initial mass. They predict black hole fractions in the range of 10–25 % with typical initial black hole masses of 3 $M_\odot$. This is in rough agreement with previous population synthesis calculations of Fryer and Kalogera (2001) and Belczynski et al. (2002).

However, there is strong observational evidence of black holes in low-mass x-ray binary systems throughout the Galaxy (Remillard and McClintock 2006). Hence, at least in some core-collapse events a black hole must be the final outcome. Observational studies (cf. the study of Smartt et al. 2009 mentioned above) aim to determine which stars explode in core-collapse supernovae and

[1]This chapter is largely based on the article *Black Hole Formation in Failing Core-Collapse Supernovae*, O'Connor, E. & Ott, C.D., The Astrophysical Journal **730** 70 (2011): Reproduced with permission from IOP Publishing. This chapter also contains both unpublished work and work from the article *The Arduous Journey to Black-Hole Formation in Potential Gamma-Ray Burst Progenitors.* Dessart, L., O'Connor, E. & Ott. C.D. *submitted to The Astrophysical Journal* 2012.

which form black holes by observing the pre-explosion progenitor stars. Complementary, Kochanek et al. (2008) suggest to actively look for the disappearance of massive stars in failed supernovae, or *unnova*. The electromagnetic discovery of such an event would provide crucial constraints on progenitor mass and structure. Furthermore, if occurring nearby (D $\lesssim$ 100 kpc), the observed neutrino signal would herald black hole formation by a steep signal decrease as the protoneutron star is engulfed by the black hole horizon (Beacom et al. 2001, Burrows 1988). Gravitational wave emission from a core-collapse event has the potential to be measured for a galactic or near galactic supernova at current and future ground-based gravitational wave detectors (Ott 2009 and references therein). As with neutrinos, a failed galactic supernova may have unique gravitational wave signal (Ott et al. 2011). If collapsar-type failed supernovae are indeed connected with long GRBs, as suggest by Woosley (1993) and MacFadyen et al. (2001), an electromagnetic signal may accompany the event. Observational evidence exists linking long GRBs and broad line Type-Ic supernova, first discovered with the correlation of GRB 980425 and SN 1998bw. Several other GRB-SN pairs have since been observed.

Early spherically symmetric (one-dimensional, 1D) simulations of black hole formation in failing core-collapse supernovae were carried out by Wilson (1971) and van Riper and Arnett (1978). Burrows (1988) performed a set of quasi-stationary 1D protoneutron star accretion and cooling simulations to investigate the possibility of black hole formation in SN 1987A. Delayed black hole formation (by tens of seconds), due to, e.g., a nuclear EOS phase transition, was studied by Baumgarte et al. (1996a,b). More recently, 1D full Boltzmann neutrino radiation-hydrodynamics calculations of failing nonrotating core-collapse supernovae were carried out by Liebendörfer et al. (2004) and more recently Sumiyoshi et al. (2007, 2008, 2009) and Fischer et al. (2009). These studies provided detailed neutrino signature predictions for black hole-forming core-collapse events. However, owing to the complexity and computational expense of such Boltzmann-transport calculations, these groups could consider only very limited sets of progenitor models and EOS. Simplified axisymmetric (2D) simulations of black hole formation in rotating core collapse were first performed in a series of papers by Sekiguchi and Shibata (2004, 2005) and Shibata and Sekiguchi (2005). These authors used simplified EOS, no neutrino treatment, and artificially constructed initial conditions and found prompt black hole formation. Recently, the same authors performed a small set of 2D simulations with a finite-temperature nuclear EOS and a leakage scheme for neutrinos (Sekiguchi and Shibata 2011) and considered collapse, black hole formation, and subsequent evolution in an artificially constructed progenitor with an iron core mass of $\sim 13\,M_\odot$ and constant specific entropy of $8\,k_B$/baryon, initial conditions that are inconsistent with those at the precollapse stage of core-collapse supernova progenitors. The first 3D general-relativistic simulations of black hole formation and subsequent evolution in the core-collapse supernova context were recently carried out by Ott et al. (2011). An extreme, but realistic, progenitor profile was used. For computational reasons, a simplified equation

of state with a low maximum mass was employed to ensure fast black hole formation.

In this chapter, our focus is on studying and establishing the systematics of failing core-collapse supernovae and black hole formation in both nonrotating and rotating progenitors. We utilize `GR1D` and its leakage scheme exclusively. While we sacrifice accuracy in the neutrino treatment by employing an efficient energy-averaged three-species neutrino leakage scheme instead of full transport, the efficiency of `GR1D` enables us to perform more than $\sim 800$ collapse calculations, investigating for the first time in detail the effects of variations in nuclear EOS, progenitor ZAMS mass and metallicity, neutrino heating efficiency, and precollapse rotational configuration. We employ four different finite-temperature nuclear EOS and draw a total of 153 progenitor models from seven stellar evolution studies. We divide this chapter into two main sections. The first section focuses on nonrotating progenitors. The work is drawn from O'Connor and Ott (2011). The second section contains results of rotating progenitors, this section draws stage-setting work from O'Connor and Ott (2011) and quantitative results from Dessart et al. (2012).

In Section 4.1 we study nonrotating black hole formation. Sections 4.1.1 and 4.1.2 we introduce our nonrotating progenitor model set and numerical grid setup. We also discuss the various differences in presupernova model sets, with particular focus on the mass loss rates invoked. In Section 4.1.3.1, we introduce key aspects of failing core-collapse supernovae and black hole formation by discussing the evolution of black hole formation in a fiducial nonrotating 40 $M_\odot$ solar-metallicity progenitor. We go on in Section 4.1.3.3 to study the influence of the EOS and thermal effects on the time to black hole formation and on the maximum (baryonic and gravitational) mass of the protoneutron star. We discover that for nuclear EOS with physically plausible stiffness, the maximum (baryonic and gravitational) mass of the protoneutron star is always greater than the corresponding cold NS mass and discuss that the difference is due entirely to thermal pressure support of material in the hot outer protoneutron star core. In Section 4.1.3.4, we analyze the impact of variations in progenitor structure on the time to black hole formation and the maximum protoneutron star mass in failing core-collapse supernovae. We find that the postbounce dynamics can be predicted rather robustly by a single parameter, the compactness of the progenitor structure at core bounce. The same approximate single-parameter dependence emerges in Section 4.1.3.5, where we determine the neutrino heating efficiencies required (modulo ignored multidimensional effects) to induce a neutrino-driven explosion in a large set of progenitors. The combined results of Sections 4.1.3.4 and 4.1.3.5 allow us to make predictions on the outcome of core collapse for progenitors with varying ZAMS mass and metallicity in Sections 4.1.3.6 and 4.1.3.7. As we discuss in the latter section, mass loss may be the greatest uncertainty in connecting ZAMS parameters to core-collapse results.

In Section 4.2, we present results obtained by varying the precollapse rotation. We find that, not unexpectedly, increased rotation leads to a delay of black hole formation and greater maximum protoneutron star masses. We also observe that the birth spin of Kerr black holes in nature appears

to be robustly limited to values below $a^\star = J/M^2 \lesssim 0.9$ by the likely appearance of nonaxisymmetric rotational instabilities that redistribute or radiate angular momentum. This finding requires confirmation by 3D simulations. We go on in Section 4.2.2 to systematically explore the collapse evolution of a set of potential long $\gamma$-ray burst progenitors that were evolved from the ZAMS with rotation and discuss their viability as collapsar-type long-GRB progenitors. We stress the point that one must consider the bounce compactness in addition to the angular momentum budget when making predictions about progenitors of collapsars.

## 4.1 Nonrotating Black Hole Formation

### 4.1.1 Presupernova Data

We make use of single-star nonrotating presupernova models from several stellar evolution studies: Woosley and Weaver (1995) (WW95), Woosley et al. (2002) (WHW02), Limongi and Chieffi (2006) (LC06A/B) and Woosley and Heger (2007) (WH07). Each of these studies evolved stars with a range of ZAMS masses at solar metallicity ($Z_\odot$, hereafter denoted with prefix $s$ in model names) up until the onset of core collapse. In addition to solar metallicity, WHW02 evolved stars with ultra-low metallicity, $10^{-4}\,Z_\odot$ (denoted by prefix $u$) and zero metallicity (denoted by prefix $z$).

In Table 4.1, we list key parameters for all models in our nonrotating sets. These include presupernova mass, iron core mass (which we define as the baryonic mass interior to $Y_e = 0.495$), and the bounce compactness $\xi_{2.5}$. The latter is defined as

$$\xi_M = \left.\frac{M/\,M_\odot}{R(M_{\rm bary} = M)/1000\,{\rm km}}\right|_{t=t_{\rm bounce}}, \tag{4.1}$$

where we set $M = 2.5\,M_\odot$. $R(M_{\rm bary} = 2.5\,M_\odot)$ is the radial coordinate that encloses 2.5-$M_\odot$ at the time of core bounce. $\xi_{2.5}$ gives a measure of a progenitor's compactness at bounce. We choose $M = 2.5\,M_\odot$ as this is the relevant mass scale for black hole formation. $\xi_{2.5}$ is, as we shall discuss in Section 4.1.3.4, a dimensionless variable that allows robust predictions on the postbounce dynamics and the evolution of the model toward black hole formation. The evaluation of $\xi_{2.5}$ at core bounce is crucial, since this is the only physical and unambiguous point in core collapse at which one can define a zero of time and can describe the true initial conditions for postbounce evolution. Computing the same quantity at the precollapse stage leads to ambiguous results, since progenitors come out of stellar evolution codes in more or less collapsed states. Collapse washes out these initial conditions and removes ambiguities.

We point out (as is obvious from Table 4.1) that there is a clear correlation between iron core mass and bounce compactness. Since the effective Chandrasekhar mass increases due to thermal corrections (Baron and Cooperstein 1990, Burrows and Lattimer 1983), more massive iron cores are

hotter. Hence, progenitors with greater bounce compactness result in higher-temperature protoneutron stars.

One of the most uncertain, yet most important, variables in the evolution of massive stars is the mass-loss rate. Mass loss can vary significantly over the life of a star. Current estimates of mass loss, either theoretical or based on fits to observational data, can depend on many parameters, including mass, radius, stellar luminosity, effective surface temperature, surface hydrogen and helium abundance, and stellar metallicity (de Jager et al. 1988, Nieuwenhuijzen and de Jager 1990, Nugis and Lamers 2000, Vink and de Koter 2005, Wellstein and Langer 1999). The mass-loss rate is uncertain in both the massive O-star and in the stripped-envelope Wolf-Rayet star stage. O-star winds are expected to be responsible for the partial or complete removal of the hydrogen envelopes of massive stars. Recent observational results suggest that the rates used in current stellar evolution models may be too high by factors of 3–10 if clumped winds are considered correctly (Bouret et al. 2005, Fullerton et al. 2006, Puls et al. 2006). With the reduced rates, Wolf-Rayet stars would be difficult to make in standard single-star evolution and would require binary or eruptive mass-loss scenarios (Smith et al. 2011).

In Figure 4.1, we plot the mass-loss-induced mapping between ZAMS mass and presupernova mass for the ensemble of nonrotating progenitors listed in Table 4.1. WW95 models do not include mass loss — the presupernova models of this study have a mass equal to the ZAMS mass. WHW02 and WH07 employ the mass-loss rates of Nieuwenhuijzen and de Jager (1990) and Wellstein and Langer (1999) and use significantly reduced rates for low and zero metallicity stars. The $u$ and $z$ models of WHW02 have almost no mass loss and their presupernova masses are very close to their ZAMS values. The solar-metallicity stars of the $s$WHW02 and $s$WH07 model sets have significant mass loss, generally scaling with ZAMS mass. The most massive stars in these model sets have presupernova masses that are a small fraction of the initial ZAMS mass. For main sequence and giant phases, Limongi and Chieffi (2006) adopt mass-loss rates following Vink et al. (2000, 2001) and de Jager et al. (1988). For Wolf-Rayet stars, they either use the mass-loss rates of Nugis and Lamers (2000) (hereinafter referred to as LC06A models) or Langer (1989) (LC06B models). The latter are close to the values used for solar-metallicity stars in the WHW02 and WH07 model sets. The difference in the LC06A and LC06B mass-loss rates is roughly a factor of two. This, as portrayed by Figure 4.1 and evident from Table 4.1, can significantly alter the total mass at the onset of collapse and also has a strong effect on the iron core mass and bounce compactness.

An additional uncertainty in massive star evolution is the phenomenon of large episodic mass loss (Quataert and Shiode 2012, Smith 2007, Yoon and Cantiello 2010). Unknowns and uncertainties in both the cause and effect of large episodic mass loss currently prevent detailed stellar evolution calculations from incorporating these phenomena self consistently.

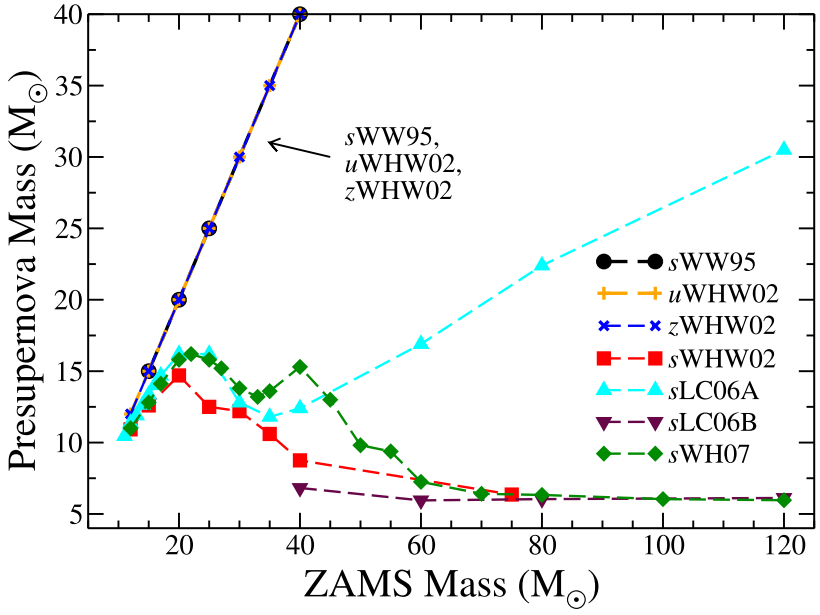


Figure 4.1: Presupernova mass as a function of ZAMS mass for the various model sets considered here. See the text for discussion.

Table 4.1: The model name contains the information necessary to uniquely specify the presupernova model. For nonrotating progenitors, the beginning letter in the model name refers to the metallicity of the progenitor, following the convention of Woosley et al. (2002), "$s$", "$u$", and "$z$" are used for solar, $10^{-4}$ solar, and zero metallicities, respectively. Following is the ZAMS mass, next we specify the progenitor model set (see the text for references).

| Model | $M_{\rm ZAMS}$ $[M_\odot]$ | $M_{\rm pre-SN}$ $[M_\odot]$ | $M_{\rm Fe\ core}$[1] $[M_\odot]$ | $\xi_{2.5}$[2] |
|---|---|---|---|---|
| s20WW95 | 20 | 20.0 | 1.74 | 0.383 |
| s25WW95 | 25 | 25.0 | 1.77 | 0.416 |
| s40WW95 | 40 | 40.0 | 1.98 | 0.583 |
| s15WHW02 | 15 | 12.6 | 1.55 | 0.150 |
| s20WHW02 | 20 | 14.7 | 1.46 | 0.127 |
| s25WHW02 | 25 | 12.5 | 1.62 | 0.326 |
| s30WHW02 | 30 | 12.2 | 1.46 | 0.223 |
| s35WHW02 | 35 | 10.6 | 1.49 | 0.205 |
| s40WHW02 | 40 | 8.75 | 1.56 | 0.266 |
| s75WHW02 | 75 | 6.36 | 1.48 | 0.112 |
| u20WHW02 | 20 | 20.0 | 1.57 | 0.338 |
| u25WHW02 | 25 | 25.0 | 1.53 | 0.223 |
| u30WHW02 | 30 | 30.0 | 1.58 | 0.326 |
| u35WHW02 | 35 | 35.0 | 1.85 | 0.664 |
| u40WHW02 | 40 | 40.0 | 1.90 | 0.719 |
| u45WHW02 | 45 | 44.9 | 1.96 | 0.655 |
| u50WHW02 | 50 | 49.8 | 1.83 | 0.574 |
| u60WHW02 | 60 | 59.6 | 1.88 | 0.623 |
| u75WHW02 | 75 | 74.1 | 2.03 | 1.146 |
| z20WHW02 | 20 | 20.0 | 1.48 | 0.163 |
| z25WHW02 | 25 | 25.0 | 1.81 | 0.404 |
| z30WHW02 | 30 | 30.0 | 1.50 | 0.221 |

Continued on Next Page...

Table 4.1 – Continued

| Model | $M_{\rm ZAMS}$ $[M_\odot]$ | $M_{\rm pre-SN}$ $[M_\odot]$ | $M_{\rm Fe\ core}$[1] $[M_\odot]$ | $\xi_{2.5}$[2] |
|---|---|---|---|---|
| z35WHW02 | 35 | 35.0 | 1.79 | 0.560 |
| z40WHW02 | 40 | 40.0 | 1.90 | 0.720 |
| s25LC06A | 25 | 16.2 | 1.43 | 0.204 |
| s30LC06A | 30 | 12.8 | 1.48 | 0.274 |
| s35LC06A | 35 | 11.8 | 1.48 | 0.242 |
| s40LC06A | 40 | 12.4 | 1.50 | 0.339 |
| s60LC06A | 60 | 16.9 | 1.63 | 0.603 |
| s80LC06A | 80 | 22.4 | 1.67 | 0.628 |
| s120LC06A | 120 | 30.5 | 1.91 | 0.905 |
| s40LC06B | 40 | 6.82 | 1.51 | 0.322 |
| s60LC06B | 60 | 5.95 | 1.35 | 0.163 |
| s80LC06B | 80 | 6.04 | 1.46 | 0.185 |
| s120LC06B | 120 | 6.12 | 1.24 | 0.143 |
| s20WH07 | 20 | 15.8 | 1.55 | 0.288 |
| s25WH07 | 25 | 15.8 | 1.60 | 0.334 |
| s30WH07 | 30 | 13.8 | 1.49 | 0.219 |
| s35WH07 | 35 | 13.6 | 1.61 | 0.369 |
| s40WH07 | 40 | 15.3 | 1.83 | 0.599 |
| s45WH07 | 45 | 13.0 | 1.79 | 0.556 |
| s50WH07 | 50 | 9.76 | 1.50 | 0.221 |
| s60WH07 | 60 | 7.25 | 1.46 | 0.175 |
| s80WH07 | 80 | 6.33 | 1.48 | 0.210 |
| s100WH07 | 100 | 6.04 | 1.46 | 0.247 |
| s120WH07 | 120 | 5.96 | 1.43 | 0.172 |

[1] We define the iron core edge to be where $Y_e = 0.495$.
[2] $\xi_{2.5}$ is determined at bounce in collapse runs using the LS180 EOS and will vary only slightly with EOS.

### 4.1.2 Grid Setup

Based on resolution studies, we employ a computational grid setup with a total of 1050 zones. Near the origin and extending out to 20 km, we employ a constant grid spacing of 80 m (250 zones). Outside of 20 km we logarithmically space the remaining 800 zones to a radius where the initial density falls to $2000\,{\rm g\,cm^{-3}}$. We require the high resolution near the center for late postbounce times when the postshock region becomes small ($r_{\rm shock} \lesssim 20\,{\rm km}$) and when the protoneutron star is close to dynamical collapse to a black hole. We interpolate the various presupernova profiles ($\rho$, $T$, $Y_e$, $v$, and $\Omega$, if rotation is included) to our grid using linear interpolation.

### 4.1.3 Results

#### 4.1.3.1 Fiducial Model

We begin our discussion with a detailed description of the evolution of a failing core-collapse supernova from core collapse, through bounce, and the subsequent postbounce evolution to black hole formation. For this, we choose the 40 $M_\odot$ ZAMS-mass progenitor model $s$40WH07. We evolve this

progenitor using the LS180 EOS, do not include rotation, and use the standard setting of $f_{\rm heat} = 1$ (see Section 3.6.2.1). In Figure 4.2, we show the evolution of the radial coordinate of select baryonic mass shells as a function of time and we highlight shells enclosing 0.5, 1.0, 1.5, 2.0, and 2.5 $M_\odot$. In addition, the figure shows the shock radius and the positions of the energy-averaged $\nu_e$ and $\nu_x$ neutrinospheres as a function of time. The prebounce collapse phase ($t < 0$) lasts $\sim 450$ ms. At bounce, the central value of the lapse function is $\alpha_c \sim 0.82$, and the metric function $X$ has a maximum of $\sim 1.1$ and peaks off-center at a baryonic mass coordinate of $\sim 0.6\,M_\odot$ which roughly corresponds to the edge of the inner core. The inner core initially overshoots to a maximum central density $\rho_c \sim 5.0 \times 10^{14}\,{\rm g\,cm^{-3}}$, then settles at $\sim 3.7 \times 10^{14}\,{\rm g\,cm^{-3}}$. $\rho_c$ subsequently increases as accretion adds mass to the protoneutron star. The bounce shock forms at a baryonic mass coordinate of $\sim 0.6\,M_\odot$. From there, it moves out quickly in mass, reaching a baryonic mass coordinate of $\sim 1.5\,M_\odot$ at 22 ms after bounce, $2\,M_\odot$ at $\sim 162$ ms, and $2.25\,M_\odot$ at $\sim 329$ ms. In radius, the shock reaches a maximum of $\sim 120$ km at 38 ms after bounce. There it stalls, then slowly recedes. At 10 ms after bounce, the accretion rate through the shock is $\sim 18\,M_\odot\,{\rm s^{-1}}$ and drops to $\sim 2.7$, $\sim 1.7$, and $\sim 1.25\,M_\odot\,{\rm s^{-1}}$ at 100, 200, and 300 ms after bounce, respectively. The drop in the accretion rate has little effect on the failing supernova engine. In agreement with previous work that employed a more accurate neutrino treatment (e.g., Liebendörfer et al. 2005, Thompson et al. 2003), the 1D neutrino mechanism is manifestly ineffective in driving the shock, yielding, in this model, a heating efficiency $\eta = L_{\rm absorbed}/L_{\nu_e+\bar{\nu}_e}$ of only $\sim 3\,\%$ (on average). The neutrinospheres (where the energy-averaged optical depth $\tau = 2/3$) are initially exterior to the shock but are surpassed by the latter in a matter of milliseconds after bounce, leading to the $\nu_e$ deleptonization burst. At all times, the $\nu_x$ neutrinosphere is interior to the $\bar{\nu}_e$ neutrinosphere, which in turn is slightly interior to the $\nu_e$ neutrinosphere. The mean neutrino energies also follow this order. They are the largest for $\nu_x$ and the lowest for $\nu_e$ and increase with decreasing neutrinosphere radii (e.g., Fischer et al. 2009, Ott et al. 2008, Sumiyoshi et al. 2007, Thompson et al. 2003).

At $\sim 408$ ms after bounce, the shock has receded to $\sim 20$ km and the protoneutron star has reached a baryonic (gravitational) mass of $\sim 2.33\,M_\odot$ ($\sim 2.23\,M_\odot$). The difference between baryonic and gravitational mass, at this point in the evolution, is due to the $\sim 1.9 \times 10^{53}$ erg of energy radiated by neutrinos. At this point, dynamical protoneutron star collapse to a black hole sets in and happens on a coordinate time scale of $\lesssim 1$ ms. In the rightmost part of Figure 4.2, we zoom in to the final 1 ms of evolution to show detail. The first signs of collapse manifest themselves in the development of a radial infall velocity profile at the protoneutron star edge. The protoneutron star then collapses in on itself and the central density increases by a factor of $\sim 3$ in only $\sim 1$ ms of coordinate time. The simulation crashes due to EOS limitations at $\rho_c \sim 4.2 \times 10^{15}\,{\rm g\,cm^{-3}}$ and with $\alpha_c = 0.006$. At this point the peak of the metric function $X = [1 - 2m(r)/r]^{-1/2}$ is $\sim 4.4$ at a coordinate radius of $\sim 6.8$ km. There, the fluid velocity also peaks at $\sim -0.83\,c$. The shock recedes by $\sim 8$ km in the

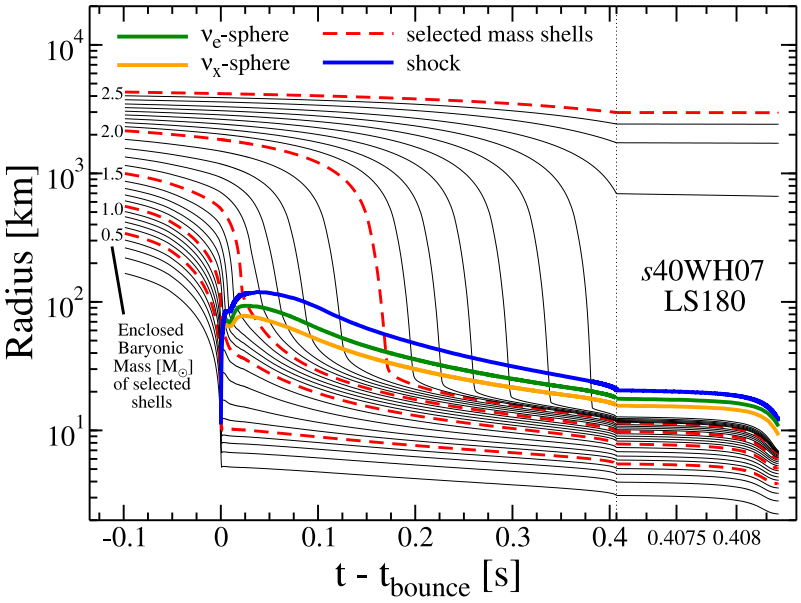


Figure 4.2: Evolution of baryonic mass shells in the nonrotating model *s*40WH07 evolved with the LS180 EOS. We also include the shock location and the radii of the $\nu_e$ and $\nu_x$ neutrinospheres. The $\bar{\nu}_e$-sphere (not shown), is inside, but very close to the $\nu_e$-sphere. The vertical dotted line denotes a change of time scale in the plot, highlighting the final $\sim 1$ ms of evolution before the central density reaches $\sim 4.2 \times 10^{15}\,\mathrm{g\,cm^{-3}}$ and the simulation halts. We specifically highlight the 0.5, 1.0, 1.5, 2.0, and 2.5 $M_\odot$ baryonic mass shells with dashed lines. With solid lines, for $M < 2\,M_\odot$, we plot every 0.1 $M_\odot$ mass shell. Above $2\,M_\odot$, we plot mass shells with a spacing of $0.05\,M_\odot$.

last $\sim 1$ ms of evolution to a radial coordinate of $\sim 12$ km. During the last $\sim 0.05$ ms, due to the central lapse dropping to nearly zero, the evolution of the mass shells slows near the origin. This is characteristic for our choice of gauge. If the simulation were to continue, $X$ would become singular at the event horizon that would appear after infinite coordinate time in our coordinates (Petrich et al. 1986).

The *s*40WH07 model discussed here is a typical example of a failing core-collapse supernova in spherical symmetry. We present the results of a large number of such models in Table 4.2, where for each EOS and progenitor model we show the time to black hole formation as measured from bounce and the mass, both baryonic and gravitational, of the protoneutron star when the central value of the lapse function $\alpha$ reaches 0.3 (roughly the point of instability). In this table, the model name describes the initial model. The metallicity is denoted by one of three letters: $s$, $u$, and $z$ which represent solar, $10^{-4}$ solar, and zero metallicity, respectively. Following the metallicity is the ZAMS mass and the progenitor model set. In many simulations, particularly in those employing stiff EOS, a black hole does not form within 3.5 s. For these simulations we include in parentheses the mass inside the shock at 3.5 s. We note that at black hole formation the shock is typically at a distance of

$\lesssim 20\,\mathrm{km}$ and there is very little mass between the shock and the protoneutron star. The dynamical collapse to a black hole happens very quickly ($t \lesssim 1\,\mathrm{ms}$) during which very little additional accretion occurs.

#### 4.1.3.2 Comparison with Previous Work

The $s40$WW95 progenitor was considered in the black hole formation studies of Liebendörfer et al. (2004), Sumiyoshi et al. (2007) (hereinafter referred to as S07), and Fischer et al. (2009) (hereinafter referred to as F09). For comparison, we perform simulations with this progenitor for both the LS180 and HShen EOS. Table 4.3 compares two key quantities, the time to black hole formation and the maximum baryonic protoneutron star mass, obtained with `GR1D` with the results obtained in the aforementioned studies.

For the LS180 EOS, we find a time to black hole formation of $\sim 524\,\mathrm{ms}$ and a maximum baryonic protoneutron star mass of $\sim 2.26\,M_\odot$, which is $\sim 3\,\%$ larger than predicted by F09. We attribute this discrepancy to the higher electron-type neutrino luminosities our leakage scheme predicts ($\sim 20\%$) resulting in lower gravitational masses compared to full Boltzmann transport calculations. Our time to black hole formation is longer by $\sim 100\,\mathrm{ms}$ or $\sim 20\,\%$. This disagreement is relatively larger than the baryonic mass disagreement due to the low accretion rate at late times that translates small differences in mass to large differences in time. At $\sim 435.5\,\mathrm{ms}$, the time to black hole formation of F09, our protoneutron star has a baryonic mass of $\sim 2.17\,M_\odot$, which is consistent to $\sim 1\,\%$ with F09. We find it more difficult to reconcile our results (and those of Liebendörfer et al. (2004) and F09) with the simulations of S07. Their maximum protoneutron star baryonic mass and the time to black hole formation suggest a lower accretion rate throughout their evolution ($\sim 2.1\,M_\odot$ in $\sim 560\,\mathrm{ms}$).

In the simulation run with the stiffer HShen EOS, the larger maximum protoneutron star mass leads to a delay of black hole formation until a postbounce time $\sim 1.129\,\mathrm{s}$ and we find a maximum baryonic protoneutron star mass of $\sim 2.82\,M_\odot$. The maximum protoneutron star mass and time to black hole formation of S07 again suggest an accretion rate in disagreement with F09 and our work. The results of F09 with the HShen EOS suffer from a glitch in F09's EOS table interpolation scheme which has since been fixed (T. Fischer 2010, private communication). This leads to a postbounce time to black hole formation of $\sim 1.4\,\mathrm{s}$ and a maximum baryonic protoneutron star mass of $\sim 3.2\,M_\odot$. Results from more recent simulations correct this error and are presented in Table 4.3 (T. Fischer 2010, private communication).

#### 4.1.3.3 Equation-of-State Dependence and Thermal Effects

The maximum protoneutron star mass and, thus, the evolution toward black hole formation, depends strongly on the EOS. This was realized early on (Burrows 1988) and has recently been investigated by S07 and F09 who compared models evolved with the LS180 and HShen EOS. Here we extend

Table 4.2: Non-rotating black hole formation properties. Black hole formation times and maximum PNS mass (both baryonic and gravitational) for nonrotating runs with $f_{\rm heat} = 1$ for all four EOS. We stop our simulations at 3.5 s after core bounce. Models that have not formed a black hole by then probably explode in nature. They are marked by $\cdots$, but we include the masses inside the shock at 3.5 s in parentheses. The progenitor models are the result of various stellar evolution studies: WW95, Woosley and Weaver (1995); WHW02, Woosley et al. (2002); LC06, Limongi and Chieffi (2006); and WH07, Woosley and Heger (2007).

| Model | LS180 | | | LS220 | | | LS375 | | | HShen | | |
|---|---|---|---|---|---|---|---|---|---|---|---|---|
| | $t_{\rm BH}$ (s) | $M_{\rm b,max}$ ($M_\odot$) | $M_{\rm g,max}$ ($M_\odot$) | $t_{\rm BH}$ (s) | $M_{\rm b,max}$ ($M_\odot$) | $M_{\rm g,max}$ ($M_\odot$) | $t_{\rm BH}$ (s) | $M_{\rm b,max}$ ($M_\odot$) | $M_{\rm g,max}$ ($M_\odot$) | $t_{\rm BH}$ (s) | $M_{\rm b,max}$ ($M_\odot$) | $M_{\rm g,max}$ ($M_\odot$) |
| $s$20WW95 | 0.787 | 2.238 | 2.108 | 1.129 | 2.377 | 2.201 | 3.351 | 3.060 | 2.653 | 2.287 | 2.751 | 2.486 |
| $s$25WW95 | 0.737 | 2.246 | 2.118 | 1.046 | 2.383 | 2.211 | 2.707 | 3.054 | 2.656 | 1.990 | 2.760 | 2.498 |
| $s$40WW95 | 0.524 | 2.263 | 2.137 | 0.666 | 2.406 | 2.240 | 1.381 | 3.043 | 2.674 | 1.129 | 2.815 | 2.562 |
| $s$20WHW02 | $\cdots$ | (1.949) | (1.794) | $\cdots$ | (1.950) | (1.798) | $\cdots$ | (1.951) | (1.807) | $\cdots$ | (1.943) | (1.805) |
| $s$25WHW02 | 1.021 | 2.211 | 2.079 | 1.504 | 2.355 | 2.172 | $\cdots$ | (2.917) | (2.559) | 2.929 | 2.736 | 2.468 |
| $s$30WHW02 | 1.820 | 2.144 | 1.978 | 2.986 | 2.331 | 2.108 | $\cdots$ | (2.416) | (2.182) | $\cdots$ | (2.405) | (2.190) |
| $s$35WHW02 | 2.073 | 2.141 | 1.976 | 3.334 | 2.328 | 2.105 | $\cdots$ | (2.351) | (2.137) | $\cdots$ | (2.340) | (2.141) |
| $s$40WHW02 | 1.512 | 2.168 | 2.019 | 2.231 | 2.336 | 2.134 | $\cdots$ | (2.634) | (2.355) | $\cdots$ | (2.615) | (2.362) |
| $s$75WHW02 | $\cdots$ | (1.920) | (1.781) | $\cdots$ | (1.920) | (1.784) | $\cdots$ | (1.921) | (1.791) | $\cdots$ | (1.913) | (1.787) |
| $u$20WHW02 | 0.938 | 2.215 | 2.082 | 1.367 | 2.358 | 2.175 | $\cdots$ | (2.852) | (2.516) | 3.004 | 2.734 | 2.466 |
| $u$25WHW02 | 1.759 | 2.160 | 2.009 | 2.798 | 2.330 | 2.124 | $\cdots$ | (2.446) | (2.218) | $\cdots$ | (2.429) | (2.220) |
| $u$30WHW02 | 0.922 | 2.217 | 2.084 | 1.353 | 2.359 | 2.178 | $\cdots$ | (2.802) | (2.483) | 3.228 | 2.731 | 2.462 |
| $u$35WHW02 | 0.379 | 2.347 | 2.242 | 0.484 | 2.465 | 2.329 | 1.308 | 3.020 | 2.693 | 1.075 | 2.847 | 2.608 |
| $u$40WHW02 | 0.369 | 2.346 | 2.241 | 0.453 | 2.469 | 2.333 | 0.946 | 3.023 | 2.710 | 0.849 | 2.874 | 2.638 |
| $u$45WHW02 | 0.441 | 2.301 | 2.187 | 0.548 | 2.433 | 2.284 | 1.108 | 3.027 | 2.694 | 0.959 | 2.842 | 2.600 |
| $u$50WHW02 | 0.563 | 2.273 | 2.154 | 0.706 | 2.408 | 2.251 | 1.365 | 3.030 | 2.676 | 1.163 | 2.816 | 2.569 |
| $u$60WHW02 | 0.432 | 2.363 | 2.267 | 0.579 | 2.460 | 2.331 | 1.346 | 3.009 | 2.693 | 1.165 | 2.849 | 2.620 |
| $u$75WHW02 | 0.226 | 2.526 | 2.449 | 0.285 | 2.592 | 2.498 | 0.626 | 3.006 | 2.775 | 0.594 | 2.984 | 2.791 |
| $z$20WHW02 | 3.295 | 2.116 | 1.934 | $\cdots$ | (2.141) | (1.955) | $\cdots$ | (2.143) | (1.968) | $\cdots$ | (2.132) | (1.968) |
| $z$25WHW02 | 0.602 | 2.283 | 2.167 | 0.956 | 2.398 | 2.239 | 3.443 | 3.050 | 2.650 | 2.351 | 2.762 | 2.505 |
| $z$30WHW02 | 1.772 | 2.149 | 1.989 | 2.964 | 2.329 | 2.114 | $\cdots$ | (2.413) | (2.187) | $\cdots$ | (2.401) | (2.192) |
| $z$35WHW02 | 0.446 | 2.321 | 2.213 | 0.619 | 2.436 | 2.291 | 1.939 | 3.027 | 2.669 | 1.380 | 2.813 | 2.569 |
| $z$40WHW02 | 0.365 | 2.350 | 2.245 | 0.450 | 2.471 | 2.335 | 0.958 | 3.023 | 2.711 | 0.856 | 2.874 | 2.639 |
| $s$25LC06A | 1.220 | 2.176 | 2.029 | 2.547 | 2.333 | 2.130 | $\cdots$ | (2.440) | (2.213) | $\cdots$ | (2.398) | (2.195) |
| $s$30LC06A | 1.101 | 2.181 | 2.035 | 1.726 | 2.342 | 2.141 | $\cdots$ | (2.767) | (2.446) | $\cdots$ | (2.695) | (2.421) |
| $s$35LC06A | 1.029 | 2.186 | 2.040 | 1.726 | 2.338 | 2.133 | $\cdots$ | (2.567) | (2.305) | $\cdots$ | (2.517) | (2.285) |
| $s$40LC06A | 0.746 | 2.232 | 2.102 | 1.138 | 2.372 | 2.193 | $\cdots$ | (2.796) | (2.470) | 3.390 | 2.723 | 2.452 |
| $s$60LC06A | 0.393 | 2.331 | 2.224 | 0.512 | 2.450 | 2.310 | 1.536 | 3.025 | 2.678 | 1.278 | 2.816 | 2.572 |
| $s$80LC06A | 0.429 | 2.308 | 2.197 | 0.530 | 2.437 | 2.293 | 1.075 | 3.021 | 2.689 | 1.083 | 2.825 | 2.581 |
| $s$120LC06A | 0.262 | 2.439 | 2.351 | 0.317 | 2.531 | 2.423 | 0.661 | 3.001 | 2.745 | 0.728 | 2.911 | 2.701 |
| $s$40LC06B | 0.958 | 2.189 | 2.043 | 1.411 | 2.349 | 2.152 | $\cdots$ | (2.957) | (2.576) | 2.887 | 2.720 | 2.444 |

Continued on Next Page...

Table 4.2 – Continued

| Model | LS180 | | | LS220 | | | LS375 | | | HShen | | |
|---|---|---|---|---|---|---|---|---|---|---|---|---|
| | $t_{\rm BH}$ (s) | $M_{\rm b,max}$ ($M_\odot$) | $M_{\rm g,max}$ ($M_\odot$) | $t_{\rm BH}$ (s) | $M_{\rm b,max}$ ($M_\odot$) | $M_{\rm g,max}$ ($M_\odot$) | $t_{\rm BH}$ (s) | $M_{\rm b,max}$ ($M_\odot$) | $M_{\rm g,max}$ ($M_\odot$) | $t_{\rm BH}$ (s) | $M_{\rm b,max}$ ($M_\odot$) | $M_{\rm g,max}$ ($M_\odot$) |
| $s$60LC06B | 3.073 | 2.117 | 1.934 | ··· | (2.166) | (1.972) | ··· | (2.165) | (1.984) | ··· | (2.126) | (1.961) |
| $s$80LC06B | 2.441 | 2.131 | 1.963 | ··· | (2.260) | (2.052) | ··· | (2.264) | (2.071) | ··· | (2.249) | (2.069) |
| $s$120LC06B | 2.983 | 2.120 | 1.944 | ··· | (2.171) | (1.984) | ··· | (2.167) | (1.992) | ··· | (2.102) | (1.947) |
| $s$20WH07 | 1.275 | 2.180 | 2.035 | 1.876 | 2.341 | 2.143 | ··· | (2.712) | (2.412) | ··· | (2.694) | (2.426) |
| $s$25WH07 | 1.066 | 2.202 | 2.065 | 1.523 | 2.352 | 2.165 | ··· | (2.975) | (2.595) | 2.796 | 2.736 | 2.466 |
| $s$30WH07 | 1.751 | 2.150 | 1.991 | 2.978 | 2.329 | 2.115 | ··· | (2.408) | (2.184) | ··· | (2.397) | (2.190) |
| $s$35WH07 | 0.836 | 2.232 | 2.104 | 1.203 | 2.369 | 2.194 | ··· | (2.918) | (2.563) | 2.689 | 2.744 | 2.481 |
| $s$40WH07 | 0.408 | 2.334 | 2.228 | 0.561 | 2.448 | 2.306 | 1.596 | 3.024 | 2.680 | 1.259 | 2.827 | 2.585 |
| $s$45WH07 | 0.454 | 2.319 | 2.210 | 0.626 | 2.435 | 2.289 | 2.027 | 3.028 | 2.667 | 1.395 | 2.812 | 2.567 |
| $s$50WH07 | 1.813 | 2.147 | 1.987 | 2.989 | 2.329 | 2.113 | ··· | (2.411) | (2.185) | ··· | (2.399) | (2.190) |
| $s$60WH07 | 2.778 | 2.124 | 1.947 | ··· | (2.230) | (2.023) | ··· | (2.232) | (2.039) | ··· | (2.220) | (2.040) |
| $s$80WH07 | 2.113 | 2.139 | 1.974 | 3.284 | 2.328 | 2.104 | ··· | (2.363) | (2.145) | ··· | (2.350) | (2.148) |
| $s$100WH07 | 1.457 | 2.163 | 2.008 | 2.355 | 2.335 | 2.124 | ··· | (2.539) | (2.281) | ··· | (2.524) | (2.289) |
| $s$120WH07 | 3.043 | 2.120 | 1.940 | ··· | (2.179) | (1.985) | ··· | (2.180) | (1.999) | ··· | (2.169) | (1.999) |

Table 4.3: Comparison of the $s40WW95$ black hole formations properties with published results.

| | LS180 | | HShen | |
|---|---|---|---|---|
| Study | $t_{\rm BH}$ ($s$) | $M_{b,\rm max}$ ($M_\odot$) | $t_{\rm BH}$ ($s$) | $M_{b,\rm max}$ ($M_\odot$) |
| Liebendörfer et al. (2004) | ∼0.5 | ∼2.20 | ... | ... |
| Sumiyoshi et al. (2007) | 0.56 | 2.1 | 1.34 | 2.66 |
| Fischer et al. (2009) | 0.4355 | 2.196 | 1.030[1] | 2.866[1] |
| This work | 0.524 | 2.263 | 1.129 | 2.815 |

[1]See the text for a discussion of the HShen EOS results from Fischer et al. (2009).

their discussion and include also the LS220 and LS375 EOS. For a given accretion history, set by progenitor structure and independent of the high-density EOS, a stiffer nuclear EOS leads to a larger postbounce time to black hole formation. In Figure 4.3, we plot the evolution of the central density $\rho_c$ of the $s40WH07$ model evolved with the four considered EOS. Each EOS leads to a characteristic maximum central density at bounce that is practically independent of progenitor model: $\sim 4.8 \times 10^{14}\,\mathrm{g\,cm^{-3}}$, $\sim 4.4 \times 10^{14}\,\mathrm{g\,cm^{-3}}$, $\sim 3.7 \times 10^{14}\,\mathrm{g\,cm^{-3}}$, and $\sim 3.4 \times 10^{14}\,\mathrm{g\,cm^{-3}}$ for the LS180, LS220, LS375, and HShen EOS, respectively. As expected, the variant using the softest nuclear EOS (LS180) shows the steepest postbounce increase in $\rho_c$ and becomes unstable to black hole formation at only $\sim 408\,\mathrm{ms}$ for this progenitor. The onset of black hole formation is marked by a quick rise in the central density. This is most obvious from the $\rho_c$ evolutions of the model variants using the stiff HShen and LS375 EOS.

Interestingly, the nominally stiffest EOS (LS375) leads to higher central densities than the softer HShen EOS up until $\sim 1.1\,\mathrm{s}$ after bounce. We find that this is due to the HShen EOS yielding higher pressure at $\rho \lesssim 3 \times 10^{14}\,\mathrm{g\,cm^{-3}}$, $T \sim 10\,\mathrm{MeV}$, and $Y_e \sim 0.3$. This higher pressure, initially in the core and later in the outer protoneutron star layers, maintains the protoneutron star at a lower central density. The cold-NS mass-radius relation shown in Figure 3.1 also exhibits this. For a given low-mass NS, the HShen EOS predicts a lower central density. For cold NSs, this trend continues until $\rho_c \sim 5.4 \times 10^{14}\,\mathrm{g\,cm^{-3}}$. Thermal effects, which are stronger in the HShen EOS, will increase this value for hot protoneutron stars.

We also plot in Figure 4.3 the evolution of the mass accretion rate $\dot{M}$ in model $s40WH07$ (evaluated at a radius of 200 km). Variations in the high-density EOS have no effect on $\dot{M}$ which is most sensitive to progenitor structure. Sudden drops in $\dot{M}$ occur when density discontinuities that go along with compositional interfaces advect in. An example of this can be seen in $s40WH07$ at $\sim 400\,\mathrm{ms}$ after bounce where $\dot{M}$ drops by $\sim 30\,\%$ due to a density jump at a baryonic mass coordinate of $\sim 2.35\,M_\odot$. Such interfaces are common features of evolved massive stars (Woosley et al. 2002) and can help jumpstart shock revival in special cases (see, e.g., the 11.2 $M_\odot$ model of

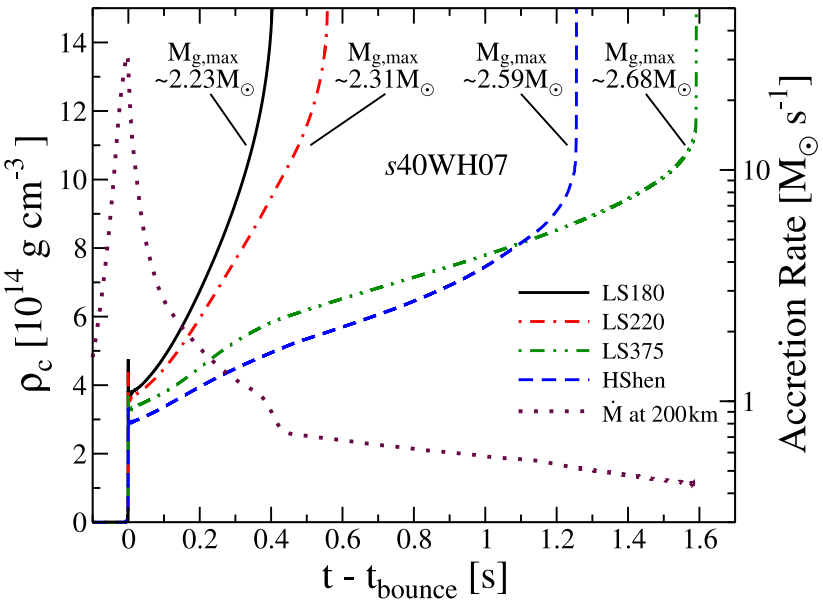


Figure 4.3: Central density (left ordinate) and accretion rate (right ordinate) vs. time since bounce for the *s*40WH07 progenitor and four EOS. Black hole formation occurs when the central density diverges. Each $\rho_c$ curve is annotated with the maximum gravitational protoneutron star mass. The drop in the accretion rate at $t \sim 0.4\,\mathrm{s}$ is due to the accretion of a mass shell where the density drops by $\sim 30\,\%$. Note the accretion rate is on a logarithmic scale.

Buras et al. (2006a), and Section 4.1.3.5 of this study). In the black hole-formation context, they lead to a disproportionate increase in the time to black hole formation in models whose EOS permit a protoneutron star with mass greater than the mass coordinate of the density jump.

The maximum gravitational (baryonic) protoneutron star masses for the four models shown in Figure 4.3 are $\sim 2.23\,M_\odot$ ($\sim 2.33\,M_\odot$), $\sim 2.31\,M_\odot$ ($\sim 2.45\,M_\odot$), $\sim 2.68\,M_\odot$ ($\sim 3.02\,M_\odot$), and $\sim 2.59\,M_\odot$ ($\sim 2.83\,M_\odot$); and the black hole formation times are $\sim 408\,\mathrm{ms}$, $\sim 561\,\mathrm{ms}$, $\sim 1.596\,\mathrm{s}$, and $\sim 1.259\,\mathrm{s}$ for the LS180, LS220, LS375, and HShen EOS, respectively. The maximum cold NS gravitational masses are $\sim 1.83\,M_\odot$, $\sim 2.04\,M_\odot$, $\sim 2.72\,M_\odot$, and $\sim 2.24\,M_\odot$ for the LS180, LS220, LS375, and HShen EOS, respectively.

In models evolved with the LS180, LS220, and HShen EOS, the maximum gravitational protoneutron star mass is larger than the maximum gravitational cold NS mass. We can understand the differences between these cold NS and protoneutron star maximum masses by comparing the protoneutron star structure with various TOV solutions. In Figure 4.4, we plot the density and temperature profiles of the *s*40WH07 model evolved with the HShen EOS just prior to collapse to a black hole. At this time, $t \sim 1.098\,\mathrm{s}$, the central lapse is $\alpha_c = 0.35$, the central density is $\rho_c \sim 1.44 \times 10^{15}\,\mathrm{g\,cm^{-3}}$, $T_c \sim 42.4\,\mathrm{MeV}$, and the protoneutron star gravitational (baryonic) mass is $\sim 2.51\,M_\odot$ ($\sim 2.74\,M_\odot$). For comparison, we include in Figure 4.4 three TOV solutions, all with

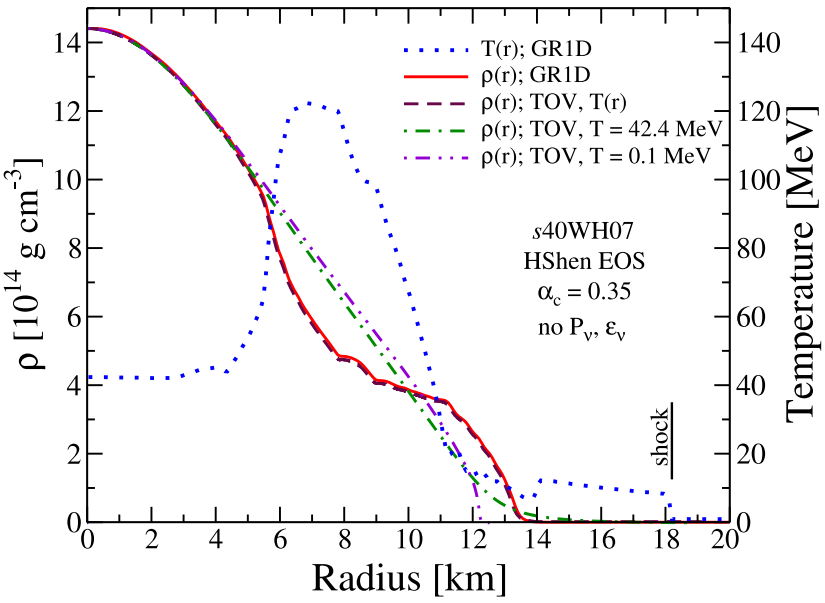


Figure 4.4: Comparison of radial density (left ordinate) and temperature (right ordinate) profiles of the protoneutron star just before collapse ($\alpha_c = 0.35$) in model $s$40WH07 evolved with the HShen EOS with profiles obtained from a TOV solution using the same central density and the same radial temperature and $Y_e$ distributions as in model $s$40WH07 (dashed). For comparison, we also include profiles obtained with the TOV equations assuming both $T = T_c = 42.4\,\mathrm{MeV}$ (dot-dashed) and $T = 0.1\,\mathrm{MeV}$ "cold" (dot-dot-dashed) and $\beta$-equilibrium. The flattening of the density profile between 5 and 11 km is due to the strong thermal pressure support in this region (dotted). The gravitational mass inside the shock (whose position we denote with a vertical black line) of the $s$40WH07 model and of the TOV star agree to within 2 %. For this comparison, we switched off neutrino contributions to the internal energy and pressure in `GR1D`.

the same central density but different temperature and $Y_e$ profiles. Specifically, we plot the density profile assuming (1) $T(r) = 0.1\,\mathrm{MeV}$, this is the "cold" NS case, (2) $T(r) = 42.4\,\mathrm{MeV}$, which corresponds to the central temperature from the `GR1D` evolution, and (3) $T(r) = T_{\texttt{GR1D}}$, assuming the same radial temperature profile as the `GR1D` model. We impose neutrinoless $\beta$ equilibrium for the former two TOV solutions and, similar to the temperature, assume the $Y_e$ profile of the `GR1D` model for the latter. For this comparison, `GR1D` is run without neutrino pressure and energy contributions, since they are also neglected in the TOV solution.

Inside of $\sim 6\,\mathrm{km}$, corresponding to a gravitational mass coordinate of $\sim 0.4\,M_\odot$, the material is not shock heated but rather is heated only via adiabatic compression. The outer regions ($\sim 6-11\,\mathrm{km}$) of the protoneutron star are hot compared to the inner core. This is due to accretion and compression of shock heated material onto the protoneutron star surface. In this region, the thermal pressure support is sufficiently strong to flatten out the protoneutron star density profile. More mass is located at larger radii compared to constant-temperature TOV solutions. This decreases protoneutron star

compactness, increasing the maximum gravitational mass. The cold-NS and the $T = T_c$ TOV solutions have a gravitational mass of $\sim 2.23\,M_\odot$ and $\sim 2.35\,M_\odot$, respectively. On the other hand, the TOV solution that assumes the same $T$ and $Y_e$ profile as the `GR1D` model yields a gravitational mass of $\sim 2.46\,M_\odot$, within $\sim 2\,\%$ of the protoneutron star gravitational mass in the full `GR1D` simulation. Tests in which we vary the $Y_e$ distribution in the TOV solution with $T = T(r)$ show that the maximum protoneutron star mass is insensitive to variations in $Y_e$ from the `GR1D` profile to neutrinoless $\beta$-equilibrium. All this leads us to the conclusion that it is thermal pressure support in the outer protoneutron star core that is responsible for increasing the maximum stable gravitational protoneutron star mass beyond that of a cold NS. Our finding is in agreement with the recent black hole formation simulations of Sumiyoshi et al. (2007) and Fischer et al. (2009), who noted the same differences to cold TOV solutions, but did not pinpoint their precise cause. However, our result is in disagreement with Burrows (1988) who reported maximum protoneutron star masses within a few percent of a solar mass off their cold-NS values. This could be related to Burrows's specific choice of EOS. As we discuss below, stiff nuclear EOS have a more limited response to thermal effects. Another resolution to this disagreement could be the nature of his protoneutron star cooling simulations that were not hydrodynamic, but rather employed a Henyey relaxation approach with imposed accretion.

We find the same overall systematics of increased maximum protoneutron star mass due to thermal pressure support for the entire set of progenitors evolved with the LS180, LS220, and HShen EOS (variations due to differences in progenitor structure are discussed in Section 4.1.3.4). In the sequence of the LS EOS, the relevance of thermal pressure support decreases with increasing stiffness. In the case of the perhaps unphysically stiff LS375 EOS, the effect of high temperatures in the outer protoneutron star core is reversed: the protoneutron stars in `GR1D` simulations become unstable to collapse at lower maximum masses then their cold counterparts. This very surprising observation is understood by considering that in GR, higher temperatures not only add thermal pressure support to the protoneutron star, but also increase its mass-energy. This results in a deeper effective potential well and, thus, is destabilizing. In the LS180, LS220, and HShen case, the added thermal pressure support is significant and dominates over the latter effect. In the very stiff LS375 EOS, the added thermal pressure component is negligible, and the destabilizing effect dominates.

Finally, we point out quantitative differences in models evolved with and without neutrino pressure in the dense neutrino-opaque core. In the $s$40WH07 model evolved with the HShen EOS, the difference in the maximum gravitational mass is $\sim 0.08\,M_\odot$ ($\sim 3\,\%$) and the difference in the time to black hole formation is $\sim 160\,\mathrm{ms}$ ($\sim 14\,\%$). These numbers depend on the employed EOS and progenitor model. In test calculations with a variety of progenitors and EOS, we generally find increases of the maximum protoneutron star gravitational mass of $\lesssim 5\,\%$.

#### 4.1.3.4 Influence of Presupernova Structure

The failure of a core-collapse supernova becomes definite only when accretion pushes the protoneutron star over its maximum mass and a black hole forms. Hence, the time to black hole formation is a hard upper limit to the time available for the supernova mechanism to reenergize the shock. We will demonstrate in this section that it is possible to estimate, for a given nuclear EOS, the postbounce time to black hole formation in non- or slowly spinning on the basis of a single parameter, progenitor bounce compactness, $\xi_{2.5}$, which we introduced in Section 4.1. In Figure 4.5, we plot the postbounce time to black hole formation ($t_{\rm BH}$) as a function of $\xi_{2.5}$ for all nonrotating models considered in this study and listed in Table 4.2. The distribution of data points for each EOS can be fit with a function $\propto (\xi_{2.5})^{-3/2}$. This remarkable result can be understood as follows: using Kepler's third law, consider the Newtonian free-fall time to the origin for a mass element $dm$ initially located at $r_*$ and on a radial orbit about a point mass of $M^* \gg dm$,

$$t_{\rm ff} = \frac{1}{2}\sqrt{\frac{4\pi^2 a^3}{GM^*}} = \pi\sqrt{\frac{r_*^3}{8GM^*}}\,. \tag{4.2}$$

Here, for clarity, the quantities are in cgs units. $G$ is the gravitational constant and $a$ is the semimajor axis equal to half of the apoapsis, $r_*$. Recalling the definition of $\xi_{2.5}$, if the mass element $dm$ is located at a mass coordinate of $2.5\,M_\odot$ and at a radial coordinate of $r_*$, then $r_* = 2500\,{\rm km}/\xi_{2.5}$ , and we can write the free fall time in terms of $\xi_{2.5}$,

$$t_{\rm ff}^{2.5M_\odot} = 0.241(\xi_{2.5})^{-3/2}\,{\rm s}. \tag{4.3}$$

In Figure 4.5, we overplot this Newtonian free fall time for a mass element at baryonic mass coordinate $2.5\,M_\odot$ as a function of $\xi_{2.5}$. For small $\xi_{2.5}$, the mass element begins its free fall from a large radius and, hence, takes longer to reach to origin. In general, material in outer layers of the star will not begin to fall freely until it loses pressure support. Hence, the free fall approximation is not exact (within a factor of $\sim 2$; Burrows 1986), but describes the general behavior of $t_{\rm BH}$ very well. The deviation of data points from the free fall curve is because the maximum protoneutron star mass is different for each model and EOS. Models evolved with the LS180 EOS have protoneutron stars with maximum baryonic masses ranging from 2.1 to $2.5\,M_\odot$. Models with low $\xi_{2.5}$ correspond to the lower end of this mass range. For these models, $t_{\rm BH}$ can be somewhat less than the free fall time of the $2.5\,M_\odot$ mass element, because less material is needed to form a black hole. The maximum baryonic protoneutron star mass range for models using the LS220 EOS is somewhat higher, $2.3 - 2.6\,M_\odot$. Black hole formation times for these models are more in line with the Newtonian free fall prediction. Models evolved with the LS375 and HShen EOS have protoneutron stars that must accrete upward of $\sim 3\,M_\odot$ of material before becoming unstable. This significantly increases $t_{\rm BH}$ above the free fall

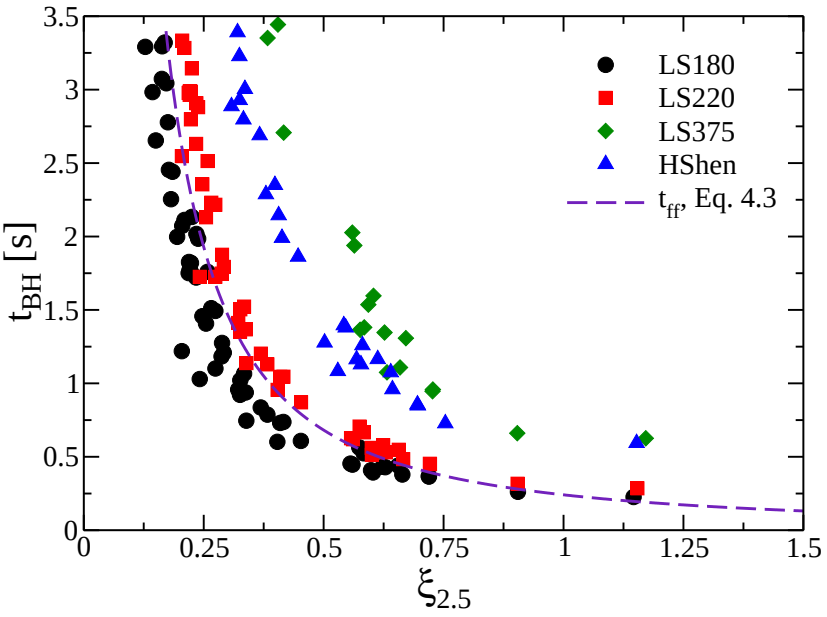


Figure 4.5: Black hole formation time as a function of the bounce compactness ($\xi_{2.5}$) for all nonrotating models presented in Table 4.2 that form black holes within 3.5 s of bounce. Simulations performed with the LS180, LS220, LS375, and HShen EOS are labeled with circles, squares, diamonds, and triangles, respectively. Also shown (dashed line) is the free fall time to the origin (Equation 4.3) of a mass element located at a baryonic mass coordinate of 2.5 $M_\odot$.

prediction for the $\xi_{2.5}$ characteristic mass element.

Thermal pressure support can increase the maximum gravitational protoneutron star mass ($M_{\mathrm{g,\,max}}$) as we have seen in Section 4.1.3.3 for the $s$40WH07 model. In Figure 4.6, we plot $M_{\mathrm{g,\,max}}$ as a function of $\xi_{2.5}$ for all nonrotating models listed in Table 4.2. As obvious from this figure, $M_{\mathrm{g,\,max}}$ depends in a predictable way not only on the EOS, but also on the bounce compactness of the presupernova model. Progenitors with high $\xi_{2.5}$, in addition to forming black holes faster, create protoneutron stars that are stable to higher masses. This is a simple consequence of the fact that progenitors with larger $\xi_{2.5}$ have iron cores with systematically higher entropies and masses significantly above the cold Chandrasekhar mass (see Table 4.1 and Baron and Cooperstein (1990) and Burrows and Lattimer (1983)). Adiabatic collapse leads to higher protoneutron star temperatures after bounce in progenitors with high $\xi_{2.5}$ and, hence, more thermal support. This leads to higher maximum protoneutron star masses. This effect can be large, up to 25% for models with large $\xi_{2.5}$ and soft EOS.

#### 4.1.3.5 Preventing Black Hole Formation with Artificial Neutrino-Driven Explosions

In a successful core-collapse supernova, the shock is reenergized before enough material can accrete onto the protoneutron star to make it unstable. While fully self-consistent spherically symmetric

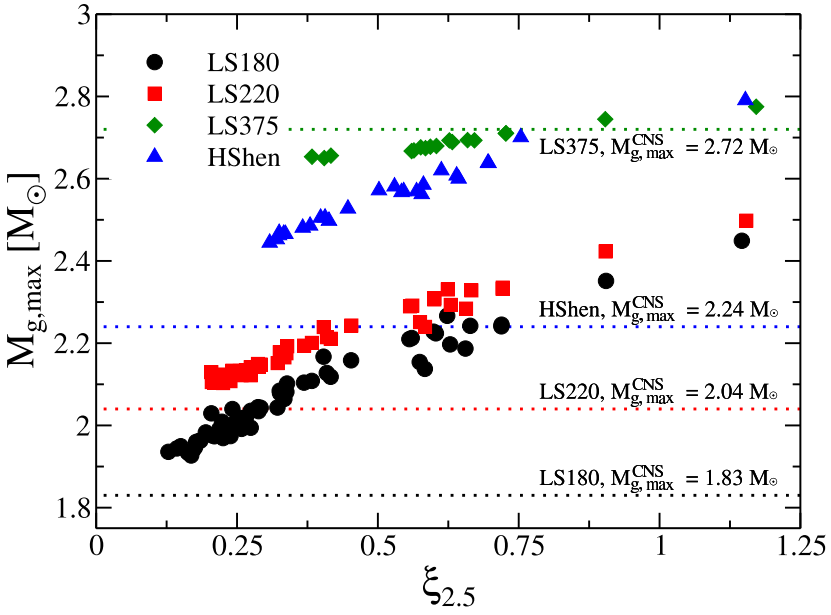


Figure 4.6: Maximum gravitational protoneutron star masses as a function of the bounce compactness ($\xi_{2.5}$) for all nonrotating models presented in Table 4.2 that form black holes within 3.5 s after bounce. Simulations performed with the LS180, LS220, LS375, and HShen EOS are labeled with circles, squares, diamonds, and triangles, respectively. Also shown (dotted lines, labeled) are the maximum gravitational cold-neutron star (CNS) masses, $M^{\rm CNS}_{\rm g,\,max}$, numerical values are 1.83, 2.04, 2.72, and 2.24 $M_\odot$ for the LS180, LS220, LS375, and HShen EOS, respectively.

simulations generally fail to explode in all but a few very low mass progenitors (cf. Burrows et al. 2007a, Kitaura et al. 2006), one can explode any star by the 1D neutrino mechanism by artificially increasing the energy deposition in the postshock region. Without such an increase, all of our simulations fail to explode. Our parameterized heating ($f_{\rm heat}$ in Equation 3.31) allows us to explore "how much" neutrino heating is needed to explode a given model (in 1D). By comparison with results from previous self-consistent radiation hydrodynamics simulations we can then estimate whether a given progenitor and EOS combination is more likely to lead to an explosion or black hole formation.

Our method for driving explosions is similar to Murphy and Burrows (2008), but has the advantage of being proportional to the neutrino luminosity obtained from the neutrino leakage scheme and therefore conserves energy. We iteratively determine the critical value of $f_{\rm heat}$ to within 1 % to what is needed for a successful explosion for a large subset of our models and the LS180, LS220, and HShen EOS. Of particular interest in this analysis is the time-averaged heating efficiency of the critical model, $\bar{\eta}^{\rm crit}_{\rm heat}$. We define $\bar{\eta}_{\rm heat}$ as

$$\bar{\eta}_{\rm heat} = \overline{\int_{\rm gain} \dot{q}^{+}_{\nu}\, dV \Big/ \left(L_{\nu_e} + L_{\bar{\nu}_e}\right)_{r_{\rm gain}}}\,, \tag{4.4}$$

where $\dot{q}_\nu^+$ is the net energy deposition rate and the neutrino luminosities are taken at the gain radius. We perform the time average between bounce and explosion, the latter time defined as when the postshock region assumes positive velocities and accretion onto the protoneutron star ceases. $\bar{\eta}_{\rm heat}^{\rm crit}$ is a useful quantity because it characterizes how much of the available luminosity must be redeposited on average to explode a given progenitor. This is rather independent of transport scheme and code. For example, for the 15 $M_\odot$ ZAMS solar-metallicity progenitor of Woosley and Weaver (1995) we find $\bar{\eta}_{\rm heat}^{\rm crit} \sim 0.13$. Buras et al. (2006b) who also artificially exploded this progenitor in 1D, though with much more sophisticated neutrino transport, find[2] an average heating efficiency of 0.1–0.15 which is consistent with our result. Note, however, that Marek and Janka (2009) observed in the same progenitor the onset of a self-consistent neutrino-driven explosion in 2D at an average heating efficiency of $\sim 0.07$. This indicates a dependence of $\bar{\eta}_{\rm heat}^{\rm crit}$ on dimensionality, should be kept in mind, and is consistent with recent work that suggest that dimensionality may be the key to successful neutrino-driven explosions (Murphy and Burrows 2008, Nordhaus et al. 2010b).

In simulations that explode, we do not track the shock past $\sim$5000 km and cannot address in this study the effect of fallback which occurs at later times and will play an important role in the final remnant mass (Zhang et al. 2008).

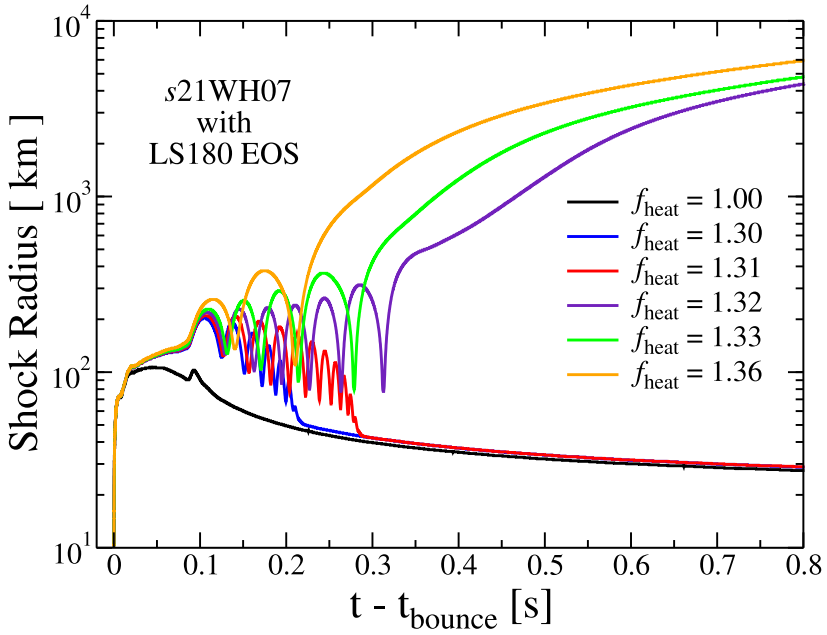


Figure 4.7: Shock radius as a function of postbounce time for the $s$21WH07 model using the LS180 EOS and various values of $f_{\rm heat}$. For $f_{\rm heat} < 1.32$, the shock fails to be reenergized, for $f_{\rm heat} \geq 1.32$, the shock is successfully reenergized and propagates out through the star.

As an example of this procedure, we briefly describe the nonspinning $s$21WH07 model run with

[2]This we deduce from their Figure 28, bottom panel. Note that their $\delta_t E_{\rm cool}$ includes all neutrinos, not just $\nu_e$ and $\bar{\nu}_e$.

the LS180 EOS and show the results in Figure 4.7. The critically exploding model has an iteratively determined value of $f_{\rm heat}^{\rm crit} = 1.32$. For values of $f_{\rm heat}$ below this critical value the shock fails to be reenergized, in these cases, the late-time evolution of the models is not significantly different from the $f_{\rm heat} = 1$ case described in previous sections. Black hole formation occurs at roughly the same time. However, if $f_{\rm heat}$ is large enough to cause an explosion, accretion onto the protoneutron star ceases. This delays, or prevents altogether, black hole formation. For the $f_{\rm heat} = 1.32$, 1.33, and 1.36 simulations, the late-time shock is propagating out at a speed of $\sim$8000 km s$^{-1}$. The gravitational (baryonic) mass inside the protoneutron star, at the time of explosion is $\sim$1.49 ($\sim$1.54) $M_\odot$, $\sim$1.48 ($\sim$1.53) $M_\odot$, and $\sim$1.46 ($\sim$1.50) $M_\odot$, respectively. The baryonic mass stays constant after this time while the gravitational mass decreases because of continued core neutrino emission. For the $s$21WH07 model, for $f_{\rm heat} = 1.32$, 1.33, and 1.36, the corresponding time-averaged heating efficiencies obtained with `GR1D` are $\bar{\eta}_{\rm heat} = \sim$0.144, $\sim$0.147, and $\sim$0.160, respectively. For comparison, in the $f_{\rm heat} = 1.0$ simulation, the time-averaged heating efficiency is $\sim$0.06 for the first $\sim$100 ms after bounce and then drops as the shock recedes in past $\sim$50 km. The $s$21WH07 model has a low bounce compactness $\xi_{2.5}$ of $\sim$0.143, and is a typical example of models with $\xi_{2.5} \lesssim 0.35$.

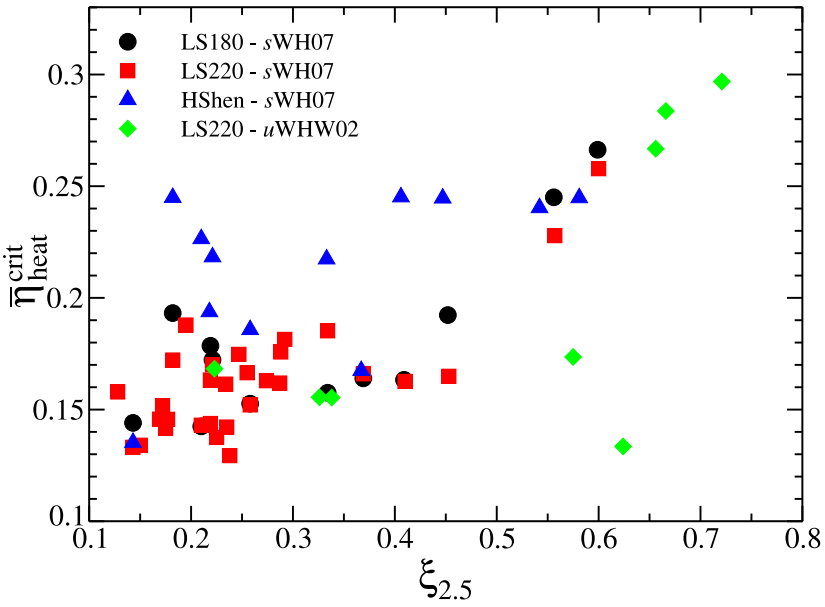


Figure 4.8: $\bar{\eta}_{\rm heat}^{\rm crit}$ obtained with `GR1D` as a function of bounce compactness. Plotted are models from the $s$WH07 data set using the LS180, LS220, and HShen EOS; and models from the $u$WHW02 data set using the LS220 EOS.

Since `GR1D`'s leakage/heating scheme is only a rough approximation to true neutrino transport, and because our simulations assume spherical symmetry, we cannot make very robust quantitative predictions for any one particular model, but rather study the collective trends exhibited by the entire

set of 62 progenitors that we consider here. In Figure 4.8, as a function of bounce compactness $\xi_{2.5}$, we plot $\bar{\eta}^{\rm crit}_{\rm heat}$ for all considered models and EOS. The data are summarized in Table 4.4. We can divide the results into two general regimes: models with $\xi_{2.5} \lesssim 0.45$ and those with $\xi_{2.5} \gtrsim 0.45$.

For many models with $\xi_{2.5} \lesssim 0.45$, oscillations in the shock position are ubiquitous near the transition from failing to exploding supernovae in 1D (cf. Murphy and Burrows 2008; Buras et al. 2006b; Fernández and Thompson 2009). For both the LS180 and LS220 EOS, the $\bar{\eta}^{\rm crit}_{\rm heat}$ required for an explosion, modulo noise, is roughly constant and $\sim 0.16$ on average for low $\xi_{2.5}$ models. Hence, explosion is the likely outcome of core collapse for progenitors with $\xi_{2.5} \lesssim 0.45$ if the nuclear EOS is similar to the LS180 or LS220 case.

The noise in the $\bar{\eta}^{\rm crit}_{\rm heat}$ distribution (absolute variations by up to $\sim 10\,\%$) is in part a consequence of variations in postbounce dynamics, such as the number and duration of preexplosion oscillations. Compositional interfaces in some progenitor models, where jumps in the density lead to jumps in the accretion rate, also affect individual models leading to variations in $\bar{\eta}^{\rm crit}_{\rm heat}$. For the LS180 and LS220 EOS, any differences in $\bar{\eta}^{\rm crit}_{\rm heat}$ with choice of EOS are indistinguishable given the noise in the data.

For progenitors with $\xi_{2.5} \gtrsim 0.45$, the $\bar{\eta}_{\rm heat}$ required to cause an explosion increases with $\xi_{2.5}$ when run with the LS180 or LS220 EOS. Progenitors in this regime have tremendous postbounce accretion rates, accumulating $\gtrsim 2\,M_\odot$ of baryonic material behind the shock within the first $\sim$ 200 ms after bounce. Without explosion, they form black holes within $\lesssim 0.8$ s (with the LS180 and LS220 EOS). Hence, a very high heating efficiency of $\bar{\eta}_{\rm heat} \gtrsim 0.23$–$0.27$ is necessary to drive an explosion at early times against the huge ram pressure of accretion. It appears unlikely, even when multidimensional dynamics are factored in, that progenitors with $\xi_{2.5} \gtrsim 0.45$ can be exploded via the neutrino mechanism. The most likely outcome of core collapse in such stars is black hole formation.

This is further supported by observing the remnant mass of the protoneutron stars in our critically exploding simulations. We do this for the *s*WH07 model set data in Table 4.4 and present the results in Figure 4.9 where we plot the remnant baryonic mass as a function of $\xi_{2.5}$. We note that assuming no fallback, the cooled neutron star will have a gravitational mass which is lower than its baryonic mass. For reference (using the LS220 EOS), a $1.6\,M_\odot$ baryonic mass cold neutron star has a gravitational mass of $1.44\,M_\odot$, and a $2.1\,M_\odot$ baryonic mass cold neutron star has a gravitational mass of $1.83\,M_\odot$. Progenitors with higher $\xi_{2.5}$ accrete more mass onto the protoneutron star before the explosion is launched, as the accretion rate roughly scales with $\xi_{2.5}$. However, at around $\xi_{2.5} = 0.45$, the remnant mass turns over and stays constant around $2.1\,M_\odot$ for the LS180 and LS220 EOS. The origin of this turnover is the same as the rise in the critical heating efficiency. For progenitors with high $\xi_{2.5}$, the explosion must be launched earlier to prevent black hole formation, this *i)* requires a higher heating efficiency and *ii)* halts the accretion onto the protoneutron star at an earlier time. The turnover does not occur for the HShen EOS, we expect such a turnover to occur for higher $\xi_{2.5}$

when the remnant mass approaches the HShen maximum mass.

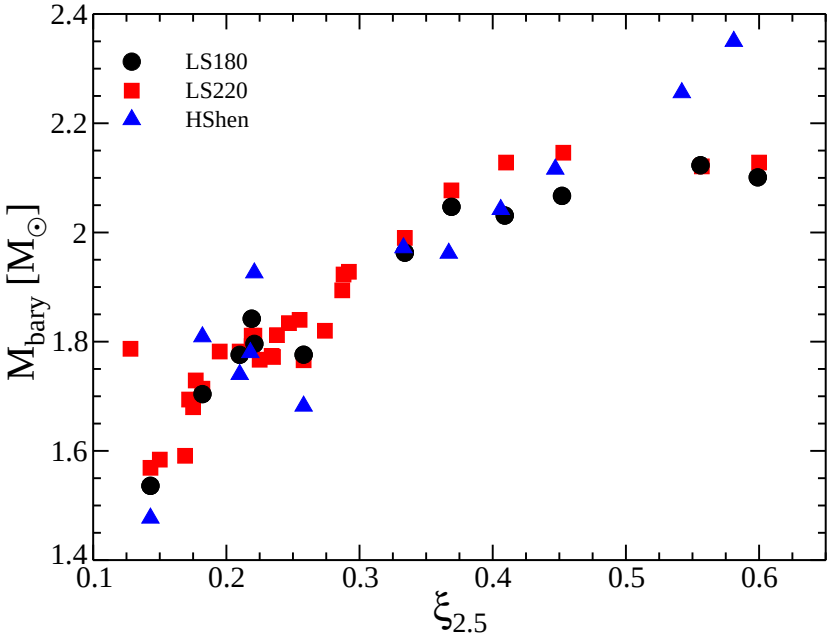


Figure 4.9: Protoneutron star remnant baryonic mass for critically exploding models as a function the $\xi_{2.5}$ assuming no late-time fall back. Progenitors with small $\xi_{2.5}$ have small remnant masses. For the LS180 and LS220 EOS, the latter increases with the former until $\xi_{2.5} \sim 0.45$ where the artificially driven explosions must occur early on in the evolution to prevent black hole formation. The HShen does not show this trend, most likely because its maximum mass is higher.

We draw the reader's attention to two outliers in the $u$WHW02 data set included in Figure 4.8, the $u$50WHW02 and $u$60WHW02 progenitors. These models have high $\xi_{2.5}$, but feature compositional interfaces where the density drops by $\sim 50\,\%$. These are located at a mass coordinate of $1.82\,M_\odot$ and $2.22\,M_\odot$ in $u$50WHW02 and $u$60WHW02, respectively. When such an interface advects through the shock, the accretion rate drops suddenly, but the core neutrino luminosity remains large and an explosion is immediately launched. This results in a small value of $f_{\rm heat}^{\rm crit}$ and, therefore, in a low required $\bar{\eta}_{\rm heat}$. This demonstrates that the single parameter $\xi_{2.5}$ is not always sufficient to predict a progenitor's fate.

In models with $\xi_{2.5} \lesssim 0.45$ and calculated using the HShen EOS, both $\bar{\eta}_{\rm heat}^{\rm crit}$ and $f_{\rm heat}^{\rm crit}$ are systematically higher than with the LS180 and LS220 EOS and explosion is less likely. Furthermore, the qualitative behavior of our simulations is different with the HShen EOS. In many models with subcritical $f_{\rm heat}$ and $\bar{\eta}_{\rm heat}$, the shock is revived and begins to propagate to large radii of $\mathcal{O}(10^3$–$10^4\,{\rm km})$, but the material behind it fails to achieve positive velocities. Hence, accretion onto the protoneutron star is slowed but does not cease. High values of $f_{\rm heat}$ are needed to avoid this and achieve full explosions. We caution the reader that this regime may not be well modeled by our neutrino treatment. Nevertheless, our results suggest that systematically higher $f_{\rm heat}^{\rm crit}$ and $\bar{\eta}_{\rm heat}^{\rm crit}$ are

required to explode models with the HShen EOS, even at low $\xi_{2.5}$. In contrast to models using the LS180 or LS220 EOS, models with $\xi_{2.5} \gtrsim 0.45$ with the HShen EOS require roughly constant $\bar{\eta}_{\rm heat}$ to explode. Since the HShen EOS can support a high maximum mass, the protoneutron star can withstand black hole formation longer and explosions may set in at later postbounce times when the accretion rate has dropped sufficiently.

As an interesting aside, we point out the evolution of the $u$75WHW02 progenitor evolved with the LS220 EOS. This model has a bounce compactness of $\sim 1.15$ and, in the absence of an explosion, forms a black hole $\sim 0.285\,$s after bounce (with the LS220 EOS). This progenitor has a compositional interface at which the density drops by $\sim 50\,\%$ that is located at a baryonic mass coordinate of $\sim 2.5\,M_\odot$. This is very close to the maximum mass of the $u$75WHW02 protoneutron star (with the LS220 EOS), and well above the maximum cold NS (baryonic) mass. The model can be made to explode with $f_{\rm heat}^{\rm crit} = 1.35$ with a corresponding $\bar{\eta}_{\rm heat}^{\rm crit} = 0.287$. The resulting protoneutron star has a baryonic (gravitational) mass of $\sim 2.54\,M_\odot$ ($2.44\,M_\odot$). Interestingly, within $\sim 100\,$ms after the launch of the explosion, cooling of the outer protoneutron star layers removes sufficient thermal pressure, rendering the unstable to collapse and black hole formation. This scenario will necessarily occur within the cooling phase for any that is initially thermally supported above the maximum cold NS baryonic mass and is another avenue to black hole formation. In our simulations, this condition is also met only in very few other models with very high $\xi_{2.5}$ and fairly soft EOS, such as the 23, 40, and 45 $M_\odot$ progenitors from the $s$WH07 series using the LS180 EOS. In order to fully investigate this black hole formation channel, a more sophisticated neutrino treatment is required that allows accurate long-term modeling of protoneutron star cooling (Pons et al. 1999), since, in general, the Kelvin-Helmholtz cooling phase of protoneutron star is $\mathcal{O}(10$–$100\,$s). This is further explored in O'Connor and Ott (2010).

#### 4.1.3.6 Connection to Stellar Evolution: ZAMS Mass and Metallicity

Having established the systematic dependence of core collapse and black hole formation on progenitor bounce compactness in Section 4.1.3.4, we now go further and attempt to connect to the conditions at ZAMS. Doing this is difficult, and, given the current state and limitations of stellar evolution theory and modeling, can be done only approximately. In general, presupernova stellar structure will depend not only on initial conditions at ZAMS (mass, metallicity, rotation), but also on particular evolution history and physics (binary effects, [rotational] mixing, magnetic fields, nuclear reaction rates, and mass loss; cf. Woosley et al. 2002). While keeping this in mind, we limit ourselves in the following to the exploration of single-star, nonrotating progenitors without magnetic fields. We focus on collapse models run with the LS220 EOS, but the general trends with EOS observed in the previous sections extend to here.

In the top panel of Figure 4.10, we plot the bounce compactness $\xi_{2.5}$ as a function of progenitor

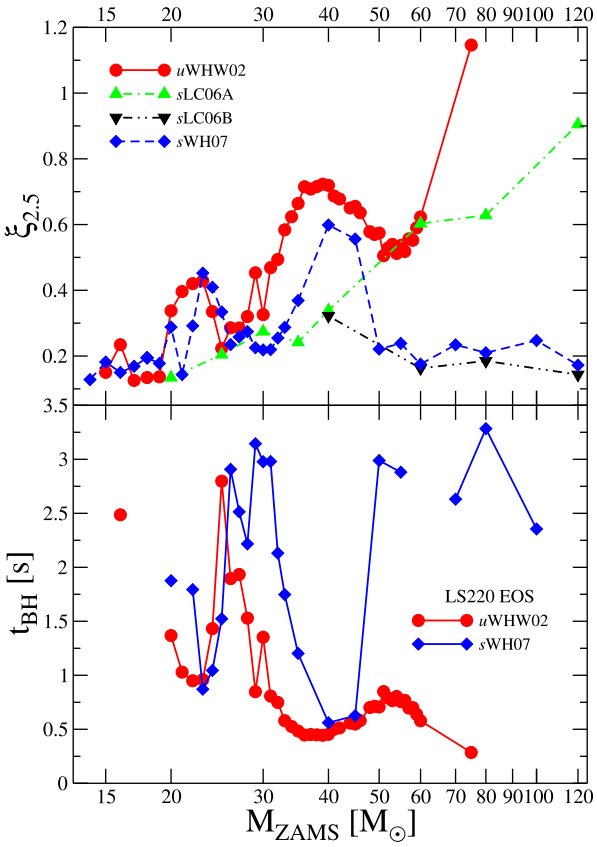


Figure 4.10: Bounce compactness (top panel) and time to black hole formation (bottom panel) as functions of ZAMS mass for various progenitor sets. $\xi_{2.5}$ is determined for each model at bounce using (Equation 4.1). $t_{\rm BH}$ for each model is obtained using the LS220 EOS and assuming no explosion. The times to black hole formation for progenitor models that take longer than 3.5 s to form a black hole are not shown. Breaks in the lines connecting models indicate this. For clarity, the time to black hole formation is not shown for the *s*LC06A/B series, but is provided in Table 4.2.

Table 4.4: Properties of artificial neutrino-driven explosions. $f_{\rm heat}^{\rm crit}$ corresponds to the critical value needed to cause a successful explosion in `GR1D`. $\bar{\eta}_{\rm heat}^{\rm crit}$ is the associated critical average heating efficiency defined in (Equation 4.4).

| $M_{\rm ZAMS}$ ($M_\odot$) | $\xi_{2.5}$ | $f_{\rm heat}^{\rm crit}$ | $\bar{\eta}_{\rm heat}^{\rm crit}$ | $M_{\rm ZAMS}$ ($M_\odot$) | $\xi_{2.5}$ | $f_{\rm heat}^{\rm crit}$ | $\bar{\eta}_{\rm heat}^{\rm crit}$ |
|---|---|---|---|---|---|---|---|
| *s*WH07 LS220 | | | | *s*WH07 LS180 | | | |
| 14 | 0.128 | 1.17 | 0.158 | 15 | 0.182 | 1.16 | 0.193 |
| 15 | 0.182 | 1.17 | 0.172 | 21 | 0.143 | 1.32 | 0.144 |
| 16 | 0.150 | 1.33 | 0.134 | 23 | 0.452 | 1.18 | 0.192 |
| 17 | 0.169 | 1.32 | 0.146 | 24 | 0.409 | 1.16 | 0.163 |
| 18 | 0.195 | 1.17 | 0.188 | 25 | 0.334 | 1.13 | 0.158 |
| 19 | 0.177 | 1.24 | 0.146 | 27 | 0.258 | 1.18 | 0.153 |
| 20 | 0.288 | 1.15 | 0.176 | 30 | 0.219 | 1.16 | 0.179 |
| 21 | 0.143 | 1.34 | 0.133 | 35 | 0.369 | 1.14 | 0.164 |
| 22 | 0.292 | 1.15 | 0.181 | 40 | 0.599 | 1.32 | 0.266 |
| 23 | 0.453 | 1.17 | 0.165 | 45 | 0.556 | 1.26 | 0.245 |
| 24 | 0.410 | 1.15 | 0.163 | 50 | 0.221 | 1.18 | 0.172 |
| 25 | 0.334 | 1.14 | 0.185 | 80 | 0.210 | 1.22 | 0.142 |

Continued on Next Page...

Table 4.4 – Continued

| $M_{\rm ZAMS}$ ($M_\odot$) | $\xi_{2.5}$ | $f_{\rm heat}^{\rm crit}$ | $\bar{\eta}_{\rm heat}^{\rm crit}$ | $M_{\rm ZAMS}$ ($M_\odot$) | $\xi_{2.5}$ | $f_{\rm heat}^{\rm crit}$ | $\bar{\eta}_{\rm heat}^{\rm crit}$ |
|---|---|---|---|---|---|---|---|
| | | | | | *s*WH07 HShen | | |
| 26 | 0.235 | 1.21 | 0.142 | | | | |
| 27 | 0.258 | 1.20 | 0.152 | 15 | 0.182 | 1.30 | 0.245 |
| 28 | 0.274 | 1.16 | 0.163 | 21 | 0.143 | 1.50 | 0.135 |
| 29 | 0.225 | 1.25 | 0.138 | 23 | 0.447 | 1.27 | 0.245 |
| 30 | 0.219 | 1.18 | 0.163 | 24 | 0.406 | 1.31 | 0.245 |
| 31 | 0.219 | 1.21 | 0.144 | 25 | 0.333 | 1.49 | 0.217 |
| 32 | 0.255 | 1.17 | 0.166 | 27 | 0.258 | 1.52 | 0.186 |
| 33 | 0.287 | 1.15 | 0.162 | 30 | 0.218 | 1.32 | 0.194 |
| 35 | 0.369 | 1.13 | 0.166 | 35 | 0.367 | 1.37 | 0.167 |
| 40 | 0.600 | 1.30 | 0.259 | 40 | 0.581 | 1.22 | 0.245 |
| 45 | 0.557 | 1.25 | 0.228 | 45 | 0.542 | 1.24 | 0.240 |
| 50 | 0.221 | 1.19 | 0.170 | 50 | 0.221 | 1.41 | 0.218 |
| 55 | 0.238 | 1.24 | 0.129 | 80 | 0.210 | 1.50 | 0.226 |
| 60 | 0.175 | 1.29 | 0.142 | | | | |
| 70 | 0.234 | 1.21 | 0.161 | | *s*WW95 LS180 | | |
| 80 | 0.210 | 1.24 | 0.143 | 15 | 0.088 | 1.33 | 0.130 |
| 100 | 0.247 | 1.15 | 0.175 | | | | |
| 120 | 0.172 | 1.25 | 0.152 | | | | |
| | | | *u*WHW02 LS220 | | | | |
| 20 | 0.338 | 1.13 | 0.155 | 40 | 0.721 | 1.44 | 0.297 |
| 25 | 0.223 | 1.16 | 0.168 | 45 | 0.656 | 1.22 | 0.267 |
| 30 | 0.326 | 1.13 | 0.156 | 50 | 0.575 | 1.09 | 0.174 |
| 35 | 0.666 | 1.37 | 0.284 | 60 | 0.624 | 1.12 | 0.133 |

ZAMS mass $M_{\rm ZAMS}$ for a range of progenitors from multiple stellar evolutionary studies. Even within a given model set, the $M_{\rm ZAMS} - \xi_{2.5}$ mapping is highly nonmonotonic. At the low end of $M_{\rm ZAMS}$ covered by Figure 4.10, where mass loss has little influence even in progenitors of solar metallicity, variations in $\xi_{2.5}$ are due predominantly to particularities in late burning stages, caused, e.g., by convective versus radiative core burning and/or differences in shell burning episodes (Woosley et al. 2002). At the high ZAMS-mass end, $\xi_{2.5}$ is determined by a competition of mass loss and rapidity of nuclear-burning evolution.

The bottom panel of Figure 4.10 depicts the time to black hole formation $t_{\rm BH}$ in a failing core-collapse supernova as a function of $M_{\rm ZAMS}$ for the *s*WH07 solar-metallicity progenitors of Woosley and Heger (2007) and the *u*WHW02 $10^{-4}$ solar-metallicity models of Woosley et al. (2002). Models of very low $\xi_{2.5}$ that require more than 3.5 s to make a black hole are omitted. As demonstrated in Section 4.1.3.4, $t_{\rm BH}$ scales $\propto (\xi_{2.5})^{-3/2}$ and, hence, progenitors that form black hole the fastest and are (generally, cf. Section 4.1.3.5) the hardest to explode are those with high values of $\xi_{2.5}$. In the low-metallicity *u*WHW02 series whose progenitors experience only minuscule mass loss, black holes form within $\lesssim 1$ s of bounce for $M_{\rm ZAMS} \gtrsim 30\,M_\odot$ and the high bounce compactness $\xi_{2.5} \gtrsim 0.45$ makes a successful shock revival rather unlikely, Section 4.1.3.5. Hence, the most likely outcome of core collapse is black hole formation in these progenitors. This may also be the case for *u*WHW02 progenitors in the ZAMS mass range from $\sim 20$ to $25\,M_\odot$. The *s*WH07 progenitors have high $\xi_{2.5}$ and

form black holes rapidly only in the $M_{\rm ZAMS}$ ranges $\sim$ 23–25 $M_\odot$ and $\sim$ 35–45 $M_\odot$. At higher ZAMS masses, strong $O$-star mass loss leads to an early removal of the hydrogen envelope. Subsequent mass loss in the Wolf-Rayet phase leads to bare, low-mass, low-compactness carbon oxygen cores in the most massive progenitors that are unlikely to make black holes.

#### 4.1.3.7 Connection to Stellar Evolution: Variations with Mass-Loss Prescriptions

Mass loss is key in determining the observational appearance of a successful core-collapse supernova (e.g., Filippenko 1997, Smith et al. 2011), but, as we have seen in Section 4.1.3.6, also has a strong effect on presupernova core structure and, thus, on the outcome of core collapse. The details of mass loss in massive stars are still rather uncertain (e.g., Smith et al. 2011), and, unfortunately, there are few stellar evolution studies that have studied the effects of variations in mass-loss prescriptions. Limongi and Chieffi (2006)[3] performed such a study, adopting two different mass-loss rates for the Wolf-Rayet stage of solar-metallicity stars with $M \gtrsim 40\,M_\odot$. The $s$LC06B models are evolved with the Wolf-Rayet mass-loss rates of Langer (1989) that are similar to those used in the $s$WH07 set of Woosley and Heger (2007). As depicted in the top panel of Figure 4.10, high-mass $s$LC06B and $s$WH07 models have similar low $\xi_{2.5}$ and most likely do not form black holes but rather explode as type-Ibc core-collapse supernovae. The models of the $s$LC06A set were evolved with the lower (factor of $\sim$ 2) Wolf-Rayet mass-loss rates of Nugis and Lamers (2000). The $s$LC06A 60, 80, and $120M_\odot$ progenitors have much more mass left at the presupernova stage ($M_{\rm pre-SN} \sim$ 17–30 $M_\odot$, Figure 4.1) and very high bounce compactness of $\xi_{2.5} \sim$ 0.6–0.9. In the likely case of core-collapse supernova failure, a black hole forms within $\sim$ 0.5 s with the LS180 EOS and within $\sim$ 1.5 s for all other EOS.

The above results highlight the sensitivity of outcome predictions on mass-loss physics and a more solid understanding of this key ingredient will be necessary to robustly connect ZAMS masses to the outcome of core collapse for massive stars around and above solar metallicity.

#### 4.1.3.8 Connection to Stellar Evolution: Estimates of Failed Supernovae

With the results of Sections 4.1.3.5–4.1.3.7 we are in a position to make quantitative estimates of black hole formation in model stellar populations. Neglecting the potentially highly relevant effects of multidimensional dynamics and assuming an EOS of intermediate stiffness (the LS220 EOS), we predicted that progenitors with bounce compactness $\xi_{2.5} \gtrsim 0.45$ most likely form black holes without explosion. This prediction, in itself, without connection to ZAMS conditions through stellar evolution, is of limited utility. Using the whole set of progenitor data made available to us by stellar evolution groups, we attempt the former in Figure 4.11. We plot the mapping between ZAMS mass and outcome of core collapse, reduced to explosion or no explosion and black hole formation, neglect-

[3]See also Limongi and Chieffi (2009) and Meynet and Maeder (2003)

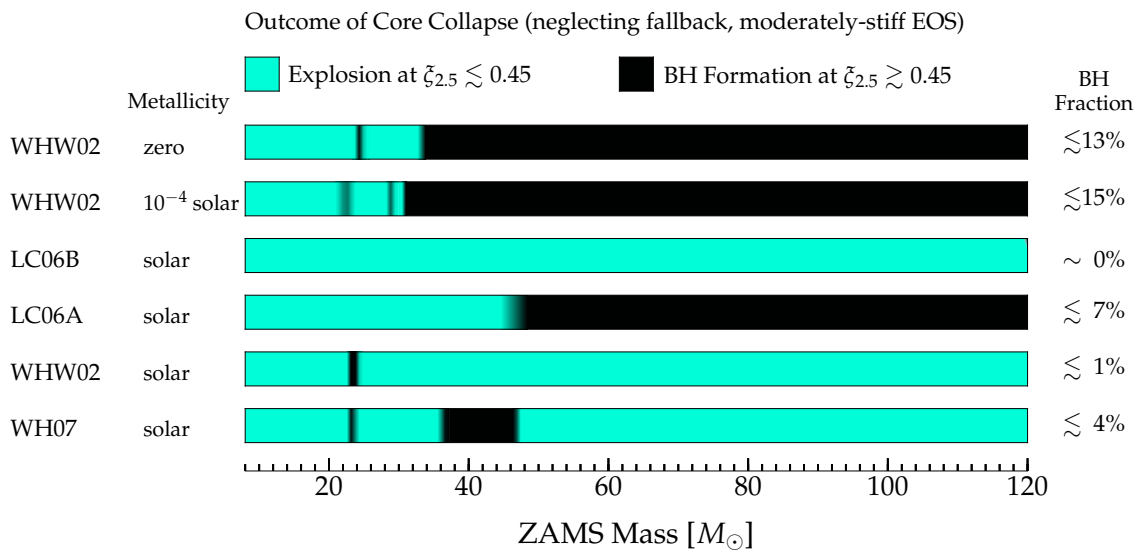


Figure 4.11: Outcome of core collapse as a function of ZAMS mass of single nonrotating massive stars, assuming that for moderately stiff nuclear EOS (e.g., LS180/LS220), neutrino-driven explosions can be launched up to a bounce compactness $\xi_{2.5} \lesssim 0.45$ (cf. Section 4.1.3.5). Other potential explosion mechanisms are neglected. We consider only explosion and black hole formation without explosion as outcomes and neglect other scenarios, including postexplosion black hole formation via fallback accretion (Dessart et al. 2010, Zhang et al. 2008), cooling or nuclear phase transitions. Shown are results for a range of model sets and metallicities (see Section 4.1). Very low metallicity stars with ZAMS masses above $\sim 30\,M_\odot$ robustly form a black hole without explosion. At higher metallicity, uncertainties in the physics of mass loss (e.g., Smith et al. 2011) make robust predictions difficult. This is reflected in the rather dramatic disagreement of the four solar-metallicity progenitor model sets that we include. The "Black hole fractions" stated at the right edge of the plot denote the fraction of massive stars with $M \gtrsim 8\,M_\odot$ that form black holes. They are obtained by convolution with a Salpeter IMF under the assumption that stars with $8\,M_\odot \lesssim M \lesssim 14\,M_\odot$ explode robustly.

ing completely the possibility of black hole formation due to fallback/cooling/phase transitions after a launched explosion. The case is clear cut at low metallicity where mass loss has negligible effect on the mapping between ZAMS conditions and core-collapse outcome. Using a Salpeter initial mass function (IMF; $\alpha = 2.35$, $M_{\rm min} = 8.0\,M_\odot$, and $M_{\rm max} = 150.0\,M_\odot$, Salpeter (1955)) we estimate that $\sim$15% of all progenitors form black holes without explosion. At (around) solar metallicity, the precise way of prescribing mass loss in stellar evolution has tremendous consequences on the mapping between ZAMS mass and core-collapse outcome. Depending on the particular mass-loss prescription, we predict a black hole fraction of 0%–7% for solar-metallicity stars. This makes mass loss the single most important unknown parameter in connecting ZAMS conditions to core-collapse outcome (in agreement with Smith et al. (2011)). Of particular interest in Figure 4.11 is the band of black hole formation around $23\,M_\odot$ in the $z$WHW02, $u$WHW02, $s$WHW02, and $s$WH07 model sets. This band signals an enhancement in the bounce compactness for models around 22–23 $M_\odot$, as we have explored in this chapter, this follows directly from the presupernova structure. Models in this

region have higher central entropies and larger iron cores. It is currently unclear what physical process during stellar evolution causes this phenomena, however such an investigation is underway by the Santa Cruz stellar evolution group using both `KEPLER` and `MESA` (Sukhbold 2011). We note that the LC06A/B model set jumps from 20 to 25 $M_{\odot}$ and therefore is not sensitive to this phenomenon.

With the neutron star mass predictions in Section 4.1.3.5, and with the assumption that after a failed supernova all of the available presupernova mass falls into the black hole, we can construct a compact remnant mass distribution plot. This is shown in Figure 4.12 for the *s*WH07 model set, the LS220 EOS. As for Figure 4.11, we assume a Salpeter initial mass function. In cyan is the remnant mass distribution of neutron stars, where we have use the formula of Lattimer and Prakash (2007) to convert the final baryonic mass to a gravitational mass. In black is the remnant mass distribution of black holes. In grey we assume that for the progenitors with $0.4 < \xi_{2.5} < 0.45$, half make black holes and half will explode as a supernova. Since we assume no fallback, we naturally have a large mass gap between $\sim 2\,M_{\odot}$ (the largest neutron stars made in a successful explosion) and $\sim 12\,M_{\odot}$ (the smallest presupernova mass that gives rise to failed supernova). Note we do not consider several important considerations. *i)* Massive stars with a ZAMS mass of less than $14\,M_{\odot}$, this will affect the low mass neutron star mass distribution. *ii)* We ignore the contribution to this distribution from binary star evolution. This point is very important because only through binary interactions can we observe stellar-mass black holes and infer their mass distribution. *iii)* We do not consider the effects of any fallback onto the protoneutron star remnant which may be significant enough to lead to the formation of black holes just above the maximum neutron star mass (Zhang et al. 2008).

## 4.2 Rotating Black Hole Formation

Massive star rotate. The rotation can influence the collapse and postbounce phase of a core-collapse supernova. Rotation also plays a strong role throughout the evolution of a massive star (Heger et al. 2005, Maeder and Meynet 2012), by, for example, affecting mass loss, and inducing rotational mixing. In order to study black hole formation, black hole birth properties and their impact on a potential subsequent evolution to a LGRB in such spinning progenitors, we use LGRB progenitor models from Woosley and Heger (2006) (WH06). We also take nonrotating presupernova models and assign a parameterized angular momentum distribution. We do this to systematically study the effect of rotation on black hole formation.

Rotation, if sufficiently rapid, alters the core-collapse supernova dynamics via centrifugal support. This important effect is captured by `GR1D`'s 1.5D rotation treatment, albeit approximately. Initially, centrifugal support acts to slow the collapse of the inner core, delaying core bounce. At bounce, lower peak densities are reached, the hydrodynamic shock forms at a larger radius, and its enclosed mass is larger (Dimmelmeier et al. 2008). Conservation of angular momentum spins up the core from

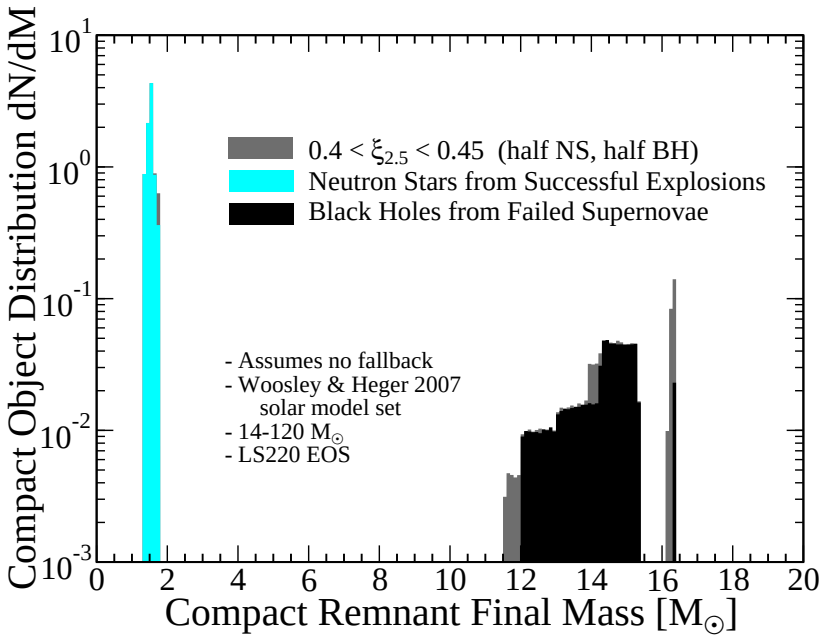


Figure 4.12: Compact Remnant Mass distribution from the *s*WH07 model set. In cyan is the neutron star remnants mass distribution from the set of critically exploding models in Section 4.1.3.5, we have converted the baryonic mass to the final gravitational mass via formula of Lattimer and Prakash (2007). In black is the black hole mass distribution. We note the sharp jumps are various locations is due to the small number of presupernova models in the *s*WH07 set that we predict to make black holes. For progenitors with $0.4 < \xi_{2.5} < 0.45$, we assume that half will form black holes and half will successfully explode, these remnants are shown in grey. The entire distribution integrates to 1, however note that we only consider mass stars with masses greater than $14\,M_{\odot}$. We assume a Salpeter initial mass function to obtain a initial stellar population.

precollapse angular velocities that may be of order $\mathrm{rad\,s^{-1}}$ to $\mathcal{O}$ $(1000\,\mathrm{rad\,s^{-1}})$ as the core, initially with $r \sim \mathcal{O}(1000\,\mathrm{km})$, collapses to a protoneutron star with $r \sim \mathcal{O}(30\,\mathrm{km})$. During the postbounce evolution, the spinning protoneutron star is stabilized at lower densities, is less compact, generally colder, and has a softer neutrino spectrum then a nonspinning counterpart (Ott et al. 2008 and references therein). `GR1D`'s 1.5D treatment of rotation cannot capture other important aspects of rotation. Rotational processes and instabilities will redistribute angular momentum, this is ignored in our calculations. As discussed in Section 2, rotation is also key to the magneto-rotational mechanism, which is a proposed mechanism for reenergizing the supernova shock wave.

### 4.2.1 Models with Parameterized Rotation

We first investigate the effect of rotation in failing core-collapse supernovae by assigning specific angular momentum profiles to the *u*WHW02 model set (see Section 4.1) via the following rotation

law,

$$j(r) = j_{16,\infty}\left[1+\left(\frac{A_{M_\odot}}{r}\right)^2\right]^{-1} 10^{16}\ \mathrm{cm}^2\ \mathrm{s}^{-1}\ , \tag{4.5}$$

where $j_{16,\infty}$ is the specific angular momentum at infinity in units of $10^{16}$ cm$^2$ s$^{-1}$. We define $A_{M_\odot}$ to be the radius where the enclosed mass is 1 $M_\odot$. This is a variation on the rotation law commonly used in simulations of rotating core collapse (e.g., Ott et al. 2006b), where $\Omega(r) = j(r)r^{-2}$ is prescribed and the differential-rotation parameter $A$ is set to some constant radius. The advantage of prescribing $j$ (which is conserved along Lagrangian trajectories) and choosing the value of $A$ based on a mass coordinate is that progenitors from different groups that are evolved to different points still yield similar protoneutron star angular momentum distributions for a given choice of $j_{16,\infty}$. Equation 4.5 leads to roughly uniform rotation in the core inside $A_{M_\odot}$ ($j(r) \propto r^2$) and angular velocity $\Omega(r)$ decreasing with $r^2$ further out ($j(r) = \mathrm{const}$). We note that when 1 $M_\odot$ of material is contained within $10^3$ km, which is typical of many progenitors, the central rotation rate is $j_{16,\infty}$ rad s$^{-1}$.

Our way of assigning rotation to precollapse models approximates well the predictions of core rotation (inner ∼few $M_\odot$) from stellar evolution studies (see, e.g., Ott et al. 2006b for comparison plots) and, thus, is useful for studying rotational effects on black hole formation. Equation 4.5 does not, however, capture the rise in specific angular momentum observed at larger radii (or mass coordinate) that is important for the potential evolution toward a LGRB and seen in recent rotating progenitor models (e.g., Woosley and Heger 2006). We will explore progenitor models evolved with rotation in the following section.

In Table 4.5, we summarize key parameters of our rotating model set. Among them is $T/|W|$, the ratio of rotational kinetic energy to gravitational binding energy. It is particularly indicative of the dynamical relevance of rotation. In the right panel of Figure 4.13, we plot the central density evolution of model $u$40WHW02 run with the LS180 EOS for $j_{16,\infty}$ ranging from 0 to 3.25 in increments of 0.25. While we choose the $u$40WHW02 model here, the results are generic and apply to all progenitors. $A_{M_\odot}$, of Equation 4.5, is 936 km for this model and the initial central rotation rate is $1.14 \times j_{16,\infty}$ rad s$^{-1}$. The nonrotating model takes ∼ 433 ms to reach bounce and a further ∼ 369 ms before the protoneutron star becomes unstable to collapse to a black hole with a gravitational mass of 2.24 $M_\odot$. For the $j_{16,\infty} = 1$, 2, and 3 models, respectively, the times to bounce are 11 ms, 47 ms, and 125 ms greater than in the nonrotating case. Their times to black hole formation $t_{\mathrm{BH}}$ are 12 ms, 52 ms, and 150 ms longer than in the nonrotating case. The maximum gravitational protoneutron star masses $M_{\mathrm{g,\,max}}$ are 0.03 $M_\odot$, 0.09 $M_\odot$, and 0.28 $M_\odot$ greater. We find that the time to bounce, time to black hole formation, and maximum gravitational protoneutron star mass increase above the nonrotating values proportional to $\sim (j_{16,\infty})^2$. The increase in $t_{\mathrm{BH}}$ is due almost entirely to the increase in $M_{g,\,\mathrm{max}}$, since the accretion rate is not significantly affected by rotation. From a Newtonian

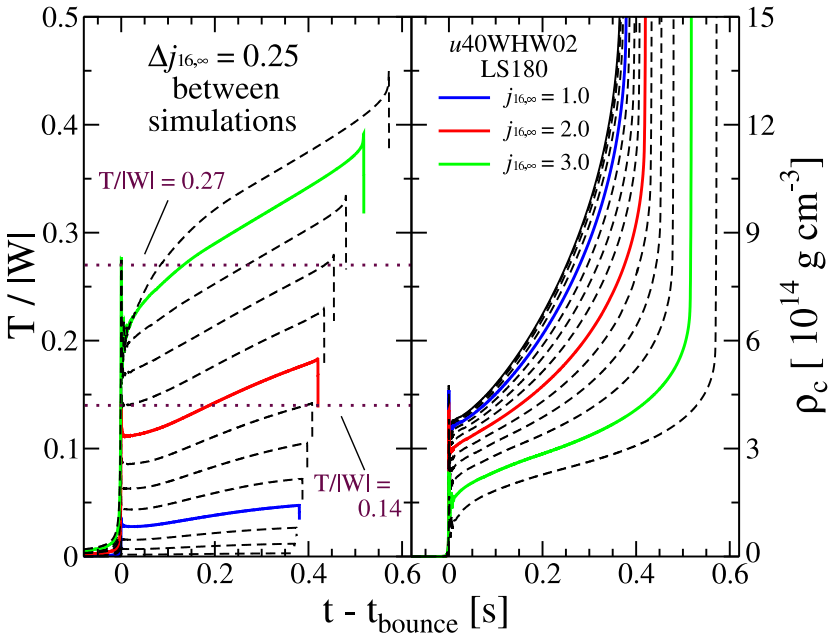


Figure 4.13: $T/|W|$ (left) and central density ($\rho_c$) (right) during the postbounce evolution of the $u$40WHW02 model using the LS180 EOS and 14 different initial specific angular momentum profiles. We vary $j_{16,\infty}$ from 0 to 3.25 in increments of 0.25. For clarity we highlight with solid lines the simulations with integer values of $j_{16,\infty}$. Lines at $T/|W| = 0.27$ and 0.14 are added to denote the dynamical and secular rotational instability thresholds.

point of view, one can understand the latter by considering the ratio of the centrifugal force to the gravitational force, $|F_{\rm cent}|/|F_{\rm grav}|$. This scales as $(v_\varphi^2/r)/(GM/r^2) \propto j^2/r$, where $j = v_\varphi r$ of a mass element is conserved. For typical specific angular momenta ($j = 2\times10^{16}\,cm^2\ s^{-1}$) and protoneutron star masses ($\sim 2\,M_\odot$) considered here, $|F_{\rm cent}|/|F_{\rm grav}| \sim 1/100$ at 1500 km, $\sim 1/10$ at 150 km, and only reaches unity at the Keplerian orbital distance which generally is inside the protoneutron star at ∼10–30 km. Hence, the basic picture of nonrotating collapse/accretion depicted by Figure 4.2 is essentially unchanged by rotation.

The lower temperatures and densities of rotating protoneutron stars lead to systematically lower mean neutrino energies and total radiated energy from the protoneutron star core (time-averaged total luminosities are summarized in Table 4.5). Fryer and Heger (2000) and Ott et al. (2008), who considered similarly rapidly rotating models, also see this effect. There is a clear trend toward lower $L_\nu$ with increasing $j_{16,\infty}$ and for a given model and at a given time, with increasing $j_{16,\infty}$, less gravitational binding energy has been carried away by neutrinos and $M_g$ is larger. Given essentially unaltered accretion rates, one may expect earlier protoneutron star collapse and black hole formation. This, however, is not the case in models run with the LS180, LS220, and HShen EOS, since the centrifugally increased $M_{g,\rm max}$ systematically outweighs the increased gravitational mass due to the lowered neutrino emission. For these EOS, the time to black hole formation is

delayed by rotation. For models run with the extremely stiff LS357 EOS the situation is different. For them, the centrifugal support provided by rotation is too weak to significantly enhance $M_{g,\max}$ and, hence, black holes form faster with increasing $j_{16,\infty}$.

In the left panel of Figure 4.13, we plot the $T/|W|$ evolution for the rotating $u$40WHW02 model series run with the LS180 EOS. During collapse, gravitational binding energy is transferred to rotational energy, increasing the value of $T/|W|$. Similar to how the central density overshoots its new equilibrium, $T/|W|$ also exhibits a local maximum at bounce. Continued accretion and contraction of the protoneutron star increases $T/|W|$ throughout the postbounce evolution for all models. Initially very rapidly spinning models experience core bounce under the strong influence of centrifugal effects, leading to reduced compactness and $T/|W|$ at bounce. These qualitative features are in good agreement with what was found by previous extensive parameter studies of rotating core collapse (Dimmelmeier et al. 2008, Ott et al. 2006b).

Quantitatively, we find and summarize in Table 4.5 that models with $j_{16,\infty} \lesssim 1.5$ yield $T/|W| \lesssim 0.14$ throughout their entire evolution. Models with $j_{16,\infty} \gtrsim 2.25$ have $T/|W| \gtrsim 0.14$ during their entire postbounce evolution. Models that have $j_{16,\infty} \lesssim 2.25$ have $T/|W| \lesssim 0.27$ at all times. Models with $j_{16,\infty} \gtrsim 2.5$ reach $T/|W| \gtrsim 0.27$ before black hole formation. When considering these numbers, it is important to keep in mind that `GR1D`'s 1.5D approach to rotation has the tendency to overestimate $T/|W|$ in rapidly spinning models. Ott et al. (2006b) found model-dependent differences in $T/|W|$ of $\mathcal{O}(10\,\%)$ between 1.5D and 2D. In addition, GR1D's neutrino leakage scheme also tends to lead to somewhat more compact protoneutron star cores and consequently higher $T/|W|$ than would be expected from full neutrino transport calculations

The systematics of $T/|W|$ depicted by Figure 4.13 (left) and listed in Table 4.5, albeit only approximate due to `GR1D`'s 1.5D treatment of rotation, shed interesting light on the potential role of nonaxisymmetric rotational instabilities during the evolution of failing core-collapse supernovae. Of course, due to its 1.5D nature, `GR1D` cannot track the development of such multidimensional dynamics. Analytic theory and to some extent 3D computational modeling have identified multiple instabilities that may lead to triaxial deformation of protoneutron stars, redistribution of angular momentum, and to the radiation of rotational energy and angular momentum via gravitational waves (see Stergioulas 2003 and Ott 2009 for reviews). A global dynamical instability sets in for $T/|W| \gtrsim 0.27$ (Chandrasekhar 1969), leading to a lowest-order $m = 2$ "bar" deformation. Global secular instability, driven by viscosity or GW back-reaction sets in at $T/|W| \gtrsim 0.14$ (Chandrasekhar 1970, Friedman and Schutz 1978). Finally, dynamical shear instabilities, arising as a result of differential rotation, may lead to partial or global nonaxisymmetric deformation at even lower values of $T/|W|$ ($\gtrsim 0.05$; e.g., Corvino et al. 2010, Ott et al. 2007a, Saijo et al. 2003, Scheidegger et al. 2008, and references therein). In nature, and in full 3D simulations, these instabilities, through gravitational radiation or redistribution of angular momentum, will effectively and robustly prevent $T/|W|$ from

surpassing the corresponding $T/|W|$ threshold. The growth times of dynamical instabilities are short, $\mathcal{O}$(ms). Secular instabilities grow on time scales set by the driving process and are typically $\mathcal{O}$(s) (Lai and Shapiro 1995). The low-$T/|W|$ shear instabilities in protoneutron stars appear to grow on intermediate time scales of $\mathcal{O}$(10–100 ms) (e.g., Ott et al. 2007a, Scheidegger et al. 2008).

In Figure 4.14, we plot the value of $T/|W|$ (left panel) and the dimensionless spin of the protoblack hole (PBH), $a^*_{\rm PBH} = J_{\rm PBH}/(M^2_{\rm g,\,PBH})$ (right panel) at the onset of black hole formation (when $\alpha_c = 0.3$) for the same values of $j_{16,\infty}$ used in Figure 4.13. Assuming that the entire protoneutron star is promptly swallowed once the horizon appears, $a^*_{\rm PBH}$ corresponds to the black hole birth spin[4]. We again show results for model $u$40WHW02, but for all four EOS. The data are also presented in Table 4.5 for these and other models. $T/|W|$ at black hole formation scales $\propto (j_{16,\infty})^2$: $T/|W|_{\rm PBH}$ is $\sim 0.05$, $\sim 0.1$, $\sim 0.2$, and $\sim 0.3$ at $j_{16,\infty}$ of $\sim 1$, $\sim 1.5$, $\sim 2.2$, and $\sim 2.75$, respectively. $a^*_{\rm PBH}$ scales linearly with $j_{16,\infty}$, reaching a maximally Kerr value of $a^*_{\rm PBH} \sim 1$ at $j_{16,\infty} \sim 2.75$. $T/|W|_{\rm PBH}$ and $a^*_{\rm PBH}$ vary little with EOS.

A disturbing fact depicted by Figure 4.14 is that our 1.5D simulations predict black hole birth spins $a^* \gtrsim 1$ for $j_{16,\infty} \gtrsim 2.75$. In Kerr theory, such black holes cannot exist with a horizon. They would instead be naked singularities, violating the cosmic censorship conjecture (Penrose 1969). However, when comparing right and left panels of Figure 4.14, one notes that all models achieving $a^* \gtrsim 1$ are predicted to reach $T/|W|$ in excess of 0.27. Hence, in nature and in a 3D simulation, these protoneutron star will be dynamically nonaxisymmetrically unstable and angular momentum redistribution and gravitational radiation will limit their $T/|W|$ robustly below $\sim 0.27$, corresponding to $a^* \lesssim 0.9$. Rotational instabilities at lower values of $T/|W|$ may also be relevant. Dynamical shear instabilities have time scales significantly less than the time to black hole formation. Secular rotational instabilities may be relevant if the true nuclear EOS allows for a large maximum protoneutron star mass as more time is needed to accrete the necessary material to form a black hole (see Section 4.1.3.3). Large $t_{\rm BH}$ is also possible if $\xi_{2.5}$ is small (see Section 4.1.3.4) therefore allowing secular instabilities to grow. In all rotating models considered here (see Table 4.5), protoneutron stars stable against the dynamical rotational instability with $T/|W| \lesssim 0.25$–$0.27$ throughout their postbounce evolution have $a^*_{\rm PBH} \lesssim 0.9$. Similarly, protoneutron stars with $T/|W| \lesssim 0.14$–$0.16$, the threshold for secular instability, have $a^*_{\rm PBH} \lesssim 0.6$–$0.7$. If low-$T/|W|$ instabilities are effective at limiting $T/|W|$ in protoneutron stars on short time scales, nascent black hole spins may be limited to low values ($a^* \lesssim 0.4$ for a $T/|W|$ instability threshold of $\sim 0.05$).

[4]Note that this may not necessarily be what happens. Outer protoneutron star material may become centrifugally supported, falling into the nascent black hole only on an accretion time scale (Duez et al. 2006).

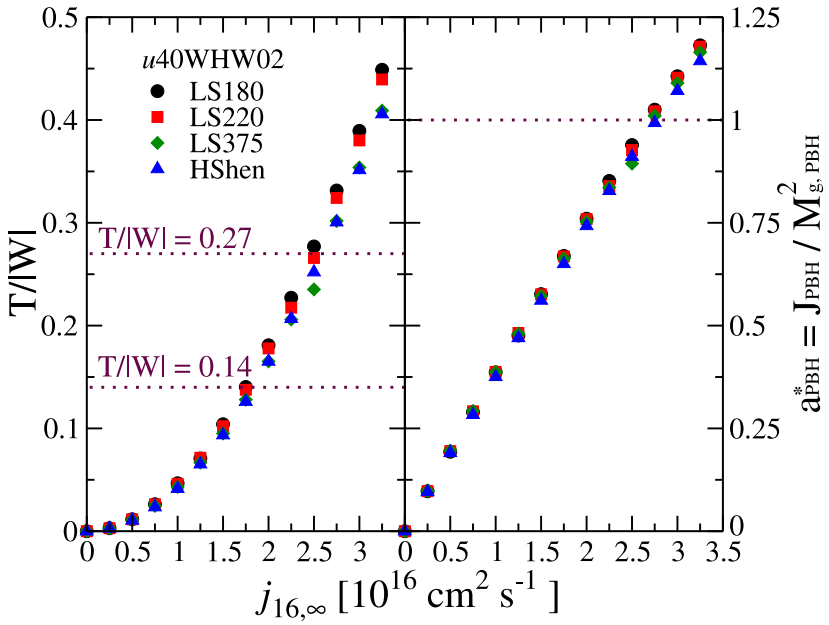


Figure 4.14: Left: $T/|W|$ for a range of initial $j_{16,\,\infty}$ and EOS for the $u$40WHW02 progenitor. We denote the value of $T/|W|$ thresholds for the dynamical rotational instability, $T/|W|_{\rm dyn} = 0.27$, and the secular instability, $T/|W|_{\rm sec} = 0.14$. Right: dimensionless spin parameter $a^*_{\rm PBH}$ for the protoneutron star at the last stable configuration prior to collapse to a black hole. Note that $a^*_{\rm PBH} > 1$ is generally allowed by GR but a black hole must have $a^* < 1$. Protoneutron stars that could reach $a^*_{\rm PBH} > 1$ are nonaxisymmetrically unstable and will be limited to $a^*_{\rm PBH}$ below 1. For the $u$WHW02 model, the initial central rotation rate is given as $\Omega_c = 1.141 \times j_{16,\,\infty}\,{\rm rad\,s^{-1}}$.

Table 4.5: Rotating black hole formation properties. The $u$ series of presupernova models in this table are taken from the $Z_\odot = 10^{-4}$ model set of Woosley et al. (2002). We imposed a rotation law via Equation 4.5, the value of $j_{16,\ \infty}$ is given in the model name following the letter J. In simulations where a black hole did not form within 3.5 s we give, in parenthesis, the values at this time.

| Model | $\Omega_{\rm c,\,init}$ [a] (rad s$^{-1}$) | $J$ [b] ($10^{49}$ erg s) | $T/\lvert W\rvert_{\rm init}$ [c] (%) | $T/\lvert W\rvert_{\rm bounce}$ [d] (%) | $t_{\rm BH}$ (s) | $M_{\rm b,max}$ ($M_\odot$) | $M_{\rm g,max}$ ($M_\odot$) | $J_{\rm PBH}$ [e] ($10^{49}$ erg s) | $T/\lvert W\rvert_{\rm PBH}$ [f] (%) | $a^*_{\rm PBH}$ [g] | $\overline{L_\nu}$ [h] (100 B s$^{-1}$) |
|---|---|---|---|---|---|---|---|---|---|---|---|
| $u$30WHW02LS180J1.0 | 1.34 | 9.97 | 0.048 | 3.32 | 0.990 | 2.24 | 2.11 | 1.61 | 5.06 | 0.41 | 2.07 |
| $u$30WHW02LS180J2.0 | 2.69 | 19.94 | 0.193 | 13.44 | 1.223 | 2.33 | 2.20 | 3.48 | 20.08 | 0.81 | 1.58 |
| $u$40WHW02LS180J0.5 | 0.57 | 8.07 | 0.006 | 0.87 | 0.371 | 2.35 | 2.25 | 0.86 | 1.16 | 0.19 | 4.99 |
| $u$40WHW02LS180J1.0 | 1.14 | 16.14 | 0.025 | 3.50 | 0.381 | 2.37 | 2.27 | 1.75 | 4.66 | 0.39 | 4.77 |
| $u$40WHW02LS180J1.5 | 1.71 | 24.21 | 0.057 | 7.96 | 0.398 | 2.41 | 2.30 | 2.69 | 10.41 | 0.58 | 4.41 |
| $u$40WHW02LS180J2.0 | 2.28 | 32.29 | 0.101 | 14.26 | 0.421 | 2.45 | 2.35 | 3.69 | 18.09 | 0.76 | 3.95 |
| $u$40WHW02LS180J2.5 | 2.85 | 40.36 | 0.157 | 21.91 | 0.455 | 2.52 | 2.41 | 4.81 | 27.70 | 0.94 | 3.46 |
| $u$40WHW02LS180J3.0 | 3.42 | 48.43 | 0.226 | 24.92 | 0.519 | 2.63 | 2.52 | 6.19 | 38.94 | [1.11] | 2.93 |
| $u$50WHW02LS180J1.0 | 1.31 | 22.51 | 0.020 | 3.05 | 0.588 | 2.30 | 2.18 | 1.66 | 4.79 | 0.40 | 3.30 |
| $u$50WHW02LS180J2.0 | 2.62 | 45.02 | 0.079 | 12.58 | 0.662 | 2.38 | 2.26 | 3.54 | 18.80 | 0.78 | 2.73 |
| $u$60WHW02LS180J1.0 | 1.05 | 30.03 | 0.013 | 3.00 | 0.453 | 2.38 | 2.28 | 1.72 | 4.36 | 0.38 | 3.64 |
| $u$60WHW02LS180J2.0 | 2.10 | 60.07 | 0.052 | 12.46 | 0.540 | 2.44 | 2.34 | 3.60 | 17.17 | 0.75 | 2.92 |
| $u$30WHW02LS220J1.0 | 1.34 | 9.97 | 0.048 | 3.30 | 1.419 | 2.38 | 2.20 | 1.75 | 4.97 | 0.41 | 1.89 |
| $u$30WHW02LS220J2.0 | 2.69 | 19.94 | 0.193 | 13.43 | 1.697 | 2.45 | 2.29 | 3.77 | 19.89 | 0.82 | 1.41 |
| $u$40WHW02LS220J0.5 | 0.57 | 8.07 | 0.006 | 0.86 | 0.455 | 2.47 | 2.34 | 0.94 | 1.16 | 0.19 | 5.19 |
| $u$40WHW02LS220J1.0 | 1.14 | 16.14 | 0.025 | 3.48 | 0.462 | 2.49 | 2.36 | 1.89 | 4.61 | 0.39 | 4.95 |
| $u$40WHW02LS220J1.5 | 1.71 | 24.22 | 0.057 | 7.94 | 0.474 | 2.51 | 2.39 | 2.89 | 10.22 | 0.58 | 4.58 |
| $u$40WHW02LS220J2.0 | 2.28 | 32.29 | 0.100 | 14.29 | 0.488 | 2.55 | 2.42 | 3.93 | 17.78 | 0.76 | 4.09 |
| $u$40WHW02LS220J2.5 | 2.85 | 40.36 | 0.157 | 22.13 | 0.508 | 2.59 | 2.48 | 5.00 | 26.58 | 0.93 | 3.57 |
| $u$40WHW02LS220J3.0 | 3.42 | 48.43 | 0.226 | 24.57 | 0.549 | 2.67 | 2.56 | 6.36 | 38.01 | [1.10] | 2.99 |
| $u$50WHW02LS220J1.0 | 1.31 | 22.51 | 0.020 | 3.04 | 0.725 | 2.43 | 2.28 | 1.82 | 4.73 | 0.40 | 3.45 |
| $u$50WHW02LS220J2.0 | 2.62 | 45.03 | 0.079 | 12.60 | 0.777 | 2.49 | 2.35 | 3.81 | 18.51 | 0.78 | 2.86 |
| $u$60WHW02LS220J1.0 | 1.05 | 30.03 | 0.013 | 2.99 | 0.602 | 2.48 | 2.35 | 1.84 | 4.31 | 0.38 | 3.48 |
| $u$60WHW02LS220J2.0 | 2.10 | 60.07 | 0.052 | 12.49 | 0.664 | 2.53 | 2.41 | 3.80 | 16.83 | 0.74 | 2.87 |
| $u$30WHW02LS375J1.0 | 1.34 | 9.97 | 0.048 | 3.24 | ··· | (2.81) | (2.50) | (2.30) | (5.14) | (0.42) | (1.35) |
| $u$30WHW02LS375J2.0 | 2.69 | 19.94 | 0.192 | 13.32 | ··· | (2.82) | (2.55) | (4.55) | (18.73) | (0.79) | (1.15) |
| $u$40WHW02LS375J0.5 | 0.57 | 8.07 | 0.006 | 0.85 | 0.941 | 3.02 | 2.71 | 1.27 | 1.10 | 0.20 | 5.53 |
| $u$40WHW02LS375J1.0 | 1.14 | 16.14 | 0.025 | 3.44 | 0.926 | 3.02 | 2.72 | 2.52 | 4.31 | 0.39 | 5.34 |
| $u$40WHW02LS375J1.5 | 1.71 | 24.22 | 0.057 | 7.88 | 0.904 | 3.01 | 2.74 | 3.77 | 9.50 | 0.57 | 5.02 |
| $u$40WHW02LS375J2.0 | 2.28 | 32.29 | 0.100 | 14.26 | 0.873 | 2.99 | 2.75 | 5.02 | 16.52 | 0.75 | 4.59 |
| $u$40WHW02LS375J2.5 | 2.85 | 40.36 | 0.157 | 22.36 | 0.845 | 2.99 | 2.78 | 6.07 | 23.52 | 0.89 | 4.11 |
| $u$40WHW02LS375J3.0 | 3.42 | 48.43 | 0.226 | 23.43 | 0.788 | 2.96 | 2.79 | 7.46 | 35.38 | [1.09] | 3.45 |
| $u$50WHW02LS375J1.0 | 1.31 | 22.51 | 0.020 | 2.99 | 1.346 | 3.02 | 2.69 | 2.56 | 4.53 | 0.40 | 4.07 |
| $u$50WHW02LS375J2.0 | 2.62 | 45.03 | 0.079 | 12.54 | 1.296 | 2.99 | 2.72 | 5.09 | 17.49 | 0.78 | 3.44 |
| $u$60WHW02LS375J1.0 | 1.05 | 30.04 | 0.013 | 2.95 | 1.330 | 3.00 | 2.71 | 2.44 | 4.08 | 0.38 | 3.62 |

Continued on Next Page...

Table 4.5 – Continued

| Model | $\Omega_{\rm c,\,init}$[a] (rad s$^{-1}$) | $J$[b] ($10^{49}$ erg s) | $T/\lvert W\rvert_{\rm init}$[c] (%) | $T/\lvert W\rvert_{\rm bounce}$[d] (%) | $t_{\rm BH}$ (s) | $M_{\rm b,max}$ ($M_\odot$) | $M_{\rm g,max}$ ($M_\odot$) | $J_{\rm PBH}$[e] ($10^{49}$ erg s) | $T/\lvert W\rvert_{\rm PBH}$[f] (%) | $a^*_{\rm PBH}$[g] | $\overline{L_\nu}$[g] (100 B s$^{-1}$) |
|---|---|---|---|---|---|---|---|---|---|---|---|
| $u$60WHW02LS375J2.0 | 2.10 | 60.07 | 0.052 | 12.47 | 1.284 | 2.98 | 2.74 | 4.93 | 16.01 | 0.75 | 3.09 |
| $u$30WHW02HShenJ1.0 | 1.34 | 9.96 | 0.049 | 3.03 | 3.335 | 2.75 | 2.49 | 2.00 | 3.81 | 0.37 | 1.25 |
| $u$30WHW02HShenJ2.0 | 2.69 | 19.92 | 0.195 | 12.45 | ··· | (2.79) | (2.56) | (4.48) | (18.10) | (0.78) | (1.03) |
| $u$40WHW02HShenJ0.5 | 0.57 | 8.07 | 0.006 | 0.79 | 0.854 | 2.88 | 2.64 | 1.17 | 1.06 | 0.19 | 4.44 |
| $u$40WHW02HShenJ1.0 | 1.14 | 16.13 | 0.025 | 3.21 | 0.873 | 2.90 | 2.67 | 2.36 | 4.13 | 0.38 | 4.28 |
| $u$40WHW02HShenJ1.5 | 1.71 | 24.20 | 0.057 | 7.33 | 0.901 | 2.93 | 2.71 | 3.64 | 9.35 | 0.56 | 4.03 |
| $u$40WHW02HShenJ2.0 | 2.28 | 32.26 | 0.101 | 13.27 | 0.932 | 2.97 | 2.76 | 5.00 | 16.51 | 0.74 | 3.69 |
| $u$40WHW02HShenJ2.5 | 2.85 | 40.33 | 0.157 | 20.79 | 0.959 | 3.01 | 2.82 | 6.36 | 25.20 | 0.91 | 3.28 |
| $u$40WHW02HShenJ3.0 | 3.42 | 48.39 | 0.226 | 25.09 | 0.999 | 3.06 | 2.88 | 7.83 | 35.14 | [1.07] | 2.80 |
| $u$50WHW02HShenJ1.0 | 1.31 | 22.49 | 0.020 | 2.78 | 1.195 | 2.85 | 2.61 | 2.35 | 4.45 | 0.39 | 3.29 |
| $u$50WHW02HShenJ2.0 | 2.62 | 44.99 | 0.080 | 11.62 | 1.266 | 2.93 | 2.71 | 4.93 | 17.23 | 0.76 | 2.86 |
| $u$60WHW02HShenJ1.0 | 1.05 | 30.01 | 0.013 | 2.72 | 1.197 | 2.88 | 2.65 | 2.31 | 4.05 | 0.37 | 3.02 |
| $u$60WHW02HShenJ2.0 | 2.10 | 60.02 | 0.052 | 11.48 | 1.273 | 2.94 | 2.73 | 4.75 | 15.38 | 0.72 | 2.65 |

[a] Initial central angular velocity of star.
[b] Total angular momentum of star.
[c] Initial $T/|W|$ of the star.
[d] $T/|W|$ of the star at bounce.
[e] Angular momentum of protoblack hole when $\alpha_c = 0.3$.
[f] $T/|W|$ of the star when $\alpha_c = 0.3$.
[g] Dimensionless spin of the protoblack hole when $\alpha_c = 0.3$. Unphysical values for a black hole are shown in braces $[\cdots]$.
[h] Total neutrino luminosity averaged over postbounce time.

### 4.2.2 Models Evolved with Rotation: Proposed LGRB Progenitors

A great puzzle in massive star evolution is to understand the necessary departures from the general core-collapse scenario to produce an LGRB in addition to a supernova explosion, as spectroscopically confirmed in, to date, six LGRB/SNe pairs. The very low occurrence rate of LGRB/SN per core-collapse supernova calls for progenitor properties that are rarely encountered in star formation/evolution.

Two LGRB central-engine models are currently favored. They suggest the key components for a successful LGRB/SN are a compact progenitor with a short light-crossing time of $\sim$1 s and fast rotation at the time of collapse. One is the collapsar model (Woosley 1993), a fast-rotating progenitor fails to explode in its early postbounce phase and instead forms a black hole, while the in-falling envelope eventually forms a Keplerian disk feeding the hole on an accretion/viscous time scale comparable to that of the LGRB. The other model involves a protomagnetar (Wheeler et al. 2000), in which the LGRB is born after a successful supernova explosion, either by the neutrino or the magneto-rotational mechanism, although the latter seems more likely given the rapid rotation required for the magnetar (Dessart et al. 2008).

In this section we focus on one important aspect of the collapsar model to validate, or invalidate, the assumption, often made but so far never checked, that the LGRB progenitor models available in the literature indeed collapse to form a black hole. We do this by collapsing the LGRB progenitor models of Woosley and Heger (2006). This is the only stellar-evolutionary model set for LGRB progenitors that is evolved until the onset of collapse owing to the difficulty of such simulations. This issue of black hole formation in these progenitors is critical for testing the potential of progenitor stars for producing LGRBs via the collapsar mechanism, but may also serve to diagnose an attractive channel for the formation of protomagnetars. Such "failed" collapsars (because they explode before forming a black hole) represent a serious alternative for the production of LGRBs, although they have their own caveats. For example, it is yet to be demonstrated that large, ordered magnetic fields can be generated via the MRI on short enough time scales to successfully explode rapidly rotating stars, although see Obergaulinger et al. (2009).

We have performed core-collapse simulations for the entire set of models produced in the `KEPLER` stellar evolution code for the study performed by Woosley and Heger (2006)[5]. We first consider the rapidly spinning progenitors evolved without magnetic fields. All these models have a dimensionless Kerr spin ($a^\star = Jc/GM^2$) at $3\,M_\odot$ greater than unity (with the exception of model HE16J, which has $a^\star = 0.91$) and are thus considered as promising collapsar candidates by Woosley and Heger (2006). Unfortunately, when evolved with `GR1D`, the collapsing iron core of all such models halts its collapse and expands. We associate this problem with the neglect of the centrifugal acceleration in the momentum equation in `KEPLER`, an approximation that fails in the fastest rotating models.

[5]Models are available from http://homepages.spa.umn.edu/~alex/GRB2/

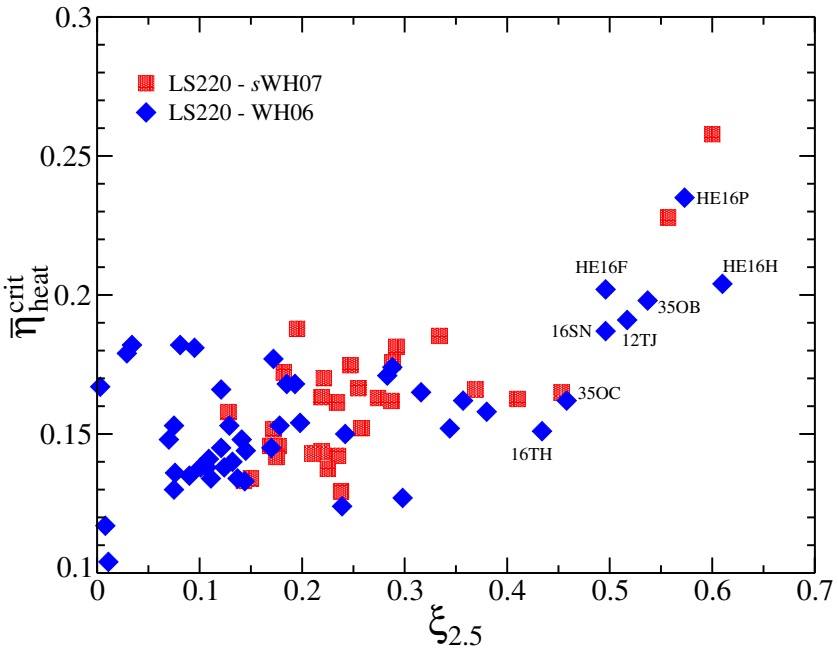


Figure 4.15: Illustration of the critical heating efficiency $\bar{\eta}^{\rm crit}_{\rm heat}$ versus bounce compactness $\xi_{2.5}$ for our GR1D simulations of the Woosley and Heger (2006) models, whose properties are summarized in Table 1 (blue diamonds). For comparison, we overplot the same quantity for the standard nonrotating core-collapse supernova progenitor models of Woosley and Heger (2007) evolved at solar metallicity (red squares). For the most part, the two distributions overlap, suggesting that the propensity to black hole formation and explosion is comparable for both. Only models with the fastest rotation rates achieve a larger compactness in excess of 0.4–0.5, but these may then be diverted from black hole formation through an early magneto-rotational explosion.

This term is included in GR1D. The mismatch suggests that their fastest models may be significantly affected by the addition of this term. Even if they did collapse, it is not clear that such extremely fast rotating cores would avoid a centrifugal bounce, where the collapse is halted by centrifugal support before nuclear densities are reached. We thus limit our discussion to models evolved with magnetic fields and therefore subject to magnetic torques during their evolution. Of the 46 models that fulfill this criterion, we identify 4 additional models (12OM, 16TJ, 35OD, and HE16G) that do not collapse but instead expand when restarted with GR1D. We exclude these as well from our study. Finally, for reference and completeness, we include the nonrotating models associated with each series (12SA, 12OA, 12TA, 16SA, 16OA, 16TA), making a total of 48 models. Each simulation is continued after core bounce until a black hole forms or until a time of 3.5 s has passed, whichever comes first. We present the results for these 48 models evolved with magnetic fields in Table 4.6 (for the table layout, we group models in bundles first of increasing mass, then of decreasing metallicity, and finally in alphabetical order which generally corresponds to an increased initial rotation rate).

#### 4.2.2.1 LGRB Progenitors: Very Low Bounce Compactness

Our simulations first demonstrate that most of the models have a small bounce compactness, $\xi_{2.5}$. We have argued in Section 4.1.3.5 that a compactness of $\sim 0.45$ represents a threshold value, for the neutrino mechanism, since above it an unrealistic neutrino-heating efficiency is required to prevent black hole formation. We also find this relationship for the models in Table 4.2. We note that this criterion is for explosions via the neutrino mechanism in spherical symmetry and therefore neglects any multidimensional and magneto-rotational contributions to the powering of an explosion (Dessart et al. 2008, Murphy and Burrows 2008), so this threshold value is probably a lower limit. We plot in Figure 4.15 the critical heating efficiency of the nonrotating solar metallicity stars from Woosley and Heger (2007), (taken from Figure 4.8), together with the generally fast-rotating progenitors of Woosley and Heger (2006), we find that both datasets in fact overlap for the most part. In other words, in terms of compactness, most of these progenitors are similar to garden variety, low-mass, nonrotating, progenitors and do not seem to have any more reason to form a black hole then, e.g., the red supergiant progenitors expected to produce Type II-Plateau supernovae. As shown in Table 4.6, provided no explosion is launched, half of these models have not formed a black hole after 3.5 s, and only $\sim 15\%$ do within $\sim 1$ s. We note that this result is not so surprising given the small iron-core mass ($\sim 1.4\,M_{\odot}$) of most Woosley and Heger (2006) models (see their Tables 1 and 2). The first conclusion from this exploration is therefore that most of the models presented here are rather unlikely to form a black hole and thus may fail in a very fundamental way to produce a collapsar, irrespective of their angular-momentum budget.

Within each sequence presented in Table 4.2, the models that form a black hole within 3.5 s of core bounce, and thus at least in principle susceptible to form a collapsar, are the faster rotating ones characterized by very low mass-loss rates. These properties conspire to produce larger CO cores, more typical of more massive stars that do not rotate. In the following discussion, we group these models into several additional categories.

#### 4.2.2.2 LGRB Progenitors: Low Bounce Compactness, Slow Spin

The first category are models which obviously do not give rise to a LGRB, either by the standard collapsar or the protomagnetar mechanism, because they contain too little angular momentum. Optimistically assuming a failed core-collapse supernova, which is unlikely given the modest values of $\xi_{2.5}$, models 12SG ($\xi_{2.5} = 0.239$), 16OG ($\xi_{2.5} = 0.193$), 16SI ($\xi_{2.5} = 0.380$), and 16TG ($\xi_{2.5} = 0.288$) possess too little angular momentum in the remainder of the star to form a disk about the central black hole within $10^6$ s of collapse. This behavior is reflected by the stellar type at the time of death, i.e. a blue supergiant star for model 12SG and a red supergiant star for models 16OG and 16TG, only 16SI is a Wolf-Rayet star at the time of death. Quantitatively, this can be further inspected

Table 4.6: Long $\gamma$-ray burst progenitor model properties

| Model[a] | $\xi_{2.5}$ | $\Omega_c$[b] ($s^{-1}$) | $t_{BH}$[c] (s) | $M_{b,max}$[d] ($M_\odot$) | $M_{g,max}$[e] ($M_\odot$) | $M^{DF}_{b,BH}$[f] ($M_\odot$) | $a^\star_{BH,DF}$[g] | $t_{DF}$[h] (s) | $M_{preSN} - M^{DF}_{b,BH}$[i] ($M_\odot$) | $\bar{\eta}^{crit}_{heat}$ | $P_{ref}$[j] (ms) | $I$[k] ($10^{45}$ g cm$^2$) | $F^{100ms}_{rot}$[l] (B) |
|---|---|---|---|---|---|---|---|---|---|---|---|---|---|
| 12SA | 0.003 | 0.000 | ··· | (1.56) | (1.47) | (10.9) | ··· | ··· | ··· | 0.167 | ··· | ··· | ··· |
| 12SG | 0.239 | 0.198 | 2.728 | 2.33 | 2.12 | (7.57) | ··· | ··· | ··· | 0.124 | 18.1 | 3.37 | 0.034 |
| 12SH | 0.141 | 0.144 | ··· | (2.08) | (1.91) | (5.43) | ··· | ··· | ··· | 0.148 | 25.5 | 3.35 | 0.008 |
| 12SI | 0.075 | 0.208 | ··· | (1.75) | (1.64) | (6.95) | ··· | ··· | ··· | 0.153 | 24.7 | 3.17 | 0.010 |
| 12SJ | 0.121 | 0.751 | ··· | (2.05) | (1.90) | 6.77 | 0.470 | 91.6 | 2.27 | 0.166 | 4.10 | 3.53 | 0.305 |
| 12OA | 0.011 | 0.000 | ··· | (1.52) | (1.44) | (11.9) | ··· | ··· | ··· | 0.104 | ··· | ··· | ··· |
| 12OG | 0.029 | 0.149 | ··· | (1.88) | (1.75) | 4.50 | 0.217 | $4.42\times10^6$ | 7.32 | 0.179 | 22.5 | 3.17 | 0.006 |
| 12OH | 0.090 | 0.285 | ··· | (1.84) | (1.71) | 7.62 | 0.210 | 710. | 0.07 | 0.135 | 17.1 | 3.30 | 0.020 |
| 12OI | 0.095 | 1.061 | ··· | (1.86) | (1.73) | 5.91 | 0.535 | 68.8 | 3.81 | 0.181 | 4.49 | 3.27 | 0.270 |
| 12OL | 0.076 | 0.299 | ··· | (1.75) | (1.64) | 6.99 | 0.259 | 554. | 0.36 | 0.136 | 19.7 | 3.61 | 0.017 |
| 12ON | 0.170 | 1.709 | ··· | (2.21) | (2.02) | 2.67 | 0.496 | 8.51 | 8.26 | 0.145 | 2.38 | 3.27 | 1.013 |
| 12TA | 0.008 | 0.000 | ··· | (1.59) | (1.49) | (12.0) | ··· | ··· | ··· | 0.117 | ··· | ··· | ··· |
| 12TG | 0.034 | 0.148 | ··· | (1.91) | (1.77) | 4.59 | 0.228 | $3.73\times10^6$ | 7.35 | 0.182 | 24.9 | 3.43 | 0.007 |
| 12TH | 0.107 | 1.042 | ··· | (1.93) | (1.79) | 6.67 | 0.495 | 85.2 | 2.56 | 0.138 | 5.06 | 3.59 | 0.313 |
| 12TI | 0.145 | 1.323 | ··· | (2.02) | (1.86) | 3.33 | 0.507 | 15.3 | 7.46 | 0.144 | 3.26 | 3.48 | 0.610 |
| 12TJ | 0.517 | 1.281 | 0.853 | 2.51 | 2.37 | 2.97 | 0.640 | 2.64 | 8.58 | 0.191 | 1.10 | 4.31 | 3.286 |
| 16SA | 0.101 | 0.000 | ··· | (1.88) | (1.74) | (14.6) | ··· | ··· | ··· | 0.138 | ··· | ··· | ··· |
| 16SG | 0.109 | 0.203 | ··· | (1.91) | (1.77) | 9.79 | 0.404 | $2.71\times10^7$ | 2.16 | 0.141 | 20.8 | 3.27 | 0.010 |
| 16SH | 0.081 | 0.341 | ··· | (1.76) | (1.64) | (7.70) | ··· | ··· | ··· | 0.182 | 16.8 | 2.68 | 0.019 |
| 16SI | 0.380 | 0.189 | 1.132 | 2.38 | 2.20 | (9.85) | ··· | ··· | ··· | 0.158 | 11.9 | 3.82 | 0.062 |
| 16SL | 0.075 | 0.207 | ··· | (1.73) | (1.62) | (6.30) | ··· | ··· | ··· | 0.130 | 28.4 | 3.31 | 0.007 |
| 16SM | 0.121 | 0.229 | ··· | (2.02) | (1.85) | (8.31) | ··· | ··· | ··· | 0.145 | 20.0 | 3.51 | 0.016 |
| 16SN | 0.496 | 0.455 | 0.777 | 2.42 | 2.27 | 9.45 | 0.508 | 40.6 | 1.77 | 0.187 | 3.25 | 3.69 | 0.451 |
| 16OA | 0.144 | 0.000 | ··· | (2.15) | (1.96) | (15.8) | ··· | ··· | ··· | 0.133 | ··· | ··· | ··· |
| 16OG | 0.193 | 0.176 | 3.437 | 2.33 | 2.11 | 7.16 | 0.230 | $4.37\times10^6$ | 8.49 | 0.168 | 17.6 | 3.82 | 0.018 |
| 16OH | 0.185 | 0.248 | ··· | (2.21) | (2.00) | 9.18 | 0.133 | 810. | $7.9\times10^{-5}$ | 0.150 | 20.5 | 3.59 | 0.023 |
| 16OI | 0.344 | 0.733 | 1.449 | 2.37 | 2.19 | 7.10 | 0.553 | 18.2 | 5.11 | 0.152 | 3.21 | 4.06 | 0.700 |
| 16OL | 0.124 | 0.316 | ··· | (2.02) | (1.86) | 8.63 | 0.200 | 593. | 0.05 | 0.138 | 14.1 | 3.41 | 0.030 |
| 16OM | 0.172 | 1.059 | ··· | (2.17) | (1.98) | 5.64 | 0.590 | 24.5 | 6.31 | 0.177 | 2.60 | 3.02 | 0.480 |
| 16ON | 0.357 | 1.382 | 1.458 | 2.40 | 2.22 | 3.36 | 0.582 | 4.70 | 10.8 | 0.162 | 1.40 | 3.59 | 2.082 |
| 16TA | 0.070 | 0.000 | ··· | (1.76) | (1.64) | (16.0) | ··· | ··· | ··· | 0.148 | ··· | ··· | ··· |
| 16TG | 0.288 | 0.242 | 1.738 | 2.35 | 2.16 | 13.3 | 0.366 | $3.44\times10^4$ | 2.41 | 0.174 | 10.4 | 4.02 | 0.083 |
| 16TH | 0.434 | 0.598 | 0.958 | 2.41 | 2.25 | 8.01 | 0.511 | 23.7 | 3.44 | 0.151 | 2.57 | 3.80 | 0.599 |
| 16TI | 0.242 | 1.367 | 2.791 | 2.41 | 2.21 | 3.51 | 0.554 | 10.6 | 10.4 | 0.150 | 2.17 | 3.77 | 1.341 |
| 35OA | 0.178 | 0.289 | ··· | (2.26) | (2.05) | (12.9) | ··· | ··· | ··· | 0.153 | 14.6 | 3.53 | 0.044 |
| 35OB | 0.537 | 1.545 | 0.776 | 2.42 | 2.25 | 16.4 | 0.545 | 31.5 | 4.80 | 0.198 | 1.44 | 3.48 | 3.617 |
| 35OC | 0.458 | 1.980 | 0.972 | 2.43 | 2.29 | 4.44 | 0.622 | 4.84 | 23.6 | 0.162 | 1.10 | 4.49 | 7.521 |
| HE16C | 0.137 | 0.133 | ··· | (2.06) | (1.90) | (5.15) | ··· | ··· | ··· | 0.134 | 25.5 | 3.11 | 0.007 |

Continued on Next Page...

Table 4.6 – Continued

| Model[a] | $\xi_{2.5}$ | $\Omega_c$[b] ($s^{-1}$) | $t_{BH}$[c] (s) | $M_{b,max}$[d] ($M_\odot$) | $M_{g,max}$[e] ($M_\odot$) | $M^{DF}_{b,BH}$[f] ($M_\odot$) | $a^\star_{BH,DF}$[g] | $t_{DF}$[h] (s) | $M_{preSN} - M^{DF}_{b,BH}$[i] ($M_\odot$) | $\bar{\eta}^{crit}_{heat}$ | $P_{ref}$[j] (ms) | $I$[k] ($10^{45}$ g cm$^2$) | $F^{100ms}_{rot}$[l] (B) |
|---|---|---|---|---|---|---|---|---|---|---|---|---|---|
| HE16D | 0.283 | 0.440 | 1.706 | 2.35 | 2.16 | 8.65 | 0.367 | 117. | 0.88 | 0.171 | 4.74 | 3.65 | 0.206 |
| HE16E | 0.129 | 1.428 | ··· | (2.00) | (1.85) | 6.82 | 0.594 | 43.1 | 6.05 | 0.153 | 3.77 | 3.27 | 0.447 |
| HE16F | 0.496 | 1.096 | 0.837 | 2.48 | 2.33 | 4.29 | 0.567 | 8.97 | 10.5 | 0.202 | 1.46 | 4.28 | 2.323 |
| HE16H | 0.610 | 1.196 | 0.641 | 2.52 | 2.38 | 4.12 | 0.597 | 5.95 | 11.6 | 0.204 | 1.26 | 4.23 | 3.335 |
| HE16K | 0.132 | 0.134 | ··· | (2.04) | (1.88) | (5.16) | ··· | ··· | ··· | 0.140 | 26.6 | 3.11 | 0.007 |
| HE16L | 0.316 | 0.315 | 1.497 | 2.36 | 2.17 | 9.34 | 0.286 | 195. | 0.24 | 0.165 | 6.73 | 3.73 | 0.116 |
| HE16M | 0.111 | 1.206 | ··· | (1.91) | (1.77) | 10.4 | 0.532 | 94.0 | 2.61 | 0.134 | 4.42 | 3.23 | 0.348 |
| HE16N | 0.198 | 1.203 | 3.424 | 2.36 | 2.15 | 7.81 | 0.604 | 35.9 | 7.15 | 0.154 | 2.59 | 3.84 | 0.970 |
| HE16O | 0.298 | 1.209 | 1.891 | 2.39 | 2.20 | 6.77 | 0.594 | 25.0 | 8.86 | 0.127 | 1.98 | 3.61 | 1.414 |
| HE16P | 0.573 | 1.038 | 0.672 | 2.49 | 2.35 | 6.42 | 0.584 | 14.2 | 9.46 | 0.235 | 1.58 | 4.16 | 2.523 |

[a] Model designation from Woosley and Heger (2006). See text for details.
[b] Initial central angular velocity.
[c] Time elapsed between bounce and black hole formation, ··· indicates that no black hole formed within 3.5 s of bounce.
[d] Baryonic mass of the protoneutron star at the time of black hole formation. If no black hole forms in 3.5 s, we give the protoneutron star baryonic mass at 3.5 s.
[e] Gravitational mass of the protoneutron star at the time of black hole formation. If no black hole forms in 3.5 s, we give the protoneutron star baryonic mass at 3.5 s.
[f] Baryonic mass interior to the ISCO at the time of disk formation. If the angular momentum is too low to foster disk formation, we give the progenitor mass in parentheses instead.
[g] Dimensionless spin of the black hole when the disk forms. ··· indicates no disk forms.
[h] Twice the free-fall time of the mass element at the ISCO. ··· indicates no disk forms.
[i] Baryonic mass outside of the black hole at disk formation. ··· indicates no disk forms.
[j] Rotational period $P_{ref} = 2\pi/\bar{\omega}$ computed by appoximating $\bar{\omega}$ as the ratio of the total angular momentum to the moment of inertia of the protoneutron star, Equation 4.10. ··· indicates a nonrotating model.
[k] Proto-neutron star moment of inertia, note this can be up to two times the value for a nonrotating cold neutron star. This is the origin of the discrepancy with the values presented by Woosley and Heger (2006), who consider a cold nonrotating 1.4 $M_\odot$ neutron star with a moment of inertia $I = 1.4 \times 10^{45}$ g cm$^2$. ··· indicates a nonrotating model.
[l] Free energy stored in differential rotation. This amounts to the energy difference between the protoneutron star we obtain with `GR1D` and the corresponding protoneutron star with the same total angular momentum and moment of inertia but assuming solid-body rotation. ··· indicates a nonrotating model.

in Table 4.2 where we include the disk formation time, the black hole mass and spin at that time, and the mass exterior to the disk. We define disk formation to be when the accreting material will first be supported at the innermost stable circle orbit about a black hole with the enclosed mass and angular momentum using the formulae of Bardeen et al. (1972). We estimate the disk formation time as twice the free fall time of the innermost mass element that reaches a Keplerian velocity (Burrows 1986).

$$t_{\rm DF} \sim 2 \times \pi \sqrt{\frac{[r_{\rm pre\text{-}SN}(M_{\rm disk})]^3}{8GM_{\rm disk}}} \tag{4.6}$$

where $r_{\rm pre\text{-}SN}(M_{\rm disk})$ is the radius of the disk-forming Lagrangian mass element in the presupernova model. If no such mass element exists, no disk will form. In this case we include, instead of the enclosed black hole mass, the total presupernova stellar mass in parentheses. In the four models mentioned above, either no disk forms or the disk formation time is $\gtrsim 10^6$ s.

Additionally, we can discuss the potential for these models to form a LGRB via the protomagnetar model. Since uniform rotation is the lowest energy state, the *shear energy* of differential rotation is to be interpreted as a free energy that will be tapped by any process (e.g., nonaxisymmetric rotational shear instabilities, viscosity, or the MRI) capable of redistributing angular momentum. Viscosity would lead to additional heating in the postshock region to enhance the neutrino mechanism (Thompson et al. 2005) while the MRI action could strengthen the magnetic fields, driving bipolar outflows in the magneto-rotational mechanism (Burrows et al. 2007b). In our simulations, we estimate the available free energy of differential rotation by computing the difference in rotational energy of the protoneutron star model in `GR1D` and the rotational energy of a uniformly spinning protoneutron star of the same angular momentum and moment of inertia,

$$F_{\rm rot} = T - \frac{I\bar{\omega}^2}{2}\,, \tag{4.7}$$

where from section 3.4, for `GR1D`,

$$T = \frac{4\pi}{3}\int_0^{R_{\rm PNS}} \rho h X W^2 v_\varphi^2 r^2 dr\,, \tag{4.8}$$

$$I = \frac{8\pi}{3}\int_0^{R_{\rm PNS}} \rho h X W^2 r^4 dr\,, \tag{4.9}$$

$$\bar{\omega} = \int_0^{R_{\rm PNS}} \rho h X W^2 r v_\varphi r^2 dr \Big/ \int_0^{R_{\rm PNS}} \rho h X W^2 r^4 dr\,. \tag{4.10}$$

For reference we repeat the definitions of the hydrodynamic and metric quantities in Equations 4.8–4.10. $T$ is the rotational energy, $I$ is the moment of inertia, and $\bar{\omega}$ is the uniform rotation frequency, $h$ is the specific enthalpy, $X^2$ is the $g_{rr}$ component of the metric, $W$ is the Lorentz factor, and $v_\varphi$ is the angular velocity. We take $R_{\rm PNS}$ to be the radius where the matter density, $\rho = 10^{10}\,{\rm g\,cm^{-3}}$.

Using Equations 4.7–4.10, we calculate the free energy available in differential rotation at 100 ms

after bounce. We also calculate a reference spin period ($P_{\rm ref} = 2\pi/\bar{\omega}$), measured at the onset of the neutrino driven explosion, by assuming solid-body rotation for the entire protoneutron star with the same total angular momentum and moment of inertia. The corresponding values are given in Table 4.2. In Figure 4.16, we show the free energy available in differential rotation at 100 ms and the spin period of the protoneutron star at the onset of explosion. The total rotational energy of the protoneutron star, estimated as $I\bar{\omega}^2/2$, will increase as the protoneutron star cools and contracts. In models 12SG, 16OG, 16SI, and 16TG, which are contained within the green (lightest shade) box of Figure 4.16, $\lesssim$0.1B of free energy could be extracted from differential rotation via the MRI and converted to explosion energy, much less than is needed for a magneto-rotational explosion. Also, the protoneutron star spin periods are $\gtrsim$ 10 ms,[6] significantly larger than the $\lesssim$ 2 ms periods required for the protomagnetar model to reproduce classical LGRB energies (Metzger et al. 2011).

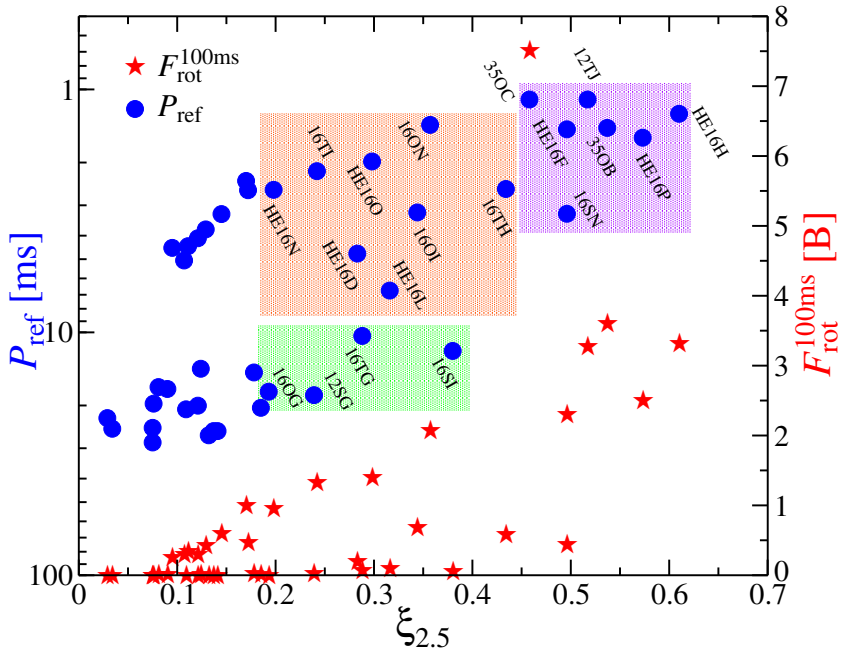


Figure 4.16: Reference protoneutron star spin period, $P_{\rm ref}$, taken at the onset of explosion (left axis, blue dots; Equation 4.10) and the free energy stored in differential rotation 100 ms after bounce $F_{\rm rot}^{100\rm ms}$ (right axis, red stars; Equation 4.7) versus bounce compactness $\xi_{2.5}$ for all rotating models in Table 4.6. While models with a low bounce compactness show a diversity in core-rotation properties, those with a high bounce compactness systematically have short spin periods and a large budget of free energy stored in the differential rotation. Shaded boxes refer to specific groupings of models discussed in the text. Using $\xi_{2.5} > 0.45$ as a black hole formation criterion for nonrotating progenitors, we can qualitatively compare the reference spin periods of this figure to Metzger et al. (2011), who sketches the outcome of collapse as a function of progenitor spin and mass. From this, one would predict that none of the LGRB progenitor models studied here formed black holes.

[6] Even taking into account the spin up due to the protoneutron star cooling and contraction, which will decrease the moment of inertia from the value in Table 4.2 to $\sim 0.4 M_{\rm PNS} R_{\rm PNS}^2 \sim 1.6 \times 10^{45} (M/1.4\,M_\odot)(R/12\,{\rm km})^2$ (Metzger et al. 2011), or roughly a factor of 2, the spin periods are $\gtrsim$ 5 ms.

#### 4.2.2.3 LGRB Progenitors: Low Bounce Compactness, Fast Spin

The second category are models with a larger angular-momentum budget but unfavorable bounce compactness. Although compact enough to lead to black hole formation within 3.5 s of core bounce, we find that the predicted critical heating efficiencies are similar to that expected for a standard $15\,M_\odot$ nonrotating red supergiant progenitor star. These properties make them unlikely collapsar progenitors, but in contrast, make them ideal candidates for protomagnetar formation, and perhaps LGRBs through that channel. These models include 16OI ($\xi_{2.5} = 0.344$), 16ON ($\xi_{2.5} = 0.357$), 16TH ($\xi_{2.5} = 0.434$), 16TI ($\xi_{2.5} = 0.242$), HE16D ($\xi_{2.5} = 0.283$), HE16L ($\xi_{2.5} = 0.316$), HE16N ($\xi_{2.5} = 0.198$), and HE16O ($\xi_{2.5} = 0.298$) and are contained in the orange (medium shade) box of Figure 4.16. In addition to having critical heating efficiencies similar to what is needed to explode typical low-mass massive stars, the free energy available in rotation is $\mathcal{O}(1\,\mathrm{B})$. This energy may be converted to explosion energy via the magneto-rotational mechanism. The spin period of these protoneutron stars is in the range 1–6 ms, thus on the order of what is needed for the protomagnetar model of LGRBs (Metzger et al. 2011).

#### 4.2.2.4 LGRB Progenitors: High Bounce Compactness, Fast Spin

Eventually, the fastest rotating progenitor models evolved with a strongly inhibited stellar-wind mass loss represent more suitable collapsar candidates, although each model has caveats. This set is contained in the purple (darkest shade) box of Figure 4.16 and includes models 12TJ ($\xi_{2.5} = 0.517$), 16SN ($\xi_{2.5} = 0.496$), 35OB ($\xi_{2.5} = 0.537$), and 35OC ($\xi_{2.5} = 0.458$). Model 12TJ will form a $\sim 2.4\,M_\odot$ (gravitational mass) black hole $\sim 0.85$ s after core bounce, followed by a Keplerian disk after $\sim 2.6$ s, with a potential ejecta mass of $\sim 8.6\,M_\odot$. However, much like the models in the previous category, model 12TJ has $\sim 3$ B of free energy available in rotation that may lead to a magneto-rotational explosion early-on, preventing collapsar formation. This model is evolved at 1% solar metallicity, with an additional mass-loss rate scaling of 0.1, equivalent to an overall evolution at $10^{-4}$ solar metallicity, much below that observed for LGRB/SN sites (Modjaz et al. 2008). We find that models HE16F, HE16H, and HE16P have similar characteristics to model 12TJ. Model 16SN forms a $\sim 2.3\,M_\odot$ black hole $\sim 0.8$ s after bounce. Being evolved at an effective metallicity of 0.01 solar, it has a lower angular-momentum budget at death and is thus more likely to avoid a magneto-rotational explosion. However, it forms a Keplerian disk only $\sim 41$ s after core bounce, with only $\sim 1.8\,M_\odot$ left over for the supernova ejecta. Such characteristics might in fact be more amenable to reproduce recent observations of LGRB/SNe characterized by a very early and narrow light-curve peak, as witnessed for example for GRB100316D/SN 2010bh (Chornock et al. 2010). They may even explain why no supernova is found in association with some nearby LGRBs (Fynbo et al. 2006). Finally, models 35OB and 35OC form a black hole within $\sim 0.78$ and $\sim 0.97$ s of bounce,

respectively. Model 35OB will accrete $\sim 16\,M_\odot$ before a Keplerian disk forms $\sim 32\,$s after the onset of collapse, $\sim 4.8\,M_\odot$ is then available for the supernova ejecta. With the 35OC model, a disk forms very quickly after collapse, in 4.8 s, and a significant amount of mass is exterior to the disk, $\sim 24 M_\odot$, and thus much too large to accommodate inferred LGRB/SN ejecta masses. However, the propensity to collapsar formation of the 35OB and 35OC model may be ill-founded if the MRI is successful at powering a magneto-rotational explosion. The free energy available in rotation is huge, i.e., on the order of 4–7.5 B. In fact, in the 2D magneto-hydrodynamic simulations of Dessart et al. (2008) based on the 35OC model, it was found that, despite the large progenitor compactness, a magneto-rotational explosion was initiated $\sim 200\,$ms after core bounce and that the protoneutron star mass decreased thereafter, never reaching the mass threshold for black hole formation. In our models, the protoneutron stars in models 35OB and 35OC have $\sim$ 30–70 B of total rotational energy at the onset of explosion, amply matching the inferred energies of observed hypernovae.

#### 4.2.2.5 Discussion

Our quantitative study spells out the various shortcomings of these progenitor stars for producing collapsars. Even in those models that have the right compactness for black hole formation and sufficient angular momentum for disk formation, it is still unresolved today how they would avoid the magneto-rotational mechanism of explosion that is used to explain hypernovae (Bisnovatyi-Kogan et al. 1976, Burrows et al. 2007b, Dessart et al. 2008, LeBlanc and Wilson 1970, Moiseenko et al. 2006, Takiwaki and Kotake 2011, Wheeler et al. 2000, Yamada and Sawai 2004) The difficulty of forming a black hole and avoiding a magneto-rotational explosion in fast-rotating cores, at least in the models of Woosley and Heger (2006), lends credence to the protomagnetar model of LGRB/SNe.

Overall, this suggests that studies of collapsar progenitors would benefit from a second look. Angular momentum is key in the current collapsar and protomagnetar models, but there is a stiff requirement on the progenitor compactness to speculate on its propensity for forming a black hole, and thus for producing a LGRB through one or the other channel. A major step forward in resolving those issues would be to conduct massive-star evolution with rotation, centrifugal force, and magnetic fields always all the way to the formation of a degenerate neutronized core on the verge of collapse. This would allow a straightforward comparison of results between groups, and an easy determination of the compactness using `GR1D` to test the suitability of the core for black hole formation.

The ultimate check on the collapsar model requires multidimensional simulations covering the whole evolution from progenitor collapse, bounce, failed explosion during the protoneutron star phase, formation of a black hole followed by the formation of a Keplerian disk, and the powering of a $\sim 10\,$B supernova explosion. As we emphasize, black hole formation is perhaps one of the most difficult steps in this sequence of events, and in that respect, renders the protomagnetar channel quite attractive for the production of hypernovae and LGRBs. The diversity of LGRB/SNe, the

existence of supernova-less LGRBs and of LGRB-less hypernovae, may in fact call for a variety of formation channels for these rare events, including both collapsars and protomagnetars.

# Chapter 5

# Neutrino Radiation Transport[1]

## 5.1 Neutrino Transport Approximations for Core-Collapse Supernovae

One of the largest deficiencies of `GR1D` is its treatment of neutrinos. While the leakage/heating scheme is efficient and captures qualitative aspects of the postbounce phase, it cannot be quantitatively trusted and it does not predict, for example, the emitted energy spectrum of neutrinos. To properly treat neutrinos one must solve for the neutrino distribution function at all spatial points, for all neutrino energies, species, and propagation angles. The evolution of the neutrino distribution function, $f_\nu$, is governed by the relativistic Boltzmann transport equation (Lindquist 1966)

$$\delta(dN) = \left[ p^\alpha \frac{\partial f_\nu}{\partial x^\alpha} - \Gamma^\alpha{}_{\beta\gamma}\, p^\beta p^\gamma \frac{\partial f_\nu}{\partial p^\alpha} \right] dW dP\,, \tag{5.1}$$

where $dN$ is the number of particles in volume $dV$ at position $\vec{x}$ within a momentum volume of $dP$ at momentum $\mathbf{p}$, $dW = -(\mathbf{p}\cdot\mathbf{u})dVd\tau$ is the 4-volume traced out by a family of world lines at position $\vec{x}$ and momentum $\mathbf{p}$. $\Gamma^{\cdots}$ are the Christoffel symbols. When collisions with matter are ignored $\delta(dN) = 0$. Scattering of neutrinos with other neutrinos or the surrounding matter and the absorption and emission of neutrinos by the matter (i.e., collisional processes) lead to changes in $\delta(dN) = [\delta(dN)]_{\rm coll} = (\partial f_\nu/\partial\tau)_{\rm coll} dW dP$, giving the collisional Boltzmann equation (Lindquist 1966),

$$p^\alpha \left[ \frac{\partial f_\nu}{\partial x^\alpha} - \Gamma^\beta{}_{\alpha\gamma}\, p^\gamma \frac{\partial f_\nu}{\partial p^\beta} \right] = \left[ \frac{df_\nu}{d\tau} \right]_{\rm coll}\,. \tag{5.2}$$

In practice, solving the full Boltzmann equation for neutrinos in the core-collapse supernova context is a formidable task. For typical postbounce configurations, the neutrino distribution function transitions from its thermal equilibrium value in the protoneutron star core to almost free streaming at distances of $\gtrsim$200 km. This is difficult to capture numerically as the nature of the equations

[1] This chapter contains unpublished work in progress.

change from a diffusive regime, where the governing equations are parabolic, to the free streaming regime where the governing equations are hyperbolic. Regardless, the transition from the diffusive regime to the free streaming regime is absolutely crucial for the neutrino mechanism of core-collapse supernovae. It is in this region where interactions between the neutrino field and the matter are still appreciable—a net positive amount of energy can be transferred to the matter. It is commonplace to make approximations to simplify the calculation from the fully relativistic 3+2+1+1 (3 spatial dimensions, 2 neutrino propagation angle dimensions, 1 neutrino energy spectrum, and time dimension) problem for each neutrino species down to a more tractable problem. For most approximations the simplifying assumption bridges, in some way, the two regions, diffusive and free streaming. We briefly discuss the various neutrino transport schemes used in the core-collapse supernova community and discuss the advantages and disadvantages of each. We start with the most approximate and then increase in complexity of the scheme. Within each section we discuss current implementations in spherically symmetric (1D), axisymmetric (2D), and full 3D simulations.

## Leakage Schemes

Perhaps the crudest approximation to neutrino transport, neutrino leakage, cannot really be called a transport method at all as no evolution of the neutrino distribution function actually occurs. In general, a leakage scheme estimates the local neutrino energy and number emission rates by an interpolation between the free emission rate and the emission rate based on the diffusion approximation. This emitted energy and lepton number is then explicitly extracted from the matter. The leakage scheme used in `GR1D` is described in great detail in Section 3.6. Several methods are available for computing the local emission rates. In heating/cooling schemes, such as those used in Hanke et al. (2011), Murphy and Burrows (2008), Nordhaus et al. (2010b), Ott et al. (2011), the analytic formula of Janka (2001) are used, with suppression at high optical depths, to determine the energy emission and absorption rates. This method does not allow one to track the lepton number and, therefore, one does not capture the neutronization burst or the deleptonization of material in the postshock region. It has the advantage of being an almost completely local and analytic calculation; this makes it attractive for multidimensional simulations (Hanke et al. 2011, Murphy and Burrows 2008, Nordhaus et al. 2010b). It also allows one to study the neutrino mechanism in a parameterized way via the so-called *light bulb* method of neutrino heating where a user-specified neutrino luminosity is used to calculate the heating rate. More detailed leakage schemes track individual neutrino species spatially and temporally and therefore can follow the deleptonization of the postshock material. Examples in the core-collapse supernova context include, Kotake et al. (2003), Liebendörfer et al. (2009), Ott et al. (2012), Sekiguchi (2010), Takiwaki and Kotake (2011) and the work in Chapter 4 of this thesis. A disadvantage of neutrino leakage schemes in their purest form is that they cannot self-consistently reproduce the neutrino heating. In spherically symmetric problems this can be

overcome by integrating the luminosity coming from smaller radii, as we have done in `GR1D`, however in simulations of accretion disks, (Sekiguchi and Shibata 2011), or neutron star mergers, (Rosswog et al. 2003, Ruffert et al. 1996), this is not possible.

### Moment Schemes

An approximation often made in neutrino transport is to remove the full angular dependence of the Boltzmann transport equation and decompose the neutrino distribution function into moments. This decomposition is convenient as the first few moments have an intuitive physical meaning. The zeroth moment of the neutrino distribution function is the neutrino energy density, the first is the neutrino flux vector, and the second is the neutrino pressure tensor. For problems that remain highly spherical, this decomposition is well justified. Within the moment scheme framework there is a lot of room for further approximations. For example, one can truncate the moment expansion at any order by specifying a *closure*, an expression that approximates the $n+1$ moment as a function of the first $n$ moments. The simplest variant, where one closes the moment expansion after the zeroth moment, is flux-limited diffusion (FLD). Examples in the core-collapse supernova context include Bruenn (1985) in 1D and Burrows et al. (2007c), Fryer (1999), Yakunin et al. (2010) in 2D. In FLD schemes, the underlying equation one solves is a diffusion equation for the neutrino energy density. A flux-limiter must be invoked that ensures the radiation does not travel faster than the speed of light in regions where the diffusion approximation fails. The M1 moment scheme for neutrino radiation transport (Kuroda et al. 2012, Obergaulinger and Janka 2011, Shibata et al. 2011, Swesty and Myra 2009), evolves both the energy density and the flux vector but assumes an analytic closure for required higher moments. One can also define moment schemes where the closure is not analytic, but rather is obtained from, for example, a model Boltzmann equation solution (Buras et al. 2006a,b, Burrows et al. 2000, Rampp and Janka 2002). In this case in one uses the evolved moments as source terms to a formal integration of a Boltzmann-like equation, from this solution the higher moments are calculated and the system is iterated until convergence is reach.

We note that, in principle, moment schemes can be either energy dependent or energy independent. The latter are referred to as *grey* transport methods. Grey methods are computationally appealing as they remove an entire dimension of the parameter space. However, the energy dependence of the neutrino transport problem is crucial as the cross sections of neutrinos with matter typically scale as the square of the energy. In fact, early grey transport scheme were successful is obtaining explosions (Burrows and van Riper 1995, Fryer 1999, Herant et al. 1994). This strong energy dependence warrants a multienergy (or often referred to as multigroup) treatment of neutrinos. Moment schemes can also either include or ignore velocity dependent terms, general-relativistic terms, and/or energy-coupling terms, depending on the complexity of the method.

### Boltzmann Schemes

It is also possible to solve the full Boltzmann equation taking explicitly into account both the energy and angular dependence of the neutrino distribution function. This has been done in spherical symmetry (Liebendörfer et al. 2005, Mezzacappa and Bruenn 1993a,b,c, Rampp and Janka 2002, Sumiyoshi et al. 2005, Thompson et al. 2003), in 2D (Brandt et al. 2011, Livne et al. 2004, Ott et al. 2008), and recently in 3D (Sumiyoshi and Yamada 2012). The latter two ignore velocity terms and do not couple the energy groups. The work of Sumiyoshi and Yamada (2012) is a challenging task, present results are only for static backgrounds with very low resolution in all quantities considered.

### Monte Carlo Schemes

Like many numerical problems, the transport of neutrinos can be solved by throwing computational time at the problem. For this, Monte Carlo methods for solving the Boltzmann transport equations can be used. Monte Carlo scales almost perfectly to large problem sizes and therefore is very attractive for 3D simulations. Monte Carlo methods have been used in the core-collapse supernova context for many years, (Abdikamalov et al. 2012, Janka 1992, Janka and Hillebrandt 1989a,b), and are potentially promising for large-scale 3D simulations in the future.

## 5.2 M1 Scheme for Neutrino Transport

We present here a fully general-relativistic neutrino transport scheme. We will use the M1 approximation, which involves evolving both the neutrino energy density and the neutrino flux vector and assuming an analytic closure relation for the neutrino pressure tensor. The transport scheme is built as an extension of `GR1D`, what we will now call `nuGR1D`. As with `GR1D`, `nuGR1D` will be open source once complete. Half of the battle with neutrino transport is having a full set of neutrino interaction with matter. To this end, we have developed `NuLib`, an open-source neutrino interaction library currently available at `http://www.nulib.org`. `NuLib` is described in full in Appendix C. `NuLib` and `nuGR1D` will grow together as more neutrino interaction physics is added, such as inelastic scattering and detailed electron capture rates. It is our goal that `NuLib` be used as a community repository of neutrino interaction rates to ensure consistent implementation between groups.

### 5.2.1 Derivation of M1 Equations in Flat Space

For demonstrative and testing purposes, we first derive the spherically symmetric M1 evolution equations in hyperbolic form without considering the consequences of fluid motions, gravitational effects, or energy-exchanging collisional terms. The latter we leave until the next section where we consider a fully covariant form of the neutrino radiation evolution equations, in which the gravitational and

velocity terms manifest themselves naturally. In the flat space limit, Equation 5.2 reduces to

$$E_\nu \left[ \frac{\partial f_\nu}{\partial t} + \mu \frac{\partial f_\nu}{\partial r} + \frac{1-\mu^2}{r} \frac{\partial f_\nu}{\partial \mu} \right] = \left[ \frac{df_\nu}{d\tau} \right]_{\rm coll} , \tag{5.3}$$

where $\mu = \cos(\theta_\nu)$ is the neutrino propagation angle measured from the radial direction and $E_\nu$ is the neutrino energy. In the moment formalism for neutrino transport one typically rewrites this equation in terms of the specific neutrino intensity rather then the neutrino distribution function,

$$\frac{\partial \mathcal{I}_\nu}{\partial t} + \mu \frac{\partial \mathcal{I}_\nu}{\partial r} + \frac{1-\mu^2}{r} \frac{\partial \mathcal{I}_\nu}{\partial \mu} = \frac{cE_\nu^2}{(2\pi\hbar c)^3} \left[ \frac{df_\nu}{d\tau} \right]_{\rm coll} , \tag{5.4}$$

where the specific neutrino intensity and the neutrino distribution function are related via $\mathcal{I}_\nu = cE_\nu^3 f_\nu/(2\pi\hbar c)^3$. We note that this equation is fully energy dependent, i.e., $\mathcal{I}_\nu$ and $[df_\nu/d\tau]_{\rm coll}$ both will be functions of energy.

Applying the operator $\int_{-1}^{1} \mu^n d\mu$ to the collisional Boltzmann equation we can derive evolution equations for the $n^{\rm th}$ moment of the specific neutrino intensity. The first few radiation moments are defined as (Castor 2004),

$$J_\nu = \frac{1}{2} \int_{-1}^{1} \mathcal{I}_\nu d\mu , \tag{5.5}$$

$$H_\nu = \frac{1}{2} \int_{-1}^{1} \mu \mathcal{I}_\nu d\mu , \tag{5.6}$$

$$K_\nu = \frac{1}{2} \int_{-1}^{1} \mu^2 \mathcal{I}_\nu d\mu . \tag{5.7}$$

Taking the $n = 0$ moment of Equation 5.4 gives us the evolution equation for $J_\nu$, the spectral, or energy-dependent, neutrino energy density.

$$\begin{aligned}
\int_{-1}^{1} \left[ \frac{\partial \mathcal{I}_\nu}{\partial t} + \mu \frac{\partial \mathcal{I}_\nu}{\partial r} + \frac{1-\mu^2}{r} \frac{\partial \mathcal{I}_\nu}{\partial \mu} \right] d\mu = \int_{-1}^{1} \frac{cE_\nu^2}{(2\pi\hbar c)^3} \left[ \frac{df_\nu}{d\tau} \right]_{\rm coll} d\mu &= \mathcal{S}_\nu^0 , \\
\frac{\partial J_\nu}{\partial t} + \frac{\partial H_\nu}{\partial r} + \int_{-1}^{1} \frac{1}{r} \frac{\partial \mathcal{I}_\nu}{\partial \mu} d\mu - \int_{-1}^{1} \frac{\mu^2}{r} \frac{\partial \mathcal{I}_\nu}{\partial \mu} d\mu &= \mathcal{S}_\nu^0 , \\
\frac{\partial J_\nu}{\partial t} + \frac{\partial H_\nu}{\partial r} + \frac{1}{r} \mathcal{I}_\nu \Big|_{-1}^{1} - \frac{\mu^2}{r} \mathcal{I}_\nu \Big|_{-1}^{1} + \int_{-1}^{1} \frac{2\mu}{r} \mathcal{I}_\nu d\mu &= \mathcal{S}_\nu^0 , \\
\frac{\partial J_\nu}{\partial t} + \frac{\partial H_\nu}{\partial r} + \frac{2H_\nu}{r} &= \mathcal{S}_\nu^0 ,
\end{aligned} \tag{5.8}$$

where in the second last step we integrated by parts. The collisional term, $\mathcal{S}_\nu^0$, can be written as a compilation of emission terms, absorption terms, and scattering terms. The complexity depends on the neutrino interaction assumptions being made. We leave the discussion of the collisional source term to Appendix C, there we begin with defining $[df_\nu/d\tau]_{\rm coll}$ in terms of the neutrino interactions currently including in `NuLib`. In general, this term will have a complicated dependence on both

$\mu$ and $E_\nu$. Notice that the evolution equation for the spectral energy density $J_\nu$ depends on the spectral flux $H_\nu$. This hierarchy of moments persists to higher moment evolution equations; one will never obtain a closed set of moment equations, although higher-order moments should become subdominant, especially in systems with large-scale symmetries. Next we determine the evolution equation for the spectral flux vector $H_\nu$,

$$\begin{aligned}
\int_{-1}^{1}\mu\left[\frac{\partial\mathcal{I}_\nu}{\partial t}+\mu\frac{\partial\mathcal{I}_\nu}{\partial r}+\frac{1-\mu^2}{r}\frac{\partial\mathcal{I}_\nu}{\partial\mu}\right]d\mu=\int_{-1}^{1}\mu\frac{cE_\nu^2}{(2\pi\hbar c)^3}\left[\frac{df_\nu}{d\tau}\right]_{\rm coll}d\mu &= \mathcal{S}_\nu^1\\
\frac{\partial H_\nu}{\partial t}+\frac{\partial K_\nu}{\partial r}+\int_{-1}^{1}\frac{\mu}{r}\frac{\partial\mathcal{I}_\nu}{\partial\mu}d\mu-\int_{-1}^{1}\frac{\mu^3}{r}\frac{\partial\mathcal{I}_\nu}{\partial\mu}d\mu &= \mathcal{S}_\nu^1\\
\frac{\partial H_\nu}{\partial t}+\frac{\partial K_\nu}{\partial r}+\frac{\mu}{r}\mathcal{I}_\nu\Big|_{-1}^{1}-\int_{-1}^{1}\frac{1}{r}\mathcal{I}_\nu d\mu-\frac{\mu^3}{r}\mathcal{I}_\nu\Big|_{-1}^{1}+\int_{-1}^{1}\frac{3\mu^2}{r}\mathcal{I}_\nu d\mu &= \mathcal{S}_\nu^1\\
\frac{\partial H_\nu}{\partial t}+\frac{\partial K_\nu}{\partial r}+\frac{3K_\nu-J_\nu}{r} &= \mathcal{S}_\nu^1\,, \qquad (5.9)
\end{aligned}$$

where again lump all collisional physics into $S_\nu^1$. Some geometric source terms in both Equations 5.8 and 5.9 can be removed by writing the flux term, eg. $\partial H_\nu/\partial r$, in the form of $r^{-2}\partial(r^2H_\nu)/\partial r$, giving,

$$\frac{\partial J_\nu}{\partial t}+\frac{1}{r^2}\frac{\partial(r^2H_\nu)}{\partial r} = \mathcal{S}_\nu^0\,, \qquad (5.10)$$

$$\frac{\partial H_\nu}{\partial t}+\frac{1}{r^2}\frac{\partial(r^2K_\nu)}{\partial r}+\frac{K_\nu-J_\nu}{r} = \mathcal{S}_\nu^1\,. \qquad (5.11)$$

In the M1 scheme of radiation transport, the set of evolution equations are closed at this point by setting $K_\nu = k_\nu J_\nu$ Audit et al. (2002). $k_\nu$ is known as the Eddington factor. Diffusion theory provides limits on $k_\nu$, it has the well known values of 1/3 in optically thick environments and 1 in free streaming regions. $k_\nu$ is therefore usually taken as a function of $h_\nu = H_\nu/J_\nu$, when $h_\nu = 0$, $k_\nu = 1/3$, and when $h_\nu = 1$, $k_\nu = 1$. The region in between depends on the choice of closure. Two common choices of the closure relation are the Levermore-Pomraning (LP) closure (Levermore and Pomraning 1981),

$$k_\nu(h_\nu) = \frac{3+4h_\nu^2}{5+2\sqrt{4-3h_\nu^2}}\,, \qquad (5.12)$$

and the Minerbo maximum entropy (ME) closure (Minerbo 1978), modified by Cernohorsky and Bludman (1994) to have an analytic form,

$$k_\nu(h_\nu) = \frac{1}{3}+\frac{h_\nu^2}{15}(6-2h_\nu+6h_\nu^2)\,. \qquad (5.13)$$

We make use of both of these closures in our analytic tests of the transport scheme, although Smit

et al. (1997) find that the maximum entropy closure corrected for Fermi-Dirac statistics (MEFD),

$$k_\nu(h_\nu) = \frac{1}{3} + (1 - J'_\nu)(1 - 2J'_\nu)\frac{x^2}{15}(6 - 2x + 6x^2)\Big|_{x=h_\nu/(1-J'_\nu)} . \tag{5.14}$$

where $J'_\nu = J_\nu \times (2\pi\hbar c)^3/(cE_\nu^3)$ is the occupation density, reproduces Monte Caro results much better then the LP of ME closures. We perform several tests with this closure but leave detailed studies to future work.

Within the closure assumption, the evolution equations become,

$$\frac{\partial J_\nu}{\partial t} + \frac{1}{r^2}\frac{\partial(r^2 H_\nu)}{\partial r} = \mathcal{S}^0_\nu , \tag{5.15}$$

$$\frac{\partial H_\nu}{\partial t} + \frac{1}{r^2}\frac{\partial(r^2 k_\nu J_\nu)}{\partial r} - J_\nu\frac{1 - k_\nu}{r} = \mathcal{S}^1_\nu . \tag{5.16}$$

These equations can be written in the form of

$$\partial_t \vec{\mathcal{U}}_\nu + \partial_r \vec{\mathcal{F}}_\nu(\vec{\mathcal{U}}_\nu) = \vec{\mathcal{S}}_\nu(\vec{\mathcal{U}}_\nu) , \tag{5.17}$$

where in our case $\vec{\mathcal{U}}_\nu = (J_\nu, H_\nu)$, $\vec{\mathcal{F}}_\nu(\vec{\mathcal{U}}_\nu) = (H_\nu, k_\nu J_\nu)$, and $\vec{\mathcal{S}}_\nu(\vec{\mathcal{U}}_\nu) = (S^0_\nu, S^1_\nu + J_\nu(1 - k_\nu)/r)$. This forms a hyperbolic system of equations provided the characteristic speeds are real and causal. This is the case for the closures considered here (Pons et al. 2000). These equations can then be solved with the standard methods used for hydrodynamics. However, the source terms of Equations 5.15 and 5.16 can be stiff in regions of high Peclet number $\mathrm{Pe} = \kappa\Delta x$. The Peclet number is the product of the local opacity ($\kappa$) times the numerical grid zone width ($\Delta x$), and therefore can be thought of as the effective optical depth of a grid zone. Numerical tests show that standard methods fail when $\mathrm{Pe} \gtrsim 1$. Audit et al. (2002) have examined this problem in great detail. For regions of high opacity the neutrino flux is essentially zero and not changing with time. The evolution equations, Equations 5.15 and 5.16, then reduce to a diffusion equation for $J_\nu$[2]. The diffusion coefficient is $[c/(2\kappa_\nu)] \times (1 + 3\mathrm{Pe}/2)$, (Audit et al. 2002), and therefore is dominated by a numerical term if $\mathrm{Pe} = \kappa_\nu\Delta x > 1$. Audit et al. (2002) then go on to present a scheme to modify the flux returned from the Riemann solver to explicitly take into account the high Peclet number. We present the basics and results of that scheme here.

[2]We note that while we have not yet given an explicit form for the source terms, the methods laid out by Audit et al. (2002) assume the standard form of the M1 equations source terms, i.e., there is a source term in the flux evolution equation of the form $-\kappa_\nu H_\nu$, this is the ultimate source of the issues in evolving these equations. In our work $\kappa_\nu = \kappa_{s,\nu} + \kappa_{a,\nu}$, see Appendix C for details.

First we write down the numerical expression for the flux term in Equations 5.15 and 5.16,

$$\frac{1}{r^2}\frac{\partial(r^2 H_\nu)}{\partial r} = \frac{r^2_{i+1/2}H_\nu^{i+1/2} - r^2_{i-1/2}H_\nu^{i-1/2}}{r_i^2(r_{i+1/2}-r_{i-1/2})} \tag{5.18}$$

$$\frac{1}{r^2}\frac{\partial(r^2 K_\nu)}{\partial r} = \frac{r^2_{i+1/2}K_\nu^{i+1/2} - r^2_{i-1/2}K_\nu^{i-1/2}}{r_i^2(r_{i+1/2}-r_{i-1/2})} \tag{5.19}$$

where $H_\nu^{i\pm1/2}$ ($K_\nu^{i\pm1/2}$) is the flux of the $J_\nu$ ($H_\nu$) evolution equation at the cell interfaces derived from the HLLE approximate Riemann solver (Einfeldt 1988) and given as

$$H_\nu^{i+1/2} = \frac{\lambda_\nu^{+,\max}H_\nu^{i,R} - \lambda_\nu^{-,\min}H_\nu^{i+1,L} + \lambda_\nu^{+,\max}\lambda_\nu^{-,\min}(J_\nu^{i+1,L} - J_\nu^{i,R})}{\lambda_\nu^{+,\max} - \lambda_\nu^{-,\min}}, \tag{5.20}$$

and,

$$K_\nu^{i+1/2} = \frac{\lambda_\nu^{+,\max}K_\nu^{i,R} - \lambda_\nu^{-,\min}K_\nu^{i+1,L} + \lambda_\nu^{+,\max}\lambda_\nu^{-,\min}(H_\nu^{i+1,L} - H_\nu^{i,R})}{\lambda_\nu^{+,\max} - \lambda_\nu^{-,\min}}, \tag{5.21}$$

where $\mathcal{U}_\nu^{i,R/L}$ is the reconstructed moment vector at the right $(i+1/2)$ and left $(i-1/2)$ interface. $\lambda_\nu^{+,\max}$ is the maximum right-going characteristic speed (maximum of the value predicted from the reconstructed left (L) state in zone $i+1$, right (R) state in zone $i$, and 0) of the Riemann solution at the $i+1/2$ boundary and $\lambda_\nu^{-,\min}$ is the minimum left-going characteristic speed (minimum of the value predicted from the reconstructed left (L) state in zone $i+1$, right (R) state in zone $i$, and 0) of the Riemann solution at the $i+1/2$ boundary. These characteristic speeds are the eigenvalues of the Jacobian matrix $\partial\mathcal{F}_\nu(\mathcal{U}_\nu)/\partial\mathcal{U}_\nu$,

$$\lambda_\nu^{\pm} = \frac{k'_\nu \pm \sqrt{(k'_\nu)^2 + 4(k_\nu - h_\nu k'_\nu)}}{2}, \tag{5.22}$$

where again $k_\nu = K_\nu/J_\nu$ and $h_\nu = H_\nu/J_\nu$, $k'_\nu = \partial k_\nu/\partial h_\nu$ and is obtainable from the closure relation (Equations 5.12 and 5.13). We note again that the characteristic speeds are calculated from the reconstructed moments at the interface and the maximum/minimum of both the left and right states is chosen as the overall maximum/minimum characteristic speed. Audit et al. (2002) modifies these expressions to obtain the correct diffusion rate in the high Peclet number limit by introducing $\epsilon_\nu = 1/\mathrm{Pe} = 1/(\kappa_\nu \Delta x)$ and rewriting the evolution equations in a form that avoids the numerical diffusion constant term dominating when the Peclet number is $> 1$. We limit $\epsilon_\nu$ to be less than one, therefore if the Peclet number is $< 1$, the flux calculation is unaffected. This changes the characteristics entering into the Riemann problem, now denoted as $\tilde{\lambda}_\nu^{\pm}$,

$$\tilde{\lambda}_\nu^{\pm} = \frac{\epsilon_\nu k'_\nu \pm \sqrt{(\epsilon_\nu k'_\nu)^2 + 4(k_\nu - h_\nu k'_\nu)}}{2}. \tag{5.23}$$

Similarly, the fluxes calculated in Equations 5.20 and 5.21 are modified. Equation 5.20 for $H_\nu^{i+1/2}$

becomes

$$H_\nu^{i+1/2} = \frac{\tilde{\lambda}_\nu^{+,\max} H_\nu^{i,R} - \tilde{\lambda}_\nu^{-,\min} H_\nu^{i+1,L} + \epsilon_\nu \tilde{\lambda}_\nu^{+,\max} \tilde{\lambda}_\nu^{-,\min} (J_\nu^{i+1,L} - J_\nu^{i,R})}{\tilde{\lambda}_\nu^{+,\max} - \tilde{\lambda}_\nu^{-,\min}} \,. \tag{5.24}$$

The modified version of Equation 5.21 is slightly more complicated,

$$K_\nu^{i+1/2} = \epsilon_\nu \tilde{K}_\nu^{i+1/2} + (1-\epsilon_\nu^2)(K_\nu^{i+1,L} + K_\nu^{i,R})/2 \,, \tag{5.25}$$

with,

$$\tilde{K}_\nu^{i+1/2} = \frac{\epsilon_\nu (\tilde{\lambda}_\nu^{+,\max} K_\nu^{i,R} - \tilde{\lambda}_\nu^{-,\min} K_\nu^{i+1,L}) + \tilde{\lambda}_\nu^{+,\max} \tilde{\lambda}_\nu^{-,\min} (H_\nu^{i+1,L} - H_\nu^{i,R})}{\tilde{\lambda}_\nu^{+,\max} - \tilde{\lambda}_\nu^{-,\min}} \,. \tag{5.26}$$

All that is left to describe before Equations 5.15 and 5.16 are ready to be solved numerically is the handling of the source terms. We present here a basic representation of the moment source terms taken directly from Appendix C. In general these source terms will become more complicated when one includes inelastic (energy-exchanging) terms,

$$\frac{\partial J_\nu}{\partial t} + \mathcal{F}_\nu^0 = -\kappa_{a,\nu} J_\nu + \eta_\nu \,, \tag{5.27}$$

$$\frac{\partial H_\nu}{\partial t} + \mathcal{F}_\nu^1 = -(\kappa_{s,\nu} + \kappa_{a,\nu}) H_\nu + J_\nu \frac{1-k_\nu}{r} \,. \tag{5.28}$$

In these equations we have, for simplicity, renamed the flux terms to $\mathcal{F}_\nu^0$ and $\mathcal{F}_\nu^1$. $\kappa_{a,\nu}$ is the absorptive cross section, $\kappa_{s,\nu}$ is the scattering cross section, and $\eta_\nu$ is emissivity of neutrinos. The naive and simplest discretization of the radiation moment evolution equations is the following,

$$\begin{aligned} J_\nu^{(n+1)} &= J_\nu^{(n)} + \Delta t(-\mathcal{F}_\nu^0 - \kappa_{a,\nu} J_\nu + \eta_\nu)^{(n)} \,, \\ H_\nu^{(n+1)} &= H_\nu^{(n)} + \Delta t(J_\nu \frac{1-k}{r} - \mathcal{F}_\nu^1 - (\kappa_{a,\nu} + \kappa_{s,\nu}) H_\nu)^{(n)} \,, \end{aligned} \tag{5.29}$$

where $(n)$ denotes the current state variables and $(n+1)$ is the new state we are trying to solve for. Even solved with a multistep Runge-Kutta scheme this method fails because the source terms of the moment equations are very stiff, e.g., $|-\Delta t(\kappa_{a,\nu} + \kappa_{s,\nu}) H_\nu|$ can be $\gg H_\nu$, which would lead to numerical instability in the equations. Ideally one solves this set of equations fully implicitly, i.e.,

$$\begin{aligned} J_\nu^{(n+1)} &= J_\nu^{(n)} + \Delta t(-\mathcal{F}_\nu^0 - \kappa_{a,\nu} J_\nu + \eta_\nu)^{(n+1)} \,, \\ H_\nu^{(n+1)} &= H_\nu^{(n)} + \Delta t(J_\nu \frac{1-k_\nu}{r} - \mathcal{F}_\nu^1 - (\kappa_{a,\nu} + \kappa_{s,\nu}) H_\nu)^{(n+1)} \,, \end{aligned} \tag{5.30}$$

however, this is computationally demanding and not well suited for multidimensional situations as the flux terms, $\mathcal{F}_\nu^0$ and $\mathcal{F}_\nu^1$, are coupled to neighboring (spatial) bins. A fully implicit solution involves inverting a large matrix to self-consistently solve for the fluxes. However, the beauty of the flux determining scheme presented above is that it removes the stiff dependence of the flux term

on the evolution variables and a fully implicit solution is not required, rather we use modified flux calculated from the $(n)$ state variables and this particular term explicitly. We then only require the remaining source terms, which may be stiff, be solved implicitly,

$$\begin{aligned} J_\nu^{(n+1)} &= J_\nu^{(n)} - \Delta t \mathcal{F}_\nu^{0,(n)} + \Delta t(-\kappa_{a,\nu} J_\nu + \eta_\nu)^{(n+1)} , \\ H_\nu^{(n+1)} &= H_\nu^{(n)} - \Delta t \mathcal{F}_\nu^{1,(n)} + \Delta t(J_\nu \frac{1-k_\nu}{r} - (\kappa_{a,\nu} + \kappa_{s,\nu}) H_\nu)^{(n+1)} . \end{aligned} \tag{5.31}$$

In our scheme we first evolve the matter field which allows us to compute the $(n+1)$ state values of $\kappa_{s,\nu}$, $\kappa_{a,\nu}$, and $\eta_\nu$. We then can solve for $J_\nu^{(n+1)}$,

$$J_\nu^{(n+1)} = \frac{J_\nu^{(n)} - \Delta t(\mathcal{F}_\nu^{0,(n)} - \eta_\nu)}{1 + \Delta t\, \kappa_{a,\nu}} , \tag{5.32}$$

and then for $H_\nu^{(n+1)}$,

$$H_\nu^{(n+1)} = \frac{H_\nu^{(n)} - \Delta t(\mathcal{F}_\nu^{1,(n)} - J_\nu^{(n+1)}(1 - k_\nu^{(n)})/r)}{1 + \Delta t\, (\kappa_{a,\nu} + \kappa_{s,\nu})} . \tag{5.33}$$

To avoid having to iterate the solution, we use the $(n)$ value of the Eddington factor. This explicit treatment of the geometric term should be okay in most situations as this term does not make the first moment evolution equation stiff, unlike the $(\kappa_{a,\nu} + \kappa_{s,\nu}) H_\nu$ term.

### 5.2.2 Flat Space Test Cases

We now perform several code tests of our flat space neutrino radiation transport scheme. A common test in radiative transfer is the homogeneous radiating sphere. It is an attractive test problem because it tests a code's ability to transition from an arbitrarily diffusive region to a free streaming region and it has an analytic solution. We also test our code's ability to reproduce the neutrino spectra coming from a model protoneutron star and compare with recent Monte Carlo results.

#### 5.2.2.1 Homogeneous Radiating Sphere

The homogeneous sphere test is standard among neutrino radiation transport codes. For other implementations of this test we refer the reader to Abdikamalov et al. (2012), Rampp and Janka (2002), Smit et al. (1997). We briefly present here the analytic solution following Smit et al. (1997). The solution for the neutrino distribution function is

$$F(r, \mu) = b\left[1 - \exp\left(-\kappa s(r, \mu)\right)\right] , \tag{5.34}$$

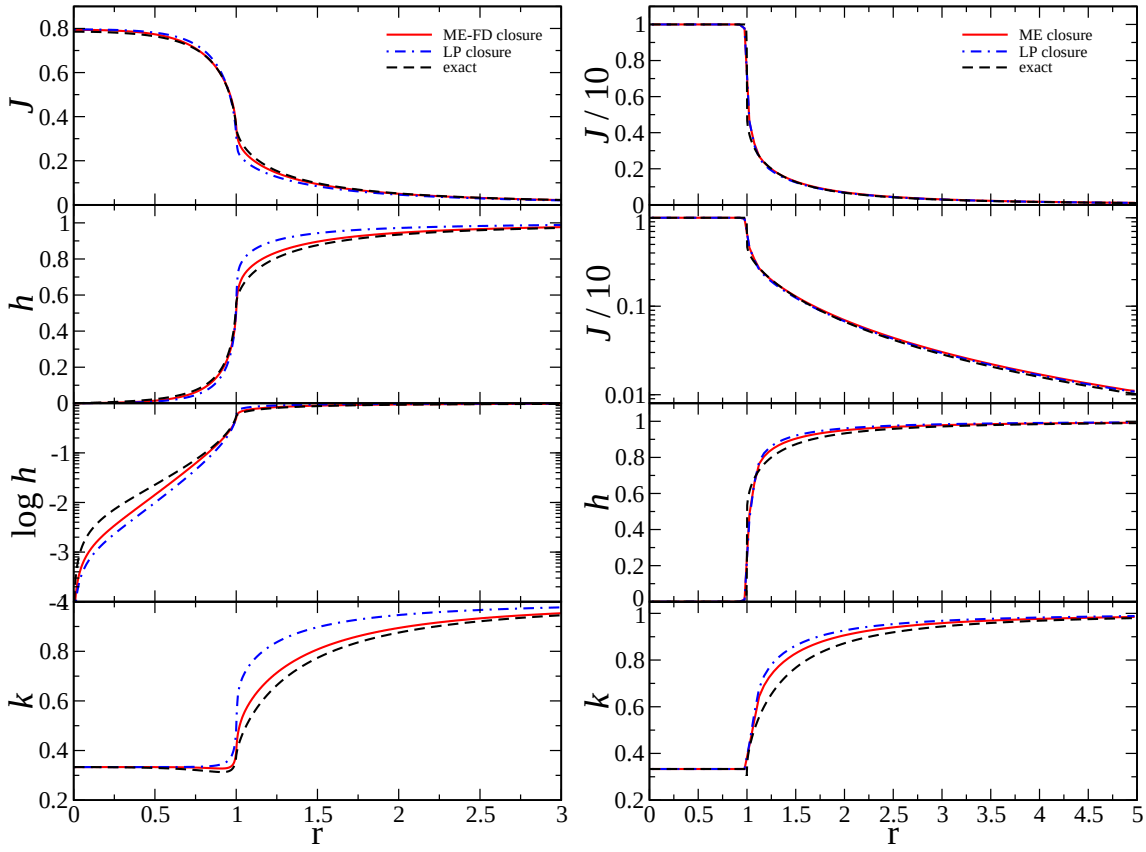


Figure 5.1: M1 transport of homogeneous radiating spheres for two sets of initial conditions. We show the zeroth moment of the neutrino distribution function, $J$, the flux factor, $h$, and the Eddington factor, $k$ for two test cases and several closures. The radiating sphere of Smit et al. (1997) has an optical depth at the center of 4, this makes it moderately diffusive. The strongly diffusive test of Abdikamalov et al. (2012) at an optical depth at the center of 250. For the Smit test we compare the exact solution (dashed lines) to our M1 scheme using the LP closure (dashed-dotted lines, Equation 5.12) and the MEFD closure (solid lines, Equation 5.14). For ease of comparison we use the same line choice as Smit et al. (1997). As the initial conditions for the Abdikamalov test do not consider potential Fermi-blocking of the neutrinos (their b is 10), we simply use the ME closure (solid lines, Equation 5.13), the LP closure (dashed-dotted lines, Equation 5.12) along with the exact solution (dashed lines). However, we note that tests with the MEFD closure with a strongly diffusive and degenerate core do improve the solution in the free streaming region much like in the Smit test.

where

$$s = \begin{cases} r\mu + r_s g(r,\mu) & \text{for} \quad r < r_s \quad \& \quad -1 < \mu < 1 \\ 2 r_s g(r,\mu) & \text{for} \quad r \geq r_s \quad \& \quad \left[1 - \left(\frac{r_s}{r}\right)^2\right]^{1/2} < \mu < 1 \\ 0 & \text{else} \end{cases} , \tag{5.35}$$

and

$$g(r,\mu) = \left[1 - \left(\frac{r}{r_s}\right)^2 \left(1 - \mu^2\right)\right]^{1/2} . \tag{5.36}$$

To determine an arbitrary moment we simply use the operator $\int_{-1}^{1} \mu^n d\mu$. We do this numerically[3]. The parameters of this solution are $b$, which sets the strength of the emission in the sphere; $\kappa$, which is the opacity of the material in the sphere; and $r_s$ which sets the radius of the sphere. We neglect the hydrodynamics and the gravity of the sphere. The test is difficult for two reasons: The sharp discontinuity at the surface of the homogeneous sphere where both the emissivity and opacity drop the zero, and the high opacity in the core. The latter changes the nature of the governing equations as discussed earlier in this section. We present the results for two tests in Figure 5.1. In the left panel of Figure 5.1 we reproduce the test in Smit et al. (1997) (hereinafter referred to the Smit test), in the right panel we reproduce the test case of Abdikamalov et al. (2012) (hereinafter referred to the Abdikamalov test). The Smit test case has an optical depth of 4 in the center ($b = 0.8$, $\kappa = 4$, $r_{\text{surface}} = 1$) and represents a moderately diffusive case. This test uses 800 equidistant zones between $0 < R < 3$, therefore this test is not affected by the modified flux terms as the Peclet number is $\text{Pe} = 0.015$. However the Abdikamalov test case, which uses 100 equidistant zones between $0 < R < 5$, has an optical depth of 250 in the center ($b = 10$, $\kappa = 250$, $r_{\text{surface}} = 1$, $\text{Pe} = 12.5$) and therefore represents a strongly diffusive case, here the modified flux terms are crucial. Our neutrino transport code performs very well in both tests. The emissivity and opacity discontinuities are handled well. In the Abdikamalov test, increased resolution would help resolve the surface. In their Monte Carlo implementation, resolution should not be an issue. It is worth commenting on the maximum entropy closure with Fermi-Dirac corrections used in the Smit test. While it matches the solution very well in Figure 5.1 we note if we choose $b \ll 1$ then the MEFD closure solution approaches the ME closure solution which is not shown, but is similar to the LP closure solution. The analytic solution is merely scaled by a change in $b$ and in no way depends on Fermi-Dirac statistics. While this may be a coincidence in this situation, Smit et al. (1997) do find that even in postbounce protoneutron star configurations, the MEFD closure does a better job at reproducing Monte Carlo results. This will be something we investigate in the future along with a detailed investigation of closures and their impact on modeling of core-collapse supernovae. Finally we note that in the diffusive region of the Smit test the numerical solution deviates quite significantly from the exact solution. Smit et al. (1997) also find and discuss this result. It stems from the numerical treatment of the flux calculation, and is expected to not appear in realistic situations where local gradients set the flux rather then the global initial conditions.

#### 5.2.2.2 Comparison to Monte Carlo Transport

The previous test was somewhat artificial in its treatment of the matter interaction terms. We now perform a test that much more closely matches the postbounce configuration found in core-collapse supernovae. We perform the same protoneutron star cooling test of Abdikamalov et al. (2012).

[3]For this we use a numerical routine provided by Ernazar Abdikamalov (Abdikamalov et al. 2012).

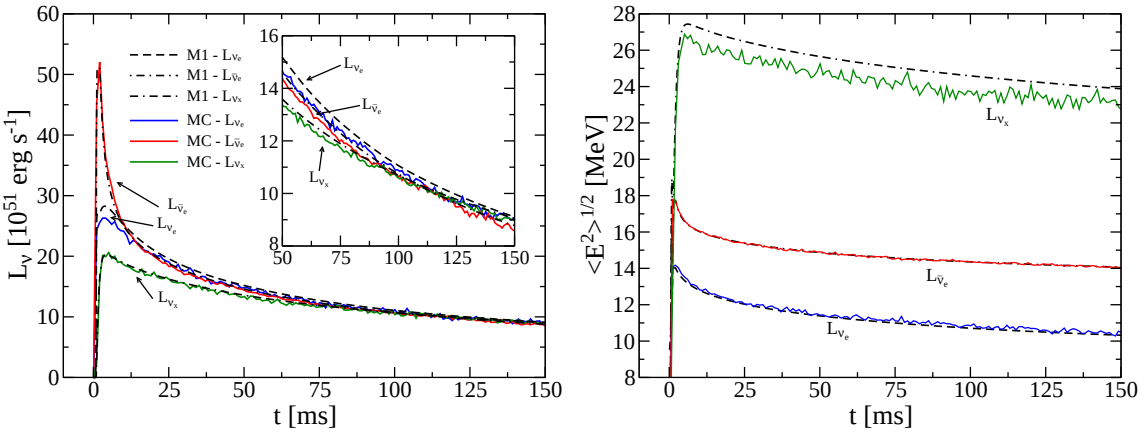


Figure 5.2: Comparison of the Monte Carlo results of Abdikamalov et al. (2012) and our M1 neutrino transport scheme. Shown in blue, red, and green are the luminosities (left panel) and root mean squared energies (right panel) averaged into 0.1 ms bins to reduce scatter (1 ms in the luminosity inset for clarity) of the electron neutrinos, electron antineutrinos and heavy-lepton neutrinos, respectively. We plot every 1 ms bin. The dashed, dashed-dotted, and dashed-dashed-dotted lines are the M1 luminosities and root mean squared energies of the electron neutrinos, electron antineutrinos and heavy-lepton neutrinos, respectively. We allow the neutrino fields to fill up for 1.2 ms before evolving $T$ and $Y_e$. For clarity we also show an inset zoomed in on the luminosity data.

Here we take a matter profile generated from an angular average of a 2D multigroup, multiangle simulation of core collapse (Ott et al. 2008). We evolve only the temperature and electron fraction of the matter, keeping the density fixed. We reproduce the grid structure of Abdikamalov et al. (2012) exactly to minimize differences, using 100 grid zones logarithmically spaced out to 300 km with a central size of 500 m. For pure Monte Carlo transport, i.e., without the hydrodynamics, the grid zone size is not as crucial as the case for our moment scheme, we have tested higher resolutions and have seen small changes in the measured quantities, but it is unclear if this comes from non-convergence of the numerical solution (because of the coarse grid structure), or from changes in the matter background (which are interpolated differently for different grid setups). To further minimize differences between the transport schemes we use the same EOS, the HShen of Section 3.5 and the same set of neutrino emissivities and opacities (Burrows 2012). We show in Figure 5.2 the results of the comparison. The scattered points are the Monte Carlo results of Abdikamalov et al. (2012), running averaged over 0.1 ms bins to reduce the scatter (we used 1 ms running averages for the inset for clarity). The noise is characteristic of Monte Carlo scheme and depends on the number of particles used to model the neutrino transport. The lines are the predicted luminosities (left panel) and root mean squared energies (right panel) from our M1 scheme. For reference, blue and dashed lines refer to electron neutrinos, red and dashed-dotted lines refer to electron antineutrinos, and green and dashed-dashed-dotted lines refer to one characteristic heavy-lepton neutrino. Initially there are transients that arise from the differences between the matter profile and the equilibrium

matter profile. The equilibrium configuration is very sensitive to the neutrino interaction rates, small deviations from the equilibrium profile, from, for example, the 2D averaging of the profile, give large deviations in the neutrino luminosities. These transient differences quickly radiate away, and in a similar fashion, for both the M1 and the Monte Carlo transport schemes. At later times the luminosities and root mean squared energies agree very well and simply are set by the diffusion of neutrinos out of the cooling protoneutron star core. The test confirms that the modified flux terms of Equations 5.24 and 5.25 are accurately capturing the correct diffusion rate. For this test we used the ME closure, Equation 5.13. Tests using the LP closure, Equation 5.12, show differences only early on but not significant differences in the later phases. With a Monte Carlo code one can in principle test current and derive new closure relations, this is something that will be done in the near future.

## 5.3 General-Relativistic M1 Scheme for Neutrino Transport

We now extend the above transport scheme to full general relativity. While the approach to deriving the evolution equations is different then the last section, as we shall see, the methods in the previous section will be directly applicable to the fully general-relativistic case, for example, the modified flux determination. We will see that the flat space equations are obtained if we ignore gravitational effects, and any velocity and energy-coupling dependence.

We adopt the formulation of Shibata et al. (2011) in the derivation of our evolution equations. Therefore we take the time to introduce and motivate their approach to solving the neutrino transport equations. The work of Shibata et al. (2011) is based on the moment formalism of Thorne (1981). It is truncated after two moments, and has all of the multidimensional benefits of the scheme presented in the previous section. They obtain the moment evolution equations in conservative form by writing the moment tensor of the distribution function in the laboratory frame,

$$M^{\alpha\beta}_{(\nu)} = E_{(\nu)} n^\alpha n^\beta + F^\alpha_{(\nu)} n^\beta + F^\beta_{(\nu)} n^\alpha + P^{\alpha\beta}_{(\nu)} \,, \tag{5.37}$$

where we follow Shibata et al. (2011) and denote the energy dependent moments with a subscript $(\nu)$. We note the distinction with the radiation moments in the flat space case where the subscripts are simply $\nu$ without the parenthesis. Here $n^\alpha = (1/\alpha, -\beta^i/\alpha)$ is the 4-velocity of a stationary observer in the laboratory frame, in `GR1D` $n^\alpha = (1/\alpha, 0)$. The physical interpretation of $E_{(\nu)}$, $F^\alpha_{(\nu)}$, and $P^{\alpha\beta}_{(\nu)}$ is that they are the radiation fields measured in the frame of a stationary observer in the laboratory frame. However, with this formulation it is unclear what energy is measured by this observer. The inconvenient fact that we do not know the explicit energy dependence of the radiation fields in the laboratory frame is acceptable, as long as we can describe the source terms in the laboratory frame

without the knowledge of the energy in the laboratory frame, which turns out to be the case. We ultimately want to have predictions for the neutrino observables as a function of energy. As long as we extract the neutrino spectra at large enough radii, the fluid rest frame and the laboratory frame are the same. One may suggest that we instead choose the fluid rest frame in the coordinates of the laboratory frame to construct the moment tensor, i.e.,

$$M^{\alpha\beta}_{(\nu)} = J_{(\nu)} u^\alpha u^\beta + H^\alpha_{(\nu)} u^\beta + H^\beta_{(\nu)} u^\alpha + L^{\alpha\beta}_{(\nu)} \,, \tag{5.38}$$

where $u^\alpha$ is the four velocity of the fluid in the laboratory frame. While the physical interpretation of this equation is clear, $J_{(\nu)}$ here would be the energy density of neutrinos with energy $\nu$ in the fluid rest frame measured in the fluid rest frame, the evolution equations for $J_{(\nu)}$ and $H_{r,(\nu)}$ are nonconservative. This is why we, and Shibata et al. (2011), choose Equation 5.37.

From Thorne (1981) and Shibata et al. (2011), the evolution equation for the radiation moment (Equation 5.37) in frame independent notation is,

$$\nabla_\beta M^{\alpha\beta}_{(\nu)} - \frac{\partial}{\partial \nu}\left(\nu M^{\alpha\beta\gamma}_{(\nu)} \nabla_\gamma u_\beta\right) = S^\alpha_{(\nu)} \,. \tag{5.39}$$

For the time being we will ignore the energy derivative term, although this will be crucial to correctly model the velocity and energy dependence of the radiation field. These velocity-dependent effects include the Doppler shift of neutrinos being emitted from a fluid moving with respect to the laboratory frame, compression/decompression effects, and gravitational red shift. Before we derive the moment evolution equations in the coordinate frame of `GR1D`, we must derive the expressions for the source term, $S^\alpha_{(\nu)}$, and define the closure relation for $P^{\alpha\beta}_{(\nu)}$. We consider absorption and emission of neutrinos via thermal and charged current processes and iso-energetic scattering off of nuclear matter. From Shibata et al. (2011), the neutrino interaction source term is then,

$$S^\alpha_{(\nu)} = \kappa_{a,(\nu)}(J^{\rm eq}_{(\nu)} - J_{(\nu)}) u^\alpha - (k_{a,(\nu)} + k_{s,(\nu)}) H^\alpha_{(\nu)} \,, \tag{5.40}$$

where $\kappa_a$ and $\kappa_s$ are the absorption and scattering cross sections, respectively, $J^{\rm eq}_{(\nu)} = B_{(\nu)}$ is the equilibrium energy density. These quantities depend on the thermodynamic state of the matter ($\rho$, $T$, $Y_e$, and an equation of state) and on the neutrino species and neutrino energy. Expressions are derived in Appendix C and are available as the open-source neutrino interaction library `NuLib`. $J_{(\nu)}$ and $H^\alpha_{(\nu)}$ are the neutrino energy density and flux vector in the fluid rest frame, they are related to the neutrino energy density and flux vector in the laboratory frame via,

$$J_{(\nu)} = E_{(\nu)} W^2 - 2 F_{i,(\nu)} W u^i + P_{ij,(\nu)} u^i u^j \tag{5.41}$$

and

$$H^{\alpha}_{(\nu)} = (E_{(\nu)}W - F_{i,(\nu)}u^{i})h^{\alpha}{}_{\beta}n^{\beta} + Wh^{\alpha}{}_{i}F^{i}_{(\nu)} - h^{\alpha}{}_{i}u_{j}P^{ij}_{(\nu)}\,, \tag{5.42}$$

where we note that in the laboratory frame $F^0 = P^{0\alpha} = 0$, hence the Latin indices on the flux vector and pressure tensor. $h_{\alpha\beta} = g_{\alpha\beta} + u_{\alpha}u_{\beta}$, is the projection tensor. With these definitions, we can derive the source terms in laboratory frame with the laboratory radiation fields. We note that since we are using the fluid frame radiation moments (i.e., $J_{(\nu)}$ and $H_{r,(\nu)}$), we use the neutrino interactions terms (i.e., the opacities and emissivities) associated with the fluid rest frame energy. As stated earlier, this must be the case as we do not know the energies associated with the laboratory frame radiation moments. For reference we list the expressions for $J_{(\nu)}$, $H^{\alpha}_{(\nu)}$, and $S^{\alpha}_{(\nu)}$ in the laboratory frame of `GR1D` using the laboratory radiation fields and the fluid rest frame opacities.

$$\begin{aligned}
J_{(\nu)} &= W^2\left[E_{(\nu)} - 2F_{r,(\nu)}v/X + v^2P_{rr,(\nu)}/X^2\right] && (5.43)\\
H^{t}_{(\nu)} &= W^3\left[-(E_{(\nu)} - F_{r,(\nu)}v/X)v^2/\alpha + vF_{r,(\nu)}/(\alpha X) - v^2P_{rr,(\nu)}/(\alpha X^2)\right] && (5.44)\\
H^{r}_{(\nu)} &= W^3\left[-(E_{(\nu)} - F_{r,(\nu)}v/X)v/X + F_{r,(\nu)}/X^2 - vP_{rr,(\nu)}/X^3\right] && (5.45)\\
S^{t}_{(\nu)} &= W^3/\alpha\big[\kappa_{a,(\nu)}(B_{(\nu)}/W^2 - E_{(\nu)} + 2F_{r,(\nu)}v/X - P_{rr,(\nu)}v^2/X^2)\\
&\quad +(\kappa_{a,(\nu)} + \kappa_{s,(\nu)})\left\{(E_{(\nu)} - F_{r,(\nu)}v/X)v^2 - vF_{r,(\nu)}/X + v^2P_{rr,(\nu)}/X^2\right\}\big] && (5.46)\\
S^{r}_{(\nu)} &= W^3\big[\kappa_{a,(\nu)}(B_{(\nu)}/W^2 - E_{(\nu)} + 2F_{r,(\nu)}v/X - P_{rr,(\nu)}v^2/X^2)v/X\\
&\quad +(\kappa_{a,(\nu)} + \kappa_{s,(\nu)})\left\{(E_{(\nu)} - F_{r,(\nu)}v/X)v/X - F_{r,(\nu)}/X^2 + vP_{rr,(\nu)}/X^3\right\}\big]\,, && (5.47)
\end{aligned}$$

where we define $\kappa_{a,(\nu)}B_{(\nu)} = \eta_{(\nu)}$ as given by Kirchhoff's law and derived in Appendix C. The closure we use is described in Shibata et al. (2011),

$$P_{ij,(\nu)} = \frac{3k_{(\nu)} - 1}{2}P_{ij,(\nu),\mathrm{thin}} + \frac{3(1 - k_{(\nu)})}{2}P_{ij,(\nu),\mathrm{thick}}\,. \tag{5.48}$$

This is the general multidimensional closure relation, however we only are concerned with the diagonal components for `GR1D`,

$$\begin{aligned}
P_{rr,(\nu),\mathrm{thin}} &= E_{(\nu)}X^2 && (5.49)\\
P_{rr,(\nu),\mathrm{thick}} &= J_{(\nu),\mathrm{thick}}X^2\frac{1 + 4v^2W^2}{3} + 2H_{r,(\nu),\mathrm{thick}}XWv && (5.50)\\
P_{\theta\theta,(\nu),\mathrm{thick}} &= g_{\theta\theta}\frac{J_{(\nu),\mathrm{thick}}}{3} && (5.51)\\
P_{\phi\phi,(\nu),\mathrm{thick}} &= g_{\phi\phi}\frac{J_{(\nu),\mathrm{thick}}}{3}\,. && (5.52)
\end{aligned}$$

The values of $J_{(\nu),\mathrm{thick}}$ and $H_{r,(\nu),\mathrm{thick}}$ derived in Shibata et al. (2011), we neglect the shear compo-

nents in spherical symmetry. In `GR1D`, these become,

$$J_{(\nu),\rm thick} = 3\frac{(2W^2-1)E_{(\nu)} - 2W^2 F_{r,(\nu)} v/X}{2W^2+1} \tag{5.53}$$

$$H_{r,(\nu),\rm thick} = F_{r,(\nu)}/W + \frac{-4W^3 X v E_{(\nu)} + (4W^2+1) W v^2 F_{r,(\nu)}}{(2W^2+1)}\,. \tag{5.54}$$

$k_{(\nu)}$ in Equation 5.48 is the Eddington factor and is determined by invoking a closure relations, see Section 5.2.1. However, a subtlety arises of how to define the flux factor, $h_{(\nu)}$, used in computing the Eddington factor. We follow Shibata et al. (2011) and use,

$$h_{(\nu)} = \left(\frac{h_{\alpha\beta} H^{\alpha}_{(\nu)} H^{\beta}_{(\nu)}}{J^2_{(\nu)}}\right)^{1/2}\,, \tag{5.55}$$

where $J_{(\nu)}$ and $H^{\alpha}_{(\nu)}$ are defined in Equations 5.43–5.45 and $h_{\alpha\beta} = g_{\alpha\beta} + u_\alpha u_\beta$. As can be seen, $k_{(\nu)}$ is used to set the closure relation and define the pressure tensor but the flux factor used to calculate $k_{(\nu)}$ depends on the pressure tensor. An iterative process is needed to self-consistently solve for $k_{(\nu)}$.

### 5.3.1 Moment Evolution Equations

We are now ready to solve for the evolution equations of the neutrino radiation moments. We plug Equation 5.37 into Equation 5.39 and taking $\alpha = t$ gives us the evolution equation for the radiation energy density in the laboratory frame. We use the simplifying equation of Equation A.2 with $T^{\alpha\beta}$ replaced with $M^{\alpha\beta}$;

$$\begin{aligned}
\left(\sqrt{-g} M^{t\beta}_{(\nu)}\right)_{,\beta} &= \sqrt{-g} S^{t}_{(\nu)} - \sqrt{-g}\Gamma^{t}{}_{\beta\mu} M^{\beta\mu}_{(\nu)} \\
\partial_t\left(X E_{(\nu)}/\alpha\right) + \frac{1}{r^2}\partial_r\left(X r^2 F^{r}_{(\nu)}\right) &= \alpha X\left[S^{t}_{(\nu)} - \Gamma^{t}{}_{tt} M^{tt}_{(\nu)} - 2\Gamma^{t}{}_{tr} M^{tr}_{(\nu)} - \Gamma^{t}{}_{rr} M^{rr}_{(\nu)}\right]\,.
\end{aligned} \tag{5.56}$$

Next we use the chain rule to extract a factor of $X/\alpha$ from the $\partial_t$ and $\partial_r$ terms, then we multiply by $\alpha/X$. We also use $F^{r}_{(\nu)} = g^{rr} F_{r,(\nu)} = F_{r,(\nu)}/X^2$ to rewrite the flux term in terms of $F_{r,(\nu)}$. We use Table A.1 and Equations A.4-A.8 for evaluating the derivatives and Christoffels.

$$\begin{aligned}
\partial_t E_{(\nu)} + \frac{1}{r^2}\partial_r\left(\frac{\alpha r^2}{X^2} F_{r,(\nu)}\right) &= \alpha^2\left[S^{t}_{(\nu)} - E_{(\nu)}/\alpha^2 \partial_t\phi - 2F_{r,(\nu)}\partial_r\phi/(X^2\alpha) - \frac{P_{rr,(\nu)}}{\alpha^2 r}\partial_t m\right] \\
&\quad - \frac{\alpha E_{(\nu)}}{X}\left(X\partial_t\alpha^{-1} + \alpha^{-1}\partial_t X\right) - \frac{\alpha^2 F_{r,(\nu)}}{X^3}\left(X\partial_r\alpha^{-1} + \alpha^{-1}\partial_r X\right) \\
&= \alpha^2 S^{t}_{(\nu)} - \alpha F_{r,(\nu)}\left(\frac{m}{r^2} + 4\pi r(P + \rho h W^2 v^2)\right) - \frac{P_{rr,(\nu)}}{r}\partial_t m \\
&\quad - \frac{E_{(\nu)} X^2}{r}\partial_t m - \alpha F_{r,(\nu)}\left(\frac{\partial_r m}{r} - \frac{m}{r^2}\right) \\
&= \alpha^2 S^{t}_{(\nu)} + \alpha 4\pi r\rho h W^2\left[v E_{(\nu)} X(1 + p_{(\nu)}/X^2) - F_{r,(\nu)}(1+v^2)\right]
\end{aligned} \tag{5.57}$$

where $p_{(\nu)} = P_{rr,(\nu)}/E_{(\nu)}$. We note that the factor of $X^2$ arises due to our choice of definition for $p_{(\nu)}$. As in Section 5.2.1, we solve this equation implicitly but treat the modified flux term explicitly to avoid iterations of the modified flux calculation. Unlike the flat space case, the solution for $E_{(\nu)}^{(n+1)}$ requires knowledge of $F_{r,(\nu)}$. Therefore we must invert a simple $2 \times 2$ matrix for the solution of $E_{(\nu)}^{(n+1)}$ and $F_{r,(\nu)}^{(n+1)}$. In the notation of Equations 5.32 and 5.33, we substitute Equation 5.46 into Equation 5.57 to obtain,

$$E_{(\nu)}^{(n+1)}(1 + \Delta t\overline{\kappa}_{E,(\nu)}) - F_{r,(\nu)}^{(n+1)}\Delta t\overline{\psi}_E = E_{(\nu)}^{(n)} - \Delta t(\mathcal{F}_{(\nu)}^{0(n)} - \overline{\eta}_{E,(\nu)}) \,, \tag{5.58}$$

where we collect all of the general-relativistic and velocity-dependent terms into the effective opacities, $\overline{\kappa}_{E,(\nu)}$, the effective emissivities, $\overline{\eta}_{E,(\nu)}$ and $\overline{\psi}_{E,(\nu)}$, defined as

$$\begin{aligned}
\overline{\kappa}_{E,(\nu)} &= \alpha W^2\big[\kappa_{a,(\nu)} - 4\pi r\rho h v X(1 + p_{(\nu)}^{(n)}/X^2) + \kappa_{a,(\nu)} W v^2 p_{(\nu)}^{(n)}/X^2 \\
&\quad -(\kappa_{a,(\nu)} + \kappa_{s,(\nu)}) W v^2 (1 + p_{(\nu)}^{(n)}/X^2)\big] && (5.59)\\
\overline{\eta}_{E,(\nu)} &= \alpha W \eta_{(\nu)} && (5.60)\\
\overline{\psi}_{E,(\nu)} &= \alpha W^2\big[ -4\pi r\rho h(1 + v^2) + 2\kappa_{a,(\nu)} W v/X - (\kappa_{a,(\nu)} + \kappa_{s,(\nu)}) W v(1 + v^2)/X\big] \,, && (5.61)
\end{aligned}$$

where the first term on the right hand side of $\overline{\kappa}_{E,(\nu)}$ is the standard opacity term, corrected for general relativity, the second term is a general-relativistic term arising from the curvature of the space-time. The third and fourth terms are of order $(v/c)^2$ and come from the neutrino interaction source term defined in the laboratory frame, Equations 5.43 and 5.44. In this equation, we use the Eddington factor from the $(n)$ state to avoid nonlinearities and iteration of the new state variables, all others are the $(n + 1)$ state. The term in $\overline{\eta}_{E,(\nu)}$ is the standard flat space emissivity corrected for general relativity. The terms in the emissivity-like term $\overline{\psi}_{E,(\nu)}$ all arise from either general relativistic curvatures terms or velocity terms. We note that the neutrino contributions to the total stress energy tensor of the combined hydrodynamic plus radiation system, $T^{\alpha\beta} = T^{\alpha\beta}_{\text{matter}} + T^{\alpha\beta}_{\text{radiation}}$. Their contribution must be taken into account when computing the metric terms, Equations 3.1–3.5. We ignore the contribution of $\epsilon_{\text{radiation}}$ and $P_{\text{radiation}}$ to the radiation and matter sources terms via the specific enthalpy, $h$ and the pressure, $P$. Including these terms self-consistently requires including the radiation fields in the primitive variable recovery step of the conservative hydrodynamics, this is not attempted in our, or in any other that we know of, implementation of neutrino-radiation hydrodynamics. We will lay out the solution for the $E_{(\nu)}^{(n+1)}$ variable after deriving a similar equation for the laborartory radiation flux vector, its evolution equation follows in a similar manner,

$$
\begin{aligned}
\left(\sqrt{-g}M_r^{\ \beta}{}_{(\nu)}\right)_{,\beta} &= \sqrt{-g}S_{r,(\nu)} + \sqrt{-g}\Gamma^{\mu}_{\ \beta r}M_{\mu}^{\ \beta}{}_{(\nu)} \\
\partial_t\left(XF_{(\nu)}\right) + \frac{1}{r^2}\partial_r\left(\alpha X r^2 P_r^{\ r}{}_{(\nu)}\right) &= \alpha X\left[S_{r,(\nu)} + \Gamma^t_{\ rt}M_t^{\ t}{}_{(\nu)} + \Gamma^t_{\ rr}M_r^{\ t}{}_{(\nu)} + \Gamma^r_{\ rt}M_r^{\ t}{}_{(\nu)}\right. \\
&\quad \left. + \Gamma^r_{\ rr}M_r^{\ r}{}_{(\nu)} + \Gamma^{\phi}_{\ r\phi}M_{\phi}^{\ \phi}{}_{(\nu)} + \Gamma^{\theta}_{\ r\theta}M_{\theta}^{\ \theta}{}_{(\nu)}\right] \\
\partial_t F_{(\nu)} + \frac{1}{r^2}\partial_r\left(\frac{\alpha r^2}{X^2}P_{rr,(\nu)}\right) &= \alpha\left[S_{r,(\nu)} - E_{(\nu)}\partial_r\phi + \left(\frac{\partial_r m}{r} - \frac{m}{r^2}\right)P_{rr,(\nu)}\right] \\
&\quad + \alpha\frac{P_{\theta\theta,(\nu)} + P_{\phi\phi,(\nu)}}{r} - \frac{F_{r,(\nu)}}{X}\partial_t X - \frac{\alpha}{X^3}P_{rr,(\nu)}\partial_r X \\
&= \alpha X^2 S^r_{(\nu)} - \alpha E_{(\nu)}X^2\left[\frac{m}{r^2} + 4\pi r(P + \rho h W^2 v^2)\right] \\
&\quad + \frac{3\alpha(1-k_{(\nu)})}{r(2W^2+1)}\left[(2W^2-1)E_{(\nu)} - 2W^2 F_{r,(\nu)}v/X\right] \\
&\quad + \alpha F_{r,(\nu)}X 4\pi r\rho h W^2 v\,, \qquad (5.62)
\end{aligned}
$$

As we have done with Equation 5.58 we write the numerical expression that we employ for calculating the new neutrino flux vector,

$$
F^{(n+1)}_{r,(\nu)}(1 + \Delta t\overline{\kappa}_{F,(\nu)}) - E^{(n+1)}_{(\nu)}\Delta t\overline{\psi}_{(\nu)} = F^{(n)}_{(\nu)} - \Delta t(\mathcal{F}^{1(n)}_{(\nu)} - \overline{\eta}_{F,(\nu)})\,, \qquad (5.63)
$$

where the effective opacity and effective emissivities are given as,

$$
\begin{aligned}
\overline{\kappa}_{F,(\nu)} &= \alpha W^3\kappa_{s,(\nu)}(1+v^2) + \alpha W\kappa_{a,(\nu)} + \frac{6\alpha(1-k^{(n)}_{(\nu)})W^2 v}{r(2W^2+1)X} \qquad (5.64) \\
\overline{\eta}_{F,(\nu)} &= \alpha W v X\eta_{(\nu)} \qquad (5.65) \\
\overline{\psi}_{F,(\nu)} &= \frac{3\alpha(1-k^{(n)}_{(\nu)})(2W^2-1)}{r(2W^2+1)} - \alpha X^2\left[\frac{m}{r^2} + 4\pi r(P + \rho h W^2 v^2)\right] \\
&\quad -\alpha W^3 v X\kappa_{a,(\nu)}(1 + v^2 p^{(n)}_{(\nu)}/X^2) \\
&\quad \alpha W^3 v X(\kappa_{a,(\nu)} + \kappa_{s,(\nu)})(1 + p^{(n)}_{(\nu)}/X^2)\,. \qquad (5.66)
\end{aligned}
$$

We solve the matrix formed byEquations 5.58 and 5.63 for $(E^{(n+1)}_{(\nu)}, F^{(n+1)}_{r,(\nu)})$,

$$
\left[\begin{array}{cc|c} 1+\Delta t\overline{\kappa}_E & -\Delta t\overline{\psi}_E & E^{(n)}_{(\nu)} - \Delta t(\mathcal{F}^{0,(n)}_{(\nu)} - \overline{\eta}_E) \\ -\Delta t\overline{\psi}_F & 1+\Delta t\overline{\kappa}_F & F^{(n)}_{r,(\nu)} - \Delta t(\mathcal{F}^{1,(n)}_{(\nu)} - \overline{\eta}_F) \end{array}\right] = \left[\begin{array}{cc|c} a_E & b_E & S_E \\ b_F & a_F & S_F \end{array}\right], \qquad (5.67)
$$

which gives,

$$
\begin{aligned}
E^{(n+1)}_{(\nu)} &= \frac{S_E a_F - S_F b_E}{a_E a_F - b_E b_F} \qquad (5.68) \\
F^{(n+1)}_{r,(\nu)} &= \frac{S_F a_E - S_E b_F}{a_E a_F - b_E b_F}\,. \qquad (5.69)
\end{aligned}
$$

We note that the flat space limit of these equations is identical, as expected, to the equations derived in the previous section, Equations 5.32 and 5.33.

### 5.3.2 General-Relativistic Radiation Test Cases

#### 5.3.2.1 Comparison to Full Boltzmann Transport Simulations

In Liebendörfer et al. (2005), two independent implementations of Boltzmann neutrino transport in a $15\,M_{\odot}$ progenitor from Woosley and Weaver (1995) were compared. They have made the results of the comparison available for download[4]. This is a useful data set to compare our code with. The two independent codes are fully general-relativistic `AGILE-BOLTZTRAN` of the Oak Ridge group (Liebendörfer et al. 2004, Mezzacappa and Bruenn 1993a,b,c) and the Newtonian plus general-relativistic corrections code `VERTEX`, from the Garching group (Rampp and Janka 2002). Both codes solve the full Boltzmann equation in spherical symmetry, unlike `nuGR1D` which simply solves for the first two moments of the distribution function. Both of the codes used in Liebendörfer et al. (2005) have additional neutrino physics that is not yet included in `nuGR1D` as of the writing of this thesis. This, most notably, includes inelastic electron scattering. Additionally, the full velocity dependence described in the previous section currently leads to unphysical behavior when the velocities are large, most likely due to the neglect of the energy-coupling term in Equation 5.39. For this reason we must take the no-velocity limit of the general-relativistic radiation equations. This does *not* reduce the equations to the flat space equations of Section 5.2.1, it maintains the general-relativistic nature of the equations modulo velocity and energy dependent effects; we will discuss the difference later in this section. We point out where these assumptions are expected to make a difference as we compare our results to those of Liebendörfer et al. (2005). We note the comment that was added during the proofing process of Liebendörfer et al. (2005). It says a bug was discovered in the general-relativistic treatment in `VERTEX` after the comparison was made that greatly reduced the difference between the results, for this reason we assume the `AGILE-BOLTZTRAN` results represent a more correct solution. The corrected `VERTEX` results are not publicly available, however see Mueller et al. (2011), Figure 6 and 7 for a comparison with the updated versions of `VERTEX`.

In Figure 5.3, we compare the evolution of the central $Y_e$ during the collapse phase. As commonly displayed, we show this plotted as a function of central density, the curve is then parameterized by the time. The evolution begins at high $Y_e$ and low density and evolves in time to lower $Y_e$ and higher densities as the core collapses and deleptonizes. Shown are both the `AGILE-BOLTZTRAN` and `VERTEX` results, red dashed-dotted and blue dashed, respectively. We also include unpublished results of Liebendörfer (2011) using `AGILE-BOLTZTRAN` with inelastic scattering turned off, the green dashed-dotted-dotted line. The solid black line is `nuGR1D`'s $Y_e(\rho)$. We notice two large effects of the

[4] http://iopscience.iop.org/0004-637X/620/2/840/fulltext/datafiles.tar.gz

neglected physics in `nuGR1D`. *a)* The drop in $Y_e$ starting around $\rho \sim$ few $10^{11}$ g cm$^{-3}$ in the full radiation transport simulations is due to inelastic scattering of neutrinos on electrons, as is evident from the two `AGILE-BOLTZTRAN` simulations. As the neutrinos inelastically down-scatter off electrons to lower energies, their mean free path in the matter increases because of the energy dependence of the neutrino cross sections. They are now able to escape, accelerating deleptonization. We note that neutrinos are not fully degenerate during the collapse phase, otherwise this process would be blocked. An important consequence not evident in this plot is the thermalization of the neutrinos due to this process. *b)* At densities around $10^{12}$ g cm$^{-3}$, the neutrinos become effectively trapped because the advection time of the infalling matter is shorter than the diffusion time. This stops the deleptonization of the core and $Y_e(\rho)$ levels off. This does not occur in `nuGR1D` because we neglect these terms, the radiation does not become trapped until nuclear densities. When we do attempt to include the full velocity dependence (solid orange curve in Figure 5.3), we begin to see the trapping of the neutrinos at a few $10^{12}$ g cm$^{-3}$ but the code soon is unable to progress because of unphysical conditions, this issue is currently being investigated.

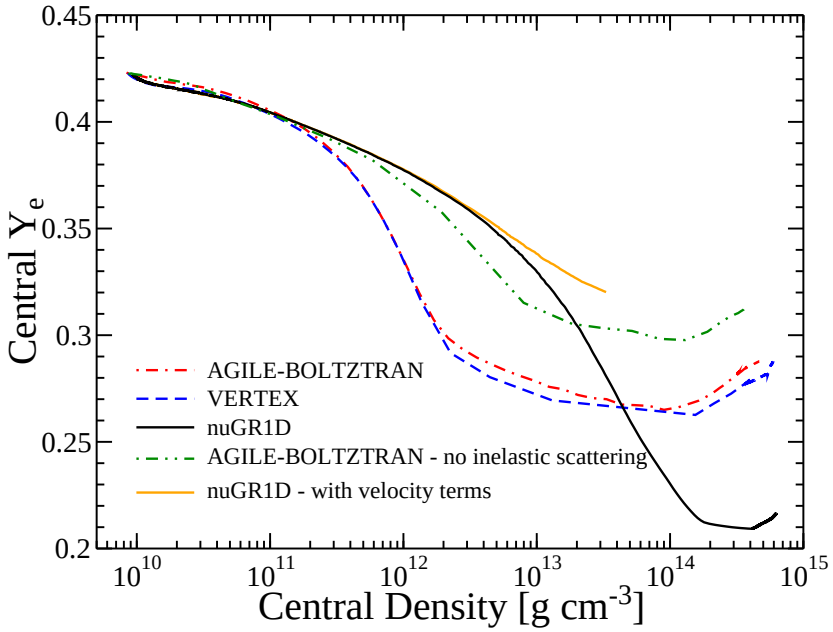


Figure 5.3: Comparison of central electron fractions ($Y_e$) vs. central density for `nuGR1D` and the results of Liebendörfer et al. (2005). For demonstration purposes, we show the effect of neglecting inelastic scattering in the simulations of Liebendörfer et al. (2005) (data from Liebendörfer (2011)). As well as the preliminary effect of full velocity terms in `nuGR1D`.

Next we focus on the postbounce neutrino signals. In Figure 5.4 we plot the three neutrino luminosities and root mean squared energies as a function of postbounce time. For each panel we plot the results of `AGILE-BOLTZTRAN` (red dashed-dotted line) and `VERTEX` (blue dashed line)

from Liebendörfer et al. (2005) and nuGR1D (black solid line). Overall the results agree very well. The differences seen in the collapse phase do not strongly influence the postbounce phase neutrino signal. While the inner core has a lower $Y_e$ value, the neutrinos produced in the core are trapped on the timescales we look at here ($\sim 250$ ms) and have no influence on the signal extracted at large radii. However, the low $Y_e$ of the core reduces the mass coordinate of the shock formation and the energy initially departed to the shock. The stalling of our shock is $\sim 25$ km short of both the AGILE-BOLTZTRAN and VERTEX results. This points out the importance of having the full suit of physics as recently emphasized by Lentz et al. (2011) who see similar results.

One systematic difference in the neutrino luminosities from nuGR1D is the decrease starting around 150 ms after bounce instead of 180 ms as seen in the VERTEX simulation. This drop in the neutrino luminosity is a direct consequence of the drop in the accretion rate of material through the shock. This mass coordinate of the drop corresponds to the outer edge of the silicon shell. We attribute this to the treatment of the low density equation of state. Below a density of $6\times10^7$ g cm$^{-3}$ VERTEX uses an equation of state that tracks the compositions of the original progenitor models whereas we assume nuclear statistical equilibrium everywhere. This difference will adjust key quantities, such as the speed of sound, which ultimately set the collapse time of the outer layers. We note that the times to core bounce in these three simulations are 172.4 ms, 177.0 ms, and 177.5 ms for AGILE-BOLTZTRAN, VERTEX, and nuGR1D. The excellent agreement between nuGR1D and the full radiation transport simulations deserves comment. To achieve a collapse time of 177.5 ms we had to remove the energy shift in our EOS, otherwise the collapse time is 224.6 ms. This inconsistency arises from both the conversion from baryonic number density typically used in equations of state to mass density used in hydrodynamic codes and from the energy-zero point of the EOS. The solution is ambiguous unless the stellar evolutionary model explicitly has taken into account the effect of the binding energy of the material. Finally, we comment on the lack of a sharp drop in the accretion luminosity in AGILE-BOLTZTRAN. The adaptive grid used in AGILE-BOLTZTRAN induces artificial diffusion and smears out sharp density features (Liebendörfer et al. 2005). By the time the silicon shell is accreted through the shock there is no longer a significant drop in the density, and therefore, there is not a significant drop in the accretion luminosity, rather the drop is smeared out over a longer time.

We can see some other systematic differences between the curves produced by nuGR1D and the full Boltzmann transport codes. In the last stages of collapse, the trapping of the neutrinos via the velocity terms produces a characteristic spike before the main neutronization burst. This is not present to the same extent in the nuGR1D results as seen in the inset of panel 1 in Figure 5.4. Several other systematic differences are seen in the root mean squared energies. For the electron neutrinos, the lack of velocity-dependent trapping before bounce increases the root mean squared energy. Similarly, for the heavy-lepton neutrinos, the higher values in nuGR1D are most likely due to the lack of inelastic neutrino-electron scattering which softens the spectrum of the radiation in the

postbounce phase. This is nicely shown in Thompson (2002) Figure 4.19 (with inelastic neutrino-electron scattering) and Figure 4.27 (without inelastic neutrino-electron scattering) and also in Lentz et al. (2011). The effect is strongest for the $\nu_x$ neutrinos ($\sim 5\,\mathrm{MeV}$), noticeable for the $\bar{\nu}_e$ neutrinos ($\sim 1\,\mathrm{MeV}$), and the weakest in the $\nu_e$ neutrinos signal. Gravitational redshift of the neutrinos will also effect the observed root mean squared energies, although this effect will not be as significant as most neutrinos are emitted at $10s$ of gravitational radii ($2GM/r \sim 3$–$5\,\mathrm{km}$ compared to the neutrinosphere locations of $\sim 50\,\mathrm{km}$) in the early postbounce phase. The postbounce velocities are much smaller than the collapse phase velocities. Especially at the relevant densities ($\sim$ few $10^{12}\mathrm{g\ cm^{-3}}$) here we do not expect to see a strong influence. This does not mean that the disregard of these terms in justified, they must be included to accurately model neutrino transport in core-collapse supernovae.

Finally we note the effect of the (partial) treatment of the radiation in general relativity versus flat space. The thin dashed curves in Figure 5.4 are from the flat space treatment of the radiation transport in Section 5.2.1, these simulations were done with general-relativistic hydrodynamics. The general-relativistic treatment of the radiation (solid lines) reduces the $\nu_e$ and $\bar{\nu}_e$ luminosities by $\sim 10\%$ and the $\nu_x$ luminosities, which are emitted deeper in the protoneutron star where relativistic effects are stronger, by $\sim 15\%$. Additional relativistic effects, such as gravitational red shift, will further effect the neutrino observables and must be included.

## 5.4 Preliminary Investigations with `nuGR1D`

Keeping all of the shortcomings in the current version of `nuGR1D` in mind, we attempt a first look at the progenitor dependence in core-collapse supernovae. While the lack of inelastic neutrino-electron scattering and full velocity-dependent transport will quantitatively change the picutre, there are many unanswered questions that can be explored qualitatively. Systematic trends are waiting to be discovered!

### 5.4.1 Progenitor Dependence of Neutrino Observables

No systematic study of the progenitor dependence of the neutrino observables (luminosities, average energies) has ever been attempted. With a neutrino transport code we can start to perform such a study. The systematic trends of neutrino observables have important implications for the next galactic supernova; ideally we want to be able to identify the internal structure (i.e., $\xi_M$, Equation 4.1) based solely on the neutrino signature. It is unclear how degeneracies factor in. For example, the nuclear equation state may be degenerate with the bounce compactness. Rotation, viewing angle, and neutrino oscillations may also play a role.

We present a first attempt at such a determination. We use 23 progenitor models ranging in mass from $12\,M_\odot$ to $120\,M_\odot$ from Woosley and Heger (2007) and evolve them with `nuGR1D`. We use

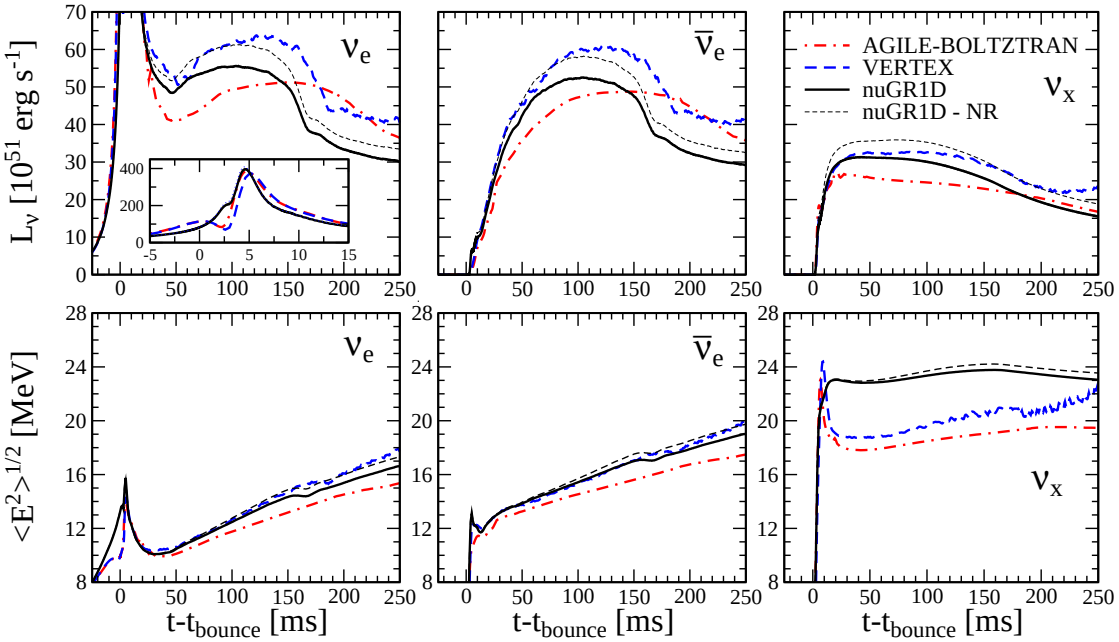


Figure 5.4: Comparison of postbounce neutrino luminosities and root mean squared energies from the full Boltzmann neutrino transport simulations of Liebendörfer et al. (2005) and `nuGR1D`. Shown in the upper panels, from left to right, are the $\nu_e$, $\bar{\nu}_e$, and $\nu_x$ neutrino luminosities. Shown in the bottom panels, from left to right, are the root mean squared $\nu_e$, $\bar{\nu}_e$, and $\nu_x$ neutrino energies. Shown as an inset in the upper left panel is the neutronization burst. All neutrino signals are extracted at 500 km. The thin dashed lines are the luminosities and root mean squared energies predicted with the flat-space neutrino transport, but general-relativistic hydrodynamics. We note that the root mean squared energy definition of Liebendörfer et al. (2005) is different from that of Abdikamalov et al. (2012).

the LS220 and the HShen equation of state for a total of 46 simulations. All of these simulations fail to explode within 450 ms of bounce, as expected for 1D simulations. In Figure 5.5 we analyse the progenitor dependence of the $\bar{\nu}_e$ luminosity. Here we choose the $\bar{\nu}_e$ luminosity as it is the primary observable in water-Cherenkov detectors such as the currently-operational Super-Kamiokande and IceCube and a proposed next-generation megaton-scale detector, Hyper-Kamiokande (Abe et al. 2011). In the left panels are the neutrino luminosity curves of models simulated with the LS220 EOS, the right panels are luminosity curves from the simulations done using the HShen EOS. The top panels are the emitted $\bar{\nu}_e$ luminosities, the middle are the cumulative emitted $\bar{\nu}_e$ energies. Models with high values of $\xi_{2.5}$ have much higher accretion rates during the postbounce phase and therefore have higher neutrino luminosities. The drop in accretion luminosity due to the accretion of the silicon-oxygen shell interface is notable in almost every model. We note that if the shock wave is reenergized, the accretion will cease and the accretion luminosity will drop accordingly.

In the bottom two panels we plot the cumulative emitted $\bar{\nu}_e$ energy at four different postbounce times and the two EOS versus the bounce compactness, Equation 4.1, with the standard $M_{\rm bary} = 2.5$

and also with $M_{\rm bary} = 1.7$. We choose the latter because at these earlier postbounce times the accreted baryonic mass is closer to $1.7\,M_\odot$ than $2.5\,M_\odot$. $\xi_{1.7}$ does a better job at parameterizing the progenitor models, this is evident in the smoothness of the cumulative emitted energy as a function of $\xi_{1.7}$ for the low $\xi_{1.7}$ progenitors, whereas there is more scatter when plotted as a function of $\xi_{2.5}$. $\xi_{2.5}$ is more relevant for black hole formation as investigated in Chapter 4.

An accurate measure of the early time cumulative emitted $\bar{\nu}_e$ energy in a galactic or near galactic supernova can potentially be used to discern details of the progenitor core structure. For the electron antineutrino capture rate on protons in water-Cherenkov detectors we restate the estimate in Ott et al. (2012) based on Horiuchi et al. (2009), Vogel and Beacom (1999),

$$R_{\bar{\nu}_e}^{\rm SK/HK} \sim \frac{L_{\bar{\nu}_e}}{4\pi r^2}\frac{\sigma_0(1+3g_A^2)}{4m_e^2c^4}\frac{\langle E_{\bar{\nu}_e}^2\rangle}{\langle E_{\bar{\nu}_e}\rangle}\frac{M_{\rm SK/HK}X_{\rm p}}{m_{\rm p}}\ , \tag{5.70}$$

where $\sigma_0 = 1.76\times10^{-44}{\rm cm}^2$ is the reference weak-interaction cross section, $g_A = -1.254$ is the axial coupling constant, $M_{\rm SK} = 22.4\,{\rm kT}$, $M_{\rm HK} = 740\,{\rm kT}$ is the fiducial water mass of Super-Kamiokande and Hyper-Kamiokande, respectively, $X_{\rm p}$ is the number fraction of protons (for $H_2O$, $X_{\rm p} = 2/18$), $m_{\rm p}$ is the proton mass, and $\langle E^2\rangle/\langle E\rangle$ is the energy-averaged spectral factor. We estimate $T_{\bar{\nu}_e} \sim 4\,{\rm MeV}$ and zero chemical potential, giving $\langle E^2\rangle/\langle E\rangle \sim 16.4\,{\rm MeV}$. With these numbers, for Super-Kamiokande, $R_{\bar{\nu}_e}^{\rm SK} \sim 12000\ {\rm s}^{-1}L_{\bar{\nu}_e,53}/r_{10\,{\rm kpc}}^2$ and for Hyper-Kamiokande, $R_{\bar{\nu}_e}^{\rm HK} \sim 400000\ {\rm s}^{-1}L_{\bar{\nu}_e,53}/r_{10\,{\rm kpc}}^2$, where $L_{\bar{\nu}_e,53}$ is the electron anti-neutrino luminosity in units of $10^{53}{\rm erg\ s}^{-1}$ and $r_{10\,{\rm kpc}}$ is the distance in kpc.

For a fiducial distance of 10 kpc, 20 B of cumulative $\bar{\nu}_e$ energy could be inferred to $\lesssim$1 B in Super-Kamiokande. Taking into account the difference in predicted cumulative emitted $\bar{\nu}_e$ energy due to the nuclear equation of state, if 20 B of energy was inferred within 300 ms of bounce, this would signify a value of $1.4 < \xi_{1.7} < 1.6$. Hyper-Kamiokande would be able to increase the signal-to-noise ratio by a factor of 6, allowing for more precise measurements of the cumulative emitted energy.

### 5.4.2 Progenitor Dependence of Collapse Trajectory

One can ask if the collapse trajectories of progenitors with different bounce compactnesses also have systematic trends. This has been investigated to a certain extent (Dimmelmeier et al. 2008, Liebendörfer 2005), but never systematically with many progenitors. Quantifying such trends and the impact on the subsequent postbounce evolution can help determine the validity and range of the deleptonization scheme presented in Liebendörfer (2005) and increase our understanding of the postbounce initial conditions. For example, smaller inner core masses are detrimental to the core-collapse supernova mechanism. There are two reasons for this. First, the energy departed to the outgoing shock wave is directly proportional to the kinetic energy of the core, smaller cores lead to smaller total outgoing energy in the shock. Second, for progenitors with small inner cores,

more material must be shocked before a successful explosion when compared to a progenitor with a larger inner core. A priori, one would expect that progenitors with a high bounce compactness will deleptonize more during collapse. This is because tthe higher entropies will increase the amount of free protons, the dominant production channel for neutrinos during collapse. In turn, this will reduce the electron fraction and therefore the inner core mass. This systematic dependence of the inner core mass may make it even harder for high bounce compactness models to explode, in addition to the reasons laid out in Section 4.1.3.5. The question that remains to be answered is how much dependence is there and can it affect the postbounce dynamics.

With the caveat that the $Y_e(\rho)$ collapse trajectories currently predicted by `nuGR1D` suffer from the neglect of several key physical processes, we can investigate if/what the dependence of the collapse trajectory is on the progenitor. In Figure 5.6 we plot the $Y_e(\rho)$ trajectory for 23 progenitor models varying in bounce compactness from 0.025 to 0.60. Progenitors with high bounce compactness begin to core collapse at lower central densities, higher central temperatures, and because the electron chemical potential is smaller at lower densities, a higher ratio of electrons to nucleons. We do indeed see enhanced deleptonization from the high bounce compactness models throughout the collapse phase. Following from the reduced $Y_e$ is a reduction in the inner core mass. The later is shown in the inset of Figure 5.6 for each of the 23 models. We define the inner core mass to be the mass enclosed inside the shock at shock formation, which is when the entropy of the core first reaches $s = 3\,k_B$/baryon. However, this trend first must be reproduced after including both full velocity dependence and inelastic neutrino-electron scattering. At the very least, when the velocities and small and inelastic scattering is not yet important ($\rho \lesssim 10^{11}\,\mathrm{g\,cm^{-3}}$), we can assume the results are robust, in this regime we see a significant progenitor dependence.

## 5.5 Future Directions for `nuGR1D`

In the immediate future, the general-relativistic transport in `nuGR1D` will be completed by finishing the implementation of velocity terms. This, along with including inelastic neutrino-electron scattering in `NuLib`, will allow us to make concret statements on the progenitor dependence of neutrino observables.

Progressing forward, more detailed neutrino interactions will be implemented in `NuLib` that will refine our predictions and elevate our code to state-of-the-art status. At this point we will release `nuGR1D` as a major update to the current open-source version of `GR1D`.

Meanwhile, we will begin to apply the transport scheme developed here to mutli-dimensional simulations of stellar collapse. Without making simplifying assumptions, this will dramatically increase the computational time. For each species, there are $4\times N_g$ variables that need to be evolved. For this first-generation energy-dependent three-dimensional neutrino transfer code it is likely we

will neglect the velocity dependence, use a reduced set of neutrino interactions and employ a parameterized deleptonization scheme during collapse. To acheive this, `nuGR1D` must be generalized to multiple dimensions and optimized to reduce computational time.

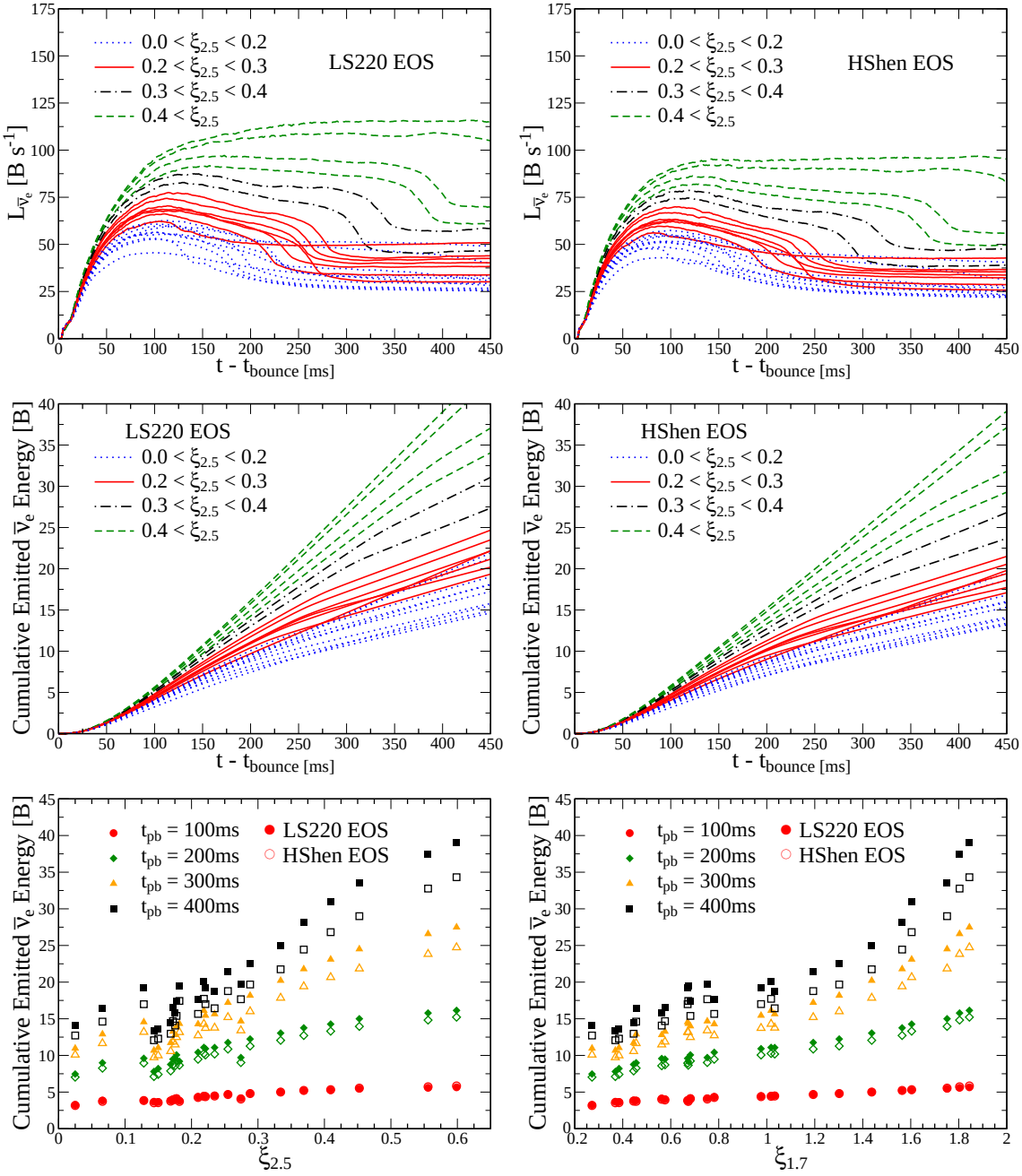


Figure 5.5: Progenitor dependence of $\bar{\nu}_e$ luminosity for two EOS. In the top two panels are the emitted neutrino luminosities for 23 models from Woosley and Heger (2007). The simulations in the left panel use the LS220 EOS while the simulations in the right panel use the HShen EOS. We group the curves by their $\xi_{2.5}$ value. The $\bar{\nu}_e$ luminosity scales with $\xi_{2.5}$. In the middle two panels we show the cumulative emitted $\bar{\nu}_e$ energy for the same set of models and EOS. The bottom two panels show how the cumulative emitted energy at various postbounce times and EOS vary with $\xi_{2.5}$ and $\xi_{1.7}$. Water-Cherenkov detectors can make direct measurements of the cumulative emitted $\bar{\nu}_e$ luminosity, and therefore can provide a quantitative measure of the internal structure that does not strongly depend on the EOS.

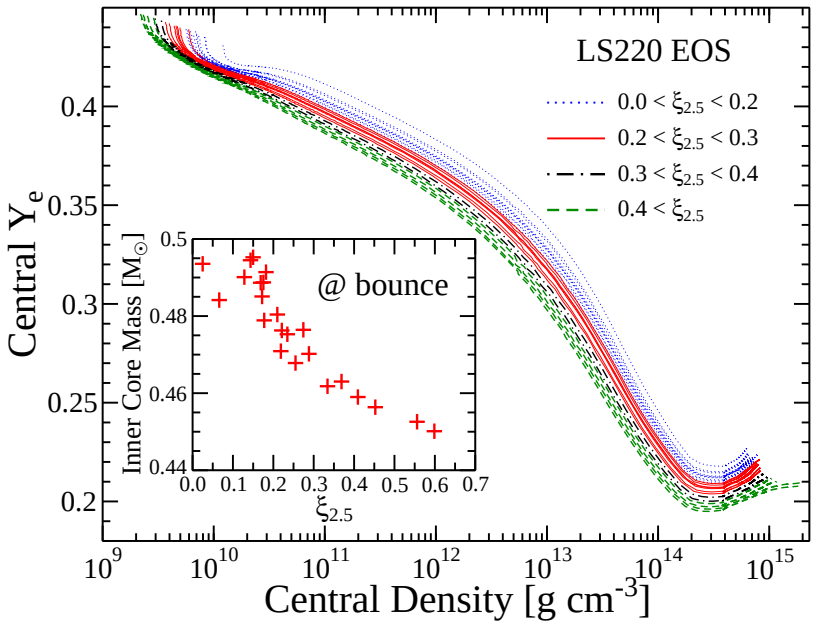


Figure 5.6: Progenitor dependence of collapse trajectories for 23 models from Woosley and Heger (2007) using the LS220 EOS. This $Y_e(\rho)$ curves suffer from the neglect of inelastic neutrino-electron scattering and velocity dependence, however the systematic trend of increased deleptonization with bounce compactness is significant nonetheless. Shown in the inset are the inner core masses for each of the 23 models. Progenitors with higher bounce compactnesses have lower $Y_e$ cores and therefore smaller inner core masses at bounce.

# Appendix A

# General-Relativistic Hydrodynamics Evolution Equations[1]

In this appendix we derive the evolution equations for the conserved variables $D, DY_e, S^r, S_\phi$ and $\tau$ used in `GR1D` and presented in Sections 3.3 and 3.4. `GR1D` uses the spherically symmetric metric $g_{\mu\nu} = \mathrm{diag}(-\alpha^2, X^2, r^2, r^2 \sin^2\theta)$ with $\alpha = \exp\left(\Phi(r,t)\right)$ with $\Phi(r,t)$ defined through Equation 3.5, $X = (1 - \frac{2m(r,t)}{r})^{-1/2}$ where $m(r,t)$ is the enclosed gravitational mass at coordinate radius $r$. We assume the matter to be a perfect fluid described by a mass current density of $J^\mu = \rho u^\mu$ and a stress-energy tensor, $T^{\mu\nu} = \rho h u^\mu u^\nu + g^{\mu\nu} P$ where $\rho$ is the rest mass density, $P$ is the fluid pressure, $h = 1 + \epsilon + P/\rho$ is the specific enthalpy with $\epsilon$ the specific internal energy; $u^\mu = (W/\alpha, Wv/X, 0, 0)$ is the fluid 4-velocity (without taking into account rotation) with $W = 1/\sqrt{1-v^2}$ is the Lorentz factor and $v$ is the physical radial velocity.

While evaluating the covariant derivative of the stress-energy tensor and matter current density, we make use of the following formula,

$$\nabla_\mu J^\mu = \frac{1}{\sqrt{-g}} \left(\sqrt{-g} J^\mu\right)_{,\mu} \tag{A.1}$$

and

$$\nabla_\mu T^{\mu\nu} = \frac{1}{\sqrt{-g}} \left(\sqrt{-g} T^{\mu\nu}\right)_{,\mu} + \Gamma^\nu_{\alpha\mu} T^{\mu\alpha}\,, \tag{A.2}$$

where $\sqrt{-g} = \alpha X r^2$ is the determinant of the metric and $\Gamma^\nu{}_{\alpha\mu}$ are Christoffel symbols and are defined through derivatives of the metric,

$$\Gamma^\nu{}_{\alpha\mu} = \frac{1}{2} g^{\nu\beta} (g_{\mu\beta,\alpha} + g_{\alpha\beta,\mu} - g_{\alpha\mu,\beta})\,. \tag{A.3}$$

[1] This appendix is reproduced from Appendix A of the article *A New Open-Source Code for Spherically-Symmetric Stellar Collapse to Neutron Stars and Black Holes*. O'Connor, E. & Ott, C.D., Classical and Quantum Gravity **27** 114103 (2010). Special Issue of invited papers from MICRA2009 held at the Niels Bohr International Academy, Copenhagen, August 24–28, 2009. Reproduced with permission from IOP Publishing.

For our metric, all nonzero Christoffels are given in Table A.1, $\Gamma^{\nu}{}_{\alpha\mu}$ is symmetric in the last two indices, duplicates are omitted.

| | | | |
|---|---|---|---|
| $\Gamma^{t}{}_{tt} =$ | $\partial_t \phi(r,t)$ | $\Gamma^{r}{}_{\theta\theta} =$ | $-\frac{r}{X^2}$ |
| $\Gamma^{t}{}_{tr} =$ | $\partial_r \phi(r,t)$ | $\Gamma^{r}{}_{\phi\phi} =$ | $-\frac{r \sin^2\theta}{X^2}$ |
| $\Gamma^{t}{}_{rr} =$ | $\alpha^{-2}\frac{X^4}{r}\partial_t m(r,t)$ | $\Gamma^{\theta}{}_{r\theta} =$ | $\frac{1}{r}$ |
| $\Gamma^{r}{}_{tt} =$ | $\frac{\alpha^2}{X^2}\partial_r \phi(r,t)$ | $\Gamma^{\theta}{}_{\phi\phi} =$ | $-\sin\theta\cos\theta$ |
| $\Gamma^{r}{}_{tr} =$ | $\frac{X^2}{r}\partial_t m(r,t)$ | $\Gamma^{\phi}{}_{r\phi} =$ | $\frac{1}{r}$ |
| $\Gamma^{r}{}_{rr} =$ | $\frac{X^2}{r}(\partial_r m(r,t) - \frac{m(r,t)}{r})$ | $\Gamma^{\phi}{}_{\theta\phi} =$ | $\frac{\cos\theta}{\sin\theta}$ |

Table A.1: Connection coefficients.

It is useful to note the following derivatives needed in the derivation of the evolution equations:

$$\partial_r \Phi(r,t) = X^2\left[\frac{m}{r^2} + 4\pi r(P + \rho h W^2 v^2)\right], \tag{A.4}$$

$$\partial_r X = X^3\left[\frac{\partial_r m}{r} - \frac{m}{r^2}\right], \tag{A.5}$$

$$\partial_t X = X^3\frac{\partial_t m}{r}, \tag{A.6}$$

$$\partial_r m = 4\pi r^2(\rho h W^2 - P), \tag{A.7}$$

$$\partial_t m = -4\pi r^2\frac{\alpha\rho h W^2 v}{X}. \tag{A.8}$$

## A.1 Source Terms

The evolution equations follow from $\nabla_\mu J^\mu = 0$ and $\nabla_\mu T^{\mu\nu} = 0$. Since we treat neutrinos through a leakage scheme, we add in neutrino source terms explicitly to the RHS of these equations. The neutrino physics of `GR1D` occurs in the rest frame of the fluid; in this frame the energy and lepton rates are calculated with the neutrino leakage scheme, $Q^0_E$ and $R^0_{Y_e}$ are given in Equation 3.34. Momentum exchange in the fluid rest frame is taken into account approximately via $Q^0_M = -\frac{\partial P_\nu}{\partial r}$ where the gradient is evaluated numerically in the coordinate frame. This introduces a slight inconsistency, since in a full radiation-transport treatment the momentum transfer is computed fully locally via the second angular moment of the local neutrino radiation intensity (Müller et al. 2010).

By writing the evolution equations in the comoving orthonormal frame of the fluid (fluid rest frame, [FRF]) with 4-velocity $\vec{u} = (1,0,0,0)_{\rm FRF}$ and unit radial normal $\vec{n} = (0,1,0,0)_{\rm FRF}$ and expressing them as frame-independent tensor equations we can derive expressions for the evolution equations in any frame. For the lepton fraction,

$$\begin{aligned}
\partial_t(\rho Y_e) &= R^0_{Y_e}\,, \\
\partial_t(\rho Y_e u^t) &= R^0_{Y_e}\,, \\
\partial_\mu(\rho Y_e u^\mu) &= R^0_{Y_e}\,, \\
\nabla_\mu(\rho Y_e u^\mu) &= R^0_{Y_e}\,.
\end{aligned} \tag{A.9}$$

We write the energy and momentum source terms in the fluid rest frame as a 4-vector, $\vec{q} = (Q^0_E, Q^0_M, 0, 0)_{\rm FRF}$ or in frame-independent notation, $Q^0_E\vec{u} + Q^0_M\vec{n}$. In the fluid rest frame, the evolution equations for energy and momentum become,

$$\partial_t T^{tt} = Q^0_E = q^t, \tag{A.10}$$

and

$$\partial_t T^{tr} = Q^0_M = q^r, \tag{A.11}$$

or in frame-independent tensor notation,

$$\nabla_\mu T^{\mu\nu} = q^\nu\,. \tag{A.12}$$

For the evolution equations, we must transform $\vec{q}$ from the fluid rest frame, to the coordinate frame (CF) of `GR1D`. In a general frame $\vec{n}$ is a vector that is both *i)* normalized and *ii)* orthogonal to $\vec{u}$. In the CF of `GR1D`, where $\vec{u}$ is the 4-velocity, these two conditions (along with the assumption of spherical symmetry) on $\vec{n}$ give $\vec{n} = (Wv/\alpha, W/X, 0, 0)_{\rm CF}$. $\vec{q}$ in the CF then becomes $\vec{q} = \left(\frac{W}{\alpha}(Q^0_E + vQ^0_M), \frac{W}{X}(vQ^0_E + Q^0_M), 0, 0\right)_{\rm CF}$. This can also be derived via a Lorentz transformation. In principle, nonzero rotation will give rise to source terms for the $\phi$-momentum evolution through $q^\phi$ and modify the radial source terms $q^r$. In consideration of the significant approximations already present in both our neutrino leakage scheme and in our treatment of rotation, we neglect the influence of rotation on the source terms. This is justified as long as $v_\varphi \ll c$.

## A.2 GR1D Evolution Equations

In the coordinate frame of GR1D where $u^\mu = (W/\alpha, Wv/X, 0, 0)$, the continuity equation, $\nabla_\mu J^\mu = 0$ gives the evolution of the rest mass density,

$$\begin{aligned} \nabla_\mu(\rho u^\mu) &= 0\,, \\ \frac{1}{\sqrt{-g}}\left[\partial_t\left(\sqrt{-g}\frac{\rho W}{\alpha}\right) + \partial_r\left(\sqrt{-g}\frac{\rho W v}{X}\right)\right] &= 0\,, \\ \partial_t(D) + \frac{1}{r^2}\partial_r\left(\frac{\alpha r^2}{X} D v\right) &= 0\,. \end{aligned} \tag{A.13}$$

The evolution of the electron fraction $Y_e$ follows a similar derivation but contains a source term from the neutrino leakage scheme. In the coordinate frame of GR1D Equation A.9 becomes,

$$\begin{aligned} \nabla_\mu(\rho Y_e u^\mu) &= R^0_{Y_e}\,, \\ \frac{1}{\sqrt{-g}}\left[\partial_t\left(\sqrt{-g}\frac{\rho W Y_e}{\alpha}\right) + \partial_r\left(\sqrt{-g}\frac{\rho W Y_e v}{X}\right)\right] &= R^0_{Y_e}\,, \\ \frac{1}{\alpha X}\left[\partial_t\left(X\rho W Y_e\right) + \frac{1}{r^2}\partial_r\left(\frac{\alpha r^2}{X} X\rho W Y_e v\right)\right] &= R^0_{Y_e}\,, \\ \partial_t(DY_e) + \frac{1}{r^2}\partial_r\left(\frac{\alpha r^2}{X} D Y_e v\right) &= \alpha X R^0_{Y_e}\,. \end{aligned} \tag{A.14}$$

The momentum evolution equation for `GR1D` is obtained by evaluating Equation A.12 with $\nu = r$.

$$
\begin{aligned}
\nabla_\mu T^{\mu r} &= q^r\,, \\
\left(\sqrt{-g}\; T^{\mu r}\right)_{,\mu} &= \sqrt{-g}\; q^r - \sqrt{-g}\; \Gamma^r_{\nu\mu} T^{\mu\nu}\,, \\
\partial_t\left(\rho h W^2 v\right) + \frac{1}{r^2}\partial_r\left(\frac{\alpha r^2}{X}\left(\rho h W^2 v^2 + P\right)\right) &= \alpha X q^r - \alpha X\big(\Gamma^r_{\nu t} T^{t\nu} + \Gamma^r_{\nu r} T^{r\nu} \\
&\quad + \Gamma^r_{\nu\phi} T^{\phi\nu} + \Gamma^r_{\nu\theta} T^{\theta\nu}\big)\,, \\
\partial_t\left(S^r\right) + \frac{1}{r^2}\partial_r\left(\frac{\alpha r^2}{X}\left(S^r v + P\right)\right) &= \alpha X q^r - \alpha X\big(\Gamma^r_{tt} T^{tt} + \Gamma^r_{rt} T^{tr} \\
&\quad + \Gamma^r_{tr} T^{rt} + \Gamma^r_{rr} T^{rr} + \Gamma^r_{\phi\phi} T^{\phi\phi} + \Gamma^r_{\theta\theta} T^{\theta\theta}\big)\,, \\
\partial_t\left(S^r\right) + \frac{1}{r^2}\partial_r\left(\frac{\alpha r^2}{X}\left(S^r v + P\right)\right) &= -\alpha X\left[2\frac{X}{r}\frac{\rho h W^2 v}{\alpha X}\partial_t m\right. \\
&\quad + \frac{X^2}{r}\left(\partial_r m - \frac{m}{r}\right)\left(\frac{\rho h W^2 v^2 + P}{X^2}\right) \\
&\quad \left. - \frac{2P}{X^2 r} + \frac{\alpha^2}{X^2}\frac{\rho h W^2 - P}{\alpha^2}\partial_r\Phi\right] + \alpha X q^r\,, \\
\partial_t\left(S^r\right) + \frac{1}{r^2}\partial_r\left[\frac{\alpha r^2}{X}\left(S^r v + P\right)\right] &= \alpha X\left[\left(S^r v - \tau - D\right)\left(8\pi r P + \frac{m}{r^2}\right)\right. \\
&\quad \left. + \frac{P m}{r^2} + \frac{2P}{X^2 r}\right] + \alpha W\left(v Q^0_E + Q^0_M\right)\,. \qquad \text{(A.15)}
\end{aligned}
$$

where in the last step we have reorganized the source terms to the form of Romero et al. (1996) using the derivatives defined in Equations A.4–A.8. If nonzero, $u^\phi = W v_\varphi / r$ leads to an additional term $(\alpha\rho h W^2 v_\varphi^2 \sin(\theta)^2 / X r)$ arising through $\Gamma^r_{\phi\phi} T^{\phi\phi}$ on the RHS of Equation A.15, averaging this term over the spherical shell gives $2/3\ \alpha\rho h W^2 v_\varphi^2 / X r$. When rotation is included, the evolution equation for $S_\phi = \rho h W^2 v_\varphi r$ is,

$$
\begin{aligned}
\nabla_\mu T^\mu_\phi &= 0\,, \\
\left(\sqrt{-g}\; T^\mu_\phi\right)_{,\mu} &= \sqrt{-g}\; \Gamma^\nu_{\phi\mu} T^\mu_\nu\,, \\
\partial_t\left(\alpha X r^2 g_{\phi\phi} T^{t\phi}\right) + \partial_r\left(\alpha X r^2 g_{\phi\phi} T^{r\phi}\right) &= \sqrt{-g}\left(\Gamma^r_{\phi\phi} T^\phi_r + \Gamma^\phi_{\phi r} T^r_\phi\right)\,, \\
\partial_t(X\rho h W^2 v_\varphi r) + \frac{1}{r^2}\partial_r\left(\frac{\alpha r^2}{X}\rho h W^2 v_\varphi r v X\right) &= 0\,, \\
\partial_t(S_\phi) + \frac{1}{r^2}\partial_r\left(\frac{\alpha r^2}{X} S_\phi v\right) &= \frac{\rho h W^2 v_\varphi r}{X}\left(-\partial_t X - \frac{\alpha v}{X}\partial_r X\right)\,, \\
\partial_t(S_\phi) + \frac{1}{r^2}\partial_r\left(\frac{\alpha r^2}{X} S_\phi v\right) &= \alpha\rho h W^2 v_\varphi v X\left(4\pi r^2 P + \frac{m}{r}\right)\,. \qquad \text{(A.16)}
\end{aligned}
$$

The energy evolution equation for `GR1D` is derived by taking $\nu = t$ in Equation A.12,

$$\begin{aligned}
\nabla_\mu T^{\mu t} &= q^t\,, \\
\left(\sqrt{-g}\; T^{\mu t}\right)_{,\mu} &= \sqrt{-g}\; q^t - \sqrt{-g}\; \Gamma^t_{\nu\mu} T^{\mu\nu}\,, \\
\partial_t\left(\frac{X}{\alpha}(\rho h W^2 - P)\right) + \frac{1}{r^2}\partial_r\left(\frac{\alpha r^2}{X}\rho h W^2 v \frac{X}{\alpha}\right) &= \alpha X q^t - \alpha X\left(\Gamma^t_{t\mu} T^{\mu t} + \Gamma^t_{r\mu} T^{\mu r}\right)\,, \\
\frac{X}{\alpha}\left[\partial_t(\tau + D) + \frac{1}{r^2}\partial_r\left(\frac{\alpha r^2}{X} S^r\right)\right] &= \alpha X q^t - \alpha X\big(\Gamma^t_{tt} T^{tt} + 2\Gamma^t_{tr} T^{rt} \\
&\quad + \Gamma^t_{rr} T^{rr}\big) - (\rho h W^2 - P)\partial_t\left(\frac{X}{\alpha}\right) \\
&\quad - \frac{\alpha \rho h W^2 v}{X}\partial_r\left(\frac{X}{\alpha}\right)\,, \\
\partial_t(\tau + D) + \frac{1}{r^2}\partial_r\left(\frac{\alpha r^2}{X} S^r\right) &= \alpha^2 q^t\,, \\
\partial_t(\tau) + \frac{1}{r^2}\partial_r\left(\frac{\alpha r^2}{X}(S^r - Dv)\right) &= \alpha W(Q^0_E + v Q^0_M)\,. \qquad \text{(A.17)}
\end{aligned}$$

where in the last step we use the continuity equation Equation A.13 to subtract out the evolution of the rest mass density, obtaining the evolution equation for $\tau$. A nonzero $u^\phi$ does not contribute source terms to this evolution equation.

# Appendix B

# Neutrino Luminosities in GR1D's Leakage Scheme[1]

The luminosity computed from the neutrino leakage scheme is derived in the rest frame of the fluid. We require knowledge of the neutrino luminosity as measured by an observer at rest in the coordinate frame to determine *i)* the luminosity measured by an observer at rest at infinity and *ii)* the luminosity in the fluid rest frame at some other coordinate radius for our neutrino heating scheme. We derive these relationships by assuming the neutrinos are emitted radially in the fluid rest frame with energy $E^{\rm FRF}$.

In the fluid rest frame (FRF), the 4-momentum of the neutrino is $p^a = (E^{\rm FRF}, E^{\rm FRF}, 0, 0)_{\rm FRF}$. We use the orthonormal tetrad in Section A.1, in the fluid frame, $\vec{u} = \vec{e}_0 = (1,0,0,0)_{\rm FRF}$ and $\vec{n} = \vec{e}_1 = (0,1,0,0)_{\rm FRF}$, in the coordinate frame (CF), $u^\beta = e_0^\beta = (W/\alpha, Wv/X, 0, 0)_{\rm CF}$ and $n^\beta = e_1^\beta = (Wv/\alpha, W/X, 0, 0)_{\rm CF}$. In this we have neglected rotational effects which will be small for $v_\varphi \ll c$. Transforming $p^a$ to the coordinate basis of GR1D,

$$p^\beta = p^a e_a^\beta \quad = \quad E^{\rm FRF}\left(\frac{W}{\alpha}(1+v), \frac{W}{X}(1+v), 0, 0\right)_{\rm CF}.$$

An observer at rest in the coordinate frame ($U^\alpha = (1,0,0,0)_{\rm CF}$) then sees the neutrino with energy,

$$E^{\rm CF} = -\vec{p}\cdot\vec{U} = -g_{\alpha\beta}p^\beta U^\alpha = \alpha^2 E^{\rm FRF}\frac{W}{\alpha}(1+v) = \alpha W(1+v)E^{\rm FRF}\,. \tag{B.1}$$

Noting that (see Misner et al. 1973, Equation 25.25), for massless particles emitted from rest at $r$ and observed by a observer at rest at $r'$, $\lambda(r)|g_{00}(r)|^{-1/2} = \lambda(r')|g_{00}(r')|^{-1/2}$ implies,

$$\frac{E^{\rm CF}(r')}{E^{\rm CF}(r)} = \frac{\lambda_r}{\lambda_{r'}} = \frac{|g_{00}(r)|^{1/2}}{|g_{00}(r')|^{1/2}} = \frac{\alpha(r)}{\alpha(r')}\,, \tag{B.2}$$

[1] This appendix is reproduced from Appendix A of the article *A New Open-Source Code for Spherically-Symmetric Stellar Collapse to Neutron Stars and Black Holes*. O'Connor, E. & Ott, C.D., Classical and Quantum Gravity **27** 114103 (2010). Special Issue of invited papers from MICRA2009 held at the Niels Bohr International Academy, Copenhagen, August 24–28, 2009. Reproduced with permission from IOP Publishing.

this is the redshift formula for particles leaving a gravitational well.

# Appendix C

# NuLib: Neutrino Interaction Library for Neutrino Transport Calculations[1]

The ultimate goal of NuLib is to provide a full set of standard, complete, and computationally efficient neutrino matter interaction routines that can be readily incorporated in radiation-hydrodynamics codes for physics benchmarking via on-the-fly routines or via tabular interpolation. The first version of NuLib is available as a GitHub repository at www.nulib.org.

## C.1 Definitions:

### C.1.1 Constants and Units

In NuLib, all temperatures $T$, chemical potentials $\mu_i$, and energies are measured in MeV, densities in g/cm$^3$. Emissivities will be given in units corresponding to specific intensity, erg/s/cm$^3$/sterad/MeV. Absorption and scattering opacities have units of inverse mean free path, cm$^{-1}$.

Throughout NuLib, we will use the following values for common constants:

| | | | |
|---|---|---|---|
| Reference weak interaction cross section | $\sigma_0$ | = | $1.761 \times 10^{-44}\,\mathrm{cm}^2$ |
| Fermi's Weak coupling constant | $G_{\mathrm{Fermi}}$ | = | $1.16637 \times 10^{-11}\,\mathrm{MeV}^{-2}$ |
| Axial coupling constant | $g_{\mathrm{A}}$ | = | 1.254 |
| Neutron-proton mass difference | $\Delta_{np} = m_n - m_p$ | = | 1.293332 MeV |
| Electron Mass | $m_e$ | = | 0.510998910 MeV |
| Neutron Mass | $m_n$ | = | 939.565346 MeV |
| Proton Mass | $m_p$ | = | 938.272013 MeV |
| Weinberg angle | $\sin^2\theta_W$ | = | 0.23 |
| Fine Structure Constant | $\alpha_{FS}$ | = | $7.2973525376 \times 10^{-3}$ |

[1] This appendix contains unpublished work in progress.

### C.1.2 Black Body Function for Neutrinos

We derive the black body function for neutrinos, by considering that the total energy density $\mathcal{E} = E/V$ of a quantum gas is given by

$$\mathcal{E} = \int \epsilon_\nu f_\nu \frac{g d^3 p_\nu}{(2\pi\hbar)^3} \ , \tag{C.1}$$

where $f_\nu$ is the distribution function and $g = 1$ for massless neutrinos. In equilibrium, $f_\nu = f_\nu^{\rm eq}$,

$$f_\nu^{\rm eq} = \frac{1}{\exp\left[(\epsilon_\nu - \mu_\nu)/T\right] + 1} \ . \tag{C.2}$$

Furthermore, in equilibrium, $\mu_{\nu_e} = \mu_e - \hat{\mu}$ with $\hat{\mu} = \mu_n - \mu_p$. Also, $\mu_{\bar{\nu}_e} = -\mu_{\nu_e}$, and $\mu_{\nu_x} = 0$.

The black body function $B_\nu$ describes the specific radiation intensity in equilibrium. In order to obtain it in the desired specific intensity units, we first use $\epsilon_\nu = p_\nu c$ to rewrite Equation C.1 to

$$\mathcal{E} = 4\pi \int f_\nu^{\rm eq} \frac{\epsilon_\nu^3}{(2\pi\hbar c)^3} d\epsilon_\nu \ , \tag{C.3}$$

then differentiate $(d/d\epsilon_\nu\, \mathcal{E})$ to get the spectral radiation energy density in equilibrium. To obtain the black body function in the standard units above we multiply by $c/(4\pi)$. We obtain

$$B_\nu = \frac{c\epsilon_\nu^3}{(2\pi\hbar c)^3} f_\nu^{\rm eq} \ . \tag{C.4}$$

### C.1.3 Emission and Absorption: Kirchhoff's Law and Stimulated Absorption

The interaction term on the RHS of the Boltzmann equation (which is usually written in terms of the distribution function $f_\nu$) that is due to emission and absorption may be written as

$$\left[\frac{df_\nu}{dt}\right]_{\rm coll}^{\rm em-abs} = \epsilon_\nu \left[\eta_\nu (1 - f_\nu) - \kappa_{\rm a} f_\nu\right] \ , \tag{C.5}$$

where $\eta_\nu$ is the emissivity. The term $(1 - f_\nu)$ accounts for final state fermion phase space blocking and $\kappa_{\rm a}$ is the inverse mean-free-path for absorption. In equilibrium,

$$\left[\frac{df_\nu^{\rm eq}}{dt}\right]_{\rm coll} = 0 = \eta_\nu (1 - f_\nu^{\rm eq}) - \kappa_{\rm a} f_\nu^{\rm eq} \ . \tag{C.6}$$

Hence,

$$\eta_\nu = \kappa_{\rm a} \frac{f_\nu^{\rm eq}}{(1 - f_\nu^{\rm eq})} \ . \tag{C.7}$$

Inserting this into Equation C.5 yields

$$\begin{aligned}\left[\frac{df_\nu}{dt}\right]_{\rm coll} &= \epsilon_\nu\left[\kappa_{\rm a}\frac{f_\nu^{\rm eq}}{(1-f_\nu^{\rm eq})}(1-f_\nu)-\kappa_{\rm a}f_\nu\right]\\ &= \epsilon_\nu\left[\frac{\kappa_{\rm a}}{(1-f_\nu^{\rm eq})}(f_\nu^{\rm eq}-f_\nu)\right]\\ &= \epsilon_\nu\left[\kappa_{\rm a}^*(f_\nu^{\rm eq}-f_\nu)\right]\ ,\end{aligned} \tag{C.8}$$

where we have followed Burrows et al. (2006b) and absorbed the $1/(1-f_\nu^{\rm eq})$ term into $\kappa_{\rm a}^*$, the absorptive opacity corrected for *stimulated absorption* of neutrinos (the analog of stimulated emission of photons). For practical purposes it is useful to rewrite these relationships in terms of the specific radiation intensity $I_\nu = c\epsilon_\nu^3/(2\pi\hbar c)^3 f_\nu$. Introducing the neutrino black body function derived in the previous Section C.1.2, we arrive at

$$\frac{c}{(2\pi\hbar c)^3}\epsilon_\nu^2\left[\frac{df_\nu}{dt}\right]_{\rm coll} = \kappa_{\rm a}^*(B_\nu - I_\nu)\ , \tag{C.9}$$

where the left-hand side of this equation relates back to the evolution equations for the radiation moments Equation 5.4. Also from this we identify Kirchhoff's law,

$$\eta_\nu = \kappa_{\rm a}^* B_\nu\ . \tag{C.10}$$

Using Kirchhoff's law, we can compute the emissivity of any process as soon as we have derived its absorptive opacity $\kappa_{\rm a}^*$ (corrected for stimulated absorption). Similarly, for neutrino interactions derived directly from emissivities, such as electron-positron annihilation, we can use Kirchhoff's law to derive the corresponding absorptive opacity. We stress that this is needed to maintain balance in the optically thick regions where the evolved neutrino field is very similar to the black body, ideally one properly treats these emission processes (Shibata et al. 2011, Swesty and Myra 2009), we leave this to future versions of `NuLib` when we begin to take energy bin and species coupling into account.

### C.1.4 From Cross Section to Opacity

Cross sections $\sigma$ are given in units of $\rm cm^2$ per particle. In transport calculations, the inverse mean free path (the opacity; in units of $\rm cm^{-1}$) is needed and is typically of the form

$$\kappa_a = \frac{1}{\lambda} = \sum_i \sigma_i X_i\,\rho/m_{\rm ref}\ , \tag{C.11}$$

where $X_i$ is the mass fraction of the nucleus or nucleon partaking in the interaction, $\rho$ is the baryonic density in $\rm g\,cm^{-3}$ and $m_{\rm ref}$ is the reference nucleon mass. Note that $N = X_i\rho/m_{\rm ref}$ is the number density of absorbers. The sum over $i$ denotes all absorption processes. The value of the

reference nucleon mass must be consistent with the nuclear EOS. Depending on the particular process considered, correction terms for stimulated absorption, nucleon degeneracy etc. must be applied. For practical reasons in `NuLib`, the stimulated absorption term is handled during the evaluation of the cross section (see Section C.2.2), while the final state nucleon blocking is calculated when going from cross section to opacity. From Bruenn (1985), the final state neutron blocking term, relevant for $\bar{\nu}_e$ capture on free protons is,

$$b_{\rm p} = \frac{n_n/n_p - 1}{\exp\left(-\mu_{n,0} + \mu_{p,0}\right)/T - 1}\,, \tag{C.12}$$

where $n_N$ is the respective nucleon number density, and where we explicitly note that the chemical potentials are the nonrelativistic ones, i.e., they *do not* contain the nucleon rest masses, and therefore their difference *does not* contain the rest mass difference. If final state neutron nucleon blocking is unimportant, $b_{\rm p} \sim 1$. Similarly, the proton final state blocking term, relevant for $\nu_e$ capture on free neutrons is,

$$b_{\rm n} = \frac{n_p/n_n - 1}{\exp\left(-\mu_{n,0} + \mu_{p,0}\right)/T - 1}\,. \tag{C.13}$$

With this notation, for free nucleon absorption cross sections, Equation C.11 becomes,

$$\kappa_a = \frac{1}{\lambda} = \sum_i \sigma_i X_i b_i\, \rho/m_{\rm ref}\,. \tag{C.14}$$

### C.1.5 Isoenergetic Scattering Cross Section

The transport cross section for a scattering process $i$ is defined as

$$\sigma_i^{\rm tr} = \int \frac{d\sigma_i}{d\Omega}(1-\mu)d\Omega = \sigma_i(1-g_i^1)\,. \tag{C.15}$$

The transport cross section is also known as the momentum transfer cross section as it sets the rate of momentum transfer from the radiation field to the matter, but does not contribute to the energy density. $g_i^1$ in Equation C.15 is the first angular moment of the scattering cross section $\sigma_i$. If $g_i^1 > 0$, then a greater fraction of the neutrinos is forward scattered, hence the effective transport cross section is smaller than the scattering cross section, less momentum is transferred when compared to isotropic scattering. If $g_i^1 = 0$ the scattering is completely isotropic and $\sigma_i^{\rm tr} = \sigma_i$, and if $g_i^1 < 0$ a greater fraction of the neutrinos are back scattered, increasing the effective transport cross section and the momentum transfer to the matter.

As for the absorption opacity, the scattering opacity is defined as,

$$\kappa_s = \frac{1}{\lambda} = \sum_i \sigma_i^{\rm tr} X_i \rho/m_{\rm ref}\,. \tag{C.16}$$

where $X_i$ is the number fraction of target particles the a given scattering process with a transport cross section of $\sigma_i^{\rm tr}$ and the sum over $i$ denotes all scattering processes.

## C.2 Neutrino Interactions in NuLib v1.0

### C.2.1 Scattering

NuLib v1.0 includes only elastic scattering of neutrinos on the constituents of nuclear matter: neutron, protons, heavy nuclei, alpha particles, and electrons. We take the scattering cross sections from Bruenn (1985), Burrows et al. (2006b), and Horowitz (2002).

#### C.2.1.1 $\nu$–Nucleon Elastic Scattering

The differential cross section for neutrino-nucleon elastic scattering without corrections is given by Horowitz (2002),

$$\frac{d\sigma^{\rm scat}_{{\rm un},\nu{\rm N}}}{d\Omega} = \frac{G_F^2\epsilon_\nu^2(\hbar c)^2}{4\pi^2}\left[C^2_{\rm V,N}(1+\mu)+C^2_{\rm A,N}(3-\mu)\right] , \tag{C.17}$$

where $N$ denotes either neutron or proton and $C^2_{\rm V,n}$ and $C^2_{\rm V,p}$ are the neutron and proton vector coupling constants equal to $-1/2$, and $1/2-2\sin^2\theta_W$, respectively. $C^2_{\rm A,n}$ and $C^2_{\rm A,p}$ are the neutron and proton axial coupling constants equal to $-g_a/2$, and $g_a/2$, respectively. We note these values are for scattering processes only, as we shall see in Section C.2.2, these coefficients are different when considering the weak magnetism corrections for absorption processes. One can trivially calculate the total cross section, or the total transport cross section by integration of Equation C.17,

$$\sigma^{\rm scat}_{{\rm un},\nu{\rm N}}(\epsilon_\nu) = \int_\Omega \frac{d\sigma^{\rm scat}_{{\rm un},\nu{\rm N}}}{d\Omega}d\Omega = \frac{G_F^2\epsilon_\nu^2(\hbar c)^2}{\pi}\left[C^2_{\rm V,N}+3C^2_{\rm A,N}\right] , \tag{C.18}$$

and

$$\sigma^{\rm tr,scat}_{{\rm un},\nu{\rm N}}(\epsilon_\nu) = \int_\Omega \frac{d\sigma^{\rm scat}_{{\rm un},\nu{\rm N}}}{d\Omega}(1-\mu)d\Omega = \frac{2G_F^2\epsilon_\nu^2(\hbar c)^2}{3\pi}\left[C^2_{\rm V,N}+5C^2_{\rm A,N}\right] . \tag{C.19}$$

For the cross sections used in NuLib, we include the phase space, recoil, and weak magnetism corrections of Horowitz (2002). These corrections significantly complicate the expressions but, especially in the case of antineutrinos, can be as large as 10–15%. It is important to include the exact expressions as the first order corrections strongly deviate from the both the uncorrected and exact expressions at high, but attainable, energies. For completeness, we present here the full differential, total and transport cross sections for neutrino-nucleon scattering from Horowitz (2002). These corrected cross sections will also be used when calculating the absorption cross section of neutrinos on free neutrons

and protons.

$$\frac{d\sigma_{\nu\mathrm{N}}^{\mathrm{scat}}(\epsilon_\nu)}{d\Omega} = \frac{G_F^2\epsilon_\nu^2(\hbar c)^2}{4\pi^2}\eta^2\Big\{C_{\mathrm{V,N}}^2[1+\eta^2-\eta(1-x)]$$
$$+C_{\mathrm{A,N}}^2[1+\eta^2+\eta(1-x)] \quad \text{(C.20)}$$
$$\pm 2C_{\mathrm{A,N}}(C_{\mathrm{V,N}}+F_{2,\mathrm{N}})(1-\eta^2) \quad \text{(C.21)}$$
$$+\eta^2\frac{e^2}{2}(1-x)[F_{2,\mathrm{N}}^2(3-x)+4C_{\mathrm{V,N}}F_{2,\mathrm{N}}(1-x)]\Big\}, \quad \text{(C.22)}$$

where $\eta = 1/[1+e(1-x)]$, $e = \epsilon_\nu/m_N$, $x = \mu = \cos\theta$, and where $N$ denotes the nucleon involved in the scattering. Note that while we suppress the N index on $\eta$ and $e$, these depend on the nucleon via the nucleon mass. For the $\pm$, $+$ is used for neutrino scattering and $-$ for antineutrino scattering. $F_{2,\mathrm{N}}$ is 1.019 and -0.963 for elastic neutrino scattering on neutrons and protons, respectively. Following Horowitz (2002), we neglect the energy dependence of $F_2$ as the terms including $F_2$ are already $\mathcal{O}(e^2)$.

The corrected total cross section from Horowitz (2002) is,

$$\sigma_{\nu\mathrm{N}}^{\mathrm{scat}}(\epsilon_\nu) = \int_\Omega \frac{d\sigma_{\nu\mathrm{N}}^{\mathrm{scat}}(\epsilon_\nu)}{d\Omega}d\Omega = \sigma_{\mathrm{un},\nu\mathrm{N}}^{\mathrm{scat}}(\epsilon_\nu)R_{\mathrm{N}}(\epsilon_\nu)\,, \quad \text{(C.23)}$$

where $R_{\mathrm{N}}(\epsilon_\nu)$ represents the deviation from the uncorrected rate,

$$R_{\mathrm{N}}(\epsilon_\nu) = \Big\{C_{\mathrm{V,N}}^2\left(1+4e+\frac{16}{3}e^2\right)+3C_{\mathrm{A,N}}^2\left(1+\frac{4}{3}e\right)^2$$
$$\pm 4(C_{\mathrm{V,N}}+F_{2,\mathrm{N}})C_{\mathrm{A,N}}e\left(1+\frac{4}{3}e\right)+\frac{8}{3}C_{\mathrm{V,N}}F_{2,\mathrm{N}}e^2$$
$$+\frac{5}{3}e^2\left(1+\frac{2}{5}e\right)F_{2,\mathrm{N}}^2\Big\}\Big/[(C_{\mathrm{V,N}}^2+3C_{\mathrm{A,N}}^2)(1+2e)^3]\,. \quad \text{(C.24)}$$

Finally, the corrected transport cross section is similarly decomposed,

$$\sigma_{\nu\mathrm{N}}^{\mathrm{tr,scat}}(\epsilon_\nu) = \int_\Omega \frac{d\sigma_{\nu\mathrm{N}}^{\mathrm{scat}}(\epsilon_\nu)}{d\Omega}(1-\mu)d\Omega = \sigma_{\mathrm{un},\nu\mathrm{N}}^{\mathrm{tr,scat}}(\epsilon_\nu)R_{\mathrm{N}}^{\mathrm{tr}}(\epsilon_\nu)\,, \quad \text{(C.25)}$$

$$R_{\mathrm{N}}^{\mathrm{tr}}(\epsilon_\nu) = \Big\{C_{\mathrm{V,N}}^2\left[\frac{e-1}{2e^3}\ln(1+2e)+\frac{3+12e+9e^2-10e^3}{3e^2(1+2e)^3}\right]$$
$$+C_{\mathrm{A,N}}^2\left[\frac{1+e}{2e^3}\ln(1+2e)-\frac{10e^3+27e^2+18e+3}{3e^2(1+2e)^3}\right]$$
$$\pm(C_{\mathrm{V,N}}+F_{2,\mathrm{N}})C_{\mathrm{A,N}}\left[\frac{1}{e^2}\ln(1+2e)-\frac{2+10e+\frac{28}{3}e^2}{e(1+2e)^3}\right]$$
$$+C_{\mathrm{V,N}}F_{2,\mathrm{N}}\left[\frac{1}{e^2}\ln(1+2e)-\frac{2}{3}\left(\frac{3+15e+22e^2}{e(1+2e)^3}\right)\right]$$
$$+F_{2,\mathrm{N}}^2\left[\frac{1}{4e^2}\ln(1+2e)+\frac{8e^3-22e^2-15e-3}{6e(1+2e)^3}\right]\Big\}\Big/\left[\frac{2}{3}(C_{\mathrm{V,N}}^2+5C_{\mathrm{A,N}}^2)\right]. \quad \text{(C.26)}$$

#### C.2.1.2 $\nu - e^-$ Elastic Scattering

Ideally one must include inelastic scattering of neutrino on electrons, for now `NuLib` includes a simple formula from Bowers and Wilson (1982), Thompson (2002).

$$\sigma^{\rm tr,scat}_{\nu e^-}(\epsilon_\nu) = \frac{3G_F^2(\hbar c)^2}{2\pi}\left(T + \frac{\epsilon_{e^-,\rm F}}{4}\right)\epsilon_\nu\left[(C_{\rm V,\nu_i} + C_{\rm A,\nu_i})^2 + \frac{1}{3}(C_{\rm V,\nu_i} - C_{\rm A,\nu_i})^2\right], \tag{C.27}$$

where $\epsilon_{e^-,\rm F}$ is the Fermi energy of the neutrino, taken to be the electron chemical potential; $C_{\rm V,\nu_i}$ is $1/2 + 2\sin^2(\theta_W)$ and $-1/2 + 2\sin^2(\theta_W)$ for $\nu_e$ and for $\nu_\mu$ and $\nu_\tau$ neutrinos, respectively; and $C_{\rm A,\nu_i}$ is $+1/2$ for $\nu_e$, $\bar{\nu}_\mu$, and $\bar{\nu}_\tau$ and $-1/2$ for $\bar{\nu}_e$, $\nu_\mu$, and $\nu_\tau$.

#### C.2.1.3 $\nu - (A, Z)$ Coherent Scattering

Neutrino scattering on heavy nuclei comprise most of the opacity during the collapse phase as $x_H$, the mass fraction of heavy nuclei, is $\sim 1$. From Burrows et al. (2006b),

$$\frac{d\sigma^{\rm scat}_{\rm A}}{d\Omega} = \frac{G_F^2(\hbar c)^2}{16\pi^2}\epsilon_\nu^2\langle A^2\rangle[\mathcal{W}\mathcal{C}_{\rm FF} + \mathcal{C}_{\rm LOS}]^2\langle\mathcal{S}_{\rm ion}\rangle(1+\mu), \tag{C.28}$$

where $\langle A^2\rangle$ is the average $A^2$ of the heavy nuclei, in principle one typically uses $\langle A\rangle^2$, as the nuclear EOS only provides this quantity. $\mathcal{W}$ is given by,

$$\mathcal{W} = 1 - \frac{2Z}{A}(1 - 2\sin^2\theta_W), \tag{C.29}$$

with $A$ and $Z$ being the characteristic average mass and charge of the heavy nucleus. The $\mathcal{C}_{\rm FF}$ and $\mathcal{C}_{\rm LOS}$ are the form factor correction and the electron polarization correction, respectively. There expressions are given by,

$$\mathcal{C}_{\rm FF} = \exp[-y(1-\mu)/2]; y \sim \left(\frac{\epsilon_\nu}{56\,\rm MeV}\right)^2\left(\frac{A}{100}\right)^{2/3}, \tag{C.30}$$

and

$$\mathcal{C}_{\rm LOS} = \frac{Z}{A}\frac{1 + 4\sin^2\theta_W}{1 + (kr_D)^2}, \tag{C.31}$$

where $k^2 = 2(\epsilon_\nu/c)^2(1-\mu)$ and $r_D = \sqrt{\pi(\hbar c)^2/(4\alpha_{FS}cp_F\epsilon_F)}$ is the Debye radius. The final term of Equation C.28 is the angle averaged static ion structure factor. We use the formalism of Horowitz (1997) who use Monte Carlo simulations to generate an approximation of this correction term[2].

[2]Later work by Itoh et al. (2004) improves the calculation of $\langle\mathcal{S}_{\rm ion}\rangle$ at low neutrino energy, Marek et al. (2005) found this has little effect in models of core-collapse supernova.

| | $j=1$ | $j=2$ | $j=3$ | $j=4$ |
|---|---|---|---|---|
| $\beta_{3j}$ | -7.362056 | 0.5371365 | -0.1078845 | $4.189612\times10^{-3}$ |
| $\beta_{4j}$ | 3.4489581 | -0.40251656 | $9.0877878\times10^{-2}$ | $-3.4353581\times10^{-3}$ |
| $\beta_{5j}$ | -0.74128645 | 0.11019855 | $-2.5359361\times10^{-2}$ | $9.0487744\times10^{-4}$ |
| $\beta_{6j}$ | $5.9573285\times10^{-2}$ | $-1.0186552\times10^{-2}$ | $2.2791369\times10^{-3}$ | $-7.4614597\times10^{-5}$ |

Table C.1: Fit coefficients for ion–ion correlation correction factor Equation C.34 from Horowitz (1997)

Their expression for $\langle \mathcal{S}_{\rm ion} \rangle$ is the following fit,

$$\langle \mathcal{S}_{\rm ion} \rangle = \begin{cases} 1 \Big/ \left[ 1 + \exp\left( - \sum_{i=0}^{6} \beta_i(\Gamma) (\bar{\epsilon})^i \right) \right] & \text{if } \bar{\epsilon} < \epsilon^*(\Gamma) = 3 + 4/\Gamma^{1/2} \\ 1 & \text{if } \bar{\epsilon} \geq \epsilon^*(\Gamma) \end{cases} \tag{C.32}$$

$\langle \mathcal{S}_{\rm ion} \rangle$ is a strong function of of the reduced neutrino energy, $\bar{\epsilon} = \epsilon_\nu a_{\rm ion}/\hbar c$ with $a_{\rm ion} = [3/(4\pi n_{\rm ion})]^{1/3}$ measuring the average distance between ions with number density $n_{\rm ion}$. Also, $\langle \mathcal{S}_{\rm ion} \rangle$ is a weak function of the relative interaction strength, $\Gamma = (Ze)^2/(4\pi\epsilon_0 a_{\rm ion} T)$. Both $\bar{\epsilon}$ and $\Gamma$ are dimensionless. The function, $\beta_i(\Gamma)$, is an expansion in $\Gamma$,

$$\beta_0(\Gamma) = \ln[0.3/(0.3+3\Gamma)],\ \beta_1 = 0,\ \beta_2 = 20/3,\ \text{and} \tag{C.33}$$

$$\beta_i(\Gamma) = \beta_{i1} + \beta_{i2}\Gamma^{1/2} + \beta_{i3}\Gamma + \beta_{i4}\Gamma^{3/2} \text{ for } i = 3,4,5,6\,, \tag{C.34}$$

where, for completeness, we include the reference table of Horowitz (1997) for the fit coefficients $\beta_{ij}$. Finally we note that the Monto Carlo results of Horowitz (1997) only cover value of $\Gamma$ between 1 and 150. As suggested by the author, we take $\Gamma = \max(1, \min(\Gamma, 150))$.

To deal with the nontrivial angular dependence of the differential cross section, we numerically integrate Equation C.28, weighted by $1-\mu$, to obtain the transport scattering cross section. We note that the ion-ion correlation term also depends on the scattering angle, the angle averaging performed by Horowitz (1997) includes a $1-\mu$, therefore it is the ion-ion correlation correction to the transport cross section.

#### C.2.1.4 $\nu - \alpha$ Scattering

As in Burrows et al. (2006b), we include a contribution to the scattering opacity from $\alpha$ particles. This is calculated from the scattering cross section on nuclei above, but dropping all of the correction terms, and setting $A = 4$, $Z = 2$.

$$\frac{d\sigma_\alpha^{\rm scat}}{d\Omega} = \frac{4G_F^2(\hbar c)^2}{\pi^2}\epsilon_\nu^2 \sin^4(\theta_W)(1+\mu)\,, \tag{C.35}$$

the transport cross section is then,

$$\sigma_{\alpha}^{\mathrm{tr,scat}} = \int_{\Omega} \frac{d\sigma_{\alpha}^{\mathrm{scat}}}{d\Omega}(1-\mu)d\Omega = \frac{32G_F^2(\hbar c)^2}{3\pi}\epsilon_{\nu}^2 \sin^4(\theta_W)\,. \tag{C.36}$$

### C.2.2 Absorption

In `NuLib` we calculate electron-type neutrino capture onto neutron and protons and heavy nuclei. We take cross sections from Burrows et al. (2006b) and weak magnetism corrections from Horowitz (2002). We do not calculate non-electron-type absorption cross sections as the energies present in the core-collapse environment are typically much smaller than the muon and tau masses.

#### C.2.2.1 $\nu_e + n \rightarrow e^- + p$ Absorption Cross Section

From Burrows et al. (2006b), the $\nu_e$ absorption cross section on free neutrons is,

$$\begin{aligned}\sigma_{\nu_e n}^{\mathrm{abs}} &= \frac{G_F^2(\hbar c)^2}{\pi}(1+3g_A^2)(\epsilon_{\nu_e}+\Delta_{np})^2\left(1-\left(\frac{m_e c^2}{\epsilon_{\nu_e}+\Delta_{np}}\right)^2\right)^{1/2} \\ &\quad \times R_{\mathrm{n}}(\epsilon_{\nu_e})[1-F_{\mathrm{e^-}}(\epsilon_{\nu_e}+\Delta_{np},\mu_e)]/[1-F_{\nu_e}^{eq}(\epsilon_{\nu_e},\mu_{\nu_e})]\,,\end{aligned} \tag{C.37}$$

where $\Delta_{np}$ in the neutron-proton mass difference, and $R_{\mathrm{N}}(\epsilon_{\nu_e})$ is the weak magnetism correction, Equation C.24 taking the + sign and values of $C_{\mathrm{V,n}} = 1$, $C_{\mathrm{A,n}} = g_A$, and $F_{2,\mathrm{n}} = \mu_p - \mu_n \sim 3.706$. $F_{\mathrm{e^-}}(\epsilon_{\nu_e}+\Delta_{np},\mu_e)$ is the occupation density of an electron with energy $\epsilon_{\nu_e}+\Delta_{np}$ and chemical potential $\mu_e$, $1-F_{\mathrm{e^-}}(\epsilon_{\nu_e}+\Delta_{np},\mu_e)$ is then the Fermi blocking term for the final state electrons. As discussed at the beginning of this Appendix, $1-F_{\nu_e}^{eq}(\epsilon_{\nu_e},\mu_{\nu_e})$ is the stimulated absorption term, $\mu_{\nu_e} = \mu_e - \mu_n + \mu_p$ is the equilibrium chemical potential of an electron neutrino. When converting this cross section to an opacity, one must take the final state nucleon blocking into account, see Section C.1.4. As a practical note, one must be very careful when evaluating the Fermi distributions for arbitrary neutrino energy and matter temperature and chemical potential as individual terms can quickly become too large for double precision mathematics, even if the end product is reasonable. In `NuLib`, we work around this by working with the logarithms of the exponentials in the Fermi functions and carefully covering all possible cases in order to construct the final cross section.

#### C.2.2.2 $\bar{\nu}_e + p \rightarrow e^+ + n$ Absorption Cross Section

From Burrows et al. (2006b), the $\bar{\nu}_e$ absorption cross section on free protons is,

$$\begin{aligned}\sigma_{\bar{\nu}_e p}^{\mathrm{abs}} &= \frac{G_F^2(\hbar c)^2}{\pi}(1+3g_A^2)(\epsilon_{\bar{\nu}_e}-\Delta_{np})^2\left(1-\left(\frac{m_e c^2}{\epsilon_{\bar{\nu}_e}-\Delta_{np}}\right)^2\right)^{1/2} \\ &\quad \times R_{\mathrm{n}}(\epsilon_{\bar{\nu}_e})[1-F_{\mathrm{e^+}}(\epsilon_{\bar{\nu}_e}-\Delta_{np},-\mu_e)]/[1-F_{\bar{\nu}_e}^{eq}(\epsilon_{\bar{\nu}_e},-\mu_{\nu_e})]\,,\end{aligned} \tag{C.38}$$

where $\Delta_{np}$ in the neutron-proton mass difference, and $R_{\rm N}(\epsilon_{\bar{\nu}_e})$ is the weak magnetism correction, Equation C.24 taking the $-$ sign and values of $C_{\rm V,p} = 1$, $C_{\rm A,p} = g_A$, and $F_{2,\rm p} = \mu_p - \mu_n \sim 3.706$. $F_{\rm e^+}(\epsilon_{\bar{\nu}_e} - \Delta_{np}, -\mu_e)$ is the occupation density of an positron with energy $\epsilon_{\bar{\nu}_e} - \Delta_{np}$ and chemical potential $\mu_{e^+} = -\mu_e$, $1 - F_{\rm e^-}(\epsilon_{\nu_e} + \Delta_{np}, -\mu_e)$ is then the Fermi blocking term for the final state positrons. As discussed at the beginning of this Appendix, $1 - F^{eq}_{\bar{\nu}_e}(\epsilon_{\bar{\nu}_e}, -\mu_{\nu_e})$ is the stimulated absorption term, $-\mu_{\nu_e} = -\mu_e + \mu_n - \mu_p$ is the equilibrium chemical potential of an electron antineutrino. When converting this cross section to an opacity, one must take the final state nucleon blocking into account, see Section C.1.4. As a practical note, if the final state positron energy is less than the positron rest mass, we set the cross section to zero.

#### C.2.2.3 $\nu_e + (A, Z+1) \rightarrow e^- + (A, Z)$ Absorption Cross Section

For `NuLib` v1.0, we treat electron capture on heavy nuclei via the simplified approach of Bruenn (1985), Burrows et al. (2006b). A much more sophisticated treatment of electron capture is possible via the formalism of Langanke et al. (2003), this will be incorporated in future versions of `NuLib`.

From Burrows et al. (2006b),

$$\sigma^{\rm abs}_{\nu_e(A,Z+1)} = \frac{2G_F^2(\hbar c)^2}{7\pi} g_A^2 N_p(Z) N_n(N) (\epsilon_{\nu_e} + Q')^2 \left[1 - \left(\frac{m_e c^2}{\epsilon_{\nu_e} + Q'}\right)^2\right]^{1/2} \times [1 - F_{\rm e^-}(\epsilon_{\nu_e} + Q', \mu_e)]/[1 - F^{eq}_{\nu_e}(\epsilon_{\nu_e}, \mu_{\nu_e})] \times \exp(-\Delta_{1f_{5/2}}/T) \quad \text{(C.39)}$$

where $Q'$ is the change in mass of the heavy nuclei due to the neutrino interactions, $Q' = M^*_{(A,Z)} - M_{(A,Z+1)} = M_{(A,Z)} - M_{(A,Z+1)} + \Delta_{1f_{5/2}} \sim \mu_n - \mu_p + \Delta_{1f_{5/2}}$. Here, $\Delta_{1f_{5/2}}$ is the energy of the excited neutron in the $1f_{5/2}$ state after electron capture onto a proton in the $1f_{7/2}$ state and is estimated by Bethe et al. (1979), and taken here, to be 3 MeV. The nucleon blocking factors $N_p(Z)$ and $N_n(N)$ are degeneracy-like parameters that give the total available protons on the $1f_{7/2}$ state, and the total number of neutron holes in the $1f_{5/2}$ state, respectively. They are given by

$$N_p(Z) = \begin{cases} 0, & Z < 20 \\ Z - 20, & 20 < Z < 28 \\ 8, & Z > 28 \end{cases}, \quad N_n(N) = \begin{cases} 6, & N < 34 \\ 40 - N, & 34 < N < 40 \\ 0, & N > 40 \end{cases}. \quad \text{(C.40)}$$

### C.2.3 Emissivities

#### C.2.3.1 Electron–Positron Annihilation

We derive the neutrino emissivity rates from electron-positron annihilation into neutrino-antineutrino pairs via the formalism of Bruenn (1985), Burrows et al. (2006b), which is based on the early work of

Yueh and Buchler (1976). We assume that the emissivity spectra for each neutrino type is isotropic in emission angle, we then need to derive the zeroth moment of the neutrino production kernels. The emitted neutrino spectrum, with units of [ergs/cm$^3$/s/srad/MeV], following from Burrows et al. (2006b), is,

$$\eta_{e^-e^+\rightarrow\nu\bar{\nu}}(\epsilon_\nu) = \frac{8\pi^2}{4\pi(2\pi\hbar c)^6}\epsilon_\nu^3 \int_0^\infty \epsilon_{\bar{\nu}}^2 \Phi_0^p(\epsilon_\nu, \epsilon_{\bar{\nu}}) d\epsilon_{\bar{\nu}} \tag{C.41}$$

where $\Phi_0^p(\epsilon_\nu, \epsilon_{\bar{\nu}})$ is given by a phase space integral over the electron and positron distributions,

$$\Phi_0^p(\epsilon_\nu, \epsilon_{\bar{\nu}}) = \frac{G_F^2(\hbar c)^2 c}{\pi} \int_0^{\epsilon_\nu+\epsilon_{\bar{\nu}}} F_{e^-}(\epsilon_{e^-}) F_{e^+}(\epsilon_\nu + \epsilon_{\bar{\nu}} - \epsilon_{e^-}) H_0(\epsilon_\nu, \epsilon_{\bar{\nu}}, \epsilon_{e^-}) d\epsilon_{e^-} \,, \tag{C.42}$$

where

$$H_0(\epsilon_\nu, \epsilon_{\bar{\nu}}, \epsilon_{e^-}) = (C_V^{\nu\bar{\nu}} + C_A^{\nu\bar{\nu}})^2 J_0^I(\epsilon_\nu, \epsilon_{\bar{\nu}}, \epsilon_{e^-}) + (C_V^{\nu\bar{\nu}} - C_A^{\nu\bar{\nu}})^2 J_0^{II}(\epsilon_\nu, \epsilon_{\bar{\nu}}, \epsilon_{e^-}) \,, \tag{C.43}$$

with $C_V^{\nu_e\bar{\nu}_e} = 1/2 + 2\sin^2(\theta_W)$ and $C_A^{\nu_e\bar{\nu}_e} = 1/2$ when calculating the emitted $\nu_e$ spectrum. To determine the spectrum of $\mu$ and $\tau$ neutrinos we replace $C_V^{\nu_e\bar{\nu}_e} \rightarrow C_V^{\nu_e\bar{\nu}_e} - 1$ and $C_A^{\nu_e\bar{\nu}_e} \rightarrow C_A^{\nu_e\bar{\nu}_e} - 1$. For all antineutrinos, change $C_A^{\nu\bar{\nu}}$ to $-C_A^{\nu\bar{\nu}}$. This leads to unique energy emission spectra for electron neutrinos, electron antineutrinos, heavy-lepton neutrinos, and heavy-lepton antineutrinos that is a function of only matter temperature and the electron chemical potential. Finally, one needs expressions for $J_0^I(\epsilon_\nu, \epsilon_{\bar{\nu}}, \epsilon_{e^-})$ and $J_0^{II}(\epsilon_\nu, \epsilon_{\bar{\nu}}, \epsilon_{e^-})$,

$$\begin{aligned} J_0^I(\epsilon_\nu, \epsilon_{\bar{\nu}}, \epsilon_{e^-}) \;=\; & \frac{1}{\epsilon_\nu \epsilon_{\bar{\nu}}} \Theta(\epsilon_\nu + \epsilon_{\bar{\nu}} - \epsilon_{e^-}) \Big\{ \big[\Theta(\epsilon_\nu - \epsilon_{e^-})\Theta(\epsilon_{\bar{\nu}} - \epsilon_\nu) + \\ & \Theta(\epsilon_{\bar{\nu}} - \epsilon_{e^-})\Theta(\epsilon_\nu - \epsilon_{\bar{\nu}})\big] a_0(\epsilon_\nu, \epsilon_{\bar{\nu}}, \epsilon_{e^-}) + \\ & \big[\Theta(\epsilon_{e^-} - \epsilon_\nu)\Theta(\epsilon_\nu - \epsilon_{\bar{\nu}}) + \Theta(\epsilon_{e^-} - \epsilon_{\bar{\nu}})\Theta(\epsilon_{\bar{\nu}} - \epsilon_\nu)\big] \times \\ & b_0(\epsilon_\nu, \epsilon_{\bar{\nu}}, \epsilon_{e^-}) + \Theta(\epsilon_{e^-} - \epsilon_\nu)\Theta(\epsilon_{\bar{\nu}} - \epsilon_{e^-}) c_0(\epsilon_\nu, \epsilon_{\bar{\nu}}, \epsilon_{e^-}) + \\ & \Theta(\epsilon_{e^-} - \epsilon_{\bar{\nu}})\Theta(\epsilon_\nu - \epsilon_{e^-}) d_0(\epsilon_\nu, \epsilon_{\bar{\nu}}, \epsilon_{e^-}) \Big\} \end{aligned} \tag{C.44}$$

where $\Theta(x)$ is the Heavy side function, equal to 0 if $x < 0$, 1 if $x > 0$ and 1/2 if $x = 0$. $a_0$ through $d_0$ are given as,

$$\begin{aligned}
a_0(\epsilon_1,\epsilon_2,\epsilon_3) &= \frac{1}{\epsilon_1\epsilon_2}\left[\frac{4}{15}\epsilon_3^5 - \frac{4}{3}\epsilon_3^4\epsilon_2 + \frac{8}{3}\epsilon_3^3\epsilon_2^2\right] \\
b_0(\epsilon_1,\epsilon_2,\epsilon_3) &= \frac{1}{\epsilon_1\epsilon_2}\Bigg[ - a_0(\epsilon_1,\epsilon_2,\epsilon_3)\epsilon_1\epsilon_2 + \frac{8}{3}\epsilon_3^2(\epsilon_1^3+\epsilon_2^3) - \\
&\quad \frac{4}{3}\epsilon_3(\epsilon_1+\epsilon_2)^2(\epsilon_2^2 - 2\epsilon_1\epsilon_2 + 3\epsilon_1^2) + \\
&\quad \frac{4}{15}(\epsilon_1+\epsilon_2)^3(\epsilon_2^2 - 3\epsilon_1\epsilon_2 + 6\epsilon_1^2)\Bigg] \\
c_0(\epsilon_1,\epsilon_2,\epsilon_3) &= \frac{\epsilon_1^2}{\epsilon_2}\left[\frac{8}{3}\epsilon_2^2 + 4\epsilon_1\epsilon_2 + \frac{8}{5}\epsilon_1^2\right] - \epsilon_3\left[\frac{16}{3}\epsilon_1^2 + 4\frac{\epsilon_1^3}{\epsilon_2}\right] + \frac{8}{3}\epsilon_3^2\frac{\epsilon_1^2}{\epsilon_2} \\
d_0(\epsilon_1,\epsilon_2,\epsilon_3) &= \frac{4}{15}\frac{\epsilon_2^4}{\epsilon_1} - \frac{4}{3}\frac{\epsilon_2^3}{\epsilon_1}\epsilon_3 + \frac{8}{3}\frac{\epsilon_2^2}{\epsilon_1}\epsilon_3^2
\end{aligned} \tag{C.45}$$

where we note the following mistake in Bruenn (1985), which is corrected here, the $a_0$ term in the expression for $b_0$ is multiplied by $\epsilon_1\epsilon_2$. Finally, the expression for $J_0^{II}$ is obtained by exchanging the neutrino and antineutrino energy,

$$J_0^{II}(\epsilon_\nu,\epsilon_{\bar\nu},\epsilon_{e^-}) = J_0^{I}(\epsilon_{\bar\nu},\epsilon_\nu,\epsilon_{e^-})\,, \tag{C.46}$$

#### C.2.3.2 Nucleon–Nucleon Bremsstrahlung

We follow Burrows et al. (2006b) who derive a simplified formula for the single-neutrino energy emission spectra from nucleon-nucleon bremsstrahlung. For astrophysical situations where this interaction dominates, such as protoneutron star cooling, there are better implementations. We leave this for a future version of `NuLib`. The fit from Burrows et al. (2006b) to the energy emission spectrum of a single neutrino is given by,

$$\eta_{\mathrm{NN}\to\mathrm{NN}+\nu\bar\nu} = \frac{0.234}{T}\left(\frac{\epsilon_\nu}{T}\right)^{2.4}\exp\left(-1.1\epsilon_\nu/T\right)\times Q_{\mathrm{NN}} \tag{C.47}$$

where $Q_{\mathrm{NN}}$ is the total energy emission of a single neutrino *pair*. From Burrows et al. (2006b), $Q_{\mathrm{NN}}$, with a correction from Burrows (2010), is given by,

$$Q_{\mathrm{NN}} = 207.78\xi(X_{\mathrm{N}}^2 + X_{\mathrm{P}}^2 + 28X_{\mathrm{N}}X_{\mathrm{P}})\rho^2\left(\frac{T}{\mathrm{MeV}}\right)^{5.5} \tag{C.48}$$

where we, as in Burrows et al. (2006b) take $\xi = 0.5$.

# Bibliography

Abdikamalov, E., Burrows, A., Ott, C. D., Löffler, F., O'Connor, E., Dolence, J. C., and Schnetter, E. A New Monte Carlo Method for Time-Dependent Neutrino Radiation Transport. *Submitted to the Astrophys. J.; arXiv:1203.2915*, March 2012.

Abe, K., Abe, T., Aihara, H., Fukuda, Y., Hayato, Y., Huang, K., Ichikawa, A. K., Ikeda, M., Inoue, K., Ishino, H., Itow, Y., Kajita, T., Kameda, J., Kishimoto, Y., Koga, M., Koshio, Y., Lee, K. P., Minamino, A., Miura, M., Moriyama, S., Nakahata, M., Nakamura, K., Nakaya, T., Nakayama, S., Nishijima, K., Nishimura, Y., Obayashi, Y., Okumura, K., Sakuda, M., Sekiya, H., Shiozawa, M., Suzuki, A. T., Suzuki, Y., Takeda, A., Takeuchi, Y., Tanaka, H. K. M., Tasaka, S., Tomura, T., Vagins, M. R., Wang, J., and Yokoyama, M. Letter of Intent: The Hyper-Kamiokande Experiment — Detector Design and Physics Potential —. *arXiv:1109.3262*, September 2011.

Anninos, P., Fragile, P. C., and Salmonson, J. D. Cosmos++: Relativistic Magnetohydrodynamics on Unstructured Grids with Local Adaptive Refinement. *Astrophys. J.*, 635:723, December 2005. doi: 10.1086/497294.

Audit, E., Charrier, P., Chièze, J.-P., and Dubroca, B. A radiation-hydrodynamics scheme valid from the transport to the diffusion limit. *arXiv:0206281*, June 2002.

Baade, W., and Zwicky, F. On Super-novae. *Proc. Nat. Acad. Sci.*, 20:254, 1934a. doi: 10.1073/pnas.20.5.254.

Baade, W., and Zwicky, F. Cosmic Rays from Super-novae. *Proc. Nat. Acad. Sci.*, 20:259, 1934b. doi: 10.1073/pnas.20.5.259.

Balbus, S. A., and Hawley, J. F. A powerful local shear instability in weakly magnetized disks. I—Linear analysis. II—Nonlinear evolution. *Astrophys. J.*, 376:214, July 1991. doi: 10.1086/170270.

Banyuls, F., Font, J. A., Ibáñez, J. M., Martí, J. M., and Miralles, J. A. Numerical 3+1 general-relativistic hydrodynamics: A local characteristic approach. *Astrophys. J.*, 476:221, 1997.

Bardeen, J. M., Press, W. H., and Teukolsky, S. A. Rotating Black Holes: Locally Nonrotating Frames, Energy Extraction, and Scalar Synchrotron Radiation. *Astrophys. J.*, 178:347, December 1972. doi: 10.1086/151796.

Baron, E., and Cooperstein, J. The effect of iron core structure on supernovae. *Astrophys. J.*, 353: 597, April 1990.

Baron, E., Cooperstein, J., and Kahana, S. Type-II supernovae in 12-solar-mass and 15-solar-mass stars The equation of state and general relativity. *Phys. Rev. Lett.*, 55:126, July 1985.

Baron, E., Myra, E. S., Cooperstein, J., and van den Horn, L. J. General relativistic neutrino transport in stellar collapse. *Astrophys. J.*, 339:978, April 1989. doi: 10.1086/167352.

Baumgarte, T. W., Shapiro, S. L., and Teukolsky, S. A. Computing supernova collapse to neutron stars and black holes. *Astrophys. J.*, 443:717, April 1995.

Baumgarte, T. W., Janka, H.-T., Keil, W., Shapiro, S. L., and Teukolsky, S. A. Delayed Collapse of Hot Neutron Stars to Black Holes via Hadronic Phase Transitions. *Astrophys. J.*, 468:823, September 1996a.

Baumgarte, T. W., Shapiro, S. L., and Teukolsky, S. A. Computing the Delayed Collapse of Hot Neutron Stars to Black Holes. *Astrophys. J.*, 458:680, February 1996b.

Bays, K., Iida, T., Abe, K., Hayato, Y., Iyogi, K., Kameda, J., Koshio, Y., Marti, L., Miura, M., Moriyama, S., Nakahata, M., Nakayama, S., Obayashi, Y., Sekiya, H., Shiozawa, M., Suzuki, Y., Takeda, A., Takenaga, Y., Ueno, K., Ueshima, K., Yamada, S., Yokozawa, T., Kaji, H., Kajita, T., Kaneyuki, K., McLachlan, T., Okumura, K., Lee, K. P., Martens, K., Vagins, M., Labarga, L., Kearns, E., Litos, M., Raaf, J. L., Stone, J. L., Sulak, L. R., Kropp, W. R., Mine, S., Regis, C., Renshaw, A., Smy, M. B., Sobel, H. W., Ganezer, K. S., Hill, J., Keig, W. E., Cho, S., Jang, J. S., Kim, J. Y., Lim, I. T., Albert, J., Scholberg, K., Walter, C. W., Wendell, R., Wongjirad, T., Ishizuka, T., Tasaka, S., Learned, J. G., Matsuno, S., Smith, S., Hasegawa, T., Ishida, T., Ishii, T., Kobayashi, T., Nakadaira, T., Nakamura, K., Nishikawa, K., Oyama, Y., Sakashita, K., Sekiguchi, T., Tsukamoto, T., Suzuki, A. T., Takeuchi, Y., Ikeda, M., Matsuoka, K., Minamino, A., Murakami, A., Nakaya, T., Fukuda, Y., Itow, Y., Mitsuka, G., Miyake, M., Tanaka, T., Hignight, J., Imber, J., Jung, C. K., Taylor, I., Yanagisawa, C., Kibayashi, A., Ishino, H., Mino, S., Sakuda, M., Mori, T., Toyota, H., Kuno, Y., Kim, S. B., Yang, B. S., Okazawa, H., Choi, Y., Nishijima, K., Koshiba, M., Totsuka, Y., Yokoyama, M., Heng, Y., Chen, S., Zhang, H., Yang, Z., Mijakowski, P., Connolly, K., Dziomba, M., and Wilkes, R. J. Supernova relic neutrino search at super-Kamiokande. *Phys. Rev. D.*, 85(5):052007, March 2012. doi: 10.1103/PhysRevD.85.052007.

Beacom, J. F., and Vogel, P. Mass signature of supernova $\nu_\mu$ and $\nu_\tau$ neutrinos in SuperKamiokande. *Phys. Rev. D.*, 58(5):053010, September 1998a. doi: 10.1103/PhysRevD.58.053010.

Beacom, J. F., and Vogel, P. Mass signature of supernova $\nu_\mu$ and $\nu_\tau$ neutrinos in the Sudbury Neutrino Observatory. *Phys. Rev. D.*, 58(9):093012, November 1998b. doi: 10.1103/PhysRevD.58.093012.

Beacom, J. F., Boyd, R. N., and Mezzacappa, A. Black hole formation in core-collapse supernovae and time-of-flight measurements of the neutrino masses. *Phys. Rev. D.*, 63:073011, April 2001. doi: 10.1103/PhysRevD.63.073011.

Belczynski, K., Kalogera, V., and Bulik, T. A Comprehensive Study of Binary Compact Objects as Gravitational Wave Sources: Evolutionary Channels, Rates, and Physical Properties. *Astrophys. J.*, 572:407, June 2002. doi: 10.1086/340304.

Bethe, H. A. Supernova mechanisms. *Rev. Mod. Phys.*, 62:801, 1990.

Bethe, H. A., Brown, G. E., Applegate, J., and Lattimer, J. M. Equation of state in the gravitational collapse of stars. *Nuclear Physics A*, 324:487, July 1979. doi: 10.1016/0375-9474(79)90596-7.

Bionta, R. M., Blewitt, G., Bratton, C. B., Casper, D., and Ciocio, A. Observation of a neutrino burst in coincidence with supernova 1987A in the Large Magellanic Cloud. *Phys. Rev. Lett.*, 58: 1494, April 1987. doi: 10.1103/PhysRevLett.58.1494.

Bisnovatyi-Kogan, G. S., Popov, I. P., and Samokhin, A. A. The magnetohydrodynamic rotational model of supernova explosion. *Astrophys. Space Sci.*, 41:287, June 1976. doi: 10.1007/BF00646184.

Bludman, S. A., and van Riper, K. A. Equation of state of an ideal Fermi gas. *Astrophys. J.*, 212: 859, March 1977.

Borexino. URL http://borex.lngs.infn.it.

Bouret, J.-C., Lanz, T., and Hillier, D. J. Lower mass loss rates in O-type stars: Spectral signatures of dense clumps in the wind of two Galactic O4 stars. *Astron. Astrophys.*, 438:301, July 2005.

Bowers, R. L., and Wilson, J. R. A numerical model for stellar core collapse calculations. *Astrophys. J. Supp. Ser.*, 50:115, November 1982. doi: 10.1086/190822.

Brandt, T. D., Burrows, A., Ott, C. D., and Livne, E. Results from Core-collapse Simulations with Multi-dimensional, Multi-angle Neutrino Transport. *Astrophys. J.*, 728:8, February 2011.

Bruenn, S. W. Stellar core collapse—Numerical model and infall epoch. *Astrophys. J. Supp. Ser.*, 58:771, August 1985.

Bruenn, S. W., Mezzacappa, A., Hix, W. R., Blondin, J. M., Marronetti, P., Messer, O. E. B., Dirk, C. J., and Yoshida, S. Mechanisms of Core-Collapse Supernovae and Simulation Results from the CHIMERA Code. In Giobbi, G., Tornambe, A., Raimondo, G., Limongi, M., Antonelli, L. A., Menci, N., and Brocato, E., editors, *AIP Phys. Conf. Ser.*, volume 1111 of *AIP Phys. Conf. Ser.*, page 593, May 2009.

Buras, R., Janka, H.-T., Rampp, M., and Kifonidis, K. Two-dimensional hydrodynamic core-collapse supernova simulations with spectral neutrino transport. II. Models for different progenitor stars. *Astron. Astrophys.*, 457:281, October 2006a.

Buras, R., Rampp, M., Janka, H.-T., and Kifonidis, K. Two-dimensional hydrodynamic core-collapse supernova simulations with spectral neutrino transport. I. Numerical method and results for a 15 Mȯ star. *Astron. Astrophys.*, 447:1049, March 2006b.

Burrows, A. Speculations on the fizzled collapse of a massive star. *Astrophys. J.*, 300:488, January 1986. doi: 10.1086/163826.

Burrows, A. Supernova neutrinos. *Astrophys. J.*, 334:891, November 1988.

Burrows, A. *Private communiciation*, 2010.

Burrows, A. *Private communiciation*, 2012.

Burrows, A., and Lattimer, J. M. The effect of trapped lepton number and entropy on the outcome of stellar collapse. *Astrophys. J.*, 270:735, July 1983.

Burrows, A., and van Riper, K. A. A Gamma-Ray Monte Carlo Study of the Clumpy Debris of SN 1987A. *Astrophys. J.*, 455:215, December 1995.

Burrows, A., Young, T., Pinto, P., Eastman, R., and Thompson, T. A. A New Algorithm for Supernova Neutrino Transport and Some Applications. *Astrophys. J.*, 539:865, August 2000.

Burrows, A., Livne, E., Dessart, L., Ott, C. D., and Murphy, J. A New Mechanism for Core-Collapse Supernova Explosions. *Astrophys. J.*, 640:878, April 2006a.

Burrows, A., Reddy, S., and Thompson, T. A. Neutrino opacities in nuclear matter. *Nuclear Physics A*, 777:356, October 2006b.

Burrows, A., Dessart, L., and Livne, E. The Multi-Dimensional Character and Mechanisms of Core-Collapse Supernovae. In Immler, S., and McCray, R., editors, *AIP Conference Series*, volume 937, page 370, October 2007a.

Burrows, A., Dessart, L., Livne, E., Ott, C. D., and Murphy, J. Simulations of Magnetically Driven Supernova and Hypernova Explosions in the Context of Rapid Rotation. *Astrophys. J.*, 664:416, July 2007b.

Burrows, A., Livne, E., Dessart, L., Ott, C. D., and Murphy, J. Features of the Acoustic Mechanism of Core-Collapse Supernova Explosions. *Astrophys. J.*, 655:416, January 2007c.

Burrows, A., Dolence, J. C., and Murphy, J. W. An Investigation into the Character of Pre-Explosion Core-Collapse Supernova Shock Motion. *ArXiv e-prints*, April 2012.

Castor, J. I. *Radiation Hydrodynamics*. Radiation Hydrodynamics, by John I. Castor, pp. 368. ISBN 0521833094. Cambridge, UK: Cambridge University Press, November 2004., November 2004.

Cernohorsky, J., and Bludman, S. A. Maximum entropy distribution and closure for Bose-Einstein and Fermi-Dirac radiation transport. *Astrophys. J.*, 433:250, September 1994. doi: 10.1086/174640.

Chadwick, J. Possible Existence of a Neutron. *Nature*, 129:312, February 1932. doi: 10.1038/129312a0.

Chakraborty, S., Fischer, T., Mirizzi, A., Saviano, N., and Tomàs, R. Analysis of matter suppression in collective neutrino oscillations during the supernova accretion phase. *Phys. Rev. D.*, 84:025002, July 2011a. doi: 10.1103/PhysRevD.84.025002.

Chakraborty, S., Fischer, T., Mirizzi, A., Saviano, N., and Tomàs, R. No Collective Neutrino Flavor Conversions during the Supernova Accretion Phase. *Phys. Rev. Lett.*, 107:151101, October 2011b. doi: 10.1103/PhysRevLett.107.151101.

Chandrasekhar, S. *Ellipsoidal Figures of Equilibrium*. Yale University Press, New Haven, USA, 1969. revised edition 1987.

Chandrasekhar, S. The Effect of Gravitational Radiation on the Secular Stability of the Maclaurin Spheroid. *Astrophys. J.*, 161:561, 1970.

Chornock, R., Berger, E., Levesque, E. M., Soderberg, A. M., Foley, R. J., Fox, D. B., Frebel, A., Simon, J. D., Bochanski, J. J., Challis, P. J., Kirshner, R. P., Podsiadlowski, P., Roth, K., Rutledge, R. E., Schmidt, B. P., Sheppard, S. S., and Simcoe, R. A. Spectroscopic Discovery of the Broad-Lined Type Ic Supernova 2010bh Associated with the Low-Redshift GRB 100316D. *ArXiv:1004.2262*, April 2010.

Claeys, J. S. W., de Mink, S. E., Pols, O. R., Eldridge, J. J., and Baes, M. Binary progenitor models of type IIb supernovae. *Astron. Astrophys.*, 528:A131, April 2011. doi: 10.1051/0004-6361/201015410.

Colella, P., and Woodward, P. R. The Piecewise Parabolic Method (PPM) for Gas-Dynamical Simulations. *J. Comp. Phys.*, 54:174, 1984.

Cook, G. B., Shapiro, S. L., and Teukolsky, S. A. Spin-up of a rapidly rotating star by angular momentum loss—Effects of general relativity. *Astrophys. J.*, 398:203, October 1992. doi: 10.1086/171849.

Corvino, G., Rezzolla, L., Bernuzzi, S., De Pietri, R., and Giacomazzo, B. On the shear instability in relativistic neutron stars. *Class. Quantum Grav.*, 27(11):114104, June 2010.

Dasgupta, B., Fischer, T., Horiuchi, S., Liebendörfer, M., Mirizzi, A., Sagert, I., and Schaffner-Bielich, J. Detecting the QCD phase transition in the next Galactic supernova neutrino burst. *Phys. Rev. D.*, 81(10):103005, May 2010. doi: 10.1103/PhysRevD.81.103005.

Dasgupta, B., O'Connor, E. P., and Ott, C. D. Role of collective neutrino flavor oscillations in core-collapse supernova shock revival. *Phys. Rev. D.*, 85:065008, March 2012.

de Jager, C., Nieuwenhuijzen, H., and van der Hucht, K. A. Mass loss rates in the Hertzsprung-Russell diagram. *Astron. Astrophys. Suppl.*, 72:259, February 1988.

Demorest, P. B., Pennucci, T., Ransom, S. M., Roberts, M. S. E., and Hessels, J. W. T. A two-solar-mass neutron star measured using Shapiro delay. *Nature*, 467:1081, October 2010.

Dessart, L., Burrows, A., Livne, E., and Ott, C. D. The Proto-Neutron Star Phase of the Collapsar Model and the Route to Long-Soft Gamma-Ray Bursts and Hypernovae. *Astrophys. J. Lett.*, 673:L43, January 2008.

Dessart, L., Livne, E., and Waldman, R. Determining the main-sequence mass of Type II supernova progenitors. *Mon. Not. Roy. Astron. Soc.*, 408:827, October 2010. doi: 10.1111/j.1365-2966.2010.17190.x.

Dessart, L., O'Connor, E., and Ott, C. D. The Arduous Journey to Black-Hole Formation in Potential Gamma-Ray Burst Progenitors. *Submitted to the Astrophys. J.; ArXiv:1203.1926*, March 2012.

Dimmelmeier, H., Font, J. A., and Müller, E. Relativistic simulations of rotational core collapse II. Collapse dynamics and gravitational radiation. *Astron. Astrophys.*, 393:523, October 2002a.

Dimmelmeier, H., Font, J. A., and Müller, E. Relativistic simulations of rotational core collapse I. Methods, initial models, and code tests. *Astron. Astrophys.*, 388:917, June 2002b.

Dimmelmeier, H., Novak, J., Font, J. A., Ibáñez, J. M., and Müller, E. Combining spectral and shock-capturing methods: A new numerical approach for 3D relativistic core collapse simulations. *Phys. Rev. D.*, 71:064023, March 2005.

Dimmelmeier, H., Ott, C. D., Janka, H.-T., Marek, A., and Müller, E. Generic Gravitational-Wave Signals from the Collapse of Rotating Stellar Cores. *Phys. Rev. Lett.*, 98:251101, June 2007.

Dimmelmeier, H., Ott, C. D., Marek, A., and Janka, H.-T. Gravitational wave burst signal from core collapse of rotating stars. *Phys. Rev. D.*, 78:064056, 2008.

Duan, H., and Kneller, J. P. TOPICAL REVIEW: Neutrino flavour transformation in supernovae. *Journal of Physics G Nuclear Physics*, 36(11):113201, November 2009. doi: 10.1088/0954-3899/36/11/113201.

Duan, H., Fuller, G. M., and Qian, Y.-Z. Collective Neutrino Oscillations. *Ann. Rev. Nuc. Part. Sc.*, 60:569, November 2010.

Duez, M. D., Liu, Y. T., Shapiro, S. L., Shibata, M., and Stephens, B. C. Evolution of magnetized, differentially rotating neutron stars: Simulations in full general relativity. *Phys. Rev. D*, 73:104015, 2006.

Einfeldt, B. On Godunov type methods for the Euler equations with a general equation of state. In *Shock tubes and waves; Proceedings of the Sixteenth International Symposium, Aachen, Germany, July 26–31, 1987. VCH Verlag, Weinheim, Germany*, page 671, 1988.

Eldridge, J. J., and Tout, C. A. The progenitors of core-collapse supernovae. *Mon. Not. Roy. Astron. Soc.*, 353:87, September 2004.

Elias-Rosa, N., Van Dyk, S. D., Li, W., Miller, A. A., Silverman, J. M., Ganeshalingam, M., Boden, A. F., Kasliwal, M. M., Vinkó, J., Cuillandre, J.-C., Filippenko, A. V., Steele, T. N., Bloom, J. S., Griffith, C. V., Kleiser, I. K. W., and Foley, R. J. The Massive Progenitor of the Type II-linear Supernova 2009kr. *Astrophys. J. Lett.*, 714:L254, May 2010. doi: 10.1088/2041-8205/714/2/L254.

Endal, A. S., and Sofia, S. The evolution of rotating stars. II—Calculations with time-dependent redistribution of angular momentum for 7- and 10-solar-mass stars. *Astrophys. J.*, 220:279, 1978.

Farr, W. M., Sravan, N., Cantrell, A., Kreidberg, L., Bailyn, C. D., Mandel, I., and Kalogera, V. The Mass Distribution of Stellar-mass Black Holes. *Astrophys. J.*, 741:103, November 2011. doi: 10.1088/0004-637X/741/2/103.

Fernández, R. Hydrodynamics of Core-collapse Supernovae at the Transition to Explosion. I. Spherical Symmetry. *Astrophys. J.*, 749:142, April 2012. doi: 10.1088/0004-637X/749/2/142.

Fernández, R., and Thompson, C. Dynamics of a Spherical Accretion Shock with Neutrino Heating and Alpha-Particle Recombination. *Astrophys. J.*, 703:1464, October 2009.

Filippenko, A. V. Optical Spectra of Supernovae. *Ann. Rev. Astron. Astrophys.*, 35:309, 1997.

Fischer, T., Whitehouse, S. C., Mezzacappa, A., Thielemann, F.-K., and Liebendörfer, M. The neutrino signal from protoneutron star accretion and black hole formation. *Astron. Astrophys.*, 499:1–15, May 2009. doi: 10.1051/0004-6361/200811055.

Font, J. A. Numerical Hydrodynamics and Magnetohydrodynamics in General Relativity. *Liv. Rev. Rel.*, 11:7, September 2008.

Font, J. A., Miller, M., Suen, W.-M., and Tobias, M. Three-dimensional numerical general relativistic hydrodynamics: Formulations, methods, and code tests. *Phys. Rev. D.*, 61:044011, February 2000. doi: 10.1103/PhysRevD.61.044011.

Friedman, J. L., and Schutz, B. F. Secular instability of rotating Newtonian stars. *Astrophys. J.*, 222:281, 1978.

Fryer, C. L. Mass Limits For Black Hole Formation. *Astrophys. J.*, 522:413, September 1999.

Fryer, C. L., and Heger, A. Core-Collapse Simulations of Rotating Stars. *Astrophys. J.*, 541:1033, October 2000.

Fryer, C. L., and Kalogera, V. Theoretical Black Hole Mass Distributions. *Astrophys. J.*, 554:548, June 2001.

Fullerton, A. W., Massa, D. L., and Prinja, R. K. The Discordance of Mass-Loss Estimates for Galactic O-Type Stars. *Astrophys. J.*, 637:1025, February 2006. doi: 10.1086/498560.

Fynbo, J. P. U., Watson, D., Thöne, C. C., Sollerman, J., Bloom, J. S., Davis, T. M., Hjorth, J., Jakobsson, P., Jørgensen, U. G., Graham, J. F., Fruchter, A. S., Bersier, D., Kewley, L., Cassan, A., Castro Cerón, J. M., Foley, S., Gorosabel, J., Hinse, T. C., Horne, K. D., Jensen, B. L., Klose, S., Kocevski, D., Marquette, J.-B., Perley, D., Ramirez-Ruiz, E., Stritzinger, M. D., Vreeswijk, P. M., Wijers, R. A. M., Woller, K. G., Xu, D., and Zub, M. No supernovae associated with two long-duration $\gamma$-ray bursts. *Nature*, 444:1047–1049, December 2006. doi: 10.1038/nature05375.

Gourgoulhon, E. Simple equations for general relativistic hydrodynamics in spherical symmetry applied to neutron star collapse. *Astron. Astrophys.*, 252:651, December 1991.

Gourgoulhon, E. Equilibre et effondrement gravitationnel des étoiles en relativité générale et en symétrie sphérique. *Ann. Phys.*, 18:1, February 1993.

Gourgoulhon, E., and Haensel, P. Upper bounds on the neutrino burst from collapse of a neutron star into a black hole. *Astron. Astrophys.*, 271:187, April 1993.

HALO. URL http://www.snolab.ca/halo/index.html. Helium and Lead Observatory.

Halzen, F., and Raffelt, G. G. Reconstructing the supernova bounce time with neutrinos in IceCube. *Phys. Rev. D.*, 80(8):087301, October 2009. doi: 10.1103/PhysRevD.80.087301.

Hanke, F., Marek, A., Müller, B., and Janka, H.-T. Is Strong SASI Activity the Key to Successful Neutrino-Driven Supernova Explosions? *Submitted to the Astrophys. J., arXiv:1108.4355*, August 2011.

Hebeler, K., Lattimer, J. M., Pethick, C. J., and Schwenk, A. Constraints on Neutron Star Radii Based on Chiral Effective Field Theory Interactions. *Phys. Rev. Lett.*, 105:161102, October 2010. doi: 10.1103/PhysRevLett.105.161102.

Heger, A., Langer, N., and Woosley, S. E. Presupernova Evolution of Rotating Massive Stars. I. Numerical Method and Evolution of the Internal Stellar Structure. *Astrophys. J.*, 528:368, January 2000.

Heger, A., Fryer, C. L., Woosley, S. E., Langer, N., and Hartmann, D. H. How Massive Single Stars End Their Life. *Astrophys. J.*, 591:288, July 2003.

Heger, A., Woosley, S. E., and Spruit, H. C. Presupernova Evolution of Differentially Rotating Massive Stars Including Magnetic Fields. *Astrophys. J.*, 626:350, June 2005.

Hempel, M. URL http://phys-merger.physik.unibas.ch/~hempel/eos.html. Matthias Hempel's EOS webpage.

Hempel, M., and Schaffner-Bielich, J. A statistical model for a complete supernova equation of state. *Nuclear Physics A*, 837:210, June 2010. doi: 10.1016/j.nuclphysa.2010.02.010.

Hempel, M., Fischer, T., Schaffner-Bielich, J., and Liebendörfer, M. New equations of state in core-collapse supernova simulations. *ArXiv:1108.0848*, August 2011.

Herant, M., Benz, W., Hix, W. R., Fryer, C. L., and Colgate, S. A. Inside the supernova: A powerful convective engine. *Astrophys. J.*, 435:339, November 1994.

Hillebrandt, W., and Niemeyer, J. C. Type IA Supernova Explosion Models. *Ann. Rev. Astron. Astroph.*, 38:191, 2000. doi: 10.1146/annurev.astro.38.1.191.

Hirata, K., Kajita, T., Koshiba, M., Nakahata, M., and Oyama, Y. Observation of a neutrino burst from the supernova SN1987A. *Phys. Rev. Lett.*, 58:1490, April 1987. doi: 10.1103/PhysRevLett.58.1490.

Hirschi, R., Meynet, G., and Maeder, A. Stellar evolution with rotation. XII. Pre-supernova models. *Astron. Astrophys.*, 425:649, October 2004. doi: 10.1051/0004-6361:20041095.

Horiuchi, S., Beacom, J. F., and Dwek, E. Diffuse supernova neutrino background is detectable in Super-Kamiokande. *Phys. Rev. D.*, 79(8):083013, April 2009. doi: 10.1103/PhysRevD.79.083013.

Horowitz, C. J. Neutrino trapping in a supernova and the screening of weak neutral currents. *Phys. Rev. D.*, 55:4577, April 1997. doi: 10.1103/PhysRevD.55.4577.

Horowitz, C. J. Weak magnetism for antineutrinos in supernovae. *Phys. Rev. D.*, 65(4):043001, February 2002. doi: 10.1103/PhysRevD.65.043001.

Hyman, James M. The method of lines solution of partial differential equations. Technical report, ERDA Mathematics and Computing Laboratory, Courant Institute of Mathematical Sciences, New York University, October 1976.

IceCube. URL http://icecube.wisc.edu. IceCube Neutrino Observatory.

Isenberg, J. A. Waveless Approximation Theories of Gravity. *Int. J. Mod. Phys. D*, 17:265, 2008.

Itoh, N., Asahara, R., Tomizawa, N., Wanajo, S., and Nozawa, S. Ion-Ion Correlation Effect on the Neutrino-Nucleus Scattering in Supernova Cores. *Astrophys. J.*, 611:1041, August 2004. doi: 10.1086/422380.

Janka, H.-T. Flux-limited neutrino diffusion versus Monte Carlo neutrino transport. *Astron. Astrophys.*, 256:452, March 1992.

Janka, H.-T. Conditions for shock revival by neutrino heating in core-collapse supernovae. *Astron. Astrophys.*, 368:527, March 2001. doi: 10.1051/0004-6361:20010012.

Janka, H.-T., and Hillebrandt, W. Monte Carlo simulations of neutrino transport in type II supernovae. *Astron. Astrophys. Suppl.*, 78:375, June 1989a.

Janka, H.-T., and Hillebrandt, W. Neutrino emission from type II supernovae—an analysis of the spectra. *Astron. Astrophys.*, 224:49, October 1989b.

Janka, H.-T., Zwerger, T., and Mönchmeyer, R. Does artificial viscosity destroy prompt type-II supernova explosions? *Astron. Astrophys.*, 268:360, February 1993.

KamLAND. URL http://www.awa.tohoku.ac.jp/KamLAND/.

Kiewe, M., Gal-Yam, A., Arcavi, I., Leonard, D. C., Emilio Enriquez, J., Cenko, S. B., Fox, D. B., Moon, D.-S., Sand, D. J., Soderberg, A. M., and CCCP, T. Caltech Core-Collapse Project (CCCP) Observations of Type IIn Supernovae: Typical Properties and Implications for Their Progenitor Stars. *Astrophys. J.*, 744:10, January 2012. doi: 10.1088/0004-637X/744/1/10.

Kitaura, F. S., Janka, H.-T., and Hillebrandt, W. Explosions of O-Ne-Mg cores, the Crab supernova, and subluminous type II-P supernovae. *Astron. Astrophys.*, 450:345, April 2006.

Kochanek, C. S., Beacom, J. F., Kistler, M. D., Prieto, J. L., Stanek, K. Z., Thompson, T. A., and Yüksel, H. A Survey About Nothing: Monitoring a Million Supergiants for Failed Supernovae. *Astrophys. J.*, 684:1336, September 2008.

Kotake, K., Yamada, S., and Sato, K. Gravitational radiation from axisymmetric rotational core collapse. *Phys. Rev. D.*, 68:044023, August 2003.

Kuroda, T., Kotake, K., and Takiwaki, T. Fully General Relativistic Simulations of Core-Collapse Supernovae with An Approximate Neutrino Transport. *Submitted to the Astrophys. J.; arXiv:1202.2487*, 2012.

Lai, D., and Shapiro, S. L. Gravitational radiation from rapidly rotating nascent neutron stars. *Astrophys. J.*, 442:259, 1995.

Landau, L. On the Theory of Stars. *Phys. Z. Sowjetunion*, 1:285, 1932.

Langanke, K., Martínez-Pinedo, G., Sampaio, J. M., Dean, D. J., Hix, W. R., Messer, O. E., Mezzacappa, A., Liebendörfer, M., Janka, H.-T., and Rampp, M. Electron Capture Rates on Nuclei and Implications for Stellar Core Collapse. *Phys. Rev. Lett.*, 90(24):241102, June 2003. doi: 10.1103/PhysRevLett.90.241102.

Langer, N. Mass-dependent mass loss rates of Wolf-Rayet stars. *Astron. Astrophys.*, 220:135, August 1989.

Lattimer, J. M., and Prakash, M. Neutron star observations: Prognosis for equation of state constraints. *Phys. Rep.*, 442:109, April 2007.

Lattimer, J. M., and Prakash, M. What a Two Solar Mass Neutron Star Really Means. In Lee, S., editor, *From Nuclei to Stars: Festschrift in Honor of Gerald E. Brown. arXiv:1012.3208*. World Scientific Publishing, UK, July 2011.

Lattimer, J. M., and Swesty, F. D. A Generalized Equation of State for Hot, Dense Matter. *Nucl. Phys. A*, 535:331, 1991.

Lattimer, J. M., Pethick, C. J., Ravenhall, D. G., and Lamb, D. Q. Physical properties of hot, dense matter: The general case. *Nuc. Phys. A*, 432:646, January 1985.

Law, N. M., Kulkarni, S. R., Dekany, R. G., Ofek, E. O., Quimby, R. M., Nugent, P. E., Surace, J., Grillmair, C. C., Bloom, J. S., Kasliwal, M. M., Bildsten, L., Brown, T., Cenko, S. B., Ciardi, D., Croner, E., Djorgovski, S. G., van Eyken, J., Filippenko, A. V., Fox, D. B., Gal-Yam, A., Hale, D., Hamam, N., Helou, G., Henning, J., Howell, D. A., Jacobsen, J., Laher, R., Mattingly, S., McKenna, D., Pickles, A., Poznanski, D., Rahmer, G., Rau, A., Rosing, W., Shara, M., Smith, R., Starr, D., Sullivan, M., Velur, V., Walters, R., and Zolkower, J. The Palomar Transient Factory: System Overview, Performance, and First Results. *Pub. Astron. Soc. Pac.*, 121:1395, December 2009.

LeBlanc, J. M., and Wilson, J. R. A Numerical Example of the Collapse of a Rotating Magnetized Star. *Astrophys. J.*, 161:541, August 1970.

Lentz, E. J., Mezzacappa, A., Bronson Messer, O. E., Liebendörfer, M., Hix, W. R., and Bruenn, S. W. On the Requirements for Realistic Modeling of Neutrino Transport in Simulations of Core-Collapse Supernovae. *Astrophys. J. in press, arXiv:1112.3595*, December 2011.

Levermore, C. D., and Pomraning, G. C. A flux-limited diffusion theory. *Astrophys. J.*, 248:321, August 1981. doi: 10.1086/159157.

Li, W., Leaman, J., Chornock, R., Filippenko, A. V., Poznanski, D., Ganeshalingam, M., Wang, X., Modjaz, M., Jha, S., Foley, R. J., and Smith, N. Nearby supernova rates from the Lick Observatory Supernova Search - II. The observed luminosity functions and fractions of supernovae in a complete sample. *Mon. Not. Roy. Astron. Soc.*, 412:1441, April 2011. doi: 10.1111/j.1365-2966.2011.18160.x.

Liebendörfer, M. A Simple Parameterization of the Consequences of Deleptonization for Simulations of Stellar Core Collapse. *Astrophys. J.*, 633:1042, November 2005.

Liebendörfer, M. *Private communiciation*, 2011.

Liebendörfer, M., Mezzacappa, A., Thielemann, F.-K., Messer, O. E., Hix, W. R., and Bruenn, S. W. Probing the gravitational well: No supernova explosion in spherical symmetry with general relativistic Boltzmann neutrino transport. *Phys. Rev. D.*, 63(10):103004, May 2001. doi: 10.1103/PhysRevD.63.103004.

Liebendörfer, M., Rosswog, S., and Thielemann, F.-K. An Adaptive Grid, Implicit Code for Spherically Symmetric, General Relativistic Hydrodynamics in Comoving Coordinates. *Astrophys. J. Supp. Ser.*, 141:229, July 2002.

Liebendörfer, M., Messer, O. E. B., Mezzacappa, A., Bruenn, S. W., Cardall, C. Y., and Thielemann, F.-K. A Finite Difference Representation of Neutrino Radiation Hydrodynamics in Spherically Symmetric General Relativistic Spacetime. *Astrophys. J. Supp. Ser.*, 150:263, January 2004.

Liebendörfer, M., Rampp, M., Janka, H.-T., and Mezzacappa, A. Supernova Simulations with Boltzmann Neutrino Transport: A Comparison of Methods. *Astrophys. J.*, 620:840, February 2005.

Liebendörfer, M., Whitehouse, S. C., and Fischer, T. The Isotropic Diffusion Source Approximation for Supernova Neutrino Transport. *Astrophys. J.*, 698:1174, June 2009.

LIGO. URL http://ligo.caltech.edu. Laser Interferometer Gravitational Wave Observatory.

Limongi, M., and Chieffi, A. The Nucleosynthesis of $^{26}$Al and $^{60}$Fe in Solar Metallicity Stars Extending in Mass from 11 to 120 $M_{\odot}$: The Hydrostatic and Explosive Contributions. *Astrophys. J.*, 647:483, August 2006.

Limongi, M., and Chieffi, A. Presupernova evolution and explosion of massive stars: the role of mass loss during the Wolf-Rayet stage. *Mem. Soc. Ast. Ital.*, 80:151, 2009.

Lindquist, R. W. Relativistic transport theory. *Annals of Physics*, 37:487–518, May 1966. doi: 10.1016/0003-4916(66)90207-7.

Livne, E., Burrows, A., Walder, R., Lichtenstadt, I., and Thompson, T. A. Two-dimensional, Time-dependent, Multigroup, Multiangle Radiation Hydrodynamics Test Simulation in the Core-Collapse Supernova Context. *Astrophys. J.*, 609:277, July 2004.

Logue, J., Ott, C. D., Heng, I. S., Kalmus, P., and Scargill, J. Inferring Core-Collapse Supernova Physics with Gravitational Waves. *Submitted to Phys. Rev. D.; arXiv:1202.3256*, February 2012.

Lund, T., Marek, A., Lunardini, C., Janka, H.-T., and Raffelt, G. Fast time variations of supernova neutrino fluxes and their detectability. *Phys. Rev. D.*, 82:063007, September 2010.

MacFadyen, A. I., Woosley, S. E., and Heger, A. Supernovae, Jets, and Collapsars. *Astrophys. J.*, 550:410, March 2001.

Maeder, A., and Meynet, G. Rotating massive stars: From first stars to gamma ray bursts. *Rev. of Mod. Phys.*, 84:25, January 2012. doi: 10.1103/RevModPhys.84.25.

Marek, A., and Janka, H.-T. Delayed Neutrino-Driven Supernova Explosions Aided by the Standing Accretion-Shock Instability. *Astrophys. J.*, 694:664, March 2009. doi: 10.1088/0004-637X/694/1/664.

Marek, A., Janka, H.-T., Buras, R., Liebendörfer, M., and Rampp, M. On ion-ion correlation effects during stellar core collapse. *Astron. Astrophys.*, 443:201, November 2005. doi: 10.1051/0004-6361:20053236.

Martí, J. M., and Müller, E. Numerical Hydrodynamics in Special Relativity. *Liv. Rev. Rel.*, 6:7, December 2003.

Marti, J. M., Ibanez, J. M., and Miralles, J. A. Godunov-type methods for stellar collapse. *Astron. Astrophys.*, 235:535, August 1990.

Martí, J. M., Ibáñez, J. M., and Miralles, J. A. Numerical relativistic hydrodynamics: Local characteristic approach. *Phys. Rev. D.*, 43:3794, 1991. doi: 10.1103/PhysRevD.43.3794.

May, M. M., and White, R. H. Hydrodynamic Calculations of General-Relativistic Collapse. *Phys. Rev.*, 141:1232, January 1966.

Metzger, B. D., Giannios, D., Thompson, T. A., Bucciantini, N., and Quataert, E. The protomagnetar model for gamma-ray bursts. *Mon. Not. Roy. Astron. Soc.*, 413:2031, May 2011.

Meynet, G., and Maeder, A. Stellar evolution with rotation. X. Wolf-Rayet star populations at solar metallicity. *Astron. Astrophys.*, 404:975, June 2003. doi: 10.1051/0004-6361:20030512.

Mezzacappa, A., and Bruenn, S. W. Type II supernovae and Boltzmann neutrino transport—The infall phase. *Astrophys. J.*, 405:637, March 1993a. doi: 10.1086/172394.

Mezzacappa, A., and Bruenn, S. W. A numerical method for solving the neutrino Boltzmann equation coupled to spherically symmetric stellar core collapse. *Astrophys. J.*, 405:669, March 1993b.

Mezzacappa, A., and Bruenn, S. W. Stellar core collapse—A Boltzmann treatment of neutrino-electron scattering. *Astrophys. J.*, 410:740, June 1993c.

Mezzacappa, A., and Matzner, R. A. Computer simulation of time-dependent, spherically symmetric spacetimes containing radiating fluids—Formalism and code tests. *Astrophys. J.*, 343:853, August 1989.

Miller, A. A., Chornock, R., Perley, D. A., Ganeshalingam, M., Li, W., Butler, N. R., Bloom, J. S., Smith, N., Modjaz, M., Poznanski, D., Filippenko, A. V., Griffith, C. V., Shiode, J. H., and Silverman, J. M. The Exceptionally Luminous Type II-Linear Supernova 2008es. *Astrophys. J.*, 690:1303, January 2009. doi: 10.1088/0004-637X/690/2/1303.

Minerbo, G. N. Maximum entropy Eddington factors. *J. Quant. Spec. Radiat. Transf.*, 20:541, 1978. doi: 10.1016/0022-4073(78)90024-9.

Miralles, J. A., Ibanez, J. M., Marti, J. M., and Perez, A. Incompressibility of hot nuclear matter, general relativistic stellar collapse and shock propagation. *Astron. Astrophys. Suppl.*, 90:283, October 1991.

Misner, C. W., and Sharp, D. H. Relativistic Equations for Adiabatic, Spherically Symmetric Gravitational Collapse. *Phys. Rev.*, 136:571, October 1964.

Misner, C. W., Thorne, K. S., and Wheeler, J. A. *Gravitation*. San Francisco: W.H. Freeman and Co., 1973.

Modjaz, M., Kewley, L., Kirshner, R. P., Stanek, K. Z., Challis, P., Garnavich, P. M., Greene, J. E., Kelly, P. L., and Prieto, J. L. Measured Metallicities at the Sites of Nearby Broad-Lined Type Ic Supernovae and Implications for the Supernovae Gamma-Ray Burst Connection. *Astron. J.*, 135: 1136, April 2008. doi: 10.1088/0004-6256/135/4/1136.

Moiseenko, S. G., Bisnovatyi-Kogan, G. S., and Ardeljan, N. V. A magnetorotational core-collapse model with jets. *Mon. Not. Roy. Astron. Soc.*, 370:501, July 2006. doi: 10.1111/j.1365-2966.2006.10517.x.

Mueller, B., Marek, A., Janka, H.-T., and Dimmelmeier, H. General Relativistic Explosion Models of Core-Collapse Supernovae. *Submitted to the Astrophys. J.;arXiv:1112.1920*, December 2011.

Müller, B. *Multi-dimensional relativistic simulations of core-collapse supernovae with energy-dependent neutrino transport*. PhD thesis, Technische Universität München, München, Germany, 2009.

Müller, B., Janka, H.-T., and Dimmelmeier, H. A New Multi-dimensional General Relativistic Neutrino Hydrodynamic Code for Core-collapse Supernovae. I. Method and Code Tests in Spherical Symmetry. *Astrophys. J. Supp. Ser.*, 189:104, July 2010. doi: 10.1088/0067-0049/189/1/104.

Müller, B., Janka, H.-T., Marek, A., Hanke, F., Wongwathanarat, A., and Müller, E. Core-Collapse Supernovae: Explosion Dynamics, Neutrinos and Gravitational Waves. *arXiv:1112.1913*, December 2011.

Müller, B., Janka, H.-T., and Marek, A. A New Multi-Dimensional General Relativistic Neutrino Hydrodynamics Code for Core-Collapse Supernovae II. Relativistic Explosion Models of Core-Collapse Supernovae. *Submitted to the Astrophys. J. ArXiv:1202.0815*, February 2012.

Murphy, J. W., and Burrows, A. Criteria for Core-Collapse Supernova Explosions by the Neutrino Mechanism. *Astrophys. J.*, 688:1159, December 2008. doi: 10.1086/592214.

Nieuwenhuijzen, H., and de Jager, C. Parametrization of stellar rates of mass loss as functions of the fundamental stellar parameters M, L, and R. *Astron. Astrophys.*, 231:134, May 1990.

Noble, S. C. A Numerical Study of Relativistic Fluid Collapse. *PhD Thesis, University of Britsh Columbia, arXiv:gr-qc/0310116*, 2003.

Nordhaus, J., Brandt, T. D., Burrows, A., Livne, E., and Ott, C. D. Theoretical support for the hydrodynamic mechanism of pulsar kicks. *Phys. Rev. D.*, 82(10):103016, November 2010a. doi: 10.1103/PhysRevD.82.103016.

Nordhaus, J., Burrows, A., Almgren, A., and Bell, J. Dimension as a Key to the Neutrino Mechanism of Core-Collapse Supernova Explosions. *Astrophys. J.*, 720:694, September 2010b.

Nugis, T., and Lamers, H. J. G. L. M. Mass-loss rates of Wolf-Rayet stars as a function of stellar parameters. *Astron. Astrophys.*, 360:227, August 2000.

Obergaulinger, M., and Janka, H.-T. Magnetic field amplification in collapsing, non-rotating stellar cores. *Submitted to Astron. AstrophysicsArXiv e-prints*, January 2011.

Obergaulinger, M., Aloy, M. A., Dimmelmeier, H., and Müller, E. Axisymmetric simulations of magnetorotational core collapse: approximate inclusion of general relativistic effects. *Astron. Astrophys.*, 457:209, October 2006a.

Obergaulinger, M., Aloy, M. A., and Müller, E. Axisymmetric simulations of magneto-rotational core collapse: dynamics and gravitational wave signal. *Astron. Astrophys.*, 450:1107, May 2006b.

Obergaulinger, M., Cerdá-Durán, P., Müller, E., and Aloy, M. A. Semi-global simulations of the magneto-rotational instability in core collapse supernovae. *Astron. Astrophys.*, 498:241, April 2009. doi: 10.1051/0004-6361/200811323.

O'Connor, E., and Ott, C. D. Thermal Effects on Black Hole Formation in Failed Core-Collapse Supernovae. In *11th Symposium on Nuclei in the Cosmos, July 19–23, 2010, Heidelberg, Germany*, Proceedings of Science, page 154, 2010.

O'Connor, E., and Ott, C. D. Black Hole Formation in Failing Core-Collapse Supernovae. *Astrophys. J.*, 730:70, April 2011.

Oppenheimer, J. R., and Volkoff, G. M. On Massive Neutron Cores. *Phys. Rev.*, 55:374, February 1939.

Ott, C. D. *Stellar Iron Core Collapse in 3+1 General Relativity and The Gravitational Wave Signature of Core-Collapse Supernovae*. PhD thesis, Universität Potsdam, Potsdam, Germany, 2006. URL http://nbn-resolving.de/urn/resolver.pl?urn=urn:nbn:de:kobv:517-opus-12986.

Ott, C. D. TOPICAL REVIEW: The gravitational-wave signature of core-collapse supernovae. *Class. Quantum Grav.*, 26:063001, March 2009. doi: 10.1088/0264-9381/26/6/063001.

Ott, C. D., Burrows, A., Dessart, L., and Livne, E. A New Mechanism for Gravitational-Wave Emission in Core-Collapse Supernovae. *Phys. Rev. Lett.*, 96:201102, May 2006a.

Ott, C. D., Burrows, A., Thompson, T. A., Livne, E., and Walder, R. The Spin Periods and Rotational Profiles of Neutron Stars at Birth. *Astrophys. J. Suppl. Ser.*, 164:130, May 2006b.

Ott, C. D., Dimmelmeier, H., Marek, A., Janka, H.-T., Hawke, I., Zink, B., and Schnetter, E. 3D Collapse of Rotating Stellar Iron Cores in General Relativity Including Deleptonization and a Nuclear Equation of State. *Phys. Rev. Lett.*, 98:261101, June 2007a.

Ott, C. D., Dimmelmeier, H., Marek, A., Janka, H.-T., Zink, B., Hawke, I., and Schnetter, E. Rotating collapse of stellar iron cores in general relativity. *Class. Quantum Grav.*, 24:139, June 2007b.

Ott, C. D., Burrows, A., Dessart, L., and Livne, E. Two-Dimensional Multiangle, Multigroup Neutrino Radiation-Hydrodynamic Simulations of Postbounce Supernova Cores. *Astrophys. J.*, 685:1069, 2008.

Ott, C. D., Reisswig, C., Schnetter, E., O'Connor, E., Sperhake, U., Löffler, F., Diener, P., Abdikamalov, E., Hawke, I., and Burrows, A. Dynamics and Gravitational Wave Signature of Collapsar Formation. *Phys. Rev. Lett.*, 106:161103, April 2011.

Ott, C. D., Abdikamalov, E., O'Connor, E., Reisswig, C., Haas, R., Kalmus, P., Drasco, S., Burrows, A., and Schnetter, E. Correlated Gravitational Wave and Neutrino Signals from General-Relativistic Rapidly Rotating Iron Core Collapse. *Submitted to Phys. Rev. D.; arXiv:1204.0512*, April 2012.

Özel, F., Baym, G., and Güver, T. Astrophysical measurement of the equation of state of neutron star matter. *Phys. Rev. D.*, 82:101301, November 2010. doi: 10.1103/PhysRevD.82.101301.

Özel, F., Psaltis, D., Narayan, R., and McClintock, J. E. The Black Hole Mass Distribution in the Galaxy. *ArXiv e-prints*, June 2010.

Özel, F., Psaltis, D., Ransom, S., Demorest, P., and Alford, M. The Massive Pulsar PSR J1614-2230: Linking Quantum Chromodynamics, Gamma-ray Bursts, and Gravitational Wave Astronomy. *Astrophys. J. Lett.*, 724:L199, December 2010. doi: 10.1088/2041-8205/724/2/L199.

Özel, F., Psaltis, D., Narayan, R., and Santos Villarreal, A. On the Mass Distribution and Birth Masses of Neutron Stars. *ArXiv e-prints*, January 2012.

Paxton, B., Bildsten, L., Dotter, A., Herwig, F., Lesaffre, P., and Timmes, F. Modules for Experiments in Stellar Astrophysics (MESA). *Astrophys. J. Supp. Ser.*, 192:3, January 2011. doi: 10.1088/0067-0049/192/1/3.

Pejcha, O., and Thompson, T. A. The Physics of the Neutrino Mechanism of Core-collapse Supernovae. *Astrophys. J.*, 746:106, February 2012. doi: 10.1088/0004-637X/746/1/106.

Pejcha, O., Thompson, T. A., and Kochanek, C. S. The observed neutron star mass distribution as a probe of the supernova explosion mechanism. *ArXiv e-prints*, April 2012.

Penrose, R. Gravitational Collapse: the Role of General Relativity. *Nuovo Cimento Rivista Serie*, 1:252, 1969.

Petrich, L. I., Shapiro, S. L., and Teukolsky, S. A. Oppenheimer-Snyder collapse in polar time slicing. *Phys. Rev. D.*, 33:2100, April 1986. doi: 10.1103/PhysRevD.33.2100.

Pons, J. A., Miralles, J. A., and Ibáñez, J. M. General Relativistic Neutrino Transport. In J. A. Miralles, J. A. Morales, and D. Saez, , editor, *Some Topics on General Relativity and Gravitational Radiation*, page 293, 1997.

Pons, J. A., Reddy, S., Prakash, M., Lattimer, J. M., and Miralles, J. A. Evolution of Proto-Neutron Stars. *Astrophys. J.*, 513:780, March 1999. doi: 10.1086/306889.

Pons, J. A., Ibáñez, J. M., and Miralles, J. A. Hyperbolic character of the angular moment equations of radiative transfer and numerical methods. *Mon. Not. Roy. Astron. Soc.*, 317:550, September 2000.

Puls, J., Markova, N., Scuderi, S., Stanghellini, C., Taranova, O. G., Burnley, A. W., and Howarth, I. D. Bright OB stars in the Galaxy. III. Constraints on the radial stratification of the clumping factor in hot star winds from a combined $H_\alpha$, IR and radio analysis. *Astron. Astrophys.*, 454:625, August 2006.

Quataert, E., and Shiode, J. Wave-Driven Mass Loss in the Last Year of Stellar Evolution: Setting the Stage for the Most Luminous Core-Collapse Supernovae. *Accepted for publication by MNRAS; arXiv:1202.5036*, February 2012.

Rampp, M., and Janka, H.-T. Spherically Symmetric Simulation with Boltzmann Neutrino Transport of Core Collapse and Postbounce Evolution of a 15 M solar mass Star. *Astrophys. J. Lett.*, 539:L33, August 2000.

Rampp, M., and Janka, H.-T. Radiation hydrodynamics with neutrinos. Variable Eddington factor method for core-collapse supernova simulations. *Astron. Astrophys.*, 396:361, December 2002.

Read, J. S., Lackey, B. D., Owen, B. J., and Friedman, J. L. Constraints on a phenomenologically parametrized neutron-star equation of state. *Phys. Rev. D.*, 79:124032, June 2009.

Remillard, R. A., and McClintock, J. E. X-Ray Properties of Black-Hole Binaries. *Ann. Rev. Astron. Astroph.*, 44:49, September 2006. doi: 10.1146/annurev.astro.44.051905.092532.

Romero, J. V., Ibanez, J. M., Marti, J. M., and Miralles, J. A. A New Spherically Symmetric General Relativistic Hydrodynamical Code. *Astrophys. J.*, 462:839, May 1996.

Romero, J. V., Miralles, J. M., Ibáñez, J. A., and Pons, J. A. General Relativistic Collapse of Hot Stellar Cores. In J. A. Miralles, J. A. Morales, D. Saez, , editor, *Some Topics on General Relativity and Gravitational Radiation*, page 289. Paris: Editions Frontieres, 1997.

Rosswog, S., and Liebendörfer, M. High-resolution calculations of merging neutron stars—II. Neutrino emission. *Mon. Not. Roy. Astron. Soc.*, 342:673, July 2003.

Rosswog, S., Ramirez-Ruiz, E., and Davies, M. B. High-resolution calculations of merging neutron stars—III. Gamma-ray bursts. *Mon. Not. Roy. Astron. Soc.*, 345:1077, 2003.

Ruffert, M., Janka, H.-T., and Schäfer, G. Coalescing neutron stars - a step towards physical models. I. Hydrodynamic evolution and gravitational-wave emission. *Astron. Astrophys.*, 311:532, July 1996.

Sagert, I., Fischer, T., Hempel, M., Pagliara, G., Schaffner-Bielich, J., Mezzacappa, A., Thielemann, F.-K., and Liebendörfer, M. Signals of the QCD Phase Transition in Core-Collapse Supernovae. *Phys. Rev. Lett.*, 102:081101, February 2009.

Saijo, M., Baumgarte, T. W., and Shapiro, S. L. One-armed Spiral Instability in Differentially Rotating Stars. *Astrophys. J.*, 595:352, September 2003.

Salpeter, E. E. The Luminosity Function and Stellar Evolution. *Astrophys. J.*, 121:161, January 1955. doi: 10.1086/145971.

Scheidegger, S., Fischer, T., Whitehouse, S. C., and Liebendörfer, M. Gravitational waves from 3D MHD core collapse simulations. *Astron. Astrophys.*, 490:231, 2008.

Schinder, P. J., Bludman, S. A., and Piran, T. General-relativistic implicit hydrodynamics in polar-sliced space-time. *Phys. Rev. D.*, 37:2722, May 1988.

Sedov, L. I. *Similarity and Dimensional Methods in Mechanics*. 1959.

Sekiguchi, Y. An implementation of the microphysics in full general relativity: a general relativistic neutrino leakage scheme. *Class. Quantum Grav.*, 27:114107, June 2010.

Sekiguchi, Y., and Shibata, M. Formation of Black Hole and Accretion Disk in a Massive High-entropy Stellar Core Collapse. *Astrophys. J.*, 737:6, August 2011. doi: 10.1088/0004-637X/737/1/6.

Sekiguchi, Y.-I., and Shibata, M. New criterion for direct black hole formation in rapidly rotating stellar collapse. *Phys. Rev. D.*, 70:084005, October 2004.

Sekiguchi, Y.-I., and Shibata, M. Axisymmetric collapse simulations of rotating massive stellar cores in full general relativity: Numerical study for prompt black hole formation. *Phys. Rev. D.*, 71:084013, April 2005.

Shapiro, L. S., and Teukolsky, S. A. *Black Holes, White Dwarfs and Neutron Stars*. John Wiley & Sons, New York U. S. A., 1983.

Shapiro, S. L., and Teukolsky, S. A. Gravitational collapse of supermassive stars to black holes—Numerical solution of the Einstein equations. *Astrophys. J. Lett.*, 234:L177, December 1979. doi: 10.1086/183134.

Shapiro, S. L., and Teukolsky, S. A. Gravitational collapse to neutron stars and black holes—Computer generation of spherical spacetimes. *Astrophys. J.*, 235:199, January 1980.

Shen, G., Horowitz, C. J., and O'Connor, E. Second relativistic mean field and virial equation of state for astrophysical simulations. *Phys. Rev. C*, 83:065808, June 2011a. doi: 10.1103/PhysRevC.83.065808.

Shen, G., Horowitz, C. J., and Teige, S. New equation of state for astrophysical simulations. *Phys. Rev. C*, 83:035802, March 2011b. doi: 10.1103/PhysRevC.83.035802.

Shen, H., Toki, H., Oyamatsu, K., and Sumiyoshi, K. Relativistic equation of state of nuclear matter for supernova and neutron star. *Nucl. Phys. A*, 637:435, July 1998a. URL http://user.numazu-ct.ac.jp/$\sim$sumi/eos.

Shen, H., Toki, H., Oyamatsu, K., and Sumiyoshi, K. Relativistic Equation of State of Nuclear Matter for Supernova Explosion. *Prog. Th. Phys.*, 100:1013, November 1998b.

Shen, H., Toki, H., Oyamatsu, K., and Sumiyoshi, K. Relativistic Equation of State for Core-Collapse Supernova Simulations. *Submitted to the Astrophys. J., arXiv:1105.1666*, May 2011c.

Shibata, M., and Sekiguchi, Y. Gravitational waves from axisymmetric rotating stellar core collapse to a neutron star in full general relativity. *Phys. Rev. D*, 69:084024, April 2004.

Shibata, M., and Sekiguchi, Y.-I. Three-dimensional simulations of stellar core collapse in full general relativity: Nonaxisymmetric dynamical instabilities. *Phys. Rev. D.*, 71:024014, January 2005.

Shibata, M., Liu, Y. T., Shapiro, S. L., and Stephens, B. C. Magnetorotational collapse of massive stellar cores to neutron stars: Simulations in full general relativity. *Phys. Rev. D.*, 74:104026, November 2006.

Shibata, M., Kiuchi, K., Sekiguchi, Y., and Suwa, Y. Truncated Moment Formalism for Radiation Hydrodynamics in Numerical Relativity. *Prog. Th. Phys.*, 125:1255, June 2011.

Smartt, S. J., Eldridge, J. J., Crockett, R. M., and Maund, J. R. The death of massive stars - I. Observational constraints on the progenitors of Type II-P supernovae. *Mon. Not. Roy. Astron. Soc.*, 395:1409, May 2009.

Smit, J. M., Cernohorsky, J., and Dullemond, C. P. Hyperbolicity and critical points in two-moment approximate radiative transfer. *Astron. Astrophys.*, 325:203, September 1997.

Smith, N., Li, W., Filippenko, A. V., and Chornock, R. Observed fractions of core-collapse supernova types and initial masses of their single and binary progenitor stars. *Mon. Not. Roy. Astron. Soc.*, 412:1522, April 2011.

Smith, Nathan. Episodic mass loss and pre-sn circumstellar envelopes. *Proceedings of the International Astronomical Union*, 3(Symposium S250):193, 2007. doi: 10.1017/S1743921308020498. URL http://journals.cambridge.org/action/displayAbstract?fromPage=online&aid=1909288&fulltextType=RA&fileId=S1743921308020498.

SNO+. URL http://snoplus.phy.queensu.ca/. Sudbury Neutrino Observatory +.

Steffen, M. A Simple Method for Monotonic Interpolation in One Dimension. *Astron. Astrophys.*, 239:443, November 1990.

Steiner, A. W., Lattimer, J. M., and Brown, E. F. The Equation of State from Observed Masses and Radii of Neutron Stars. *Astrophys. J.*, 722:33, October 2010.

Stergioulas, N. Rotating stars in relativity. *Liv. Rev. Rel.*, 6:3, 2003.

Sukhbold, T., 2011.

Sumiyoshi, K., and Yamada, S. Neutrino Transfer in Three Dimensions for Core-collapse Supernovae. I. Static Configurations. *Astrophys. J. Supp. Ser.*, 199:17, March 2012. doi: 10.1088/0067-0049/199/1/17.

Sumiyoshi, K., Yamada, S., Suzuki, H., Shen, H., Chiba, S., and Toki, H. Postbounce Evolution of Core-Collapse Supernovae: Long-Term Effects of the Equation of State. *Astrophys. J.*, 629:922, August 2005.

Sumiyoshi, K., Yamada, S., and Suzuki, H. Dynamics and Neutrino Signal of Black Hole Formation in Nonrotating Failed Supernovae. I. Equation of State Dependence. *Astrophys. J.*, 667:382, September 2007.

Sumiyoshi, K., Yamada, S., and Suzuki, H. Dynamics and Neutrino Signal of Black Hole Formation in Nonrotating Failed Supernovae. II. Progenitor Dependence. *Astrophys. J.*, 688:1176–1185, December 2008. doi: 10.1086/592183.

Sumiyoshi, K., Ishizuka, C., Ohnishi, A., Yamada, S., and Suzuki, H. Emergence of Hyperons in Failed Supernovae: Trigger of the Black Hole Formation. *Astrophys. J. Lett.*, 690:L43–L46, January 2009. doi: 10.1088/0004-637X/690/1/L43.

Super-Kamiokande. URL http://neutrino.phys.washington.edu/~superk.

Suwa, Y., Kotake, K., Takiwaki, T., Whitehouse, S. C., Liebendörfer, M., and Sato, K. Explosion Geometry of a Rotating 13 $M_{\odot}$ Star Driven by the SASI-Aided Neutrino-Heating Supernova Mechanism. *Pub. Astr. Soc. Jap.*, 62:L49, December 2010.

Suwa, Y., Kotake, K., Takiwaki, T., Liebendörfer, M., and Sato, K. Impacts of collective neutrino oscillations on core-collapse supernova explosions. *Astrophys. J.*, 738:165, 2011. doi: 10.1088/0004-637X/738/2/165.

Swesty, F. D. Implicit general relativistic hydrodynamic methods for modeling the late-time explosion mechanism in core collapse supernovae. *Astrophys. J.*, 445:811, June 1995.

Swesty, F. D., and Myra, E. S. A Numerical Algorithm for Modeling Multigroup Neutrino-Radiation Hydrodynamics in Two Spatial Dimensions. *Astrophys. J. Supp. Ser.*, 181:1, March 2009. doi: 10.1088/0067-0049/181/1/1.

Takahashi, K., El Eid, M. F., and Hillebrandt, W. Beta transition rates in hot and dense matter. *Astron. Astrophys.*, 67:185, July 1978.

Takiwaki, T., and Kotake, K. Gravitational Wave Signatures of Magnetohydrodynamically Driven Core-collapse Supernova Explosions. *Astrophys. J.*, 743:30, 2011. doi: 10.1088/0004-637X/743/1/30.

Takiwaki, T., Kotake, K., Nagataki, S., and Sato, K. Magneto-driven Shock Waves in Core-Collapse Supernovae. *Astrophys. J.*, 616:1086, December 2004. doi: 10.1086/424993.

Tasker, E. J., Brunino, R., Mitchell, N. L., Michielsen, D., Hopton, S., Pearce, F. R., Bryan, G. L., and Theuns, T. A test suite for quantitative comparison of hydrodynamic codes in astrophysics. *Mon. Not. Roy. Astron. Soc.*, 390:1267, November 2008. doi: 10.1111/j.1365-2966.2008.13836.x.

Thompson, T. A. *Topics in the theory of core-collapse supernovae*. PhD thesis, The Univeristy of Arizona, 2002.

Thompson, T. A., Burrows, A., and Pinto, P. A. Shock Breakout in Core-Collapse Supernovae and Its Neutrino Signature. *Astrophys. J.*, 592:434, July 2003.

Thompson, T. A., Quataert, E., and Burrows, A. Viscosity and Rotation in Core-Collapse Supernovae. *Astrophys. J.*, 620:861, February 2005.

Thorne, K. S. Relativistic radiative transfer—Moment formalisms. *Mon. Not. Roy. Astron. Soc.*, 194:439, February 1981.

Timmes, F. X., and Arnett, D. The Accuracy, Consistency, and Speed of Five Equations of State for Stellar Hydrodynamics. *Astrophys. J. Supp. Ser.*, 125:277, November 1999.

Timmes, F. X., and Swesty, F. D. The Accuracy, Consistency, and Speed of an Electron-Positron Equation of State Based on Table Interpolation of the Helmholtz Free Energy. *Astrophys. J. Supp. Ser.*, 126:501, February 2000.

Timmes, F. X., Woosley, S. E., and Weaver, T. A. The Neutron Star and Black Hole Initial Mass Function. *Astrophys. J.*, 457:834, February 1996.

Typel, S., Röpke, G., Klähn, T., Blaschke, D., and Wolter, H. H. Composition and thermodynamics of nuclear matter with light clusters. *Phys. Rev. C*, 81:015803, January 2010. doi: 10.1103/PhysRevC.81.015803.

van Leer, B. J. *J. Comp. Phys.*, 23:276, 1977.

van Riper, K. A. General relativistic hydrodynamics and the adiabatic collapse of stellar cores. *Astrophys. J.*, 232:558, September 1979.

van Riper, K. A., and Arnett, W. D. Stellar collapse and explosion—Hydrodynamics of the core. *Astrophys. J. Lett.*, 225:L129, November 1978.

Vink, J. S., and de Koter, A. On the metallicity dependence of Wolf-Rayet winds. *Astron. Astrophys.*, 442:587, November 2005. doi: 10.1051/0004-6361:20052862.

Vink, J. S., de Koter, A., and Lamers, H. J. G. L. M. New theoretical mass-loss rates of O and B stars. *Astron. Astrophys.*, 362:295, October 2000.

Vink, J. S., de Koter, A., and Lamers, H. J. G. L. M. Mass-loss predictions for O and B stars as a function of metallicity. *Astron. Astrophys.*, 369:574, April 2001. doi: 10.1051/0004-6361:20010127.

Virgo. URL http://www.virgo.infn.it.

Vogel, P. Future galactic supernova neutrino signal: What can we learn? *Progress in Particle and Nuclear Physics*, 48:29, 2002. doi: 10.1016/S0146-6410(02)00108-4.

Vogel, P., and Beacom, J. F. Angular distribution of neutron inverse beta decay, $\nu_e$+p→$e^+$+n. *Phys. Rev. D.*, 60(5):053003, September 1999. doi: 10.1103/PhysRevD.60.053003.

Von Neumann, J., and Richtmyer, R. D. A Method for the Numerical Calculation of Hydrodynamic Shocks. *J. Appl. Phys.*, 21:232, March 1950.

Wang, B., and Han, Z. Progenitors of type Ia supernovae. *ArXiv e-prints*, April 2012.

Weinberg, N. N., and Quataert, E. Non-linear saturation of g-modes in proto-neutron stars: quieting the acoustic engine. *Mon. Not. Roy. Astron. Soc.*, 387:L64, June 2008.

Wellstein, S., and Langer, N. Implications of massive close binaries for black hole formation and supernovae. *Astron. Astrophys.*, 350:148, October 1999.

Wheeler, J. C., Yi, I., Höflich, P., and Wang, L. Asymmetric Supernovae, Pulsars, Magnetars, and Gamma-Ray Bursts. *Astrophys. J.*, 537:810, July 2000. doi: 10.1086/309055.

Wilson, J. R. A Numerical Study of Gravitational Stellar Collapse. *Astrophys. J.*, 163:209, January 1971.

Wilson, J. R. A numerical method for relativistic hydrodynamics. In L. L. Smarr, , editor, *Sources of Gravitational Radiation*, page 423. New York: Cambridge University Press, 1979.

Wilson, J. R. Supernovae and Post-Collapse Behavior. In Centrella, J. M., Leblanc, J. M., and Bowers, R. L., editors, *Numerical Astrophysics*, page 422, 1985.

Woosley, S. E. Gamma-ray bursts from stellar mass accretion disks around black holes. *Astrophys. J.*, 405:273, March 1993.

Woosley, S. E., and Heger, A. The Progenitor Stars of Gamma-Ray Bursts. *Astrophys. J.*, 637:914, February 2006.

Woosley, S. E., and Heger, A. Nucleosynthesis and remnants in massive stars of solar metallicity. *Phys. Rep.*, 442:269, April 2007.

Woosley, S. E., and Weaver, T. A. The Evolution and Explosion of Massive Stars. II. Explosive Hydrodynamics and Nucleosynthesis. *Astrophys. J. Supp. Ser.*, 101:181, November 1995.

Woosley, S. E., Eastman, R. G., Weaver, T. A., and Pinto, P. A. SN 1993J: A Type IIb supernova. *Astrophys. J.*, 429:300, July 1994. doi: 10.1086/174319.

Woosley, S. E., Heger, A., and Weaver, T. A. The evolution and explosion of massive stars. *Rev. Mod. Phys.*, 74:1015, November 2002.

Yakunin, K. N., Marronetti, P., Mezzacappa, A., Bruenn, S. W., Lee, C.-T., Chertkow, M. A., Hix, W. R., Blondin, J. M., Lentz, E. J., Bronson Messer, O. E., and Yoshida, S. Gravitational waves from core collapse supernovae. *Class. Quantum Grav.*, 27:194005, October 2010.

Yamada, S. An Implicit Lagrangian Code for Spherically Symmetric General Relativistic Hydrodynamics with an Approximate Riemann Solver. *Astrophys. J.*, 475:720, February 1997.

Yamada, S., and Sawai, H. Numerical Study on the Rotational Collapse of Strongly Magnetized Cores of Massive Stars. *Astrophys. J.*, 608:907, June 2004. doi: 10.1086/420760.

Yamada, S., Janka, H.-T., and Suzuki, H. Neutrino transport in type II supernovae: Boltzmann solver vs. Monte Carlo method. *Astron. Astrophys.*, 344:533, April 1999.

Yoon, S.-C., and Cantiello, M. Evolution of Massive Stars with Pulsation-driven Superwinds During the Red Supergiant Phase. *Astrophys. J. Lett.*, 717:L62, July 2010. doi: 10.1088/2041-8205/717/1/L62.

Yueh, W. R., and Buchler, J. R. Neutrino processes in dense matter. *Astrophys. Space Sci.*, 41:221, May 1976. doi: 10.1007/BF00684583.

Zhang, W., Woosley, S. E., and Heger, A. Fallback and Black Hole Production in Massive Stars. *Astrophys. J.*, 679:639, May 2008.

Zwerger, T., and Müller, E. Dynamics and gravitational wave signature of axisymmetric rotational core collapse. *Astron. Astrophys.*, 320:209, April 1997.